Spectroscopic and Microscopic Characterization of Heterogenized Molecular Catalyst Systems

by

William S. Dean

A dissertation submitted in partial fulfillment
of the requirements for the degree of
Doctor of Philosophy
(Chemistry)
in the University of Michigan
2022

Doctoral Committee:

Assistant Professor Charles McCrory, Chair
Professor Zhan Chen
Assistant Professor Andrej Lenert
Professor Steven Maldonado

William S. Dean

wsdean@umich.edu

ORCID iD: 0000-0002-6686-5387

Dedication

To Grandma and Grandpa Dean, who gave me every conceivable support

And in memory of those I lost along the way, Grandma Purdy and Uncle David

Acknowledgements

This dissertation would not have been possible without the aid of many, many people. I want to take a few lines to briefly commemorate their contributions in and out of the lab.

First, I would like to thank the current and former members of the McCrory group at the University of Michigan, who have been my friends and coworkers throughout my time. Kwan, Weixuan, Yingshuo, Jeremy, and John worked incredibly hard to get the lab off the ground, and their guidance and mentorship throughout my graduate career were pivotal in my success. Sam and Bobby joined the lab the same year I did and have been exceptional companions and amiable debaters throughout. It has been an absolute honor to work with Taylor, my most frequent collaborator and sometime housemate, who works twice as hard as anyone else I know. Kevin was a beacon of sunshine even on the gloomiest Michigan days. I'm just starting to get to know Jukai, Lirong, Maiko, and Libo but I am grateful for their support during my final year of my Ph.D.

I've had the pleasure of knowing many other folks outside of my research group. Molly has been an incredible friend and confidant throughout my time, including a very memorable expedition to SSRL in March 2020. Bernadette and Matthew have been my housemates for the past five years, and I could not ask for more. Their support, especially in the depths of the pandemic, kept me going through some of my most difficult times. Although Rosie only lived with us for two years, his charming companionship and infectious laugh were a joy. Our neighbor Jade was an absolute rock during the deep pandemic and cooked me a meal for which I can never thank her enough.

In my first year at Michigan, I had the fortune to fall in with a much beloved group of Dweebs. We have remained fast friends through thick and thin, through store closings, graduations, house movings, and a global pandemic. So, from the bottom of my heart (and in no particular order), I want to thank Chris, Ryan, Marcus, Jim, Parker, Ryan, Chris, Connor, Harrison, and Max. I can't express how much their friendship has meant to me in the past several years, and no doubt in the many years to come. I also want to thank the Dweeb cats: Harald, Mirri, Ada, Cecil, the honorary cat Eleanor, and the late but much beloved Paul.

I would like to thank my family for all their love and support: Dad, Mom, Irene, Norman, Clio, Uncle Norman, and Uncle Thom. They all know how much they mean to me, but I can always say it again. Many thanks for celebrations in the good times, commiserations in the bad times, and unconditional love throughout. A very, very special thanks goes to my grandparents, Sharon and Harvey Dean. I probably wouldn't have come to Michigan if I hadn't had them here to welcome me, and what a welcome it was! I'm deeply indebted for all the meals, the cookies, the snacks, and most of all, the time I got to spend with them. I am so grateful I've had this opportunity to get to know them better.

On a different note, I would like to thank my thesis committee. I learned a ton during my rotation with Professor Maldonado, and I've never stopped talking about how great his electrochemistry class was. Professor Chen taught a very memorable and useful spectroscopy class and has provided healthy dose of candor in all of our interactions. Professor Lenert gave excellent advice and guidance during my committee meetings. Most of all, thank you to my long-suffering mentor and advisor, Charles McCrory. He has truly been with me through all the ups and downs of my Ph.D., mentoring me through times of trouble and always pushing me to look past my doubts and reach for something better. I cannot thank him enough.

Finally, thank you to my beloved friend Roland, who got me through the toughest times.

Table of Contents

List of Tables

List of Figures

List of Appendices

Abstract

The carbon dioxide reduction reaction (CO_2RR) is one among many electrocatalytic small molecule transformations important for a decarbonized energy economy. However, industrial CO_2 electrolyzer technologies are still far from meeting benchmarks for activity, reaction selectivity, and stability needed to be economically viable, and fundamental studies are still necessary to find methods of improving these parameters. Spectroscopic and microscopic techniques are essential tools for probing the structure, reaction microenvironment, and reaction mechanism of electrocatalyst materials for the CO_2RR, and provide key insights to supplement or inform electrochemical studies. My work has primarily focused on molecular catalyst-polymer composite materials, specifically cobalt phthalocyanine (CoPc) encapsulated in poly(4-vinylpyridine) (P4VP) and related polymers. Previous work by our group and others has shown this simple composite system to have high activity and selectivity for the CO_2RR to CO. However, little characterization work had been done with the system and many questions remained unanswered.

I first studied how the aggregation behavior of CoPc is influenced by codeposition with P4VP. I used UV-Vis to gauge the extent of CoPc monomerization in deposition solutions and in the resulting deposited layers. CoPc and other phthalocyanines readily self-associate through π-stacking interactions, but I found that axial coordination by P4VP or molecular pyridine disaggregated CoPc in deposition solutions, while polymers lacking axial coordination did not have the same effect. Upon deposition, the CoPc-P4VP composite forms a solid solution which retains the monomerization of the CoPc. Both the axial coordination and the presence of a

polymeric structure are needed to achieve a solid solution, and the non-coordinating structural analogue poly(4-vinylpyridine) also created a highly monomerized solid solution with CoPc when pyridine was added to the deposition solution. The ubiquitous binding polymer Nafion was found to be ineffective at promoting or retaining CoPc disaggregation in the deposited layer.

I also investigated how the composition of the electrolyte buffer solution influences the protonation of the P4VP layer. Previous investigations had revealed that proton delivery to catalytic sites in the CoPc-P4VP composite layer occurs primarily through a proton relay mechanism, which was expected to be influenced by solution pH. Through a combination of electrochemical and spectroscopic experiments, we confirmed that a lower bulk solution pH results in greater protonation of the P4VP layer, which is correlated with increased activity for HER and declining Faradaic efficiency for the CO_2RR. We also discovered that layer protonation, and thus HER activity, scales with the electrolyte concentration in the buffer. We attribute this effect to increased equilibrium partitioning of ions into the P4VP layer, which increases the maximum concentration of protons allowed by local charge balancing.

Eventually, our goal is to apply *in situ* spectroelectrochemical techniques to these questions. To that end, in a two-phase process I designed, constructed, and tested a spectroelectrochemical flow cell (SEC-FC) for polarization-modulation infrared reflection absorption spectroscopy (PM-IRRAS). The design was successful in some areas but was hindered by design challenges. Lessons learned from the PM-IRRAS SEC-FC will be inform future efforts to use *in situ* spectroelectrochemistry to probe the structure, microenvironment, and reaction mechanisms of electrocatalytic materials.

1. Introduction

1.0. Preface

This chapter provides background information related to my thesis work. Section 1.1 introduces the carbon dioxide reduction reaction and its challenges. Section 1.2 provides an overview of and outlook for industrially-relevant CO_2RR gas-fed reactors. Section 1.3 looks specifically at previous work on the CoPc-P4VP composite catalyst investigated in this dissertation and provides context for the relevance of my work to the broader project. Section 1.4 summarizes the findings of the investigations in subsequent chapters. Parts of Section 1.3 are modified from a manuscript originally published in *Accounts of Chemical Research*,[1] and Section 1.2 is modified from unpublished work originally prepared for that manuscript. I was a secondary author of the final manuscript, with some portions being my writing, and having made substantial contributions to structuring and editing the manuscript. Taylor L. Soucy was the primary manuscript author, and portions of Section 1.2 are derived from her contributions with some modifications.

1.1. Electrochemical Reduction of CO_2

As the world moves towards a decarbonized future powered primarily by renewable sources, the ability to transform electricity into useful chemicals is critical for replacing petrochemical precursors, storing intermittent energy, and creating clean fuels for high energy density applications. Electrochemical small molecule transformations are therefore poised to be

some of the most impactful chemical technologies of the 21st century. While water electrolysis and hydrogen fuel cell technologies have received significant attention,[2] other electrochemical transformations could prove to be players in a decarbonized economy. The oxidation of ammonia to N_2 has been investigated as an alternative fuel cell reaction,[3,4] and electrochemical N_2 reduction could be used to supplement or replace the Haber-Bosch reaction at the other end of the supply chain.[5,6] Combined hydrogen reduction and alcohol oxidation electrolyzers could be used to produce valuable chemicals on both sides of the reaction.[7]

However, electrocatalysis could also play a major role in the carbon economy itself. Electrocatalytic conversion can be used to recycle carbon dioxide (CO_2) from industrial waste streams into fuels or chemical precursors.[8-12] While the basic principles of the electrochemical CO_2 reduction reaction (CO_2RR) have been understood since the 19th century, research into the process gained traction in the 1970s and 1980s when concerns about declining fuel supplies prompted investment in a variety of alternative energy technologies. A robust CO_2 reduction industry would ease decarbonization difficulties in sectors such as aviation where chemical fuels are difficult to avoid. Ultimately, electrochemical CO_2 reduction could displace petrochemical processes by providing a carbon-negative source for a variety of crucial chemical products.[9] However, a wide array of technical and policy hurdles stands between this vision and the current state of CO_2RR technology.

Much of the foundational work on the CO_2RR was published by Hori and compiled in a seminal review in 2008.[13] While many transition metals are capable of catalyzing the CO_2RR, Hori demonstrated that Cu metal has high current densities and the nearly unique ability to produce multi-carbon (C_{2+}) products such as ethane and ethanol. However, while Cu electrocatalysts have excellent *activity* (in terms of mA/cm^2, current passed per unit time per unit of surface area), Cu

suffers from significant *selectivity* issues. Despite the common terminology, the CO_2RR is not a single reaction, but any combination of several different reactions leading to a variety of products. Key CO_2 reduction reactions are noted in Equations 1-7, arranged by the number of electrons transferred, corresponding roughly to the difficulty in obtaining the product. Additionally, CO_2 reduction competes with the hydrogen evolution reaction (HER, Equation 8.) Note that the reaction equations are in the form of cathodic half-reactions, with neutral water as the proton source—the dominant form of the reaction in most neutral or basic media. In principle the half reactions could be balanced by any oxidation reaction, but reoxidation of OH^- to H_2O is the most likely case.

$$CO_2 + H_2O + 2e^- \rightarrow CO + 2OH^- \quad (1)$$

$$CO_2 + 2H_2O + 2e^- \rightarrow HCOOH + 2OH^- \quad (2)$$

$$CO_2 + 5H_2O + 6e^- \rightarrow CH_3OH + 6OH^- \quad (3)$$

$$CO_2 + 6H_2O + 8e^- \rightarrow CH4 + 8OH^- \quad (4)$$

$$2CO_2 + 8H_2O + 12e^- \rightarrow C_2H4 + 12OH^- \quad (5)$$

$$2CO_2 + 9H_2O + 12e^- \rightarrow C_2H_5OH + 12OH^- \quad (6)$$

$$3CO_2 + 13H_2O + 18e^- \rightarrow C_3H_7OH + 18OH^- \quad (7)$$

$$H_2O + 2e^- \rightarrow H_2 + 2OH^- \quad (8)$$

The tantalizing promise of copper catalysts is their ability to produce highly reduced products, and crucially, C_{2+} products. This latter feature could lead to direct electrolysis of CO_2 to relevant fuels like ethane, ethanol, or propanol. Unfortunately, minor differences in reaction conditions trigger large changes in product distribution. Intrinsic local gradients in electrode potential and solution pH complicate matters by forcing a variation in conditions across the

electrode surface.[14] Moreover, the copper catalyst itself contains a variety of reaction sites (steps, faces, etc.) leading to further product variance.[14,15] Seemingly minor contamination of electrolyte solutions can lead to major changes in product distribution.[16] As a final complication, Cu surfaces are known to change morphology when voltage is applied.[17] Even under highly controlled conditions, Cu-catalyzed CO_2RR will produce a minimum of 2-3 products at a given applied voltage, as seen in Figure 1.1.[15] The products must then be separated downstream, limiting the overall efficiency of the system.

Molecular systems can be developed that improve selectivity at the cost of lower activity relative to metal nanoparticles.[18] At the extreme end of this spectrum, plants naturally convert CO_2 to a bewildering array of reduced products with exquisite selectivity through photosynthesis, but with very poor "activity." Bioinspired molecular catalyst systems mimic this enzymatic selectivity, at the cost of energy efficiency relative to heterogenous systems. Transition metal porphyrins and phthalocyanines, corroles, cyclams, and other metal complexes have all been studied for their CO_2 reduction activity.[19-22] Investigations of these systems have yielded tremendous insight into catalytic mechanisms, in part because of their reaction site specificity and the resulting product selectivity.[18,23] However, from a practical perspective, homogeneous molecular catalysts for the CO_2RR suffer from poor stability and solubility in aqueous solutions and are intrinsically limited by their kinetics.[24] The tension between activity and selectivity defines electrochemical CO_2RR research. Technoeconomic analyses suggest an industrial reactor for the $CO_2 \rightarrow CO$ reaction must achieve >200 mA cm^{-2} current density with 95%+ Faradaic efficiency to start making sense economically.[10,25] Industrial electrolyzers will be discussed in more depth in the following section, but the key imperative for researchers is to find a system that can achieve both.

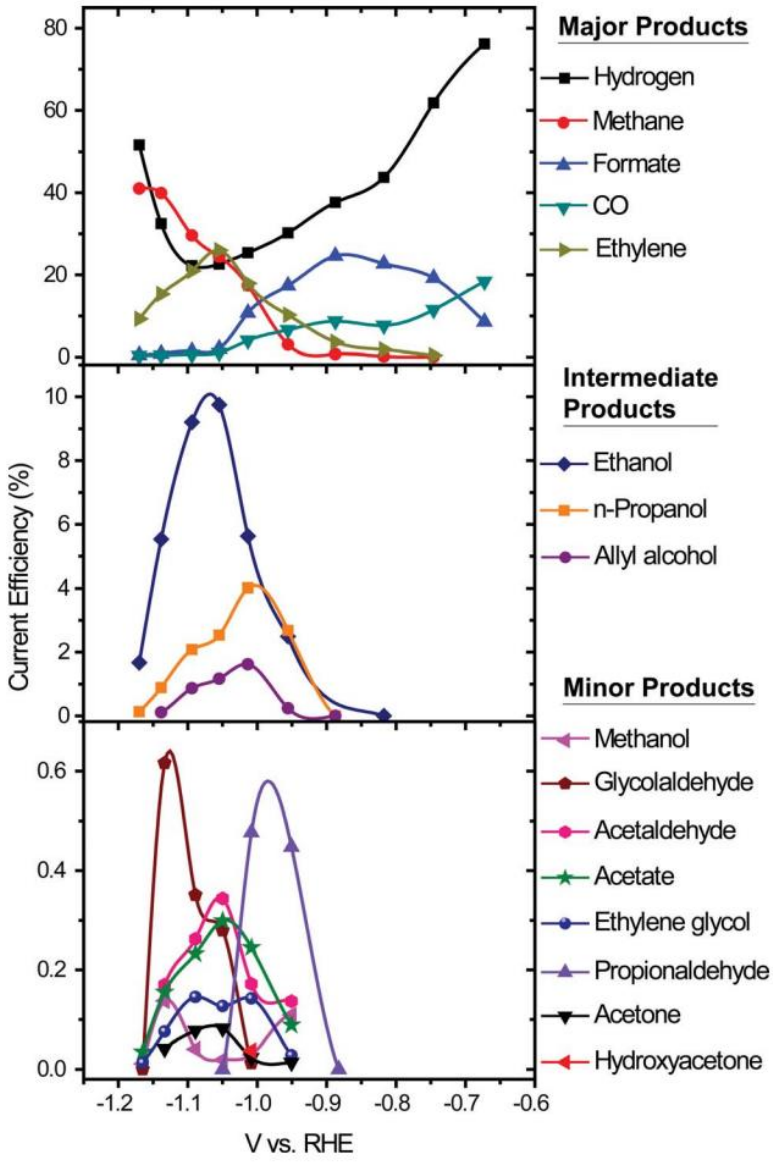

Figure 1.1 The distributions of major, intermediate, and minor products of the CO_2RR on copper as a function of applied potential, emphasizing the large number of possible products and the impossibility of selecting for only one without significant modifications to the system. Reproduced from Ref. 15 with permission from the Royal Society of Chemistry.

Heterogenized molecular catalyst systems, wherein traditionally homogeneous molecular catalysts are attached to a surface, could combine best aspects of both systems. Being attached to a surface, they benefit from the superior kinetics of heterogeneous catalysts, but since they retain the tuned, single-site structures of homogenous catalysts, they can have tremendous selectivity for a single product.[23] A number of methods are available for attaching catalysts to electrode surfaces. In the simplest case, the molecular catalyst can be physically adsorbed onto the electrode substrate. Catalysts can also be mixed with an encapsulating substrate (such as carbon nanotubes or a polymer) in solution before deposition onto the surface.[26-28] Covalent tethering, as with a click reaction, creates a more robust bond between the molecule and the surface.[29] On the extreme end, electropolymerization or the synthesis of covalent organic frameworks (COFs)[30,31] and metal-organic frameworks (MOFs)[32] can be used to build surfaces with defined molecular catalyst moieties. However, catalyst aggregation is a significant issue for the evaluation of heterogenized systems.[23]

Heterogenizing a molecular catalyst also opens up an additional avenue for tuning catalytic activity—besides altering the catalyst itself, one can alter the environment around the catalyst to influence substrate transport. The clearest example of this effect is the introduction of hydrophobic domains which can throttle the availability of protons and thus minimize parasitic HER. A recent review from our group[33] highlights the role of blocking layers and other methods for controlling substrate transport to catalytic active sites.

1.2. Using Polymer-Catalyst Composites to Address Shortcomings in CO_2 Electrolyzer Technologies

Feasibility and Performance Benchmarks of Industrial Gas-Fed CO_2RR Electrolyzers

Eventually, the goal of CO_2RR research is the creation of large-scale electrolyzers that can selectively convert industrial CO_2 waste streams to usable products as part of a carbon capture, utilization, and storage (CCUS) scenario.[34] To minimize transport costs, such electrolyzers would likely be integrated with systems producing high-concentration CO_2 streams, particularly petroleum refineries, steel plants, blue hydrogen plants, or power generation stations burning natural gas or biomass-derived fuels.[35-37] Aside from the CO_2, the only inputs for the electrolyzer are water and electricity, the latter of which could be supplied from renewable sources or from a portion of the output of the power generating station. In order to be viable, a CO_2 electrolyzer must compete economically with other CCUS technologies. On the utilization side, these include enhanced oil recovery (EOR),[38] greenhouse agriculture,[39] and thermal catalysis to value-added products.[8] Geologic storage—either through direct sequestration in saline aquifers or by EOR—receives tax incentives in the US that will likely be expanded in coming years.[40-42] Therefore, in the absence of expanded incentives, the economic benefits of electrochemical CO_2RR must be sufficient to outweigh the revenue from storage.

Several benchmarks are cited in the technoeconomic literature for CO_2 electrolyzer viability.[10,25] Specific cost-benefits for any given project will depend on many factors, including capital costs associated with installation and maintenance, transportation costs, electricity prices, and the market value of the CO_2RR products. For instance, performance targets for electrolyzers producing CO are 200-500 mA cm^{-2} of current density with 95% selectivity for CO.[10] Ideally an electrolyzer would need to operate with minimal voltage increase (<10 μV h-1) for more than 500

million turnovers, translating to an operating lifetime of about 2-3 years before the catalyst needs to be replaced.

The key difference between most lab-based CO_2 electrolysis cells and industrial electrolyzers is the method of CO_2 delivery. Traditional CO_2RR electrochemical studies use an electrolysis cell in which CO_2 is delivered to the electrode from a CO_2-saturated aqueous solution. The concentration of CO_2 in such solutions reaches a maximum at about 33 mM—and more critically, has a diffusion coefficient of only 1.6×10^{-3} mm^2 s^{-1}.[43] In contrast, humidified gaseous CO_2 at ambient pressure has a concentration around 41 mM with a diffusion coefficient around 16 mm^2 s^{-1}, enabling rapid delivery of CO_2 to the catalytic sites and dramatically enhancing the maximum CO_2RR rate.[43] To achieve commercial viability, any CO_2RR catalyst system must be integrated into a gas-fed electrolyzer due to the intrinsic limitations of aqueous CO_2 delivery.

The gaseous reactant feed dictates the basic structure of industrial CO_2 electrolyzers. An example of a standard gas-fed reactor is shown in Figure 1.2. The cathode material and any additives form a catalyst layer (CL) which is directly deposited onto a gas diffusion layer (GDL), forming a gas diffusion electrode (GDE). The gas diffusion electrode is in contact with a metal plate patterned with flow channels. The plate delivers electrons and CO_2 to the GDE and carries away reduction products. On the other side, the CL is in contact with a polymer electrolyte membrane (PEM—or ion exchange membrane). The membrane shuttles water and ions between the anode and cathode. Within the cathode layer, the electrolyte, solid cathode, and humified CO_2 gas supply combine in a triple-phase junction where the catalyst has sufficient influx of reactants (CO_2, water, and electrons) and efflux of products to maintain rapid catalytic turnover. The anode has a similar morphology to the cathode, with a thin catalyst layer in contact with the flow plate.

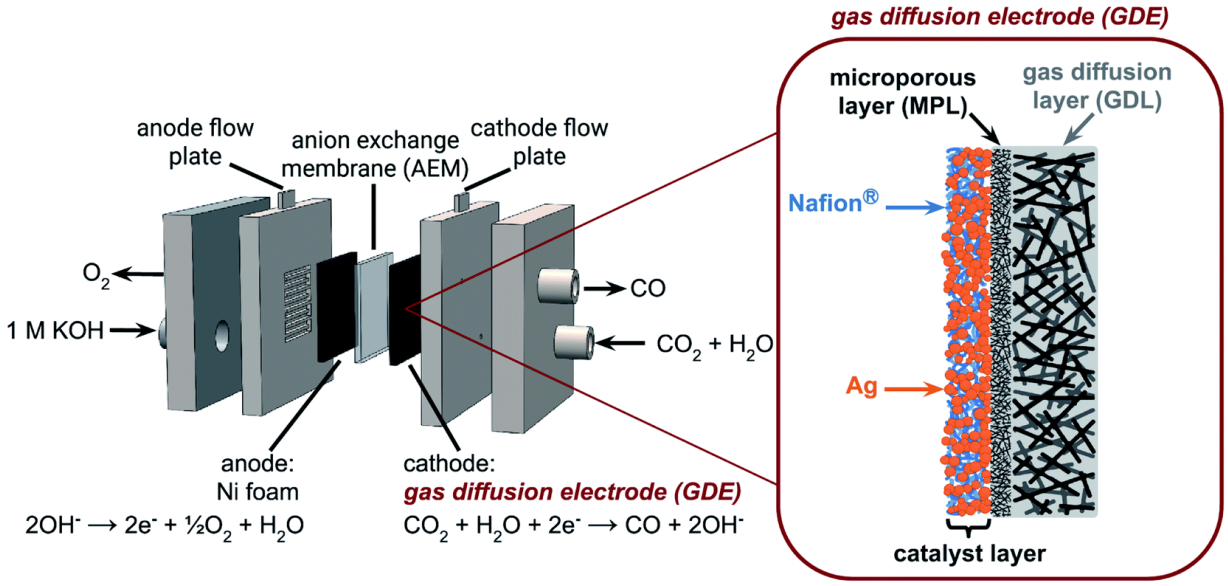

Figure 1.2 Illustration of a conventional zero-gap CO_2 flow electrolyzer. Anode and cathode flow plates supply hydroxide solution and humidified CO_2, respectively. Catalyst layers are separated by an anion exchange membrane which transports hydroxide created at the cathode to the anode to be reduced. Inset: a visualization of the gas diffusion electrode on the cathodic side. Silver nanoparticles are bound with Nafion to create a catalyst layer (CL) where the triple phase junction occurs. A microporous layer separates the CL from the microporous gas diffusion layer, which supplies the humified CO_2. Reproduced from Ref. 68 with permission from the Royal Society of Chemistry.

GDE catalyst systems must maintain a delicate triple-phase junction where gaseous CO_2, proton-carrying electrolyte, and electrons meet and react within the catalyst layer.[44,45] Because this junction can be easily disrupted, the choice of materials dictating the microenvironment of the CL is critical to maintaining device activity. The construction, challenges, and failure modes of CO_2RR GDEs have been reviewed extensively elsewhere in recent years.[10,43-48] The primary technical challenges of GDE systems are: 1) flooding, where the too much electrolyte is present in the CL and as migration to the catalytic sites is blocked, 2) carbonation, where hydroxide produced by the CO_2RR reacts directly with CO_2 to form precipitated carbonate crystals that damage the layer, and 3) reaction competition from HER. Specific GDE architectures have been devised to get around these problems, but generally come with additional complications of their own.

Electrolyzers for the $2e^-$ reduction of CO_2 to CO are closest to achieving commercialization. Despite being a toxic greenhouse gas, CO produced by electrolyzers would find a ready market in the chemicals industry, where it could replace petrochemical CO as a key chemical reagent.[12] The state-of-the-art electrolyzer for CO_2 to CO uses a silver or gold nanoparticle catalyst to achieve high activity and selectivity.[10] Ag has the advantage of being considerably less expensive, but Au catalysts may be able to accommodate lower-purity reactant streams without being poisoned or losing selectivity. A prototype commercial electrolyzer from Dioxane Materials incorporates a silver nanoparticle catalyst into a zero-gap cell with a Sustainion anion exchange membrane as a separator.[49] Since the main competitive reaction with CO_2RR is HER, CO reactors could also be tuned to produce a controlled mixture of CO and H_2, creating ready-to-use syngas for further processing into other chemical products.

Electrolyzers for generating C_{2+} products are much further from commercialization.[50] Three main strategies have been considered: 1) a “one-pot” approach that aims to generate a

specific C_{2+} product from CO_2 with a single catalyst; 2) a "two-pot" approach where two electrolyzers are employed, the first producing CO from CO_2 and the second coupling and hydrogenating CO to form C_{2+} products; and 3) a hybrid approach in which the two catalyst materials are mixed in a single electrolyzer.[10] In all cases, Cu is needed to provide C-C coupling, with all the attendant challenges of product selectivity detailed in earlier sections.

Improving CO_2RR Electrolyzer Performance by using Polymer-Catalyst Composites to Tune Catalytic Microenvironment

The innate fragility of the GDE system demands fine-tuning of the catalyst microenvironment. Integrating rationally designed polymers with targeted functionalities into the catalyst layer could mitigate many of the problems faced by researchers constructing GDE systems. GDE device composition varies considerably between studies, making generalizations about structure difficult. However, it is very common for researchers to incorporate a binding polymer in the catalyst layer,[44] which may be the same polymer material used in other cell components (e.g the GDL, microporous layers on either side of the CL, or the polymer electrolyte membrane in zero-gap configurations). Many CO_2RR GDE studies have used Nafion as a binding polymer,[51-70] popularized by its extensive application as a proton exchange membrane in fuel cells. Nafion has attractive properties, including high porosity, ionic conductivity, and resistance to degradation,[71] and has been the default polymer for this purpose. Berlinguette and coworkers[68] have investigated how optimizing Nafion loading in the catalyst layer influences device performance. However, researchers have begun to look beyond Nafion to find other systems that may improve device performance. Much of the research to-date using non-Nafion polymers to optimize GDE catalyst microenvironment has focused on CL wettability, which determines the

position and extent of the triple-phase boundary, and thus the availability of substrates.[49,71-76] The wettability of the CL must be balanced such that sufficient water permeates the layer to provide a proton source and to transport ions, but not so much water that the pores permitting gas transfer are filled.

Berlinguette and coworkers demonstrated that by increasing the weight percentage of hydrophobic PTFE in the catalyst layer, they could retain high faradaic efficiency for CO at 200 mA/cm^2 in a zero-gap MEA assembly.[74] Feng and coworkers similarly demonstrated that by mixing PTFE nanoparticles in with the Cu catalyst nanoparticles, activity and selectivity for CO_2RR could be enhanced in a GDE system.[75] A series of reports by Masel and coworkers[49,77-79] introduced imidazolium-functionalized Sustainion as a possible anion-exchange polymer for CO_2RR applications. Gewirth, Kenis, and coworkers specifically looked at PTFE and Sustainion as alternatives to Nafion, finding that combining polymer with different benefits could be advantageous.[71] Blending Nafion with PTFE hindered undesirable carbonate formation, while adding a Sustainion overlayer improved catalyst stability while retaining performance.

Maintaining the conductivity of the catalyst layer is another concern for GDE construction, as increasing the hydrophobicity of the binding polymer (e.g., by adding PTFE) tends to simultaneously depress electron conductivity.[50] This is especially the case for molecular catalysts, which lack the intrinsic conductivity of metal nanoparticle catalysts. Several publications have used GDE systems where the catalyst is codeposited with carbon nanotubes, both to improve conductivity and to disaggregate the catalyst.[27,60,80-83] For example, Liang and coworkers[27] dispersed modified nickel phthalocyanines on carbon nanotubes, achieving high selectivity to CO at up to 300 mA/cm^2. While increasing conductivity with graphitic carbon has been an effective strategy, it is possible that incorporation of functionalized conductive polymers would serve a

similar function. Depressed TOF due to aggregation[23,26,84] is also a significant concern when incorporating molecular catalysts into GDE electrolyzers. Selection of a polymer that interacts favorably with the catalyst could mitigate aggregation and remove this limitation.

To date, the CO_2 electrolysis community has only barely tapped into the immense variety of structures made possible by modern polymer chemistry. In theory, a polymer-catalyst composite is endlessly tunable, with many "knobs" that can be turned to produce different effects: blends and copolymers to provide a mixture of functional domains, covalent grafting of catalytic macrocycles to provide stability, branching structures that create diffusion pathways, and more. Electropolymerization techniques could permit structured growth of complex composite systems directly onto the electrode substrate. As an example of what the future could hold for more intricate systems, Sargent, Sinton, and coworkers presented a complex catalyst architecture[72] with a multifunctional ionomeric binding polymer. The structure combines hydrophobic domains that facilitate CO_2 transfer with hydrophilic domains that enable water and ion transport. By maximizing the extent of the triple-phase boundary layer through deposition of a ~6 μm-thick Cu/ionomer layer, the authors achieved a maximum activity of 1.32 A/cm^2 for CO_2RR, mainly to C_{2+} products.

In summary, the transition from solution-fed to gas-fed CO_2RR electrolyzers brings significant challenges related to the triple-phase boundary in the catalyst layer. Using polymers to control the catalyst wettability has been fruitful, but significant gaps remain in the literature. To date, we could find no studies that have tried using the binding polymer in the GDE catalyst layer to synergistically imbue primary or secondary coordination sphere effects, nor any studies incorporating an intrinsically conductive polymer to improve electron transport. More research is needed to look past Nafion and explore different catalyst layer compositions and morphologies

that will maximize a) intrinsic catalytic performance through manipulation of primary-sphere effects; b) substrate and product transport into, within, and out of the catalyst layer; and c) electron conductivity in the catalyst layer. Next-generation polymer architectures that incorporate multiple synergistic functionalities could be an effective strategy for optimizing device performance. Polymer blends, copolymers with different functional blocks, electropolymerized catalysts, and multilayered structures all bear further investigation.

1.3. CoPc-P4VP and Related Systems for the Electrochemical Carbon Dioxide Reduction Reaction

Previous Investigations of Cobalt Phthalocyanine Catalyst Systems for the CO_2RR

One molecular catalyst that has been heterogenized frequently for the CO_2RR is cobalt phthalocyanine (CoPc).[23] CoPc was first reported for the CO_2RR in the 1970s,[85] and has been shown to operate with moderate activity and reaction selectivity with a Faradaic efficiency of approximately 35-60% for CO production (FE_{CO}) over the competing HER in aqueous phosphate buffer when coated onto a planar carbon electrode.[86,87] The activity and stability of CoPc-based system can be tuned by modulating the electronic structure of the system through axial coordination[88] and/or synthetic modification of the Pc ring.[89,90] For these reasons, CoPc is one of the most promising and well-studied CoN_4 porphyrinoid catalysts for the CO_2RR.

It has been recently reported that CoPc can catalyze the reduction of CO_2 to formic acid and methanol under specific conditions,[90-92] making CoPc one of the only molecular catalysts capable of reducing CO_2 to highly-reduced products. Two papers published in 2019—one from Robert and coworkers[92] and the other from Wang and coworkers[90]—demonstrated that CoPc codeposited with carbon nanotubes can catalyze the six-electron reduction of CO_2 to methanol at

relevant Faradaic efficiencies (as high as 40% under certain conditions in the latter report) in addition to the expected CO and H_2 more commonly reported. The precise reasons for this activity are unclear, but the results are a promising indicator that with sufficient tuning of the reaction environment, CoPc may someday be able to produce highly-reduced products at industrially-relevant rates.

CoPc has also been incorporated into flow cell architectures. Two studies by Berlinguette and coworkers from 2019[51,70] employ CoPc mixed with carbon powder as a catalyst layer in a gas-fed flow electrolyzer. In the study published in *Nature*, the authors reached a current density of 150 mA/cm^{-2} with high Faradaic efficiency towards CO, achieving a commonly-cited benchmark for industrially-relevant systems. Together, these studies confirm that CoPc—and molecular catalysts generally—are capable of reaching the activities needed to compete with conventional metal nanoparticle catalysts in industrial electrolyzers.

Features of the CoPc-P4VP Composite System

Polymer encapsulation has been considered a method for CoPc heterogenization since the first report of CO_2RR by CoPc, where the authors demonstrated that using polystyrene as a binding agent decreased activity compared to that of the parent CoPc complex.[85] Kaneko and coworkers used polymer encapsulation within putative hydrophobic polymers to improve the selectivity of molecular CO_2RR electrocatalysts in aqueous electrolytes,[93,94] and showed that encapsulating CoPc within poly(4-vinylpyridine) (P4VP) enhanced the selectivity for CO_2 reduction to CO over the competitive HER.[95-98] In Table 1.1 are summarized a few recent studies of turnover frequency for the CO_2RR to CO by heterogenized CoPc and related Co porphyrinoid materials prepared with different binders and supports and measured in various electrolyte conditions.

Catalyst	Electrode	Polymer/ Binder	Electrolyte (pH)	Potential / V vs. RHE	TOF_{CO} / s^{-1}	Ref
CoPc	Edge-Plane Graphite	N/A	0.1 M NaH_2PO_4 (4.7)	−0.73	1.1	108
CoPc-P4VP	Edge-Plane Graphite	P4VP	0.1 M NaH_2PO_4 (4.7)	−0.73	4.2	108
CoPc-P4VP/Graphite Powder	Glassy Carbon	P4VP	0.1 M NaH_2PO_4 (4.7)	−0.73	3.1	109
CoPc/CNTs	Carbon Paper	Nafion	0.5 M $NaHCO_3$ (7.3)	−0.67	4.1	70
CoPc/CNTs	Carbon Paper	Nafion	0.1 M $NaHCO_3$ (6.8)	−0.63	4.1	110
Cobalt Protoporphyrin/CNT (CoPP)	Carbon Paper	Nafion	0.5 M $NaHCO_3$ (7.3)	−0.65	2.1	84
Cobalt Tetraphenyl Porphyrin/CNT (CoTPP)	Glassy Carbon	None	0.5 M $NaHCO_3$ (7.2)	−0.68	2.7	111
Covalent Organic Framework COF-36-Co(1%)	Carbon Fabric	None	0.5 M $NaHCO_3$ (7.3)	−0.67	2.6	112

Table 1.1 A few recent studies of CoPc and related Co-porphyrinoid materials for the CO_2RR, along with their corresponding turnover frequency (TOF) for CO production.

Although many researchers use polymers as binding agents for adhering catalysts to surfaces, relatively few studies have investigated the effects of polymer encapsulation on CO_2RR photocatalysts[99-103] and electrocatalysts.[101-107] The few studies that have considered these interactions include work by Koper and coworkers examining the impact of different encapsulating polymers on the CO_2RR performance of indium protoporphyrin (InPP);[104] studies by Grubbs, Gray, and coworkers examining the effect of brush polymer ion gels on the activity of Re-based CO_2RR molecular electrocatalysts;[105,106] and Reisner and coworkers tuning the CO:H_2 product ratio in a series of polymer-catalyst materials by tuning the hydrophobicity of the polymer moieties.[107]

Our previous work with CoPc has focused on understanding the specific influence of P4VP polymers on the activity of CoPc in CoPc-P4VP composite polymer-catalyst systems. In particular, we have shown that CoPc-P4VP operates with a ~4-fold enhancement in CO_2RR activity compared to the parent CoPc, and with nearly quantitative Faradaic Efficiency for CO production ($FE_{CO} \approx 100\%$) compared to the parent CoPc which operates with $FE_{CO} \approx 60\%$. Our work tested three core hypotheses regarding polymer-catalyst interactions (Figure 1.3): 1) pyridyl moieties from the polymer axially coordinate to the cobalt center, increasing affinity for CO_2 coordination and reduction; 2) partially protonated pyridyl moieties from P4VP provide secondary coordination sphere effects via hydrogen bonding; and 3) proton delivery in P4VP is controlled by a multisite proton relay involving the polymer pyridyl moieties.[113]

Axial Coordination

In our first studies of polymer-encapsulated CoPc, we concluded that axial coordination of pyridyl residues from the P4VP polymer in the CoPc-P4VP composite film was crucial to the

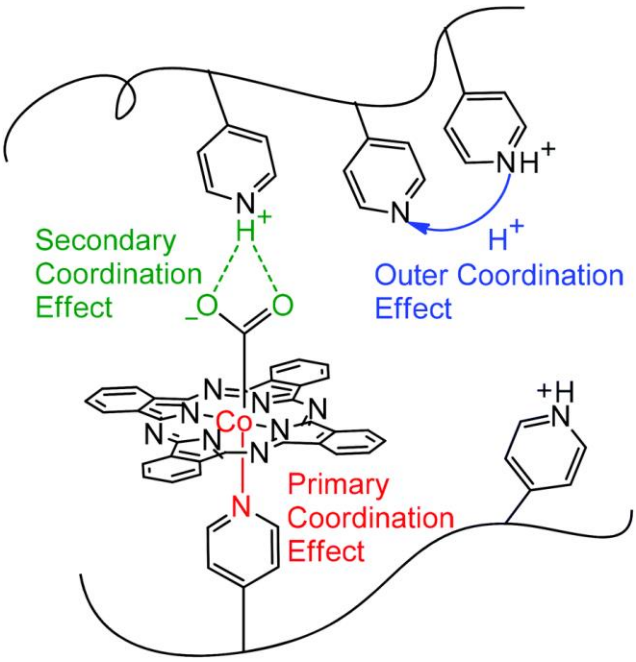

Figure 1.3 Illustration of the three coordination sphere effects contributing to the activity and selectivity of CoPc encapsulated in P4VP. Reproduced from Ref. 114 with permission from the Royal Society of Chemistry.

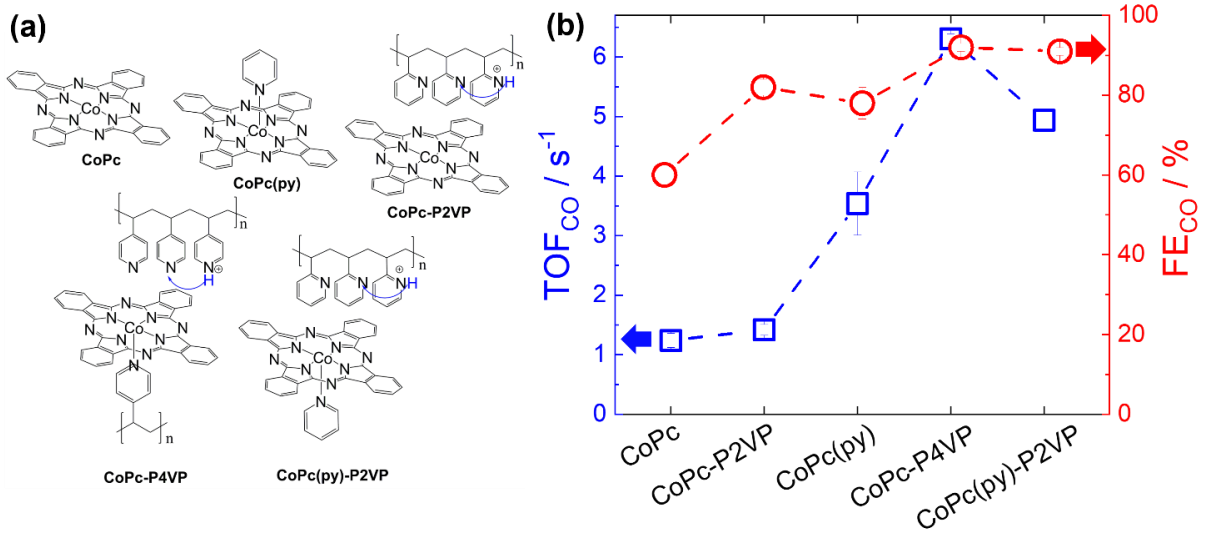

Figure 1.4 a) Different combinations of the parent complex CoPc with polymers and ligands discussed herein, along with the proposed coordination environment and proton transport mechanism. Adapted with permission from Ref. 113. Copyright 2019 Liu, Y. and McCrory, C.C.L. Published by Springer Nature under a Creative Commons CC BY 4.0 license http://creativecommons.org/licenses/by/4.0. b) The turnover frequency (TOF$_{CO}$) and Faradaic Efficiency (FE$_{CO}$) for CO production of each catalyst-polymer composites. Data from Ref. 113.

increased activity and selectivity of CoPc-P4VP for the CO_2RR compared to the CoPc parent system.[108,113] The 5-coordinate CoPc(py) complex with no polymer and an axially coordinated pyridine reduces CO_2 with a modest increase in activity and selectivity compared to the parent CoPc complex, as seen in Figure 1.4. In contrast, encapsulating CoPc with the non-coordinating P2VP polymer results in no increase in CO_2RR activity and a modest increase in selectivity compared to CoPc. Combining these effects in the CoPc(py)-P2VP system results in a large increase in CO_2RR activity and selectivity, as observed with CoPc-P4VP. We interpreted these results to suggest that 1) axial coordination in the primary coordination sphere is crucial for the observed enhanced activity and 2) this influence of the axial coordination works synergistically with other effects imbued by the polymer to achieve the enhanced activity and selectivity observed in CoPc(py)-P2VP and CoPc-P4VP.[113]

To confirm that the pyridyl residue of the P4VP was indeed axially coordinating to the CoPc molecule, we performed *in situ* X-ray Absorbance Near-Edge Structure (XANES) measurements (Figure 1.5).[114] CoPc exhibits a strong 1s-4p pre-edge peak at ~7716 eV (Figure 3a), characteristic of macrocyclic square planar Co complexes.[115,116] Conversion of the metal center into a square pyramidal geometry leads to a dramatic decrease in peak intensity,[116] as observed for CoPc(py) and CoPc-P4VP (Figures 3b-c). This loss of the 1s-4p pre-edge peak intensity is not observed for CoPc-P2VP in the non-coordinating P2VP polymer,[114] so we interpret these results to mean that the pyridyl residues in P4VP axially coordinate to the Co center in CoPc-P4VP, as hypothesized in Figure 1.3.

We further hypothesized that coordination of an axial ligand to the CoPc increases the electron density on the metal center, leading to an increase in the energy of the dz^2 orbital of the Co center, thereby increasing the metal site nucleophilicity and its ability to coordinate and activate

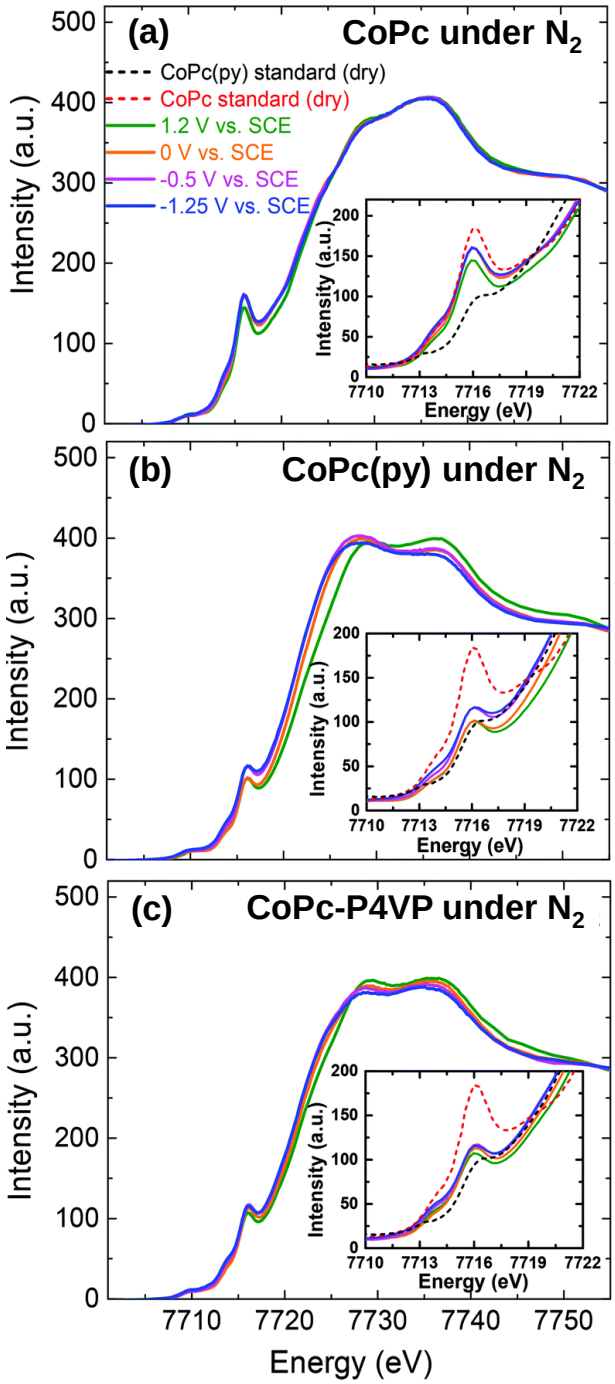

Figure 1.5 X-ray absorbance near edge structure (XANES) measurements at different applied potentials under N_2 of (a) CoPc, (b) CoPc(py), and (c) CoPc-P4VP. The insets show the 1s-4p pre-edge peak used to determine whether the system is primarily 4-coordinate or 5-coordinate. Reproduced from Ref. 114 with permission from the Royal Society of Chemistry.

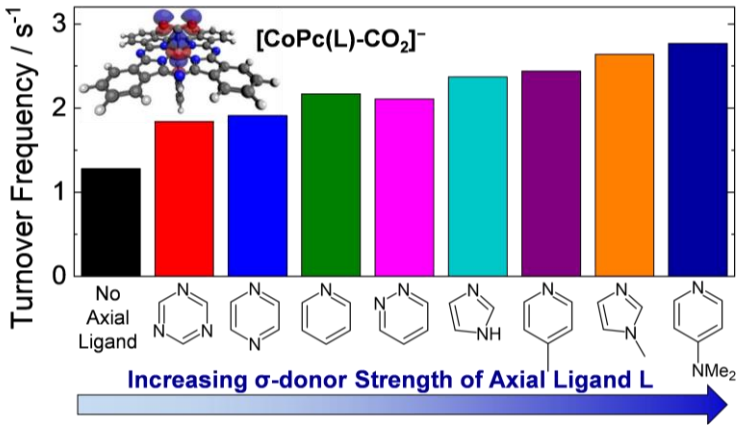

Figure 1.6 Turnover frequency for CO production for CoPc(L) with various axial ligands L. Activity increases as a function of σ-donor strength of the axially coordinating ligand. The calculated HOMO of the reduced CO_2 adduct from Mechanism 1 for CoPc(L8) is shown in the inset, highlighting the interaction between CO_2 and the Co dz^2 orbital. Adapted with permission from Ref. 88. Copyright 2021 American Chemical Society.

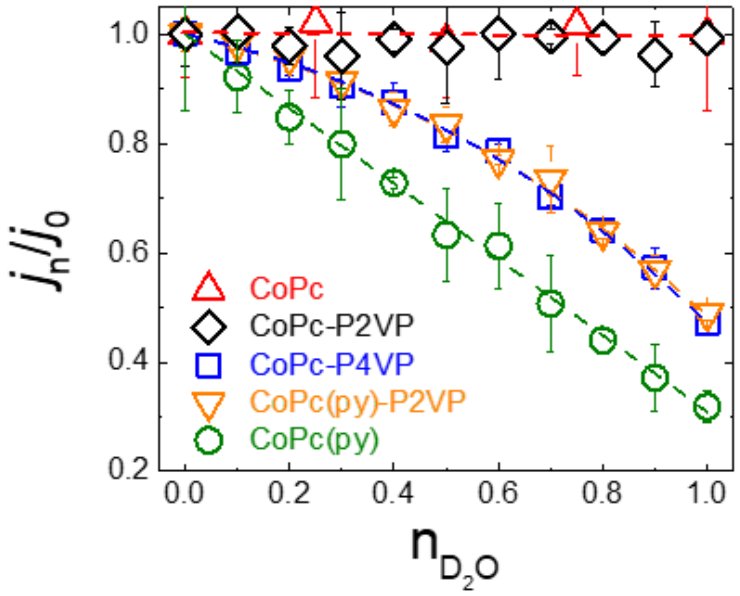

Figure 1.7 Proton-inventory studies for CoPc, CoPc-P2VP, CoPc-P4VP, CoPc(py)-P2VP, and CoPc(py). Adapted with permission from Ref. 108. Copyright 2019 Liu, Y. and McCrory, C.C.L. Published by Springer Nature under a Creative Commons CC BY 4.0 license http://creativecommons.org/licenses/by/4.0.

CO_2. Because the Co dz^2 orbital is geometrically most likely to interact with CO_2, we postulated that the increased energy of this orbital drive the increased ability of the 5-coordinate complex to bind and reduce CO_2.[113] The corollary to this hypothesis is that increasing the σ-donor ability of the axial ligand will further increase the energy of the dz^2 orbital, and further increase the activity for the CO_2RR. In a combined experimental and computational study, we showed that increasing the σ-donor ability of the axial ligand (L) results in an increase in the CO_2RR activity by CoPc(L) (Figure 1.6).[88] Computational studies confirmed that the strength of the σ-donor ability was correlated with the relative energy of the dz^2 orbitals, that the HOMO of the pertinent reduced $[CoPc(L)\text{-}CO_2]^-$ involves an interaction between the dz^2 orbital and the CO_2 adduct.[88]

Proton Transport

Encapsulating polymers are often used to increase the hydrophobicity around the catalyst, thereby enhancing CO_2RR selectivity by suppressing competitive HER.[107,117] For example, Kaneko and coworkers showed that incorporating various Re- and Co-based molecular catalysts within Nafion enhanced their activity for the CO_2RR over competitive HER due to the relative hydrophobicity of Nafion exposed to pH 7 electrolyte under their catalytic conditions.[93,94] Notably, Kaneko and coworkers also suggest that controlled proton transport plays an important role in the enhanced CO_2RR selectivity of CoPc-P4VP compared to the parent CoPc complex.[95-98] After our initial study of CoPc-P4VP for the CO_2RR,[113] we became interested in understanding better the mechanism of proton transport in the polymer-catalyst system. In particular, we hypothesized that proton transport might occur via a multisite proton relay, similar to those frequently proposed in enzymatic and bioinspired systems.[118-121] To test this hypothesis, we

conducted a series of proton inventory studies, a technique in which the attenuation in activity is measured as a function of the fractional deuteration of the system.[122-124]

For systems where the RDS involves a proton transfer event such as CoPc(py), CoPc(py)-P2VP, and CoPc-P4VP, the shape of the curve in Figure 1.7 provides information about the proton relay mechanism. For CoPc(py), the linear curve is consistent with a normal kinetic isotope effect involving a single hydrogenic site in the RDS.[125,126] However, for CoPc(py)-P2VP and CoPc-P4VP, the non-linear dome-shaped response of the relative activity as a function of fractional electrolyte deuteration is consistent with a normal isotope effect at a single hydrogenic site in the RDS preceded by an aggregate inverse isotope effect involving multiple hydrogenic sites on the polymer.[123,127] This aggregate inverse isotope effect is also responsible for the decrease in the KIE from KIE ~ 3 for CoPc(py) to KIE ~ 2.1 for CoPc-P4VP and CoPc(py)-P2VP. We interpret these results as evidence that proton delivery in the P2VP- and P4VP-encapsulated systems occur via a multisite proton relay involving the pyridyl residues on the polymer.[108]

Charge Transport and Carbon Supports

As one considers integrating polymer-catalyst composites into electrochemical reactors, it is crucial to consider not only controlling substrate transport, but also maintaining efficient charge transport.[105,128] The incorporation of carbon supports into the polymer-catalyst system is a common strategy for increasing charge transport in CoPc-based catalyst-polymer composites for the CO_2RR.[28,90,92,110,129] In some cases, incorporation of specific carbons supports have resulted in new product formation—both Wang and coworkers and Robert and coworkers demonstrated that CoPc immobilized onto multiwalled carbon nanotubes (MWCNTs) with a Nafion film reduce CO_2 to CH_3OH via a cascade catalysis mechanism.[90,92]

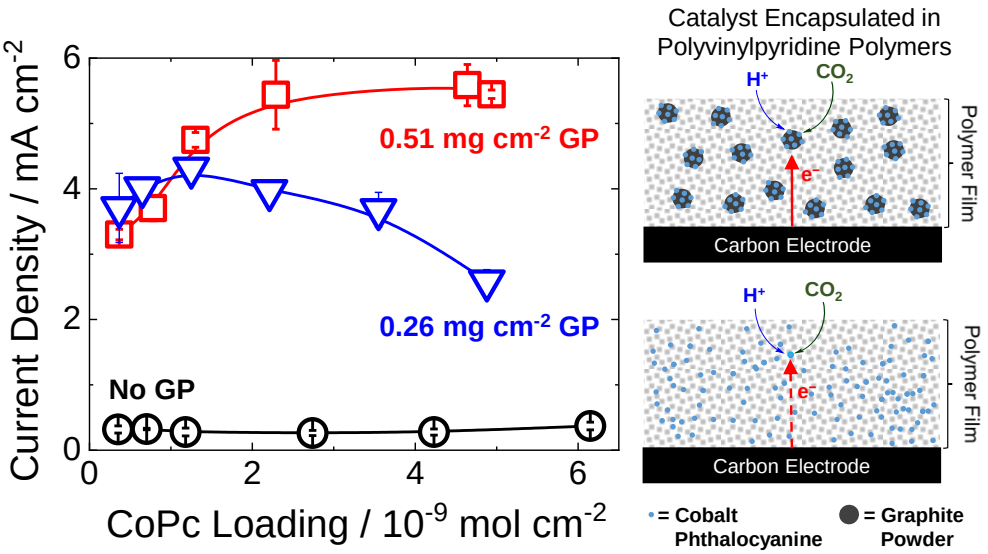

Figure 1.8 The activity of CoPc-P4VP with different loadings of graphite powder (GP) as a function of catalyst-film loading. In these studies, the ratio of CoPc:P4VP is held constant, so CoPc loading is a convenient proxy for CoPc-P4VP film loading and thickness. Reproduced with permission from Ref. 109. Copyright 2021 American Chemical Society.

Our work in this area has focused on studying how incorporating graphite powder (GP) within CoPc-P4VP systems influences the performance of these systems for the CO_2RR.[109] Importantly, it is not enough simply to mix the CoPc-P4VP and GP together—doing so results in no enhancement of activity upon the addition of GP. Instead, it is crucial to develop deposition procedures that facilitate interaction between CoPc and the GP supports. When no GP is present, we observe no appreciable change in activity for CoPc-P4VP as a function of catalyst film loading (Figure 1.8). When moderate loadings of GP (0.26 mg cm^{-2}) are incorporated into the CoPc-P4VP film using our optimized deposition procedure, we observe significantly higher activity for the CO_2RR (Figure 8), suggesting that incorporation of GP increases the effective distance of charge transport within the film and, thus, increases the number of CoPc sites that are active. At sufficiently high loadings of GP (0.51 mg cm^{-2}), the activity increases and then plateaus as a function of increasing catalyst film loading. This suggests that charge transport is not limiting at these high GP loadings, and instead, catalytic activity is limited by another parameter—possibly inefficient substrate transport to interior sites or CoPc aggregation at high catalyst loadings. Note that aggregation is particularly problematic for CO_2RR systems based on CoPc due to the molecule's high propensity to aggregate because of the strong π-π interactions between CoPc molecules. CoPc aggregation has been specifically linked to decreased activity in polymer-catalyst systems at high loadings.[23] In nanoparticulate systems, deleterious aggregation can be mitigated through polymer encapsulation in some studies.[130,131]

Motivation for Studying Aggregation of CoPc

Evidence from our work and others has raised concerns that CoPc aggregation may be a significant limiting factor in CoPc performance for the CO_2RR. The aggregating tendencies of

CoPc and other metal phthalocyanines (MPcs) are well-known and have been studied extensively outside the electrocatalysis community. Phthalocyanine rings have a flat, highly conjugated aromatic structure and thus strongly associate through π-stacking interactions. Most MPcs are difficult to solvate, and ring substituents are commonly added to increase their solubility. In the solid phase, simple MPcs have two primary crystal structures (a and b). In solution, even highly-substituted MPcs will often dimerize because of the high favorability of the π-stacking interaction. A kinetic treatment of dimerization—which extracts a dimerization rate constant—is commonly used to account for the influence of aggregation on the visible-range optical properties of MPcs.

Researchers investigating CoPc for the CO_2RR have often noted the possibility of aggregation and taken steps to mitigate it. For example, Officer and coworkers[132] adopted the approach of many spectroscopy-focused researchers by attaching bulky alkoxy groups to the ring, increasing the molecule's steric bulk and solubility in organic solvents. The most common approach for electrocatalysis groups is to mix the CoPc with carbon nanotubes (CNTs) in the deposition solution, leading to dispersion of the catalyst across the high surface area carbon.[26,90,92,129,133] This approach has the additional benefit of increasing the electron transport to catalyst sites. Wang and coworkers[90] and Robert and coworkers[92] used unmodified CNTs combined with CoPc, while Huai and coworkers[129] used the same but with pyridine as the solvent. Wu and coworkers[133] used hydroxyl functionalized CNTs. Zhu and coworkers[26] used pyridine-functionalized CNTs. These studies suggested two interactions which could drive CoPc disaggregation in deposited layers: 1) axial coordination to the Co center, as with pyridine moieties on the py-functionalized CNTs, and 2) π-stacking interactions with the carbon support.

Despite these studies, little characterization work has been done to understand the factors driving CoPc aggregation for conditions relevant to heterogeneous catalytic systems, or to confirm

a prevention of aggregation in systems specifically designed to mitigate it. A key exception is a 2018 study from Manthiram and coworkers[134] which probes how the turnover frequency (TOF) and mechanism of the CO_2RR changes as a function of CoPc loading. As the CoPc becomes more dispersed at lower loadings, the authors observed both in increase in TOF as a greater proportion of Co sites were available for catalysis, and they observed a change in the mechanism as evidenced by Tafel slope analysis. SEM was used to demonstrate the presence of micron-scale CoPc aggregates in the deposited layers. However, this report was still focused primarily on reporting the effects of inferred aggregation rather than systematically investigating how the aggregation was occurring.

Based on these literature reports, we felt that the electrocatalysis community would benefit from a fundamental investigation of how CoPc aggregates in deposition solutions and the resulting deposited layers, under conditions relevant to investigations currently being performed. At the same time, we were interested in determining whether combining CoPc with axially-coordinating P4VP would drive disaggregation in a similar manner to py-functionalized CNTs. We chose to use the simple model systems of unsubstituted CoPc and CoPc(py) for a few reasons: 1) they provide a "base case" in which aggregation is likely to be most prevalent, compared to substituted CoPc; 2) for better comparison to previously published electrocatalysis studies, most of which employ unsubstituted CoPc; and 3) CoPc cheap to produce and commonly available, increasing the relevance of the results for later industrial applications. We used deposition solutions with a concentration range matched to previous investigations. The results of this investigation are detailed in Chapter 2.

Motivation for Studying Protonation of the P4VP Layer

Our previous work on the CoPc-P4VP catalytic system has provided substantial evidence for a proton relay effect that modulates proton transport to the catalytic site. The solution pH chosen by Liu and McCrory[108] was matched to the pKa of the pyridine moieties in P4VP, aiming for a partial protonation to facilitate the proton relay effect as illustrated in Figure 1.4a. We expected that altering the solution pH would significantly affect the fractional protonation of the polymer, and thus the electrocatalytic activity and selectivity for the CO_2RR. At higher pH, the polymer is expected to be largely deprotonated, and at lower pH, it should transition to fully protonated.

Electrochemical analysis of CoPc-P4VP layers and related systems under variable pH conditions confirmed that the CO_2RR activity and selectivity did change as a function of buffer pH. More unexpectedly, the electrochemical activity also changed when the buffer concentration was altered, and when an additional "reaction innocent" perchlorate salt was added to the buffer to increase electrolyte density. To understand and contextualize the electrochemical results, it was necessary to find a characterization method that would directly probe the protonation of the P4VP layer.

Fortunately, the structure of P4VP itself provides a convenient spectroscopic handle for protonation without the need to incorporate an exogenous indicator into the layer. The breathing modes of the pyridine ring in the IR region are sensitive to the quaternization of the nitrogen atom, either by protonation or by addition of an alkyl substituent.[135-138] Specifically, protonated pyridyl moieties have a characteristic absorbance at around 1638 cm^{-1} which does not overlap with any surrounding bands and is therefore an excellent indicator of layer protonation. Previous investigations have exploited this band intensity to monitor the extent of proton transfer between

codeposited layers containing P4VP and a polymer with corresponding acidic moieties[136-138] in a process closely analogous to the protonation of P4VP layers by a buffer solution. Moreover, the IR spectrum of P4VP has a nearby CH_2 bending band at 1450 cm^{-1} arising from the vibrations of the polymer backbone.[135,139] This band is insensitive to pyridyl protonation, and therefore provides an internal calibrant for the intensity of the protonation band. Using this spectroscopic marker we were able to match *ex situ* spectroscopic analysis of the relative protonation of layers exposed to buffer solutions of varying pH with electrochemical analysis of the analogous CoPc-P4VP layers in the same buffer solutions. The results of this investigation are presented in Chapter 3.

1.4. Conclusion and Subsequent Investigations

The previous sections have detailed some of the motivations and challenges driving our work on heterogenized molecular catalyst systems for the CO_2RR. Traditionally, electrocatalytic investigations have used electrochemical methods as the primary analytical workhorse, and researchers have gleaned an incredible array of information from current and voltage traces. Spectroscopic and microscopic data tends to play a critical—but secondary—role in interpreting the relationship between the system's material composition and its electrocatalytic response. However, as research progresses and we attempt to build ever more complete pictures of catalytic mechanisms, we must rely more and more on careful spectroscopic methods that can selectively probe phenomena of interest. In the work detailed in this thesis, we put this principle into practice in three key areas of investigation, which are detailed in Chapters 2, 3, and 4. The primary methods and results of each investigation are summarized here.

In Chapter 2, we use spectroscopy to unravel a materials characterization issue with polymer-encapsulated CoPc. UV-Vis spectroscopy and scanning electron microscopy (SEM) are

used to discern how the aggregation of deposited CoPc layers is influenced by polymer codeposition. The visible-region Q-band absorbance of CoPc serves as a metric for comparing relative CoPc aggregation between samples codeposited with different polymers: P4VP, poly(4-chorostyrene) (P4CS), and Nafion. Based on the spectroscopic evidence, we conclude that P4VP serves to disaggregate CoPc, thus forming a CoPc-P4VP solid solution upon deposition. Meanwhile, Nafion serves poorly as a disaggregant, presumably due to a lack of specific interactions with the CoPc. SEM is used to corroborate the UV-Vis results and give additional insight into the mechanisms by which P4VP disaggregates CoPc. Finally, we make an electrocatalytic comparison between CoPc-P4VP and CoPc-Nafion, finding that CoPc-P4VP is more active and selective for the reduction of CO_2 to CO.

In Chapter 3, we use IR spectroscopy to make a novel comparison between the protonation level of the P4VP layer and the pH of the electrolyte solution. Deposited P4VP layers are exposed to buffer solutions with a variety of conditions, then *ex situ* transmission IR spectroscopy is used to monitor the growth of a ring vibration characteristic of a protonated pyridine. We find that the protonation of the P4VP layer scales both with solution pH (becoming more protonated when exposed to more acidic solutions) and with electrolyte concentration. These results are compared to electrocatalytic measurements to demonstrate that increased layer protonation is associated with an increase in HER activity, and thereby a decrease in Faradaic efficiency for the conversion of CO_2 to CO. In closing, we propose further experiments that exploit the pyridine IR handle to probe the *in situ* behavior of the P4VP layer under catalytic turnover.

In Chapter 4, we design and test a spectroelectrochemical flow cell (SEC-FC) specifically intended to enable the *in situ* spectroscopic observation of species on electrode surfaces, both for materials characterization and for the identification and quantification of reaction intermediates.

In particular we focus on alkanethiol self-assembled monolayers as a test substrate, and on metal-cyanate complexation as a test proxy for reaction intermediates. We choose polarization-modulation infrared reflection-absorption spectroscopy (PM-IRRAS) as the key technique for the cell, determine a set of design constraints based on the limits of the technique and the target samples, and determine a final cell design. Finally, we perform tests of the cell and identify areas for improvement in the next design iteration.

1.5. References

(1) Soucy, T. L.; Dean, W. S.; Zhou, J.; Rivera Cruz, K. E.; McCrory, C. C. L. "Considering the Influence of Polymer–Catalyst Interactions on the Chemical Microenvironment of Electrocatalysts for the CO_2 Reduction Reaction," *Accounts of Chemical Research* **2022**. http://dx.doi.org/10.1021/acs.accounts.1c00633

(2) Buttler, A.; Spliethoff, H. "Current status of water electrolysis for energy storage, grid balancing and sector coupling via power-to-gas and power-to-liquids: A review," *Renewable and Sustainable Energy Reviews* **2018**, *82*, 2440-2454.

(3) Abbasi, R.; Setzler, B. P.; Wang, J.; Zhao, Y.; Wang, T.; Gottesfeld, S.; Yan, Y. "Low-temperature direct ammonia fuel cells: Recent developments and remaining challenges," *Current Opinion in Electrochemistry* **2020**, *21*, 335-344.

(4) Adli, N. M.; Zhang, H.; Mukherjee, S.; Wu, G. "ammonia oxidation electrocatalysis for hydrogen generation and fuel cells," *Journal of The Electrochemical Society* **2018**, *165*, J3130.

(5) Montoya, J. H.; Tsai, C.; Vojvodic, A.; Nørskov, J. K. "The challenge of electrochemical ammonia synthesis: a new perspective on the role of nitrogen scaling relations," *ChemSusChem* **2015**, *8*, 2180-2186.

(6) Hochman, G.; Goldman, A. S.; Felder, F. A.; Mayer, J. M.; Miller, A. J.; Holland, P. L.; Goldman, L. A.; Manocha, P.; Song, Z.; Aleti, S. "Potential economic feasibility of direct electrochemical nitrogen reduction as a route to ammonia," *ACS Sustainable Chemistry & Engineering* **2020**, *8*, 8938-8948.

(7) Na, J.; Seo, B.; Kim, J.; Lee, C. W.; Lee, H.; Hwang, Y. J.; Min, B. K.; Lee, D. K.; Oh, H.-S.; Lee, U. "General technoeconomic analysis for electrochemical coproduction coupling carbon dioxide reduction with organic oxidation," *Nature communications* **2019**, *10*, 1-13.

(8) Bushuyev, O. S.; De Luna, P.; Dinh, C. T.; Tao, L.; Saur, G.; van de Lagemaat, J.; Kelley, S. O.; Sargent, E. H. "What Should We Make with CO_2 and How Can We Make It?," *Joule* **2018**, *2*, 825-832. http://dx.doi.org/https://doi.org/10.1016/j.joule.2017.09.003

(9) Kibria, M. G.; Edwards, J. P.; Gabardo, C. M.; Dinh, C.-T.; Seifitokaldani, A.; Sinton, D.; Sargent, E. H. "Electrochemical CO_2 Reduction into Chemical Feedstocks: From Mechanistic Electrocatalysis Models to System Design," *Advanced Materials* **2019**, *31*, 1807166. http://dx.doi.org/https://doi.org/10.1002/adma.201807166

(10) Masel, R. I.; Liu, Z.; Yang, H.; Kaczur, J. J.; Carrillo, D.; Ren, S.; Salvatore, D.; Berlinguette, C. P. "An industrial perspective on catalysts for low-temperature CO_2 electrolysis," *Nature Nanotechnology* **2021**, *16*, 118-128. http://dx.doi.org/10.1038/s41565-020-00823-x

(11) Jhong, H.-R. M.; Ma, S.; Kenis, P. J. A. "Electrochemical conversion of CO_2 to useful chemicals: current status, remaining challenges, and future opportunities," *Current Opinion in Chemical Engineering* **2013**, *2*, 191-199. http://dx.doi.org/https://doi.org/10.1016/j.coche.2013.03.005

(12) De Luna, P.; Hahn, C.; Higgins, D.; Jaffer, S. A.; Jaramillo, T. F.; Sargent, E. H. "What would it take for renewably powered electrosynthesis to displace petrochemical processes?," *Science* **2019**, *364*, eaav3506. http://dx.doi.org/10.1126/science.aav3506

(13) Hori, Y. "Electrochemical CO_2 Reduction on Metal Electrodes," In *Modern Aspects of Electrochemistry*; Vayenas, C. G., White, R. E., Gamboa-Aldeco, M. E., Eds.; Springer New York: New York, NY, 2008, p 89-189.

(14) Gattrell, M.; Gupta, N.; Co, A. "A review of the aqueous electrochemical reduction of CO_2 to hydrocarbons at copper," *Journal of Electroanalytical Chemistry* **2006**, *594*, 1-19. http://dx.doi.org/https://doi.org/10.1016/j.jelechem.2006.05.013
(15) Kuhl, K. P.; Cave, E. R.; Abram, D. N.; Jaramillo, T. F. "New insights into the electrochemical reduction of carbon dioxide on metallic copper surfaces," *Energy & Environmental Science* **2012**, *5*, 7050-7059. http://dx.doi.org/10.1039/C2EE21234J
(16) Leung, K. Y.; McCrory, C. C. L. "Effect and Prevention of Trace Ag^+ Contamination from Ag/AgCl Reference Electrodes on CO_2 Reduction Product Distributions at Polycrystalline Copper Electrodes," *ACS Applied Energy Materials* **2019**, *2*, 8283-8293. http://dx.doi.org/10.1021/acsaem.9b01759
(17) Kim, Y.-G.; Baricuatro, J. H.; Javier, A.; Gregoire, J. M.; Soriaga, M. P. "The Evolution of the Polycrystalline Copper Surface, First to Cu(111) and Then to Cu(100), at a Fixed CO_2RR Potential: A Study by Operando EC-STM," *Langmuir* **2014**, *30*, 15053-15056. http://dx.doi.org/10.1021/la504445g
(18) Boutin, E.; Merakeb, L.; Ma, B.; Boudy, B.; Wang, M.; Bonin, J.; Anxolabéhère-Mallart, E.; Robert, M. "Molecular catalysis of CO_2 reduction: recent advances and perspectives in electrochemical and light-driven processes with selected Fe, Ni and Co aza macrocyclic and polypyridine complexes," *Chemical Society Reviews* **2020**, *49*, 5772-5809. http://dx.doi.org/10.1039/D0CS00218F
(19) Barrett, A. J. A.; Brunner, B. F. M.; Cheung, C. P. L.; Kubiak, D. C. P.; Lee, E. G. L.; Miller, F. C. J.; Waldie, G. K. M.; Zhanaidarova, H. A. "Chapter 1 Approaches to Controlling Homogeneous Electrochemical Reduction of Carbon Dioxide," In *Carbon Dioxide Electrochemistry: Homogeneous and Heterogeneous Catalysis*; The Royal Society of Chemistry: 2021, p 1-66.
(20) Benson, E. E.; Kubiak, C. P.; Sathrum, A. J.; Smieja, J. M. "Electrocatalytic and homogeneous approaches to conversion of CO_2 to liquid fuels," *Chemical Society Reviews* **2009**, *38*, 89-99. http://dx.doi.org/10.1039/B804323J
(21) Inglis, J. L.; MacLean, B. J.; Pryce, M. T.; Vos, J. G. "Electrocatalytic pathways towards sustainable fuel production from water and CO_2," *Coordination Chemistry Reviews* **2012**, *256*, 2571-2600. http://dx.doi.org/https://doi.org/10.1016/j.ccr.2012.05.002
(22) Qiao, J.; Liu, Y.; Hong, F.; Zhang, J. "A review of catalysts for the electroreduction of carbon dioxide to produce low-carbon fuels," *Chemical Society Reviews* **2014**, *43*, 631-675. http://dx.doi.org/10.1039/C3CS60323G
(23) Corbin, N.; Zeng, J.; Williams, K.; Manthiram, K. "Heterogeneous molecular catalysts for electrocatalytic CO_2 reduction," *Nano Research* **2019**, *12*, 2093-2125. http://dx.doi.org/10.1007/s12274-019-2403-y
(24) Nie, W.; Tarnopol, D. E.; McCrory, C. C. L. "The effect of extended conjugation on electrocatalytic CO_2 reduction by molecular catalysts and macromolecular structures," *Current Opinion in Electrochemistry* **2021**, *28*, 100716. http://dx.doi.org/https://doi.org/10.1016/j.coelec.2021.100716
(25) Verma, S.; Kim, B.; Jhong, H.-R. M.; Ma, S.; Kenis, P. J. A. "A Gross-Margin Model for Defining Technoeconomic Benchmarks in the Electroreduction of CO_2," *ChemSusChem* **2016**, *9*, 1972-1979. http://dx.doi.org/10.1002/cssc.201600394
(26) Zhu, M.; Chen, J.; Guo, R.; Xu, J.; Fang, X.; Han, Y.-F. "Cobalt phthalocyanine coordinated to pyridine-functionalized carbon nanotubes with enhanced CO_2 electroreduction,"

Applied Catalysis B: Environmental **2019**, *251*, 112-118. http://dx.doi.org/https://doi.org/10.1016/j.apcatb.2019.03.047
(27) Zhang, X.; Wang, Y.; Gu, M.; Wang, M.; Zhang, Z.; Pan, W.; Jiang, Z.; Zheng, H.; Lucero, M.; Wang, H.; Sterbinsky, G. E.; Ma, Q.; Wang, Y.-G.; Feng, Z.; Li, J.; Dai, H.; Liang, Y. "Molecular engineering of dispersed nickel phthalocyanines on carbon nanotubes for selective CO_2 reduction," *Nature Energy* **2020**, *5*, 684-692. http://dx.doi.org/10.1038/s41560-020-0667-9
(28) Jiang, Z.; Wang, Y.; Zhang, X.; Zheng, H.; Wang, X.; Liang, Y. "Revealing the hidden performance of metal phthalocyanines for CO_2 reduction electrocatalysis by hybridization with carbon nanotubes," *Nano Research* **2019**, *12*, 2330-2334. http://dx.doi.org/10.1007/s12274-019-2455-z
(29) Devadoss, A.; Chidsey, C. E. "Azide-modified graphitic surfaces for covalent attachment of alkyne-terminated molecules by "click" chemistry," *Journal of the American Chemical Society* **2007**, *129*, 5370-5371.
(30) Lin, C. Y.; Zhang, D.; Zhao, Z.; Xia, Z. "Covalent organic framework electrocatalysts for clean energy conversion," *Advanced Materials* **2018**, *30*, 1703646.
(31) Yan, Y.; He, T.; Zhao, B.; Qi, K.; Liu, H.; Xia, B. Y. "Metal/covalent–organic frameworks-based electrocatalysts for water splitting," *Journal of Materials Chemistry A* **2018**, *6*, 15905-15926.
(32) Lu, X. F.; Xia, B. Y.; Zang, S.-Q.; Lou, X. W. "Metal–Organic Frameworks Based Electrocatalysts for the Oxygen Reduction Reaction," *Angewandte Chemie International Edition* **2020**, *59*, 4634-4650. http://dx.doi.org/https://doi.org/10.1002/anie.201910309
(33) Liu, Y.; Leung, K. Y.; Michaud, S. E.; Soucy, T. L.; McCrory, C. C. L. "Controlled Substrate Transport To Electrocatalyst Active Sites For Enhanced Selectivity In The Carbon Dioxide Reduction Reaction," *Comments on Inorganic Chemistry* **2019**, 1-28. http://dx.doi.org/10.1080/02603594.2019.1628025
(34) Smith, W. A.; Burdyny, T.; Vermaas, D. A.; Geerlings, H. "Pathways to Industrial-Scale Fuel Out of Thin Air from CO_2 Electrolysis," *Joule* **2019**, *3*, 1822-1834. http://dx.doi.org/https://doi.org/10.1016/j.joule.2019.07.009
(35) Bains, P.; Psarras, P.; Wilcox, J. "CO_2 capture from the industry sector," *Progress in Energy and Combustion Science* **2017**, *63*, 146-172. http://dx.doi.org/https://doi.org/10.1016/j.pecs.2017.07.001
(36) Romano, M. C.; Anantharaman, R.; Arasto, A.; Ozcan, D. C.; Ahn, H.; Dijkstra, J. W.; Carbo, M.; Boavida, D. "Application of Advanced Technologies for CO_2 Capture From Industrial Sources," *Energy Procedia* **2013**, *37*, 7176-7185. http://dx.doi.org/https://doi.org/10.1016/j.egypro.2013.06.655
(37) Barecka, M. H.; Ager, J. W.; Lapkin, A. A. "Carbon neutral manufacturing via on-site CO_2 recycling," *iScience* **2021**, *24*, 102514. http://dx.doi.org/https://doi.org/10.1016/j.isci.2021.102514
(38) Kuuskraa, V. A.; Godec, M. L.; Dipietro, P. "CO2 Utilization from "Next Generation" CO_2 Enhanced Oil Recovery Technology," *Energy Procedia* **2013**, *37*, 6854-6866. http://dx.doi.org/https://doi.org/10.1016/j.egypro.2013.06.618
(39) Oreggioni, G. D.; Luberti, M.; Tassou, S. A. "Agricultural greenhouse CO_2 utilization in anaerobic-digestion-based biomethane production plants: A techno-economic and environmental assessment and comparison with CO2 geological storage," *Applied Energy* **2019**, *242*, 1753-1766. http://dx.doi.org/https://doi.org/10.1016/j.apenergy.2019.03.045

(40) Edmonds, J.; Nichols, C.; Adamantiades, M.; Bistline, J.; Huster, J.; Iyer, G.; Johnson, N.; Patel, P.; Showalter, S.; Victor, N.; Waldhoff, S.; Wise, M.; Wood, F. "Could congressionally mandated incentives lead to deployment of large-scale CO_2 capture, facilities for enhanced oil recovery CO_2 markets and geologic CO_2 storage?," *Energy Policy* **2020**, *146*, 111775. http://dx.doi.org/https://doi.org/10.1016/j.enpol.2020.111775
(41) Tarufelli, B.; Snyder, B.; Dismukes, D. "The Potential Impact of the U.S. Carbon Capture and Storage Tax Credit Expansion on the Economic Feasibility of Industrial Carbon Capture and Storage," *Energy Policy* **2021**, *149*, 112064. http://dx.doi.org/https://doi.org/10.1016/j.enpol.2020.112064
(42) Esposito, R. A.; Kuuskraa, V. A.; Rossman, C. G.; Corser, M. M. "Reconsidering CCS in the US fossil-fuel fired electricity industry under section 45Q tax credits," *Greenhouse Gases: Science and Technology* **2019**, *9*, 1288-1301. http://dx.doi.org/https://doi.org/10.1002/ghg.1925
(43) Weekes, D. M.; Salvatore, D. A.; Reyes, A.; Huang, A.; Berlinguette, C. P. "Electrolytic CO_2 Reduction in a Flow Cell," *Accounts of Chemical Research* **2018**, *51*, 910-918. http://dx.doi.org/10.1021/acs.accounts.8b00010
(44) Rabiee, H.; Ge, L.; Zhang, X.; Hu, S.; Li, M.; Yuan, Z. "Gas diffusion electrodes (GDEs) for electrochemical reduction of carbon dioxide, carbon monoxide, and dinitrogen to value-added products: a review," *Energy & Environmental Science* **2021**, *14*, 1959-2008. http://dx.doi.org/10.1039/D0EE03756G
(45) Higgins, D.; Hahn, C.; Xiang, C.; Jaramillo, T. F.; Weber, A. Z. "Gas-Diffusion Electrodes for Carbon Dioxide Reduction: A New Paradigm," *ACS Energy Letters* **2019**, *4*, 317-324. http://dx.doi.org/10.1021/acsenergylett.8b02035
(46) Zheng, T.; Jiang, K.; Wang, H. "Recent Advances in Electrochemical CO_2-to-CO Conversion on Heterogeneous Catalysts," *Advanced Materials* **2018**, *30*, 1802066. http://dx.doi.org/https://doi.org/10.1002/adma.201802066
(47) Jin, S.; Hao, Z.; Zhang, K.; Yan, Z.; Chen, J. "Advances and Challenges for the Electrochemical Reduction of CO_2 to CO: From Fundamentals to Industrialization," *Angewandte Chemie International Edition* **2021**, *60*, 20627-20648. http://dx.doi.org/https://doi.org/10.1002/anie.202101818
(48) Torbensen, K.; Joulié, D.; Ren, S.; Wang, M.; Salvatore, D.; Berlinguette, C. P.; Robert, M. "Molecular Catalysts Boost the Rate of Electrolytic CO_2 Reduction," *ACS Energy Letters* **2020**, *5*, 1512-1518. http://dx.doi.org/10.1021/acsenergylett.0c00536
(49) Liu, Z.; Yang, H.; Kutz, R.; Masel, R. I. "CO_2 Electrolysis to CO and O_2 at High Selectivity, Stability and Efficiency Using Sustainion Membranes," *Journal of The Electrochemical Society* **2018**, *165*, J3371-J3377. http://dx.doi.org/10.1149/2.0501815jes
(50) Fan, L.; Xia, C.; Yang, F.; Wang, J.; Wang, H.; Lu, Y. "Strategies in catalysts and electrolyzer design for electrochemical CO_2 reduction toward C2+ products," *Science Advances* **2020**, *6*, eaay3111. http://dx.doi.org/10.1126/sciadv.aay3111
(51) Ren, S.; Joulié, D.; Salvatore, D.; Torbensen, K.; Wang, M.; Robert, M.; Berlinguette, C. P. "Molecular electrocatalysts can mediate fast, selective CO_2 reduction in a flow cell," *Science* **2019**, *365*, 367-369. http://dx.doi.org/10.1126/science.aax4608
(52) Passalacqua, E.; Lufrano, F.; Squadrito, G.; Patti, A.; Giorgi, L. "Nafion content in the catalyst layer of polymer electrolyte fuel cells: effects on structure and performance," *Electrochimica Acta* **2001**, *46*, 799-805. http://dx.doi.org/https://doi.org/10.1016/S0013-4686(00)00679-4

(53) Antoine, O.; Bultel, Y.; Durand, R. "Oxygen reduction reaction kinetics and mechanism on platinum nanoparticles inside Nafion®," *Journal of Electroanalytical Chemistry* **2001**, *499*, 85-94. http://dx.doi.org/https://doi.org/10.1016/S0022-0728(00)00492-7
(54) Wang, Q.; Dong, H.; Yu, H. "Fabrication of a novel tin gas diffusion electrode for electrochemical reduction of carbon dioxide to formic acid," *RSC Advances* **2014**, *4*, 59970-59976. http://dx.doi.org/10.1039/C4RA10775F
(55) Albo, J.; Irabien, A. "Cu_2O-loaded gas diffusion electrodes for the continuous electrochemical reduction of CO_2 to methanol," *Journal of Catalysis* **2016**, *343*, 232-239. http://dx.doi.org/https://doi.org/10.1016/j.jcat.2015.11.014
(56) Ma, S.; Sadakiyo, M.; Luo, R.; Heima, M.; Yamauchi, M.; Kenis, P. J. A. "One-step electrosynthesis of ethylene and ethanol from CO_2 in an alkaline electrolyzer," *Journal of Power Sources* **2016**, *301*, 219-228. http://dx.doi.org/https://doi.org/10.1016/j.jpowsour.2015.09.124
(57) Xu, Y.; Li, F.; Xu, A.; Edwards, J. P.; Hung, S.-F.; Gabardo, C. M.; O'Brien, C. P.; Liu, S.; Wang, X.; Li, Y.; Wicks, J.; Miao, R. K.; Liu, Y.; Li, J.; Huang, J. E.; Abed, J.; Wang, Y.; Sargent, E. H.; Sinton, D. "Low coordination number copper catalysts for electrochemical CO_2 methanation in a membrane electrode assembly," *Nature Communications* **2021**, *12*, 2932. http://dx.doi.org/10.1038/s41467-021-23065-4
(58) Torbensen, K.; Han, C.; Boudy, B.; von Wolff, N.; Bertail, C.; Braun, W.; Robert, M. "Iron Porphyrin Allows Fast and Selective Electrocatalytic Conversion of CO_2 to CO in a Flow Cell," *Chemistry – A European Journal* **2020**, *26*, 3034-3038. http://dx.doi.org/https://doi.org/10.1002/chem.202000160
(59) Kim, B.; Ma, S.; Molly Jhong, H.-R.; Kenis, P. J. A. "Influence of dilute feed and pH on electrochemical reduction of CO_2 to CO on Ag in a continuous flow electrolyzer," *Electrochimica Acta* **2015**, *166*, 271-276. http://dx.doi.org/https://doi.org/10.1016/j.electacta.2015.03.064
(60) Ma, S.; Luo, R.; Gold, J. I.; Yu, A. Z.; Kim, B.; Kenis, P. J. A. "Carbon nanotube containing Ag catalyst layers for efficient and selective reduction of carbon dioxide," *Journal of Materials Chemistry A* **2016**, *4*, 8573-8578. http://dx.doi.org/10.1039/C6TA00427J
(61) Ma , S.; Lan , Y.; Perez, G. M. J.; Moniri, S.; Kenis , P. J. A. "Silver Supported on Titania as an Active Catalyst for Electrochemical Carbon Dioxide Reduction," *ChemSusChem* **2014**, *7*, 866-874. http://dx.doi.org/https://doi.org/10.1002/cssc.201300934
(62) Salvatore, D. A.; Weekes, D. M.; He, J.; Dettelbach, K. E.; Li, Y. C.; Mallouk, T. E.; Berlinguette, C. P. "Electrolysis of Gaseous CO_2 to CO in a Flow Cell with a Bipolar Membrane," *ACS Energy Letters* **2018**, *3*, 149-154. http://dx.doi.org/10.1021/acsenergylett.7b01017
(63) Xiang, H.; Rasul, S.; Hou, B.; Portoles, J.; Cumpson, P.; Yu, E. H. "Copper–Indium Binary Catalyst on a Gas Diffusion Electrode for High-Performance CO_2 Electrochemical Reduction with Record CO Production Efficiency," *ACS Applied Materials & Interfaces* **2020**, *12*, 601-608. http://dx.doi.org/10.1021/acsami.9b16862
(64) Jeong, H.-Y.; Balamurugan, M.; Choutipalli, V. S. K.; Jeong, E.-s.; Subramanian, V.; Sim, U.; Nam, K. T. "Achieving highly efficient CO_2 to CO electroreduction exceeding 300 mA cm^{-2} with single-atom nickel electrocatalysts," *Journal of Materials Chemistry A* **2019**, *7*, 10651-10661. http://dx.doi.org/10.1039/C9TA02405K
(65) Gabardo, C. M.; Seifitokaldani, A.; Edwards, J. P.; Dinh, C.-T.; Burdyny, T.; Kibria, M. G.; O'Brien, C. P.; Sargent, E. H.; Sinton, D. "Combined high alkalinity and pressurization

enable efficient CO_2 electroreduction to CO," *Energy & Environmental Science* **2018**, *11*, 2531-2539. http://dx.doi.org/10.1039/C8EE01684D
(66) Delacourt, C.; Ridgway, P. L.; Kerr, J. B.; Newman, J. "Design of an Electrochemical Cell Making Syngas ($CO+H_2$) from CO_2 and H_2O Reduction at Room Temperature," *Journal of The Electrochemical Society* **2008**, *155*, B42. http://dx.doi.org/10.1149/1.2801871
(67) Kim, B.; Seong, H.; Song, J. T.; Kwak, K.; Song, H.; Tan, Y. C.; Park, G.; Lee, D.; Oh, J. "Over a 15.9% Solar-to-CO Conversion from Dilute CO_2 Streams Catalyzed by Gold Nanoclusters Exhibiting a High CO_2 Binding Affinity," *ACS Energy Letters* **2020**, *5*, 749-757. http://dx.doi.org/10.1021/acsenergylett.9b02511
(68) Lees, E. W.; Mowbray, B. A. W.; Salvatore, D. A.; Simpson, G. L.; Dvorak, D. J.; Ren, S.; Chau, J.; Milton, K. L.; Berlinguette, C. P. "Linking gas diffusion electrode composition to CO_2 reduction in a flow cell," *Journal of Materials Chemistry A* **2020**, *8*, 19493-19501. http://dx.doi.org/10.1039/D0TA03570J
(69) Monteiro, M. C. O.; Philips, M. F.; Schouten, K. J. P.; Koper, M. T. M. "Efficiency and selectivity of CO_2 reduction to CO on gold gas diffusion electrodes in acidic media," *Nature Communications* **2021**, *12*, 4943. http://dx.doi.org/10.1038/s41467-021-24936-6
(70) Wang, M.; Torbensen, K.; Salvatore, D.; Ren, S.; Joulié, D.; Dumoulin, F.; Mendoza, D.; Lassalle-Kaiser, B.; Işci, U.; Berlinguette, C. P.; Robert, M. "CO_2 electrochemical catalytic reduction with a highly active cobalt phthalocyanine," *Nature Communications* **2019**, *10*, 3602. http://dx.doi.org/10.1038/s41467-019-11542-w
(71) Nwabara, U. O.; Hernandez, A. D.; Henckel, D. A.; Chen, X.; Cofell, E. R.; de-Heer, M. P.; Verma, S.; Gewirth, A. A.; Kenis, P. J. A. "Binder-Focused Approaches to Improve the Stability of Cathodes for CO_2 Electroreduction," *ACS Applied Energy Materials* **2021**, *4*, 5175-5186. http://dx.doi.org/10.1021/acsaem.1c00715
(72) Arquer, F. P. G. d.; Dinh, C.-T.; Ozden, A.; Wicks, J.; McCallum, C.; Kirmani, A. R.; Nam, D.-H.; Gabardo, C.; Seifitokaldani, A.; Wang, X.; Li, Y. C.; Li, F.; Edwards, J.; Richter, L. J.; Thorpe, S. J.; Sinton, D.; Sargent, E. H. "CO_2 electrolysis to multicarbon products at activities greater than 1 A cm," *Science* **2020**, *367*, 661-666. http://dx.doi.org/doi:10.1126/science.aay4217
(73) Endrődi, B.; Samu, A.; Kecsenovity, E.; Halmágyi, T.; Sebők, D.; Janáky, C. "Operando cathode activation with alkali metal cations for high current density operation of water-fed zero-gap carbon dioxide electrolysers," *Nature Energy* **2021**, *6*, 439-448. http://dx.doi.org/10.1038/s41560-021-00813-w
(74) Reyes, A.; Jansonius, R. P.; Mowbray, B. A. W.; Cao, Y.; Wheeler, D. G.; Chau, J.; Dvorak, D. J.; Berlinguette, C. P. "Managing Hydration at the Cathode Enables Efficient CO_2 Electrolysis at Commercially Relevant Current Densities," *ACS Energy Letters* **2020**, *5*, 1612-1618. http://dx.doi.org/10.1021/acsenergylett.0c00637
(75) Xing, Z.; Hu, L.; Ripatti, D. S.; Hu, X.; Feng, X. "Enhancing carbon dioxide gas-diffusion electrolysis by creating a hydrophobic catalyst microenvironment," *Nature Communications* **2021**, *12*, 136. http://dx.doi.org/10.1038/s41467-020-20397-5
(76) Yin, Z.; Peng, H.; Wei, X.; Zhou, H.; Gong, J.; Huai, M.; Xiao, L.; Wang, G.; Lu, J.; Zhuang, L. "An alkaline polymer electrolyte CO_2 electrolyzer operated with pure water," *Energy & Environmental Science* **2019**, *12*, 2455-2462. http://dx.doi.org/10.1039/C9EE01204D
(77) Kaczur, J. J.; Yang, H.; Liu, Z.; Sajjad, S. D.; Masel, R. I. "Carbon Dioxide and Water Electrolysis Using New Alkaline Stable Anion Membranes," *Frontiers in Chemistry* **2018**, *6*. http://dx.doi.org/10.3389/fchem.2018.00263

(78) Kutz, R. B.; Chen, Q.; Yang, H.; Sajjad, S. D.; Liu, Z.; Masel, I. R. "Sustainion Imidazolium-Functionalized Polymers for Carbon Dioxide Electrolysis," *Energy Technology* **2017**, *5*, 929-936. http://dx.doi.org/https://doi.org/10.1002/ente.201600636
(79) Sajjad, S. D.; Gao, Y.; Liu, Z.; Yang, H.; Masel, R. "Tunable-High Performance Sustainion™ Anion Exchange Membranes for Electrochemical Applications," *ECS Transactions* **2017**, *77*, 1653-1656. http://dx.doi.org/10.1149/07711.1653ecst
(80) Verma, S.; Hamasaki, Y.; Kim, C.; Huang, W.; Lu, S.; Jhong, H.-R. M.; Gewirth, A. A.; Fujigaya, T.; Nakashima, N.; Kenis, P. J. A. "Insights into the Low Overpotential Electroreduction of CO_2 to CO on a Supported Gold Catalyst in an Alkaline Flow Electrolyzer," *ACS Energy Letters* **2017**, *3*, 193-198. http://dx.doi.org/10.1021/acsenergylett.7b01096
(81) Murata, K.; Tanaka, H.; Ishii, K. "Electrochemical Reduction of CO_2 by a Gas-Diffusion Electrode Composed of fac-Re(diimine)$(CO)_3$Cl and Carbon Nanotubes," *The Journal of Physical Chemistry C* **2019**, *123*, 12073-12080. http://dx.doi.org/10.1021/acs.jpcc.8b12505
(82) Jhong, H.-R. M.; Tornow, C. E.; Kim, C.; Verma, S.; Oberst, J. L.; Anderson, P. S.; Gewirth, A. A.; Fujigaya, T.; Nakashima, N.; Kenis, P. J. A. "Gold Nanoparticles on Polymer-Wrapped Carbon Nanotubes: An Efficient and Selective Catalyst for the Electroreduction of CO_2," *ChemPhysChem* **2017**, *18*, 3274-3279. http://dx.doi.org/https://doi.org/10.1002/cphc.201700815
(83) Lu, X.; Wu, Y.; Yuan, X.; Huang, L.; Wu, Z.; Xuan, J.; Wang, Y.; Wang, H. "High-Performance Electrochemical CO_2 Reduction Cells Based on Non-noble Metal Catalysts," *ACS Energy Letters* **2018**, *3*, 2527-2532. http://dx.doi.org/10.1021/acsenergylett.8b01681
(84) Zhu, M.; Chen, J.; Huang, L.; Ye, R.; Xu, J.; Han, Y.-F. "Covalently Grafting Cobalt Porphyrin onto Carbon Nanotubes for Efficient CO_2 Electroreduction," *Angewandte Chemie International Edition* **2019**, *58*, 6595-6599. http://dx.doi.org/https://doi.org/10.1002/anie.201900499
(85) Meshitsuka, S.; Ichikawa, M.; Tamaru, K. "Electrocatalysis by metal phthalocyanines in the reduction of carbon dioxide," *Journal of the Chemical Society, Chemical Communications* **1974**, 158-159. http://dx.doi.org/10.1039/C39740000158
(86) Lieber, C. M.; Lewis, N. S. "Catalytic reduction of carbon dioxide at carbon electrodes modified with cobalt phthalocyanine," *Journal of the American Chemical Society* **1984**, *106*, 5033-5034. http://dx.doi.org/10.1021/ja00329a082
(87) Furuya, N.; Matsui, K. "Electroreduction of carbon dioxide on gas-diffusion electrodes modified by metal phthalocyanines," *Journal of Electroanalytical Chemistry and Interfacial Electrochemistry* **1989**, *271*, 181-191. http://dx.doi.org/http://dx.doi.org/10.1016/0022-0728(89)80074-9
(88) Rivera Cruz, K. E.; Liu, Y.; Soucy, T. L.; Zimmerman, P. M.; McCrory, C. C. L. "Increasing the CO_2 Reduction Activity of Cobalt Phthalocyanine by Modulating the σ-Donor Strength of Axially Coordinating Ligands," *ACS Catalysis* **2021**, *11*, 13203-13216. http://dx.doi.org/10.1021/acscatal.1c02379
(89) Wu, Y.; Hu, G.; Rooney, C. L.; Brudvig, G. W.; Wang, H. "Heterogeneous Nature of Electrocatalytic CO/CO_2 Reduction by Cobalt Phthalocyanines," *ChemSusChem* **2020**, *n/a*. http://dx.doi.org/10.1002/cssc.202001396
(90) Wu, Y.; Jiang, Z.; Lu, X.; Liang, Y.; Wang, H. "Domino electroreduction of CO_2 to methanol on a molecular catalyst," *Nature* **2019**, *575*, 639-642. http://dx.doi.org/10.1038/s41586-019-1760-8

(91) Kapusta, S.; Hackerman, N. "Carbon Dioxide Reduction at a Metal Phthalocyanine Catalyzed Carbon Electrode," *Journal of the Electrochemical Society* **1984**, *131*, 1511-1514. http://dx.doi.org/10.1149/1.2115882
(92) Boutin, E.; Wang, M.; Lin, J. C.; Mesnage, M.; Mendoza, D.; Lassalle-Kaiser, B.; Hahn, C.; Jaramillo, T. F.; Robert, M. "Aqueous Electrochemical Reduction of Carbon Dioxide and Carbon Monoxide into Methanol with Cobalt Phthalocyanine," *Angewandte Chemie International Edition* **2019**, *58*, 16172-16176. http://dx.doi.org/10.1002/anie.201909257
(93) Yoshida, T.; Iida, T.; Shirasagi, T.; Lin, R.-J.; Kaneko, M. "Electrocatalytic reduction of carbon dioxide in aqueous medium by bis(2,2': 6',2"-terpyridine)cobalt(II) complex incorporated into a coated polymer membrane," *Journal of Electroanalytical Chemistry* **1993**, *344*, 355-362. http://dx.doi.org/10.1016/0022-0728(93)80066-Q
(94) Yoshida, T.; Tsutsumida, K.; Teratani, S.; Yasufuku, K.; Kaneko, M. "Electrocatalytic reduction of CO_2 in water by [Re(bpy)$(CO)_3$Br] and [Re(terpy)$(CO)_3$Br] complexes incorporated into coated nafion membrane (bpy = 2,2'-bipyridine; terpy = 2,2';6',2"-terpyridine)," *Journal of the Chemical Society, Chemical Communications* **1993**, 631-633. http://dx.doi.org/10.1039/C39930000631
(95) Zhao, F.; Zhang, J.; Abe, T.; Wöhrle, D.; Kaneko, M. "Electrocatalytic proton reduction by phthalocyanine cobalt derivatives incorporated in poly(4-vinylpyridine-co-styrene) film," *Journal of Molecular Catalysis A: Chemical* **1999**, *145*, 245-256. http://dx.doi.org/https://doi.org/10.1016/S1381-1169(99)00013-8
(96) Abe, T.; Imaya, H.; Yoshida, T.; Tokita, S.; Schlettwein, D.; Wöhrle, D.; Kaneko, M. "Electrochemical CO_2 Reduction Catalysed by Cobalt Octacyanophthalocyanine and its Mechanism," *Journal of Porphyrins and Phthalocyanines* **1997**, *01*, 315-321. http://dx.doi.org/10.1002/(sici)1099-1409(199710)1:4<315::Aid-jpp35>3.0.Co;2-v
(97) Abe, T.; Yoshida, T.; Tokita, S.; Taguchi, F.; Imaya, H.; Kaneko, M. "Factors affecting selective electrocatalytic CO_2 reduction with cobalt phthalocyanine incorporated in a polyvinylpyridine membrane coated on a graphite electrode," *Journal of Electroanalytical Chemistry* **1996**, *412*, 125-132. http://dx.doi.org/10.1016/0022-0728(96)04631-1
(98) Yoshida, T.; Kamato, K.; Tsukamoto, M.; Iida, T.; Schlettwein, D.; Wöhrle, D.; Kaneko, M. "Selective electroacatalysis for CO_2 reduction in the aqueous phase using cobalt phthalocyanine/poly-4-vinylpyridine modified electrodes," *Journal of Electroanalytical Chemistry* **1995**, *385*, 209-225. http://dx.doi.org/10.1016/0022-0728(94)03762-R
(99) Mak, C. H.; Han, X.; Du, M.; Kai, J.-J.; Tsang, K. F.; Jia, G.; Cheng, K.-C.; Shen, H.-H.; Hsu, H.-Y. "Heterogenization of homogeneous photocatalysts utilizing synthetic and natural support materials," *Journal of Materials Chemistry A* **2021**, *9*, 4454-4504. http://dx.doi.org/10.1039/D0TA08334H
(100) Orchanian, N. M.; Hong, L. E.; Skrainka, J. A.; Esterhuizen, J. A.; Popov, D. A.; Marinescu, S. C. "Surface-Immobilized Conjugated Polymers Incorporating Rhenium Bipyridine Motifs for Electrocatalytic and Photocatalytic CO_2 Reduction," *ACS Applied Energy Materials* **2019**, *2*, 110-123. http://dx.doi.org/10.1021/acsaem.8b01745
(101) Kamata, R.; Kumagai, H.; Yamazaki, Y.; Sahara, G.; Ishitani, O. "Photoelectrochemical CO2 Reduction Using a Ru(II)–Re(I) Supramolecular Photocatalyst Connected to a Vinyl Polymer on a NiO Electrode," *ACS Applied Materials & Interfaces* **2019**, *11*, 5632-5641. http://dx.doi.org/10.1021/acsami.8b05495
(102) Tsounis, C.; Kuriki, R.; Shibata, K.; Vequizo, J. J. M.; Lu, D.; Yamakata, A.; Ishitani, O.; Amal, R.; Maeda, K. "Copolymerization Approach to Improving Ru(II)-Complex/C_3N_4 Hybrid

Photocatalysts for Visible-Light CO_2 Reduction," *ACS Sustainable Chemistry & Engineering* **2018**, *6*, 15333-15340. http://dx.doi.org/10.1021/acssuschemeng.8b03782
(103) Roy, S.; Reisner, E. "Visible-Light-Driven CO_2 Reduction by Mesoporous Carbon Nitride Modified with Polymeric Cobalt Phthalocyanine," *Angewandte Chemie International Edition* **2019**, *58*, 12180-12184. http://dx.doi.org/10.1002/anie.201907082
(104) Birdja, Y. Y.; Vos, R. E.; Wezendonk, T. A.; Jiang, L.; Kapteijn, F.; Koper, M. T. M. "Effects of Substrate and Polymer Encapsulation on CO_2 Electroreduction by Immobilized Indium(III) Protoporphyrin," *ACS Catalysis* **2018**, *8*, 4420-4428. http://dx.doi.org/10.1021/acscatal.7b03386
(105) Sato, S.; McNicholas, B. J.; Grubbs, R. H. "Aqueous electrocatalytic CO2 reduction using metal complexes dispersed in polymer ion gels," *Chemical Communications* **2020**, *56*, 4440-4443. http://dx.doi.org/10.1039/D0CC00791A
(106) McNicholas, B. J.; Blakemore, J. D.; Chang, A. B.; Bates, C. M.; Kramer, W. W.; Grubbs, R. H.; Gray, H. B. "Electrocatalysis of CO2 Reduction in Brush Polymer Ion Gels," *Journal of the American Chemical Society* **2016**, *138*, 11160-11163. http://dx.doi.org/10.1021/jacs.6b08795
(107) Leung, J. J.; Vigil, J. A.; Warnan, J.; Edwardes Moore, E.; Reisner, E. "Rational Design of Polymers for Selective CO2 Reduction Catalysis," *Angew Chem Int Ed Engl* **2019**, *58*, 7697-7701. http://dx.doi.org/10.1002/anie.201902218
(108) Liu, Y.; McCrory, C. C. L. "Modulating the mechanism of electrocatalytic CO_2 reduction by cobalt phthalocyanine through polymer coordination and encapsulation," *Nature Communications* **2019**, *10*, 1683. http://dx.doi.org/10.1038/s41467-019-09626-8
(109) Soucy, T. L.; Liu, Y.; Eisenberg, J. B.; McCrory, C. C. L. "Enhancing the Electrochemical CO2 Reduction Activity of Polymer-Encapsulated Cobalt Phthalocyanine Films by Modulating the Loading of Catalysts, Polymers, and Carbon Supports. ," *ACS Applied Energy Materials* **2021**, *ASAP*. http://dx.doi.org/10.1021/acsaem.1c02689
(110) Zhang, X.; Wu, Z.; Zhang, X.; Li, L.; Li, Y.; Xu, H.; Li, X.; Yu, X.; Zhang, Z.; Liang, Y.; Wang, H. "Highly selective and active CO2 reduction electrocatalysts based on cobalt phthalocyanine/carbon nanotube hybrid structures," *Nature Communications* **2017**, *8*, 14675. http://dx.doi.org/10.1038/ncomms14675
(111) Hu, X.-M.; Rønne, M. H.; Pedersen, S. U.; Skrydstrup, T.; Daasbjerg, K. "Enhanced Catalytic Activity of Cobalt Porphyrin in CO2 Electroreduction upon Immobilization on Carbon Materials," *Angewandte Chemie International Edition* **2017**, *56*, 6468-6472. http://dx.doi.org/10.1002/anie.201701104
(112) Lin, S.; Diercks, C. S.; Zhang, Y.-B.; Kornienko, N.; Nichols, E. M.; Zhao, Y.; Paris, A. R.; Kim, D.; Yang, P.; Yaghi, O. M.; Chang, C. J. "Covalent organic frameworks comprising cobalt porphyrins for catalytic CO_2 reduction in water," *Science* **2015**, *349*, 1208-1213. http://dx.doi.org/10.1126/science.aac8343
(113) Kramer, W. W.; McCrory, C. C. L. "Polymer coordination promotes selective CO_2 reduction by cobalt phthalocyanine," *Chemical Science* **2016**, *7*, 2506-2515. http://dx.doi.org/10.1039/C5SC04015A
(114) Liu, Y.; Deb, A.; Leung, K. Y.; Nie, W.; Dean, W. S.; Penner-Hahn, J. E.; McCrory, C. C. L. "Determining the coordination environment and electronic structure of polymer-encapsulated cobalt phthalocyanine under electrocatalytic CO_2 reduction conditions using in situ X-Ray absorption spectroscopy," *Dalton Transactions* **2020**, *49*, 16329-16339. http://dx.doi.org/10.1039/D0DT01288B

(115) Dodelet, J.-P. "Oxygen Reduction in PEM Fuel Cell Conditions: Heat-Treated Non-Precious Metal-N4 Macrocycles and Beyond," In *N4-Macrocyclic Metal Complexes*; Zagal, J. H., Bedioui, F., Dodelet, J.-P., Eds.; Springer New York: New York, NY, 2006, p 83-147.
(116) Kau, L. S.; Spira-Solomon, D. J.; Penner-Hahn, J. E.; Hodgson, K. O.; Solomon, E. I. "X-ray absorption edge determination of the oxidation state and coordination number of copper. Application to the type 3 site in Rhus vernicifera laccase and its reaction with oxygen," *Journal of the American Chemical Society* **1987**, *109*, 6433-6442. http://dx.doi.org/10.1021/ja00255a032
(117) Chen, X.; Chen, J.; Alghoraibi, N. M.; Henckel, D. A.; Zhang, R.; Nwabara, U. O.; Madsen, K. E.; Kenis, P. J. A.; Zimmerman, S. C.; Gewirth, A. A. "Electrochemical CO2-to-ethylene conversion on polyamine-incorporated Cu electrodes," *Nature Catalysis* **2020**, *4*, 20-27. http://dx.doi.org/10.1038/s41929-020-00547-0
(118) O'Hagan, M.; Shaw, W. J.; Raugei, S.; Chen, S.; Yang, J. Y.; Kilgore, U. J.; DuBois, D. L.; Bullock, R. M. "Moving Protons with Pendant Amines: Proton Mobility in a Nickel Catalyst for Oxidation of Hydrogen," *Journal of the American Chemical Society* **2011**, *133*, 14301-14312. http://dx.doi.org/10.1021/ja201838x
(119) Cornish, A. J.; Ginovska, B.; Thelen, A.; da Silva, J. C. S.; Soares, T. A.; Raugei, S.; Dupuis, M.; Shaw, W. J.; Hegg, E. L. "Single-Amino Acid Modifications Reveal Additional Controls on the Proton Pathway of [FeFe]-Hydrogenase," *Biochemistry* **2016**, *55*, 3165-3173. http://dx.doi.org/10.1021/acs.biochem.5b01044
(120) Shaw, W. J. "The Outer-Coordination Sphere: Incorporating Amino Acids and Peptides as Ligands for Homogeneous Catalysts to Mimic Enzyme Function," *Catalysis Reviews* **2012**, *54*, 489-550. http://dx.doi.org/10.1080/01614940.2012.679453
(121) Laureanti, J. A.; Ginovska, B.; Buchko, G. W.; Schenter, G. K.; Hebert, M.; Zadvornyy, O. A.; Peters, J. W.; Shaw, W. J. "A Positive Charge in the Outer Coordination Sphere of an Artificial Enzyme Increases CO2 Hydrogenation," *Organometallics* **2020**, *39*, 1532-1544. http://dx.doi.org/10.1021/acs.organomet.9b00843
(122) Barbara Schowen, K.; Schowen, R. L. "[29] Solvent isotope effects on enzyme systems," In *Methods in Enzymology*; Daniel, L. P., Ed.; Academic Press: 1982; Vol. Volume 87, p 551-606.
(123) Schowen, R. L. "The use of solvent isotope effects in the pursuit of enzyme mechanisms," *Journal of Labelled Compounds and Radiopharmaceuticals* **2007**, *50*, 1052-1062. http://dx.doi.org/10.1002/jlcr.1436
(124) Fan, G.; Wasuwanich, P.; Furst, A. L. "Biohybrid Systems for Improved Bioinspired, Energy-Relevant Catalysis," *ChemBioChem* **2021**, *22*, 2353-2367. http://dx.doi.org/https://doi.org/10.1002/cbic.202100037
(125) Karsten, W. E.; Cook, P. F. "Substrate and pH dependence of isotope effects in enzyme catalyzed reactions," In *Isotope Effects in Chemistry and Biology* 2006, p 793-810.
(126) Northrop, D. B. "Steady-state analysis of kinetic isotope effects in enzymic reactions," *Biochemistry* **1975**, *14*, 2644-2651. http://dx.doi.org/10.1021/bi00683a013
(127) Kohen, A.; Limbach, H. H. *Isotope effects in chemistry and biology*; cRc Press: Boca Raton, 2005.
(128) Costentin, C.; Savéant, J.-M. "Molecular approach to catalysis of electrochemical reaction in porous films," *Current Opinion in Electrochemistry* **2019**, *15*, 58-65. http://dx.doi.org/10.1016/j.coelec.2019.03.014

(129) Huai, M.; Yin, Z.; Wei, F.; Wang, G.; Xiao, L.; Lu, J.; Zhuang, L. "Electrochemical CO_2 reduction on heterogeneous cobalt phthalocyanine catalysts with different carbon supports," *Chemical Physics Letters* **2020**, *754*, 137655. http://dx.doi.org/10.1016/j.cplett.2020.137655
(130) Tang, J.-K.; Zhu, C.-Y.; Jiang, T.-W.; Wei, L.; Wang, H.; Yu, K.; Yang, C.-L.; Zhang, Y.-B.; Chen, C.; Li, Z.-T.; Zhang, D.-W.; Zhang, L.-M. "Anion exchange-induced single-molecule dispersion of cobalt porphyrins in a cationic porous organic polymer for enhanced electrochemical CO2 reduction via secondary-coordination sphere interactions," *Journal of Materials Chemistry A* **2020**, *8*, 18677-18686. http://dx.doi.org/10.1039/D0TA07068H
(131) Wang, Y.; Wang, D.; Dares, C. J.; Marquard, S. L.; Sheridan, M. V.; Meyer, T. J. "CO2 reduction to acetate in mixtures of ultrasmall (Cu) n ,(Ag) m bimetallic nanoparticles," *Proc Natl Acad Sci U S A* **2018**, *115*, 278-283. http://dx.doi.org/10.1073/pnas.1713962115 10.1073/pnas.1713962115. Epub 2017 Dec 26.
(132) Choi, J.; Wagner, P.; Gambhir, S.; Jalili, R.; MacFarlane, D. R.; Wallace, G. G.; Officer, D. L. "Steric Modification of a Cobalt Phthalocyanine/Graphene Catalyst To Give Enhanced and Stable Electrochemical CO2 Reduction to CO," *ACS Energy Letters* **2019**, *4*, 666-672. http://dx.doi.org/10.1021/acsenergylett.8b02355
(133) Wu, X.; Sun, J. W.; Liu, P. F.; Zhao, J. Y.; Liu, Y.; Guo, L.; Dai, S.; Yang, H. G.; Zhao, H. "Molecularly Dispersed Cobalt Phthalocyanine Mediates Selective and Durable CO2 Reduction in a Membrane Flow Cell," *Advanced Functional Materials*, *n/a*, 2107301. http://dx.doi.org/https://doi.org/10.1002/adfm.202107301
(134) Zhu, M.; Ye, R.; Jin, K.; Lazouski, N.; Manthiram, K. "Elucidating the Reactivity and Mechanism of CO2 Electroreduction at Highly Dispersed Cobalt Phthalocyanine," *ACS Energy Letters* **2018**, *3*, 1381-1386. http://dx.doi.org/10.1021/acsenergylett.8b00519
(135) Panov, V. P.; Vorontsov, E. D.; Evdakov, V. P. "Spectroscopic determination of the extent of protonation and alkylation of poly-4-vinylpyridine derivatives," *Journal of Applied Spectroscopy* **1975**, *23*, 958-962. http://dx.doi.org/10.1007/BF00608822
(136) Chen, W.; Sauer, J. A.; Hara, M. "The effect of ionic cross-links on the deformation behavior of homoblends made of poly(styrene-co-styrenesulfonic acid) and poly(styrene-co-4-vinylpyridine)," *Polymer* **2003**, *44*, 7729-7738. http://dx.doi.org/https://doi.org/10.1016/j.polymer.2003.09.053
(137) Smith, P.; Eisenberg, A. "Infrared spectroscopic study of blends of poly(styrene-co-styrenesulfonic acid) with poly(styrene-co-(4-vinylpyridine))," *Macromolecules* **1994**, *27*, 545-552. http://dx.doi.org/10.1021/ma00080a032
(138) Sakurai, K.; Douglas, E. P.; MacKnight, W. J. "Spectroscopic study of an ionic blend made from the acid form of sulfonated polystyrene and poly[ethyl acrylate-co-(4-vinylpyridine)]," *Macromolecules* **1992**, *25*, 4506-4510. http://dx.doi.org/10.1021/ma00044a008
(139) Atvars, T. D. Z.; Dibbern, D. N.; Sabadini, E. "Infrared Spectroscope And Conformational Analysis Of Poly(4-Vinyl Pyridine) and Its Model Compounds," *Spectroscopy Letters* **1987**, *20*, 1-15. http://dx.doi.org/10.1080/00387018708082271

2. Mitigating Cobalt Phthalocyanine Aggregation Through Codeposition with an Axially-Coordinating Polymer

2.0. Preface

This chapter discusses the aggregation behavior of cobalt phthalocyanine deposited onto electrode surfaces as a heterogenized molecular catalyst, and how aggregation can be mitigated using poly(4-vinylpyridine). This chapter of my thesis is derived from a manuscript in preparation for submission. I was the primary author on the study and was responsible for all sample preparation, UV-Vis and SEM studies, data organization, manuscript writing, figure creation, and preparation of the manuscript. Taylor L. Soucy performed the electrochemical studies. Bradley D. Terry and Bart M. Bartlett provided assistance with conceptualizing and performing the diffuse reflectance measurements. Dr. Charles C. L. McCrory provided significant direction for the project and useful insight and expertise for characterization techniques and experimental interpretation.

2.1. Abstract

Cobalt phthalocyanine is a promising molecular catalyst for aqueous electroreduction of CO_2, but its catalytic activity is limited by aggregation at high loadings. Codeposition with axially coordinating poly(4-vinylpyridine) mitigates aggregation in addition to providing other catalytic enhancements. Transmission and diffuse reflectance UV-Vis measurements demonstrate that a combination of axial coordination and π-stacking effects from pyridyl moieties serve to disperse

CoPc in the deposition solution and ensure it remains monomeric upon deposition. Polymers lacking axial coordination, such as Nafion, are ineffective at CoPc dispersion. SEM images corroborate these findings through particle counts and morphological analysis. Electrochemical measurements show that codeposition of CoPc with P4VP provides higher activity and selectivity for the CO_2RR than codeposition with Nafion.

2.2. Introduction

Capturing industrial CO_2 waste and electrochemically transforming it to value-added products is an appealing strategy for mitigating atmospheric CO_2 release, and the subject of intense scientific study.[1-9] Transition metal nanoparticles or nanostructured surfaces are the conventional catalyst materials for the CO_2 reduction reaction (CO_2RR),[10-13] but heterogenized molecular catalysts have recently gained attention as a viable alternative with high product selectivity.[14-16] Cobalt phthalocyanine (CoPc) immobilized onto various carbon supports has emerged as a particularly promising heterogenized molecular catalyst system for the CO_2RR,[17-30] and has demonstrated high activity and stability, even when operating under long-term electrolysis conditions.[31] However, CoPc has strong π-stacking interactions and tends to form micron-sized aggregates.[32] Aggregation may hinder substrate access to Co catalytic centers in CoPc,[33] and this aggregation has been suggested as a reason for the plateauing in CO_2RR activity and declining turnover frequency (TOF) with increasing CoPc loading observed in several studies.[25,34,35] In addition, various studies have modified heterogenized CoPc systems to improve dispersion, and correlated this improved dispersion with increased CO_2RR performance.[35-38]

Previous studies by our group[24-28] and others[29,30] have demonstrated the efficacy of encapsulating CoPc within the coordinating polymer poly(4-vinylpyridine) (P4VP) to increase the

system's electrocatalytic activity and selectivity for the CO_2RR compared to the nonencapsulated CoPc parent complex. The increased activity of the polymer-encapsulated CoPc-P4VP system has been attributed to the modification of the CoPc catalyst's primary, secondary, and outer coordination sphere by the encapsulating P4VP polymer.[24-26] Of particular interest is the propensity of the pyridyl moieties in the P4VP polymer to axially coordinate to the Co centers in the CoPc-P4VP system, as demonstrated by in situ X-ray absorbance near edge structure measurements of CoPc-P4VP under electrocatalytic conditions.[27] This result is consistent with numerous other reports showing that pyridine readily coordinates with CoPc.[35,39-42] The axial coordination of the pyridyl residues to CoPc increases the binding affinity of the CoPc for CO_2,[28] increasing the overall electrocatalytic rate for the CO_2RR.[25,28]

We hypothesize that the axial coordination of the P4VP polymer to the CoPc may play an additional synergistic role by mitigating CoPc aggregation. Due to the ability of pyridine to coordinate CoPc, pyridine is an effective solvent for CoPc.[43,44] We postulate that in the CoPc-P4VP system, the P4VP polymer may similarly "solvate" CoPc, facilitating disaggregation of CoPc particles and resulting in the dispersion of monomeric CoPc throughout the polymer layer. Previous studies citing CoPc aggregation as a limited factor in CO_2RR activity for catalytic layers on high-surface area carbon mainly used a combination of scanning electron microscopy (SEM)[34,35,38] and electrochemical CO_2RR activity measurements[25,34-36,39] as indicators of aggregation at high CoPc loadings. However, the extent of CoPc aggregation is difficult to probe directly using electrochemistry, especially for CoPc-P4VP where rate-influencing effects besides aggregation affect electrocatalytic activity.[24,25]

In this study we build upon these previous studies by using a combination of UV-Vis spectroscopy and SEM to identify quantitative trends in CoPc aggregation both in the CoPc-

polymer deposition solution and when deposited as CoPc-polymer films. We explore the extent of CoPc aggregation in three model polymer systems (Figure 2.1): 1) P4VP, our standard coordinating polymer that promotes enhanced activity for the CO_2RR in CoPc-P4VP catalyst-polymer composite films; 2) poly(4-chlorostyrene) (P4CS), a structural analogue to P4VP which lacks the coordinating ability of the pyridyl moiety; and 3) Nafion, perhaps the most ubiquitous binding polymer used in heterogeneous electrocatalysis, including molecular CO_2RR systems.[17,21,31,34,45-49] The extent of CoPc aggregation in each polymer system is compared to CoPc films deposited without any polymer from deposition solutions containing either CoPc alone, or CoPc with exogenous pyridine (py) to explore the effect of axially-coordinating moieties on CoPc aggregation without a polymeric structure.

We show that deposited CoPc-P4VP and CoPc(py)-P4VP films show the lowest extent of CoPc aggregation of all systems studied. This result suggests that both the axial coordination of P4VP to the cobalt center and the aromatic interactions of the polymer with the Pc ring play important roles in producing a disaggregated CoPc-polymer layer. This postulate is supported by additional studies showing that adding pyridine into the CoPc deposition solution does promote CoPc disaggregation in solution but does not prevent reaggregation upon surface deposition and film formation, suggesting that the axial coordination by itself is not enough for low-aggregate film formation. However, CoPc(py)-P4CS films do show lower aggregation compared to CoPc(py) and CoPc films. The CoPc(py)-P4CS result further suggests that both axial coordination and the aromaticity of the polymer are important for promoting disaggregation. Crucially, we also find that Nafion is entirely ineffective at mitigating CoPc aggregation, with or without added py in the deposition solutions. Targeted electrochemical comparisons of CoPc and CoPc(py) films prepared with P4VP and Nafion on edge-plane graphite surfaces demonstrate higher activity and selectivity

when P4VP is used as the binder compared to Nafion, possibly in part due to increased CoPc disaggregation. We believe that these insights into the influence of polymer choice on catalyst aggregation will aid in the rational design of practical catalyst-polymer composite systems with improved dispersion of CoPc and similar porphyrinoid catalysts.

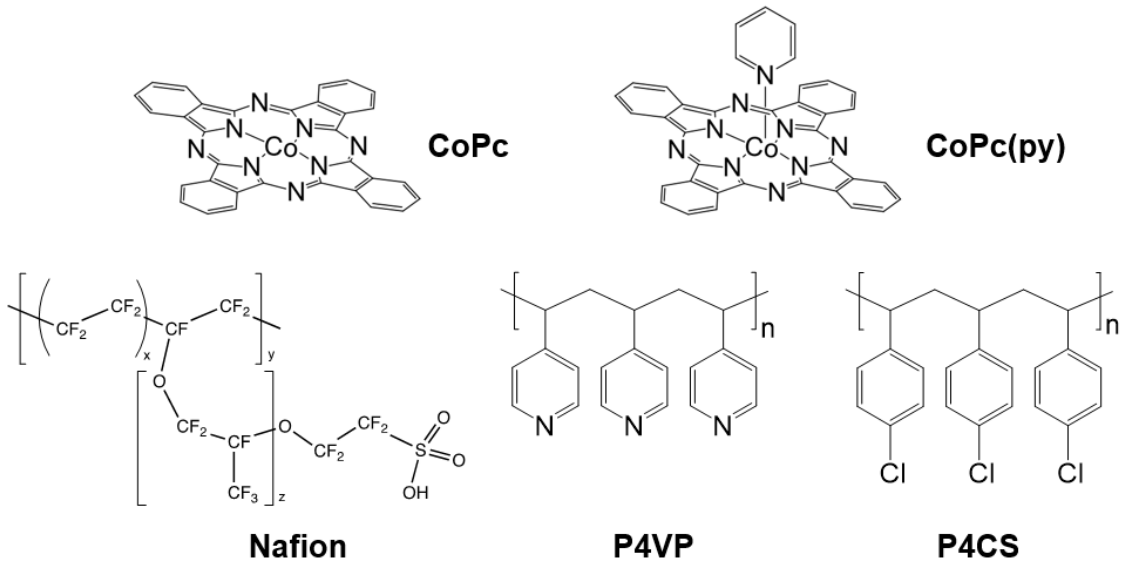

Figure 2.1 Deposition solutions in this study contained either cobalt phthalocyanine (CoPc) or cobalt phthalocyanine with added pyridine to form the 5-coordinated CoPc(py), and one of three polymers: poly(4-vinylpyridine), poly(4-chlorostyrene), and Nafion.

2.3. Methods

Materials

All purchased chemicals were used as received unless otherwise specified. All water used in this study was ultrapure water (18.2MΩ cm resistivity), purified with a Thermo Scientific GenPure UV-TOC/UF x CAD-plus water purification system. Cobalt phthalocyanine (CoPc, 97%), poly(4-vinylpyridine) (P4VP, average MW ~160,000), N,N-dimethylformamide (DMF, ACS grade), pyridine (ACS Reagent), methanol (>99.9%), 2-propanol (>99.9%), sodium phosphate monobasic monohydrate (BioXtra, >99.0%), sodium hydroxide (TraceMetal grade), ferrocene carboxylic acid (97%), Nafion-117 cation exchange membrane (Nafion membrane separator), and Nafion-117 cation exchange membrane (Nafion, 5% solution) were purchased from Sigma Aldrich. Poly(4-chlorostyrene) (P4CS, formula weight 51,000) was purchased from Acros Organics. Nitric acid (ACS grade) was purchased from Millipore. Acetone (ACS grade) was purchased from Fisher.

Quartz microscope slides (25 cm x 25 cm) were purchased from Electron Microscopy Sciences. A 6" degeneratively-doped silicon wafer was purchased from UniversityWafer, Inc. and diced into 1 cm x 1 cm segments with an ADT 7100 Dicing Saw. Edge-plane graphite (EPG) electrodes were 3.81 mm EPG disks encapsulated in epoxy with 0.114 cm2 surface area and were purchased from Pine Research Instrumentation.

Preparation of Deposition Solutions

Standard Procedure for Deposition Solutions – All sonication steps were performed using a heated Fisherbrand 112xx Ultrasonic Cleaner, set to 37 kHz in sweep mode. The bath was set to the desired sonication temperature (typically 50 °C), and a cooling coil with circulating room temperature water was submerged in the sonication bath to help maintain the temperature set level. All CoPc-containing solutions were wrapped in aluminum foil during all sonication steps to

mitigate photodegradation. All solutions were vortexed immediately before taking aliquots in order to maintain the nominal CoPc concentration despite the presence of precipitating aggregates.

A stock solution was prepared by first adding 50.0 mL of DMF to 0.0056 g (±1%) CoPc in a polypropylene centrifuge tube. The resulting 2×10^{-4} M CoPc mixture was sonicated for 2.0 h at 50 °C to achieve maximum disaggregation, and then vortexed to resuspend any remaining undissolved CoPc. A 5.00 mL aliquot was removed and diluted to 50.0 mL in a volumetric flask resulting in a 2×10^{-5} M CoPc stock solution, which was then sonicated for 1h at 50 °C. The 2 x 10-5 M CoPc stock solution was then diluted to the desired CoPc concentration by adding an appropriate amount of the CoPc stock solution to a 25.0 mL volumetric flask, and then filling the flask with DMF. The diluted CoPc/DMF solutions were then transferred into polypropylene centrifuge tubes and sonicated for another 1.0 h at 50 °C.

For deposition solutions containing only CoPc, 2.00 mL of the appropriate diluted CoPc/DMF solution was added to a high-density polyethylene (HDPE) scintillation vial for further processing and deposition. For deposition solutions containing P4VP or P4CS, 0.0200 g (±5%) of the polymer was added to an HDPE vial followed by 2.00 mL of the appropriate diluted CoPc/DMF solution, resulting in a 1% w/v polymer solution. The deposition solutions were sonicated for 2h at 70°C, then vortexed.

Deposition Solutions Containing Nafion – For deposition solutions containing Nafion, a slightly modified procedure was used. Because Nafion is supplied as a 5% solution in a proprietary mixture of aliphatic alcohols, all Nafion-containing solutions were prepared with 20% of the alcohol mixture by volume. As such, all dilutions were performed using a correspondingly 25% more concentrated CoPc/DMF solution (e.g., 2.5×10^{-5} M instead of 2×10^{-5} M) to achieve a final CoPc concentration in the deposition solution equivalent to the corresponding non-Nafion

solutions. In the final solution preparation step, 1.60 mL of the more concentrated CoPc/DMF solution was added to 0.400 mL of the Nafion solution, resulting in a deposition solution with 1% Nafion w/v (~0.0200 g) and ~80% DMF v/v. For non-Nafion containing solutions intended to approximate the DMF-alcohols mixture, solutions were prepared with 20% of a proxy solution containing 78% 2-propanol, 20% ultrapure water, and 2% methanol.

Deposition Solutions Containing Pyridine – All pyridine-containing solutions were prepared with a 5% v/v mixture of pyridine in DMF. No pyridine was added during the initial 2×10^{-4} M CoPc/DMF solution preparation, but rather added during the dilution to the 2×10^{-5} M CoPc stock solution. In subsequent dilutions, sufficient pyridine was added to return the solution to a 5% v/v pyridine composition (e.g., when diluting 2×10^{-5} M CoPc/py/DMF to 1×10^{-5} M, the volumetric flask contained 12.50 mL of the original 5% py/DMF solution, 1.25 mL of additional pyridine, and 11.25 mL of additional DMF).

Deposition Solutions for Low Concentration Studies – A slightly modified procedure was used for deposition solutions prepared for absorbance calibration curves of CoPc/DMF and CoPc(py)/DMF at low concentrations. After the 2×10^{-5} M stock solution was prepared as described above, aliquots of stock solution were added directly to HDPE scintillation vials and diluted with the appropriate quantities of DMF and pyridine to create calibration solutions. Solutions were then sonicated for 2h at 70°C, vortexed, allowed to cool to room temperature, and absorbances were measured using a Varian Cary 100Bio spectrophotometer and a 1 cm pathlength quartz cuvette.

Transmission UV-Vis Measurements

Transmission UV-Vis measurements of CoPc Q-band absorbance in the deposition solutions were performed using a PerkinElmer Lambda 265 spectrophotometer and a 1 cm pathlength quartz

cuvette unless noted otherwise. The cuvette was rinsed with DMF and dried in a stream of N_2 between each measurement, and all absorbance spectra were blanked against pure DMF. Absorbance spectra were collected immediately after solution preparation, and all solutions were vortexed to ensure homogeneity before being decanted into the cuvette. A linear background subtraction was used to account for variations in measured absorbance due to background scattering and determine CoPc monomer peak absorbance values for analysis. An example spectrum demonstrating the background subtraction is provided in Figure A.1.

Diffuse Reflectance UV-Vis Measurements

For diffuse reflectance analysis, quartz microscope slides were selected as a deposition substrate due to their visible-range transparency. The quartz slides were washed by sonication in DMF, then rinsed with water and acetone and dried under stream of N_2. The slides were preheated to 70 °C prior to deposition. Onto each 25mm x 25mm slide, 200 µL of the deposition solution was drop cast and spread to ensure the deposition solution was in contact with the entire surface. The slides were dried overnight in a 70 °C oven. Drop casting was chosen as the deposition method over spin coating due to the high boiling point of DMF, which resulted in extremely low and inconsistent CoPc loading on spin coated surfaces. While drop casting resulted in significant variation of the layer thickness across the slide surface, total CoPc loadings remained consistent between samples deposited using deposition solutions of equivalent concentration. For each quartz slide, one reflectance spectrum was collected in each of the four quadrants to approximately account for uneven distribution of the deposited layer. All diffuse reflectance spectra are presented in Figures S8-S15, to demonstrate the variation in absorbance.

Diffuse reflectance measurements of CoPc Q-band absorbance on quartz slides were performed using a Cary 5000 UV-Vis-NIR instrument with a diffuse reflectance accessory. For each measurement, the sample slide was fixed in position against the beam outlet with Scotch tape with the deposition layer facing the beam, then compressed against a puck packed with $BaSO_4$ (see Figure A.2). The spectra of 100% reflectance and 0% reflectance were determined by, respectively, collecting a spectrum with only the $BaSO_4$ puck, and by blocking the beam. All measurements were collected in terms of a %R bracketed by these two extremes. The %R was transformed into F(R)—analogous to absorbance—using the Kubelka-Munk transform:[50,51]

$$F(R) = \frac{(1-R)^2}{2R} \quad (1)$$

Once in terms of F(R), a linear background subtraction was used before determining the height of the CoPc monomer Q-band peak. An example spectrum demonstrating the linear background subtraction is provided in Figure A.1b.

Preparation of SEM Samples

For SEM analysis, degeneratively-doped Si wafers were selected as a deposition substrate due to their micron-level smoothness and conductivity. An as-received 6-inch diameter Si wafer was diced into 1 cm x 1 cm Si substrates. The Si substrates were washed by sequential sonication in DMF, isopropyl alcohol, 3 M nitric acid, and ultrapure water for 10 minutes each. The Si substrates were then dried under a stream of N_2 before being preheated to 70 °C. Onto each 1 cm x 1 cm Si substrate, 20.0 µL of a deposition solution prepared as above was drop cast and spread to ensure the solvent droplet was in contact with the entire surface. The slides were dried overnight in a 70 °C oven.

SEM images of deposited surfaces were collected using a Thermofisher Scientific Nova 200 Nanolab SEM/FIB. Samples were affixed to aluminum stubs using double-sided conductive tape. To collect particle-counting data for each sample, nine SEM images at a magnification of x250 (image dimensions 0.584 mm x 0.505 mm) were collected in a 2 mm x 2 mm grid pattern (see Figure A.3). CoPc particles were identified based on morphology, and for one sample of each type, point-spectrum EDX was used to confirm the presence of cobalt in the particles using the characteristic Co K edge peak at 6.9 keV. This process is illustrated in Figure A.3, but in brief: for each image position, particles on the surface were identified regardless of morphology and assigned letter designations. The SEM was switched to EDX collection settings (15.0 keV beam energy, 2.2 nA beam current), and a point EDX spectrum was collected at each lettered spot. Particles were identified as CoPc based on the presence of the Co K edge peak. These data were used to confirm the morphologies characteristic of CoPc.

Electrochemical Measurements

General Procedures: Electrochemical measurements were conducted using a Bio-Logic SP200 potentiostat/galvanostat. Data were recorded using EC-Lab software. The electrolyte for all experiments was 0.10 M NaH_2PO_4 solution in ultrapure water buffered to pH 5 (pH ~4.7 after a 30-minute CO_2 purge). The electrolyte pH was confirmed using an Atlas Scientific pH probe and Fisher Scientific Accumet pH Meter, calibrated with a three-point calibration curve (pH = 4.01, 7.00, 10.01). Auxiliary electrodes were graphite rods (99.999%, Strem Chemicals), and reference electrodes were commercial saturated calomel electrodes (SCE, CH instruments) that were externally referenced to ferrocenecarboxylic acid in 0.2 M phosphate buffer at pH 7 (0.284 V vs SCE).[52]

Working electrodes were 5 mm diameter edge plane graphite (EPG) disk electrodes (3.81 mm EPG disk encapsulated in epoxy, 0.114 cm^2 effective surface area, Pine Research Instrumentation) with deposited films of CoPc-P4VP, CoPc(py)-P4VP, CoPc-Nafion, or CoPc(py)-Nafion. Prior to film deposition, the edge-plane graphite electrodes were manually polished using ultrapure water on a 600-grit silicon carbide grinding paper (Buehler, CarbiMet), then rinsed with ultrapure water, sonicated in ultrapure water for ~2 minutes, and dried under an N_2 stream. Then, 5 µL of the deposition solution was drop cast onto the surface of the EPG disk electrode, and the disk electrode was then dried in an oven at 70°C for 15 minutes to allow the solvent to evaporate.

All electrochemical measurements were conducted at least three times with independently prepared electrodes. All results are the average of these three measurements and all associated errors are standard deviations of these measurements.

Rotating Disk Electrode Chronoamperometry Measurements

For rotating disk electrode chronoamperometric step (RDE-CA) measurements, the catalyst film-modified EPG electrode was loaded into a Pine Research Instrumentation E6-series change disk rotating disk electrode (RDE) assembly attached to an MSR rotator. The experiments were conducted in a custom two-compartment glass H-cell as previously described.[25] The first compartment held the working and reference electrode submerged in ~30 mL electrolyte, and the second chamber held the auxiliary electrode submerged in ~15 mL electrolyte. The two chambers were separated by a Nafion membrane. Prior to each experiment, the working chamber was sparged with CO_2 for ~30 min. The CO_2 was saturated with electrolyte solution prior to use by bubbling through a gas washing bottle containing the same electrolyte solution as in the cell. RDE-CA measurements were conducted as 1600 rpm with a single 6-minute potential step at -1.25 V

vs. SCE. The uncompensated resistance of the cell (R_u) was measured prior to each experiment using a single-point high-frequency impedance measurement, and all RDE-CA measurements were compensated for *iR* drop at 85% through positive feedback using the Bio-Logic EC-Lab software. In a typical electrochemical cell, the measured uncompensated resistance was $R_u < 200$ Ω.

Controlled Potential Electrolysis Experiments

Controlled potential electrolysis (CPE) experiments were used to determine gaseous product distribution. CPE measurements were conducted using a custom, gastight two-chamber H-cell as previously described.[25] The first compartment held the working electrode and reference electrode submerged in ~25 mL of electrolyte. The second compartment held the auxiliary electrode submerged in ~20 mL of electrolyte. The two compartments were separated by a Nafion membrane. The working electrode was a modified EPG electrode loaded into an RDE internal hardware kit (Pine Research Instrumentation) and mounted into a custom PEEK sleeve. Prior to each experiment, the first compartment was sparged with CO_2 for ~30 min, and then was sealed under a CO_2 atmosphere. The uncompensated resistance of the cell (*R*u) was measured prior to each experiment using a single-point high-frequency impedance measurement, but the applied potential was not adjusted for *iR* drop, and the reported electrolysis potentials are the actual applied potentials. In general, the electrochemical cells used for CPE measurements had an uncompensated resistance $R_u < 400$ Ω.

After each CPE experiment, a 5 mL aliquot of the headspace was collected using a Pressure-Lok gastight syringe (10 mL, Valco VICI Precision Sampling, Inc). The amount of H_2 and CO produced was determined using a previously described product detection and quantification protocol.[25] The 5-mL aliquot was injected into a 3-mL sample loop on a Thermo Scientific Trace

1310 gas chromatography system with a custom valve system and two analyzer channels for the detection of H_2 and C_1-products. Using a custom valve system and method provided by Thermo Scientific, gases were separated such that H_2 was on the first channel using an Ar carrier gas and thermal conductivity detector (TCD), and all other gases were detected on the second channel using He carrier gas and a TCD. The GC system was calibrated using SCOTTY Specialty Gas gaseous calibration standards with H_2 at 0.01%, 0.02%, 0.05%, 0.5%, 1%v/v and CO at 0.02%, 0.05%, 0.5%, 1%, and 7% v/v. Chromatographs were analyzed using Chromeleon Console Workstation software. Faradaic efficiencies (FE) of the products were calculated using Equation 2 where V_{HS} is the volume of the headspace, V_g is the molar volume of gas at 25 ºC and 1.0 atm (24,500 mL/mol), G is the volume percent of the gaseous product detected by GC (%), n is the number of electrons needed to reduce each gaseous product (n = 2 for both H_2 and CO), F is the Faraday constant (96,485 Coulombs/mol), and Q is the charge passed during the CPE passed (Coulombs).

$$\mathrm{FE} = \frac{\frac{V_{\mathrm{HS}}}{V_{\mathrm{g}}} \times G \times n \times F}{Q} \tag{2}$$

The volume of the headspace, V_{HS}, was determined after each electrolysis by measuring the volume of H_2O needed to fill the first chamber when the cell was fully assembled with the working and reference electrodes, and then subtracting from that the amount of electrolyte in the cell during the electrolysis.

2.4. Results and Discussion

We studied how the aggregation of CoPc is influenced by the inclusion of different polymers both in deposition solutions and in drop cast films using a combination of UV-Vis spectroscopy and SEM. Three polymers were investigated for their disaggregating effects: poly(4-vinylpyridine) (P4VP), poly(4-chlorostyrene) (P4CS), and Nafion. We expected that P4VP would have two effects: 1) P4VP in the deposition solution would disaggregate undissolved CoPc particles, and 2) P4VP in the deposited films would prevent reaggregation of CoPc during drying. We studied P4CS as a close structural analogue to P4VP that lacks the axial coordination of the pyridyl moiety. Nafion was chosen because of its ubiquity as an electrocatalyst binding polymer, including in several recent studies using CoPc.[17,21,31,34,46] We used UV-Vis analysis of the Q-band absorption of CoPc to measure the extent of CoPc disaggregation, both in the deposition solution and the subsequent drop cast layers. SEM of deposited layers was used to confirm the results of the UV-Vis analysis.

UV-Vis Analysis of Deposition Solutions

We anticipated that any disaggregation of the cobalt phthalocyanine would occur during the preparation of the deposition solutions. The ability of P4VP, P4CS, and Nafion to promote CoPc disaggregation was therefore assessed by studying the deposition solutions after the completion of the preparation steps. To assess the extent of CoPc aggregation, we measured changes in the Q-band absorbance in the UV-Vis spectra. All phthalocyanines have a characteristic Q-band absorbance corresponding to a ligand-based $\pi \rightarrow \pi^*$ transition in the approximate range of 600-700 nm.[32,53] For CoPc, this manifests as a prominent absorption band around 660 nm, along with one or more smaller vibronic bands closer to 600 nm.[53] If no aggregation of CoPc occurs, the

absorbance at 660 nm should increase linearly with CoPc concentration in the deposition solution according to Beer's law.

The position, shape, and absorbance of the phthalocyanine Q-band is highly influenced by aggregation.[32] Dimerization is commonly observed in phthalocyanine solutions, resulting in a blue-shifted Q-band absorbance that grows in intensity with increasing dimer concentration.[54-61] Dimers and larger aggregates do not contribute to the main monomer absorbance band, and therefore cause the monomer absorbance to deviate from Beer's law linearity as concentration increases.[32] Representative spectra and associated monomer peak absorbances for CoPc deposition solutions at a range of concentrations are shown in Figure 2.2. As concentration increases, there is no new peak associated with a dimeric species. Instead, the baseline due to scattering increases with increasing CoPc concentration. The scattering decreases over time as the solution is allowed to rest, indicating settling out of suspended CoPc aggregate particles (Figure A.4). These results suggest that non-monomeric CoPc does not primarily form dimers when in DMF but instead lingers as large aggregates that do not contribute an additional resolvable absorbance to the Q-band spectrum. At very high concentrations ([CoPc] ~2×10^{-4} M) large aggregates of undissolved CoPc are clearly visible to the naked eye.

We used a linear baseline to account for scattering from large aggregates, allowing us to plot the baseline-adjusted monomer peak absorbance as a function of the concentration of CoPc and evaluate deviation from linearity as a qualitative means of assessing relative aggregation extent between different polymer additives. At very low concentrations of CoPc ([CoPc] < 1×10^{-6} M), the peak absorbance increases linearly with concentration. At moderate concentrations of CoPc (1×10^{-6} M ≤ [CoPc] ≤ 5×10^{-6} M), the dependence of peak absorbance as a function of concentration

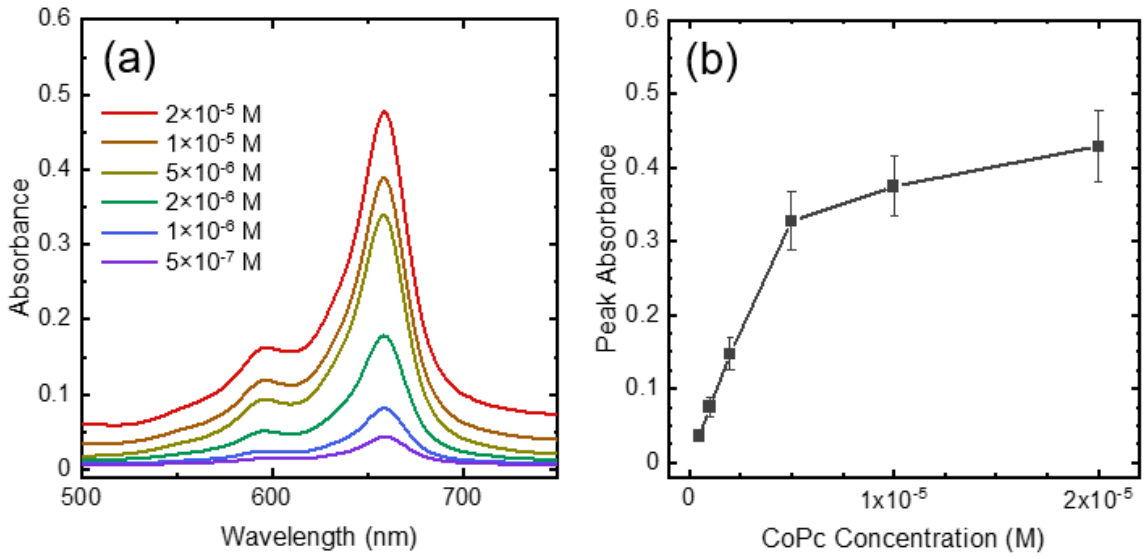

Figure 2.2 a) Representative spectra of the CoPc Q-band absorbance at a range of concentrations in DMF. To better illustrate the increased baseline at the highest concentrations, linear baselines due to background scattering have not been removed. b) Peak monomer absorbances of CoPc in DMF at a range of concentrations. Error bars indicate the first standard deviation of values across seven independently prepared samples.

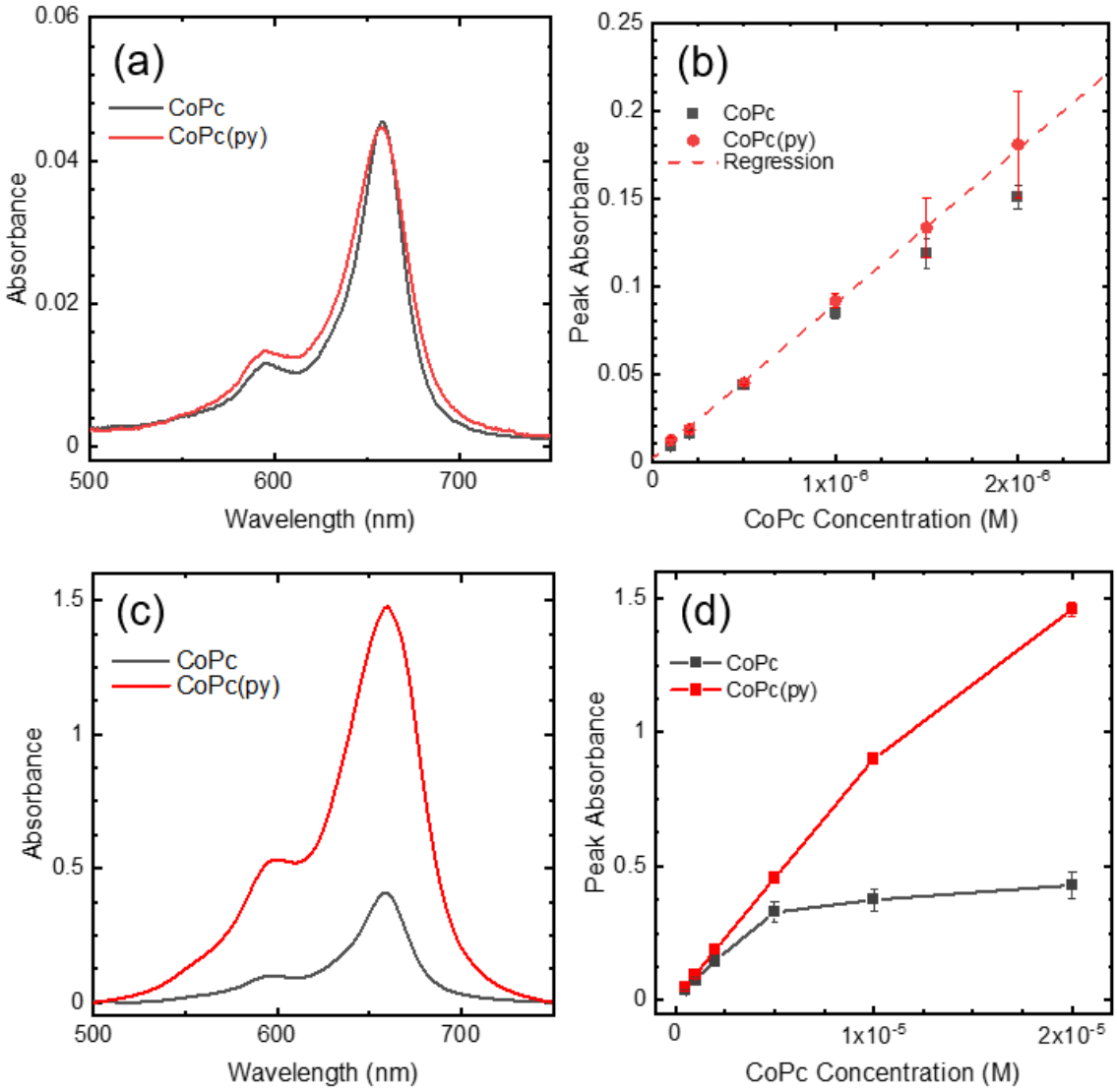

Figure 2.3 a) Representative spectra of the CoPc Q-band absorbance for 5 × 10^{-7} M CoPc and CoPc(py) solutions. b) Peak monomer absorbances for CoPc and CoPc(py) samples prepared at low CoPc concentrations. Error bars indicate the first standard deviation of values across three independently prepared samples. A line to demonstrate the Beer's law relationship was calculated using the linear least squares regression of the CoPc(py) absorbances. c) Representative spectra of the CoPc Q-band absorbances for 2 × 10^{-5} M CoPc and CoPc(py) solutions. A linear background subtraction has been applied to both spectra. d) Peak monomer absorbances for CoPc and CoPc(py) samples prepared at high CoPc concentrations. Error bars indicate the first standard deviation of values across at least three independently prepared samples.

deviates from the expected linear response, suggesting that Beer's law does not solely govern Q-band absorbance (Figure 2.2b). This deviation from linearity of peak absorbance vs concentration becomes more pronounced at high concentrations of CoPc ([CoPc] $\geq 1 \times 10^{-5}$ M) (Figure 2.2b). The deviation from the linear Beer's law response in Figure 2.2 supports the assertion that large CoPc aggregates which lack a distinct Q-band absorbance form in high-concentration CoPc solutions.

To test our hypothesis that axial coordination to CoPc facilitates disaggregation, we compared deposition solutions of CoPc by itself to those containing both CoPc and 5% w/v of pyridine (CoPc(py)). Solutions with low CoPc concentrations were prepared to compare the molar absorptivities of CoPc and CoPc(py) in a concentration range where a linear Beer's law relationship is expected. As shown in in Figure 2.3a-b, absorptivities at low concentration were very similar between the two species ($\varepsilon = \sim 8.5 \times 10^4$ M^{-1} cm^{-1} for CoPc in DMF, and $\varepsilon = \sim 8.8 \times 10^4$ M^{-1} cm^{-1} for CoPc(py) in DMF) with some deviation from linearity evident for CoPc above 1×10^{-6} M. At higher concentrations the CoPc(py) solutions maintained a much higher absorbance than CoPc (Figure 2.3c-d), confirming that axial coordination by pyridine promotes disaggregation.

We prepared deposition solutions containing 1% P4VP and 1% P4CS to determine the effect of these polymers on the CoPc disaggregation in solution. The results are presented in Figure 2.4a-b, compared to CoPc without a polymer. The addition of axially-coordinating P4VP has a more modest disaggregating effect than pyridine, but still substantial. The Q-band absorbance vs. concentration curve continues to rise past 2×10^{-6} M CoPc-P4VP, though the curve does not remain linear as concentration increases. Noncoordinating P4CS appears to slightly increase the monomerization of CoPc. The wavelength of the peak absorbance shifts by about 6 nm when P4VP

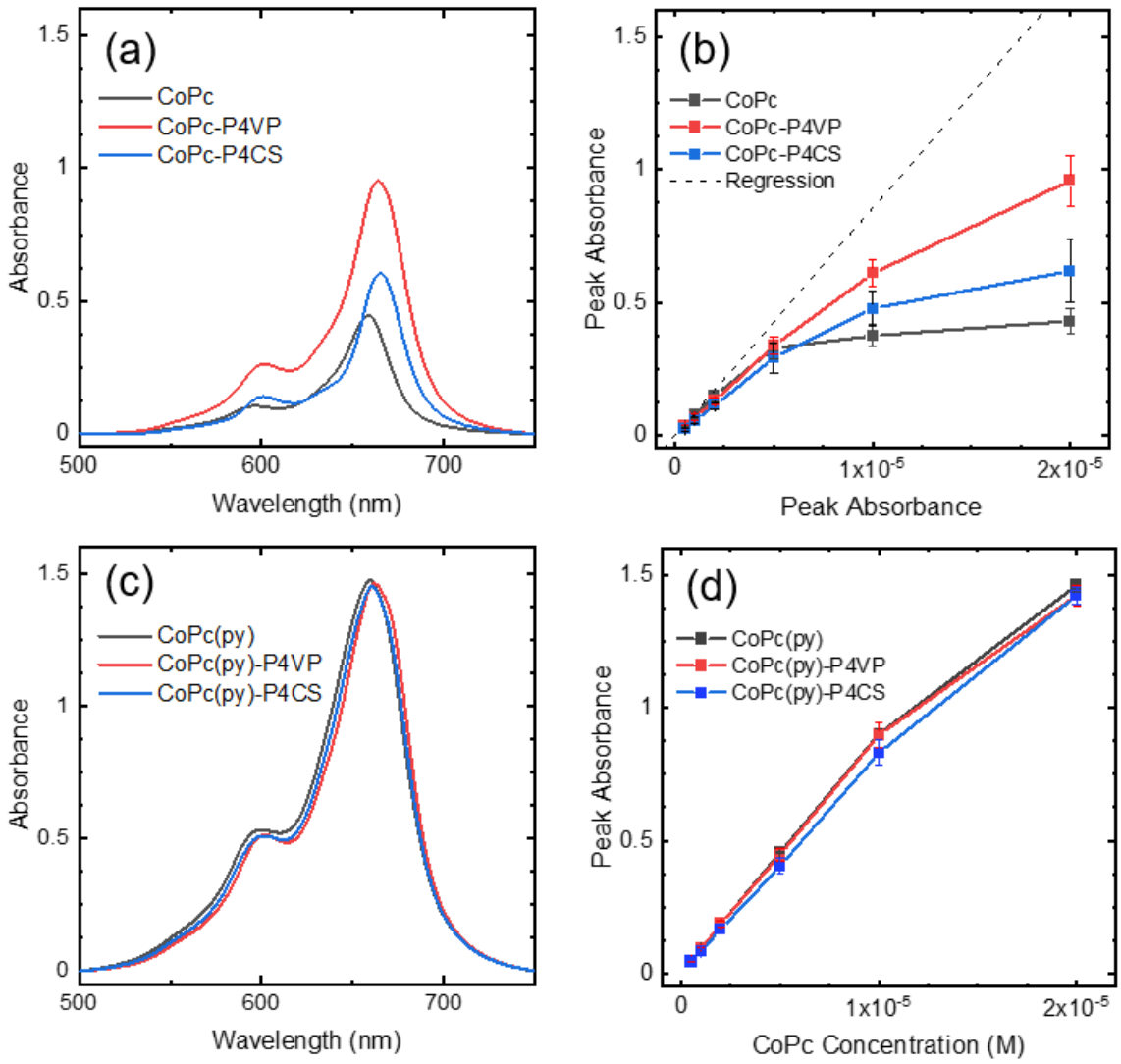

Figure 2.4 a) Representative spectra of the CoPc Q-band absorbance for 2×10-5 M CoPc, 2×10-5 M CoPc with 1% P4VP, and 2×10-5 M CoPc with 1% P4CS. b) Peak monomer absorbances of CoPc, CoPc-P4VP, and CoPc-P4CS across a range of concentrations. Error bars indicate the first standard deviation of values across seven independently prepared samples. Peak monomer absorbance values and associated errors can be found in Table A.1. c) Representative spectra of the CoPc Q-band absorbance for 2×10-5 M CoPc(py), 2×10-5 M CoPc(py) with 1% P4VP, and 2×10-5 M CoPc(py) with 1% P4CS. d) Peak monomer absorbances of CoPc(py), CoPc(py)-P4VP, and CoPc(py)-P4CS across a range of concentrations. Error bars indicate the first standard deviation of values across three independently prepared samples. Peak monomer absorbance values and associated errors can be found in Table A.2.

is present, and by 8 nm when P4CS is present. We attribute these changes to π-stacking interactions with the polymer that alter the solvation environment. In Figure 2.4c-d, spectra and peak absorbances are presented for the corresponding CoPc(py) solutions. Apart from minor shifts in the Q-band peak positions due to polymer interactions, the spectra are insensitive to added polymer, presumably because close-to-complete disaggregation has already been achieved by pyridine. These results demonstrate that a favorable coordination by the pyridyl moiety monomerizes additional CoPc from the suspended aggregates, past what would be solvated by DMF alone. This interpretation is supported by additional experiments in which we centrifuged the CoPc/DMF solutions to remove suspended aggregates before preparing the deposition inks. In this case, the addition of P4VP did not increase the monomer absorbance (Figure A.5).

Finally, we prepared deposition solutions containing 1% Nafion. Because our Nafion source was a 5% solution in a proprietary mixture of aliphatic alcohols and water, the solutions were prepared with only 80% DMF, with the balance being made up of the Nafion solution. For comparison, we also prepared CoPc and CoPc-P4VP solutions in 80% DMF, with the remainder of the volume made up with a solution containing 39% 2-propanol, 39% isopropanol, 20% water, and 2% methanol as a proxy for the proprietary mixture. As shown in Figure 2.5a, we observe that the Nafion solutions do disaggregate CoPc more readily than without a polymer in the mixed solvent. However, the mixed-solvent solutions have lower absorbances than the corresponding 100% DMF solutions. We attribute this observation partly to the mixed solvent required to create a 1% Nafion solution—the CoPc has lower solubility in an 80% DMF solution than in 100% DMF. At high CoPc concentrations, P4VP is more effective than Nafion at disaggregating CoPc, even in the mixed solvent. However, addition of 5% pyridine as shown in Figure 2.5b (for a solution with

75% DMF, 16% alcohols, 5% pyridine, and 4% water), causes disaggregation equivalent to the 95%/5% DMF/py solutions presented in Figure 2.4.

Overall, UV-Vis analysis of CoPc deposition solutions reveals that axial coordination of CoPc by a pyridyl moiety—either from P4VP or from exogenous pyridine—drives disaggregation in deposition solutions. Because aggregated CoPc remains present as large particles without a characteristic absorbance band, relative levels of disaggregation between different conditions can be evaluated through differences in the monomer peak absorbance between samples with the same CoPc concentration.

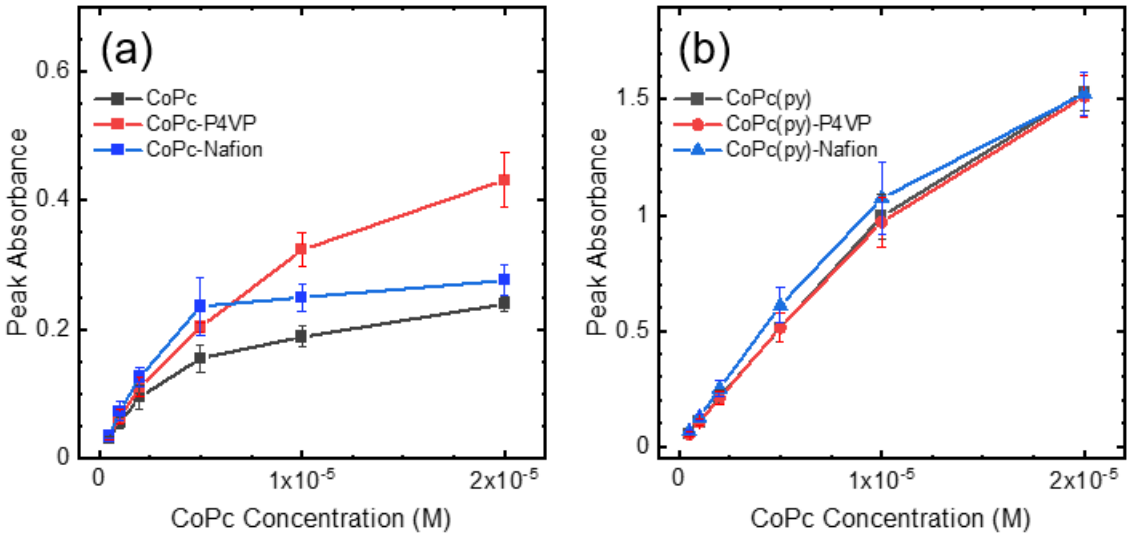

Figure 2.5 a) Peak monomer absorbances of CoPc, CoPc-P4VP, and CoPc-Nafion solutions prepared with 20% v/v of a mixture of water and aliphatic alcohols, an across a range of CoPc concentrations. Error bars indicate the first standard deviation of values across three independently prepared samples. Peak monomer absorbance values and associated errors can be found in Table A.3. b) Peak monomer absorbances of CoPc(py), CoPc(py)-P4VP, and CoPc(py)-Nafion solutions prepared with 20% v/v of a mixture of water and aliphatic alcohols, an across a range of CoPc concentrations. Error bars indicate the first standard deviation of values across three independently prepared samples. Peak monomer absorbance values and associated errors can be found in Table A.4.

UV-Vis Analysis of Deposited Layers

While the UV-Vis analysis of deposition solutions provided key insights about the mechanism of CoPc disaggregation, we also performed diffuse reflectance UV-Vis measurements of deposited layers to understand whether the codeposited polymer hinders reaggregation of CoPc. Deposition solutions were drop cast on quartz slides to minimize visible-range absorbance by the substrate. To account for the nonhomogeneous distribution of the drop cast layers, six samples were prepared for each condition, and four spectra were collected per sample in different quadrants of the slide (see Figure S2) to ensure that sampling accounted for both high-thickness and low-thickness regions of the sample layer. As with the solution transmission measurements, the baseline-corrected peak absorbance of the CoPc monomer Q-band (derived from reflectance as described in the Methods section) was used to evaluate the extent of CoPc dispersion in the CoPc-polymer layers. For comparison, CoPc and CoPc(py) were also deposited without a supporting polymer. We used SEM as a secondary confirmation of the findings from diffuse reflectance UV-Vis.

In Figure 2.6a, we present the Q-band absorbance (F(R)) vs. CoPc loading relationships for the non-polymer, P4VP, P4CS, and Nafion cases and in Figure 2.6b we present F(R) vs. CoPc loading relationships when pyridine is present. CoPc loadings are presented as deposition solution concentrations to aid in comparison with solution-phase transmission UV-Vis measurements, and the corresponding CoPc loadings in terms of mg/cm^2 are included in Table A.5. Because of the significant nonuniformity of the drop cast surfaces, error bars have been omitted for clarity, and instead box-and-whisker plots of normalized mean peak F(R) in Figure 2.6 demonstrate the distribution of F(R) values for each sample type. Non-normalized box-and-whisker plots are presented in Figure A.6 and Figure A.7, with the statistical values e presented in Table A.6 and Table A.7. To demonstrate the variance arises from inhomogeneity within the samples rather than

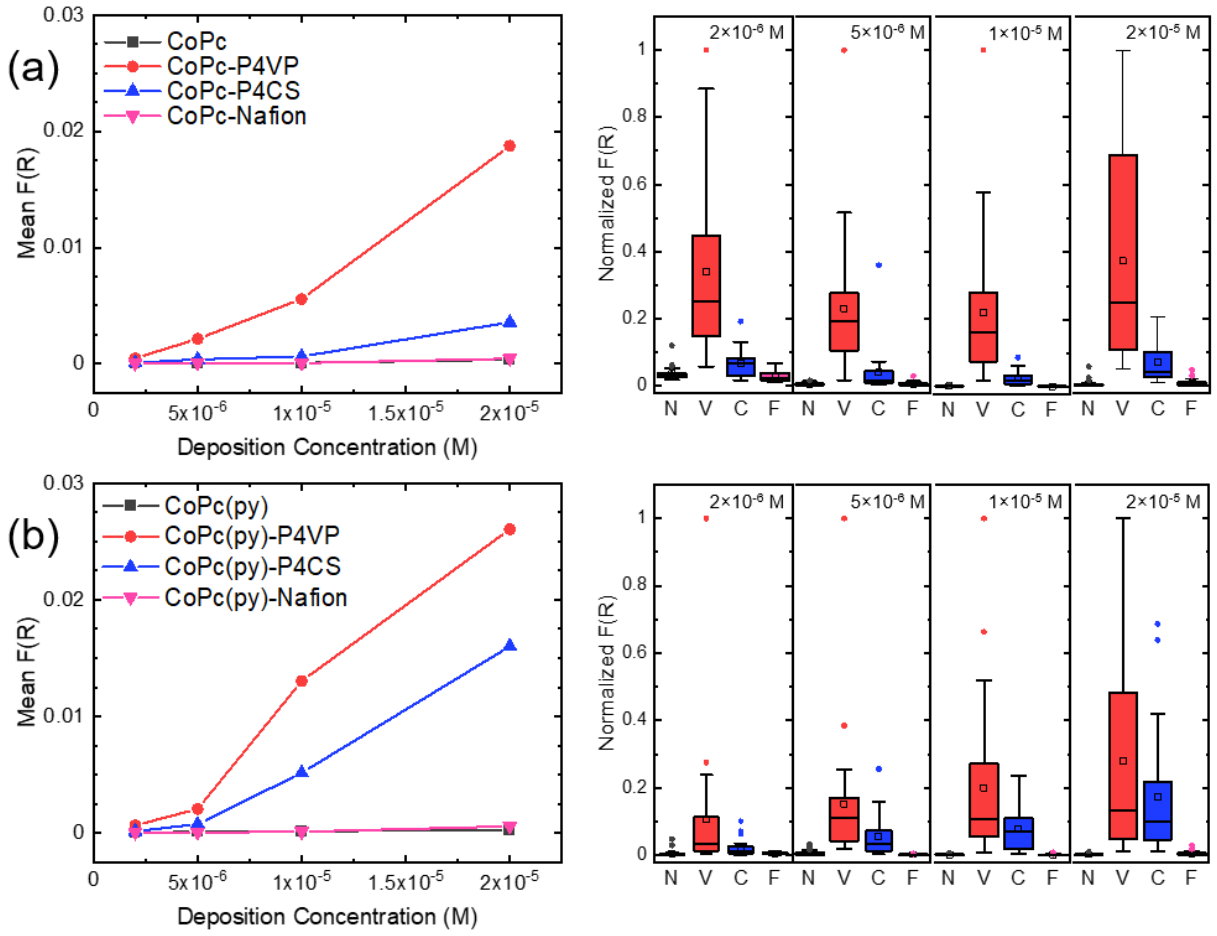

Figure 2.6 Plots of CoPc monomer Q-band absorbance vs. deposition solution CoPc concentration for diffuse reflectance spectra of deposited layers on quartz. Absorbance is plotted as the mean baseline-adjusted monomer peak F(R) value across all measurements. In lieu of error bars and to better demonstrate the data distribution within each sample type, box-and-whisker plots are presented to the right of each abs vs. conc. plot, with F(R) values normalized to the maximum data value at each concentration. Hollow squares represent the mean for each sample, the box areas show the interquartile range, the center line is the median, and the whiskers are the data in the outside the first and fourth quartiles that fall within an additional 1.5x the interquartile range. Outliers beyond 1.5x the interquartile range are presented as dots. The plots are labelled by CoPc concentration and by polymer type: N = no polymer, V = P4VP, C = P4VS, F = Nafion. (a) Plot of absorbance vs. concentration for layers deposited from 100% DMF solutions. (b) Plot of absorbance vs. concentration for layers deposited from 95% DMF, 5% pyridine solutions.

significant variation between samples, all baseline-corrected diffuse reflectance spectra for each condition are presented in Figure A.8 through Figure A.15.

The results from Figure 5a show a striking difference between P4VP layers and all other conditions. Without a codeposited polymer, the CoPc monomer absorbance largely disappears. Codeposition with P4CS results in a minor retention of monomeric CoPc, and this retention is significantly higher when P4VP is used. Nafion appears to have no efficacy whatsoever for preventing reaggregation of CoPc. In Figure 5b, a similar pattern is observed despite the addition of pyridine to the deposition solutions. Absorbance for the P4VP layers remains high and is even enhanced relative to the no-pyridine case. Addition of pyridine to axially coordinate the CoPc gives the CoPc(py)-P4CS system an equivalent absorbance to P4VP. With no polymer, and with Nafion, absorbance remains negligibly low.

We draw a few key insights from the transmission and diffuse reflectance UV-Vis data, as represented schematically in Scheme 2. These data demonstrate that not only is P4VP effective for disaggregating CoPc in the deposition solution, but it also prevents reaggregation of CoPc during deposition by formation of a solid solution. We also determined that while pyridine is highly effective for disaggregating CoPc in the deposition solution, it does not prevent reaggregation upon deposition. The disaggregation efficacy of CoPc(py)-P4CS compared to CoPc(py) and CoPc-P4CS demonstrates that both the axial coordination and the presence of a pi-stacking polymer are crucial. Nafion had no efficacy whatsoever for preventing reaggregation of CoPc(py). We attribute this both to the lack of moieties for axial coordination, and to the non-aromatic backbone structure that provides no opportunity or pi-stacking interactions.

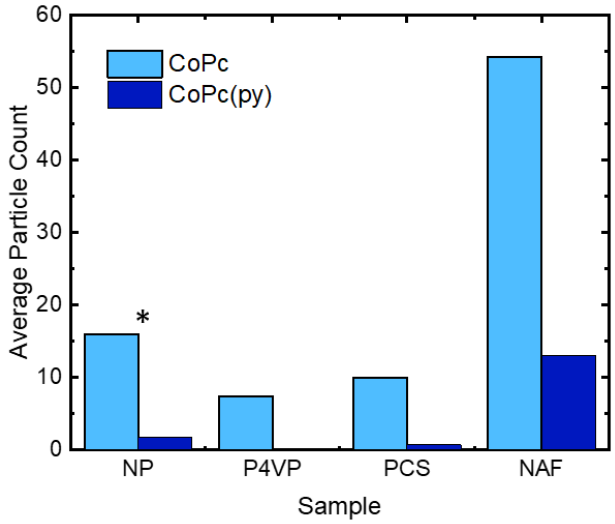

*Figure 2.7 CoPc particle count data are presented for SEM samples. Each count is the sum of CoPc particles found at all nine sampling locations, averaged across three independently prepared samples for each sample type. See Figure A.3 and Figure A.16 for more information on the sampling method and Table A.8 for the raw particle counts. There is no bar for CoPc(py)-P4VP because no CoPc particles were found in any of the three samples. The counts for samples without polymer are marked with a * to indicate that due to strong nucleation during deposition, they account only for particles outside the nucleation spot.*

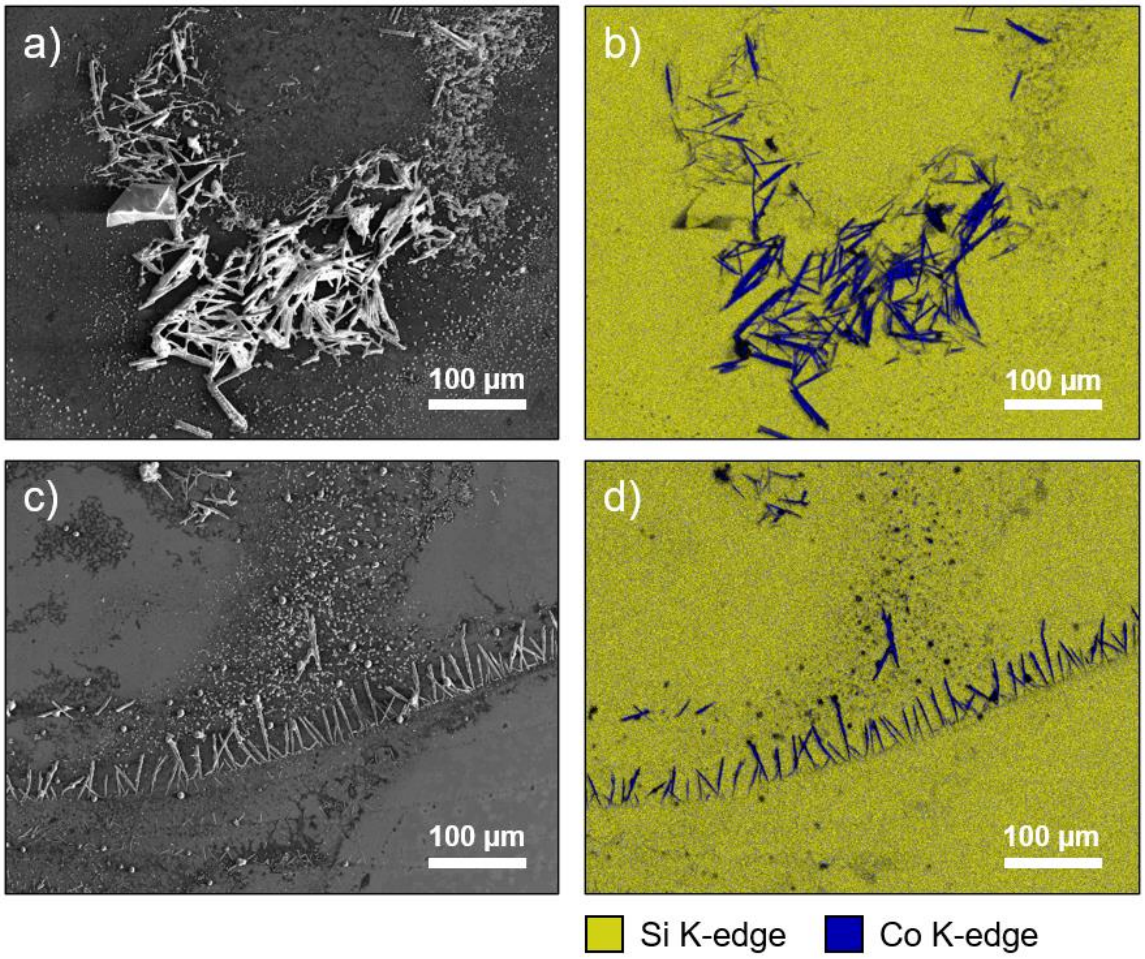

Figure 2.8 Representative SEM images of CoPc nucleation on silicon surfaces in the absence of a polymer, with a) nucleation of CoPc, b) EDX map of CoPc with Co-K edge in blue and Si-K edge in yellow, c) nucleation of CoPc(py), d) EDX map of CoPc(py) with Co-K edge in blue and Si-K edge in yellow. Separate EDX maps for C, Si, and Co are presented in Figure A.23 and Figure A.24.

SEM Analysis of Deposited Layers

SEM was used to directly image deposited layers, providing additional insights to support the conclusions drawn from UV-Vis. For all SEM samples, layers were deposited from a 2×10^{-5} M CoPc solution (corresponding to the highest solution concentration investigated with UV-Vis) onto a smooth silicon substrate.

Two types of information were drawn from the SEM samples. For each sample, a representative area (totaling about 1% of the wafer surface) was imaged at ×250 magnification. Within that area, the number of CoPc nanorods was visually determined based on characteristic morphology and confirmed by EDX point spectra (Figure A.16). For samples with polymer layers (P4VP, P4CS, and Nafion), we determined that the CoPc particles were spread relatively evenly across the wafer surface, with the sample spot pattern accounting for large nonuniformities in the polymer layer. However, for the CoPc and CoPc(py) cases without polymer, the particles tended to nucleate around a single spot on the wafer surface. Particle counts are included for these cases in Figure 2.7, but with the caveat that they represent CoPc particles left on the majority of the surface, and not at the nucleation spot. Additionally, we imaged the nucleation spots of the CoPc and CoPc(py) samples, as seen in Figure 2.8, to draw qualitative information from their morphologies.

The particle counting data in Figure 2.7 gives corroborating evidence that P4VP—and to some extent, P4CS—drive CoPc disaggregation in the deposition solution and prevent reaggregation upon drying. P4VP and P4CS both had much lower particle counts than Nafion, confirming that more CoPc was incorporated into the polymer rather than staying as undissolved aggregates. Addition of Nafion helped to scatter the particles around the surface but did not drive disaggregation. The difference with pyridine added is substantial. The number of particles seen for

the P4VP and P4CS cases went to near-zero, whereas particles were still observed in the Nafion case. While addition of pyridine to the deposition solution drives initial disaggregation, Nafion does not prevent reaggregation upon drying.

Looking at the deposition patterns in the absence of a polymer provides additional insights. In the CoPc-NP case, undissolved particles were dispersed across the surface as well as clumping at the nucleation site, whereas for CoPc(py)-NP, no particles were observed on the surface except at the nucleation site, indicating that the CoPc was initially dissolved upon solution deposition, and only precipitated as the DMF was removed. CoPc(py)-NP demonstrated the reaggregation of CoPc, corroborating the diffuse reflectance data in which CoPc(py)-NP did not have any UV-Vis absorbance. Looking at the difference morphologies of the particles in CoPc-NP and CoPc(py)-NP in Figure 8 gives further information. The nucleation spot of CoPc-NP has random clumping and fusing of particles that look otherwise identical to those seen in the other CoPc cases. In contrast, the nucleation spot of CoPc(py)-NP displays an ordered CoPc(py) deposition pattern corresponding to drying rings. This indicates that these particles precipitated out of the deposition solution from a dissolved, monomeric form rather than settling out of the solution as undissolved nanorods.

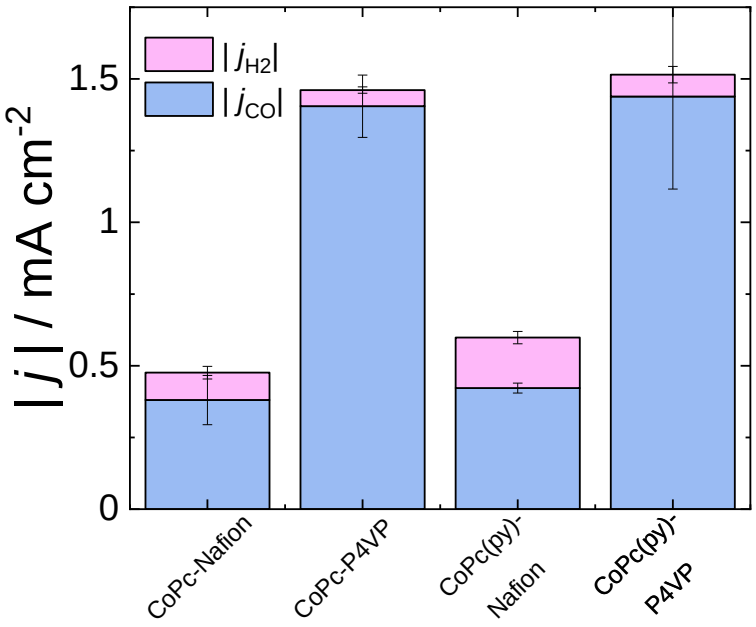

Figure 2.9 Plot of the absolute value of current density for CoPc-Nafion, CoPc-P4VP, CoPc(py)-Nafion, CoPc(py)-P4VP as measured by RDE-CA and with product distribution detected by CPE. Activity measurements were taken under rotation at 1600 rpm at -1.25 V vs. SCE. All data are reported as averages from at least three experiments on independently prepared samples, and error bars represent the standard errors combined from the CPE and RDE-CA activity measurements. For all measurements, activity data can be found in Table A.9, product distributions can be found in Table A.10, and representative RDE-CA and CPE current traces are shown in Figure A.25 through Figure A.32.

Electrochemical Comparison of P4VP and Nafion Films

To assess how the difference in disaggregation between CoPc between Nafion and P4VP influences catalytic activity, we performed CO_2 reduction measurements using drop cast CoPc-polymer layers on edge-plane graphite electrodes. CoPc-Nafion and CoPc-P4VP layers were chosen to investigate whether any beneficial substrate transport properties of Nafion were sufficient to produce better performance despite higher incidence of CoPc aggregates. The measurements were also performed with CoPc(py)-P4VP and CoPc(py)-Nafion to evaluate whether the disaggregating ability of pyridine in the deposition solution enhances the catalytic ability of the resulting layer. Relative activity was evaluated using rotating disk voltammetry, and then controlled potential electrolysis measurements were used to discern the underlying product distributions.

The results are presented in Figure 2.9. We see that for both the CoPc and CoPc(py) cases, both the activity and selectivity of the P4VP layers was superior to the Nafion layers, with the CoPc-P4VP layers producing less H_2 overall despite a threefold increase in the CO2RR activity compared to CoPc-Nafion. As expected from the diffuse reflectance results, the presence of exogenous pyridine in the deposition solution appears to have little overall influence on the activity of the deposited layers, probably in part due to CoPc(py) reaggregation upon deposition. However, it is also possible that under the conditions used, availability of catalytic sites is not the primary rate inhibitor, making the extent of aggregation irrelevant. Further studies should compare these systems in a gas diffusion electrolyzer where the number of active catalytic sites is more likely to be rate-influencing.

2.5. Conclusions

In conclusion, we demonstrate that a few different factors determine whether a CoPc deposition solution will result in a layer containing mostly dispersed, monomeric CoPc. Axial coordination is critical for the initial disaggregation of the CoPc, and for forming a solid solution of monomeric CoPc when deposited. However, axial coordination alone will not prevent reaggregation of the CoPc—for this, a binding material with strong intermolecular interactions is needed. We limited our investigation to transparent polymers in order to obtain diffuse reflectance UV-Vis data, but other strategies may also be effective. These include mixing in a carbon support like graphite powder or carbon nanotubes, or simply depositing onto a high surface area substrate such as O-functionalized carbon paper. Critically, Nafion has little or nothing to offer for this purpose, despite its ubiquity in the literature. We recommend that subsequent investigations of CoPc electrocatalyst systems account for these effects when determining the composition of catalyst layers.

2.6. References

(1) Birdja, Y. Y.; Pérez-Gallent, E.; Figueiredo, M. C.; Göttle, A. J.; Calle-Vallejo, F.; Koper, M. T. M. "Advances and challenges in understanding the electrocatalytic conversion of carbon dioxide to fuels," *Nature Energy* **2019**, *4*, 732-745. http://dx.doi.org/10.1038/s41560-019-0450-y

(2) Crabtree, R. H. "Alternate Strategies for Solar Fuels from Carbon Dioxide," *ACS Energy Letters* **2020**, *5*, 2505-2507. http://dx.doi.org/10.1021/acsenergylett.0c01359

(3) De Luna, P.; Hahn, C.; Higgins, D.; Jaffer Shaffiq, A.; Jaramillo Thomas, F.; Sargent Edward, H. "What would it take for renewably powered electrosynthesis to displace petrochemical processes?," *Science* **2019**, *364*, eaav3506. http://dx.doi.org/10.1126/science.aav3506

(4) Martín, A. J.; Larrazábal, G. O.; Pérez-Ramírez, J. "Towards sustainable fuels and chemicals through the electrochemical reduction of CO2: lessons from water electrolysis," *Green Chemistry* **2015**, *17*, 5114-5130. http://dx.doi.org/10.1039/C5GC01893E

(5) Nocera, D. G. "Solar Fuels and Solar Chemicals Industry," *Accounts of Chemical Research* **2017**, *50*, 616-619. http://dx.doi.org/10.1021/acs.accounts.6b00615

(6) Prieto, G. "Carbon Dioxide Hydrogenation into Higher Hydrocarbons and Oxygenates: Thermodynamic and Kinetic Bounds and Progress with Heterogeneous and Homogeneous Catalysis," *ChemSusChem* **2017**, *10*, 1056-1070. http://dx.doi.org/https://doi.org/10.1002/cssc.201601591

(7) Whipple, D. T.; Kenis, P. J. A. "Prospects of CO2 Utilization via Direct Heterogeneous Electrochemical Reduction," *The Journal of Physical Chemistry Letters* **2010**, *1*, 3451-3458. http://dx.doi.org/10.1021/jz1012627

(8) Windle, C. D.; Reisner, E. "Heterogenised Molecular Catalysts for the Reduction of CO_2 to Fuels," *CHIMIA* **2015**, *69*, 435. http://dx.doi.org/10.2533/chimia.2015.435

(9) Zheng, T.; Jiang, K.; Wang, H. "Recent Advances in Electrochemical CO2-to-CO Conversion on Heterogeneous Catalysts," *Advanced Materials* **2018**, *30*, 1802066. http://dx.doi.org/https://doi.org/10.1002/adma.201802066

(10) Hori, Y. "Electrochemical CO_2 Reduction on Metal Electrodes," In *Modern Aspects of Electrochemistry*; Vayenas, C. G., White, R. E., Gamboa-Aldeco, M. E., Eds.; Springer New York: New York, NY, 2008, p 89-189.

(11) Kortlever, R.; Shen, J.; Schouten, K. J. P.; Calle-Vallejo, F.; Koper, M. T. M. "Catalysts and Reaction Pathways for the Electrochemical Reduction of Carbon Dioxide," *The Journal of Physical Chemistry Letters* **2015**, *6*, 4073-4082. http://dx.doi.org/10.1021/acs.jpclett.5b01559

(12) Masel, R. I.; Liu, Z.; Yang, H.; Kaczur, J. J.; Carrillo, D.; Ren, S.; Salvatore, D.; Berlinguette, C. P. "An industrial perspective on catalysts for low-temperature CO_2 electrolysis," *Nature Nanotechnology* **2021**, *16*, 118-128. http://dx.doi.org/10.1038/s41565-020-00823-x

(13) Nitopi, S.; Bertheussen, E.; Scott, S. B.; Liu, X.; Engstfeld, A. K.; Horch, S.; Seger, B.; Stephens, I. E. L.; Chan, K.; Hahn, C.; Nørskov, J. K.; Jaramillo, T. F.; Chorkendorff, I. "Progress and Perspectives of Electrochemical CO_2 Reduction on Copper in Aqueous Electrolyte," *Chemical Reviews* **2019**, *119*, 7610-7672. http://dx.doi.org/10.1021/acs.chemrev.8b00705

(14) Corbin, N.; Zeng, J.; Williams, K.; Manthiram, K. "Heterogeneous molecular catalysts for electrocatalytic CO_2 reduction," *Nano Research* **2019**, *12*, 2093-2125. http://dx.doi.org/10.1007/s12274-019-2403-y

(15) Manbeck, G. F.; Fujita, E. "A review of iron and cobalt porphyrins, phthalocyanines and related complexes for electrochemical and photochemical reduction of carbon dioxide," *Journal of Porphyrins and Phthalocyanines* **2015**, *19*, 45-64.

http://dx.doi.org/10.1142/S1088424615300013
(16) Costentin, C.; Savéant, J.-M. "Molecular approach to catalysis of electrochemical reaction in porous films," *Current Opinion in Electrochemistry* **2019**, *15*, 58-65. http://dx.doi.org/https://doi.org/10.1016/j.coelec.2019.03.014
(17) Boutin, E.; Wang, M.; Lin, J. C.; Mesnage, M.; Mendoza, D.; Lassalle-Kaiser, B.; Hahn, C.; Jaramillo, T. F.; Robert, M. "Aqueous Electrochemical Reduction of Carbon Dioxide and Carbon Monoxide into Methanol with Cobalt Phthalocyanine," *Angewandte Chemie International Edition* **2019**, *58*, 16172-16176. http://dx.doi.org/10.1002/anie.201909257
(18) Han, N.; Wang, Y.; Ma, L.; Wen, J.; Li, J.; Zheng, H.; Nie, K.; Wang, X.; Zhao, F.; Li, Y.; Fan, J.; Zhong, J.; Wu, T.; Miller, D. J.; Lu, J.; Lee, S.-T.; Li, Y. "Supported Cobalt Polyphthalocyanine for High-Performance Electrocatalytic CO_2 Reduction," *Chem* **2017**, *3*, 652-664. http://dx.doi.org/https://doi.org/10.1016/j.chempr.2017.08.002
(19) Lu, X.; Wu, Y.; Yuan, X.; Huang, L.; Wu, Z.; Xuan, J.; Wang, Y.; Wang, H. "High-Performance Electrochemical CO_2 Reduction Cells Based on Non-noble Metal Catalysts," *ACS Energy Letters* **2018**, *3*, 2527-2532. http://dx.doi.org/10.1021/acsenergylett.8b01681
(20) Ma, J.-J.; Zhu, H.-L.; Zheng, Y.-Q.; Shui, M. "An Insight into Anchoring of Cobalt Phthalocyanines onto Carbon: Efficiency of the CO_2 Reduction Reaction," *ACS Applied Energy Materials* **2021**, *4*, 1442-1448. http://dx.doi.org/10.1021/acsaem.0c02645
(21) Wang, M.; Torbensen, K.; Salvatore, D.; Ren, S.; Joulié, D.; Dumoulin, F.; Mendoza, D.; Lassalle-Kaiser, B.; Işci, U.; Berlinguette, C. P.; Robert, M. "CO_2 electrochemical catalytic reduction with a highly active cobalt phthalocyanine," *Nature Communications* **2019**, *10*, 3602. http://dx.doi.org/10.1038/s41467-019-11542-w
(22) Zeng, J. S.; Corbin, N.; Williams, K.; Manthiram, K. "Kinetic Analysis on the Role of Bicarbonate in Carbon Dioxide Electroreduction at Immobilized Cobalt Phthalocyanine," *ACS Catalysis* **2020**, *10*, 4326-4336. http://dx.doi.org/10.1021/acscatal.9b05272
(23) Wu, Y.; Hu, G.; Rooney, C. L.; Brudvig, G. W.; Wang, H. "Heterogeneous Nature of Electrocatalytic CO/CO_2 Reduction by Cobalt Phthalocyanines," *ChemSusChem* **2020**, *13*, 6296-6299. http://dx.doi.org/https://doi.org/10.1002/cssc.202001396
(24) Kramer, W. W.; McCrory, C. C. L. "Polymer coordination promotes selective CO_2 reduction by cobalt phthalocyanine," *Chemical Science* **2016**, *7*, 2506-2515. http://dx.doi.org/10.1039/C5SC04015A
(25) Liu, Y.; McCrory, C. C. L. "Modulating the mechanism of electrocatalytic CO_2 reduction by cobalt phthalocyanine through polymer coordination and encapsulation," *Nature Communications* **2019**, *10*, 1683. http://dx.doi.org/10.1038/s41467-019-09626-8
(26) Soucy, T. L.; Dean, W. S.; Zhou, J.; Rivera Cruz, K. E.; McCrory, C. C. L. "Considering the Influence of Polymer–Catalyst Interactions on the Chemical Microenvironment of Electrocatalysts for the CO_2 Reduction Reaction," *Accounts of Chemical Research* **2022**, *55*, 252-261. http://dx.doi.org/10.1021/acs.accounts.1c00633
(27) Liu, Y.; Deb, A.; Leung, K. Y.; Nie, W.; Dean, W. S.; Penner-Hahn, J. E.; McCrory, C. C. L. "Determining the coordination environment and electronic structure of polymer-encapsulated cobalt phthalocyanine under electrocatalytic CO_2 reduction conditions using in situ X-Ray absorption spectroscopy," *Dalton Transactions* **2020**, *49*, 16329-16339. http://dx.doi.org/10.1039/D0DT01288B
(28) Rivera Cruz, K. E.; Liu, Y.; Soucy, T. L.; Zimmerman, P. M.; McCrory, C. C. L. "Increasing the CO_2 Reduction Activity of Cobalt Phthalocyanine by Modulating the σ-Donor Strength of Axially Coordinating Ligands," *ACS Catalysis* **2021**, *11*, 13203-13216.

http://dx.doi.org/10.1021/acscatal.1c02379
(29) Yoshida, T.; Kamato, K.; Tsukamoto, M.; Iida, T.; Schlettwein, D.; Wöhrle, D.; Kaneko, M. "Selective electroacatalysis for CO_2 reduction in the aqueous phase using cobalt phthalocyanine/poly-4-vinylpyridine modified electrodes," *Journal of Electroanalytical Chemistry* **1995**, *385*, 209-225. http://dx.doi.org/10.1016/0022-0728(94)03762-R
(30) Abe, T.; Yoshida, T.; Tokita, S.; Taguchi, F.; Imaya, H.; Kaneko, M. "Factors affecting selective electrocatalytic CO_2 reduction with cobalt phthalocyanine incorporated in a polyvinylpyridine membrane coated on a graphite electrode," *Journal of Electroanalytical Chemistry* **1996**, *412*, 125-132. http://dx.doi.org/https://doi.org/10.1016/0022-0728(96)04631-1
(31) Ren, S.; Joulié, D.; Salvatore, D.; Torbensen, K.; Wang, M.; Robert, M.; Berlinguette, C. P. "Molecular electrocatalysts can mediate fast, selective CO_2 reduction in a flow cell," *Science* **2019**, *365*, 367-369. http://dx.doi.org/10.1126/science.aax4608
(32) Snow, A. "Phthalocyanine Aggregation," 2003; Vol. 17, p 129-176.
(33) Chen, X.; Wei, D.; Ahlquist, M. S. G. "Aggregation and Significant Difference in Reactivity Therein: Blocking the CO_2-to-CH_3OH Reaction," *Organometallics* **2021**, *40*, 3087-3093. http://dx.doi.org/10.1021/acs.organomet.1c00431
(34) Zhu, M.; Ye, R.; Jin, K.; Lazouski, N.; Manthiram, K. "Elucidating the Reactivity and Mechanism of CO_2 Electroreduction at Highly Dispersed Cobalt Phthalocyanine," *ACS Energy Letters* **2018**, *3*, 1381-1386. http://dx.doi.org/10.1021/acsenergylett.8b00519
(35) Huai, M.; Yin, Z.; Wei, F.; Wang, G.; Xiao, L.; Lu, J.; Zhuang, L. "Electrochemical CO_2 reduction on heterogeneous cobalt phthalocyanine catalysts with different carbon supports," *Chemical Physics Letters* **2020**, *754*, 137655. http://dx.doi.org/10.1016/j.cplett.2020.137655
(36) Wu, Y.; Jiang, Z.; Lu, X.; Liang, Y.; Wang, H. "Domino electroreduction of CO_2 to methanol on a molecular catalyst," *Nature* **2019**, *575*, 639-642. http://dx.doi.org/10.1038/s41586-019-1760-8
(37) Choi, J.; Wagner, P.; Gambhir, S.; Jalili, R.; MacFarlane, D. R.; Wallace, G. G.; Officer, D. L. "Steric Modification of a Cobalt Phthalocyanine/Graphene Catalyst To Give Enhanced and Stable Electrochemical CO_2 Reduction to CO," *ACS Energy Letters* **2019**, *4*, 666-672. http://dx.doi.org/10.1021/acsenergylett.8b02355
(38) Wu, X.; Sun, J. W.; Liu, P. F.; Zhao, J. Y.; Liu, Y.; Guo, L.; Dai, S.; Yang, H. G.; Zhao, H. "Molecularly Dispersed Cobalt Phthalocyanine Mediates Selective and Durable CO_2 Reduction in a Membrane Flow Cell," *Advanced Functional Materials*, *n/a*, 2107301.
http://dx.doi.org/https://doi.org/10.1002/adfm.202107301
(39) Zhu, M.; Chen, J.; Guo, R.; Xu, J.; Fang, X.; Han, Y.-F. "Cobalt phthalocyanine coordinated to pyridine-functionalized carbon nanotubes with enhanced CO_2 electroreduction," *Applied Catalysis B: Environmental* **2019**, *251*, 112-118.
http://dx.doi.org/https://doi.org/10.1016/j.apcatb.2019.03.047
(40) Gu, T.; Kwaku Attatsi, I.; Zhu, W.; Li, M.; Ndur, S. A.; Liang, X. "Enhanced electrocatalytic hydrogen evolutions of Co(II)phthalocyanine through axially coordinated pyridine-pyrene," *Inorganica Chimica Acta* **2022**, *530*, 120696.
http://dx.doi.org/https://doi.org/10.1016/j.ica.2021.120696
(41) Riquelme, J.; Neira, K.; Marco, J. F.; Hermosilla-Ibáñez, P.; Orellana, W.; Zagal, J. H.; Tasca, F. "Biomimicking vitamin B12. A Co phthalocyanine pyridine axial ligand coordinated catalyst for the oxygen reduction reaction," *Electrochimica Acta* **2018**, *265*, 547-555. http://dx.doi.org/https://doi.org/10.1016/j.electacta.2018.01.177

(42) Ozoemena, K. I.; Nyokong, T. "Comparative electrochemistry and electrocatalytic activities of cobalt, iron and manganese phthalocyanine complexes axially co-ordinated to mercaptopyridine self-assembled monolayer at gold electrodes," *Electrochimica Acta* **2006**, *51*, 2669-2677. http://dx.doi.org/https://doi.org/10.1016/j.electacta.2005.08.007
(43) Ogunsipe, A.; Maree, D.; Nyokong, T. "Solvent effects on the photochemical and fluorescence properties of zinc phthalocyanine derivatives," *Journal of Molecular Structure* **2003**, *650*, 131-140. http://dx.doi.org/https://doi.org/10.1016/S0022-2860(03)00155-8
(44) Darwent, J. R.; Douglas, P.; Harriman, A.; Porter, G.; Richoux, M.-C. "Metal phthalocyanines and porphyrins as photosensitizers for reduction of water to hydrogen," *Coordination Chemistry Reviews* **1982**, *44*, 83-126. http://dx.doi.org/https://doi.org/10.1016/S0010-8545(00)80518-4
(45) Birdja, Y. Y.; Vos, R. E.; Wezendonk, T. A.; Jiang, L.; Kapteijn, F.; Koper, M. T. M. "Effects of Substrate and Polymer Encapsulation on CO_2 Electroreduction by Immobilized Indium(III) Protoporphyrin," *ACS Catalysis* **2018**, *8*, 4420-4428. http://dx.doi.org/10.1021/acscatal.7b03386
(46) Zhang, X.; Wu, Z.; Zhang, X.; Li, L.; Li, Y.; Xu, H.; Li, X.; Yu, X.; Zhang, Z.; Liang, Y.; Wang, H. "Highly selective and active CO2 reduction electrocatalysts based on cobalt phthalocyanine/carbon nanotube hybrid structures," *Nature Communications* **2017**, *8*, 14675. http://dx.doi.org/10.1038/ncomms14675
(47) Zhu, M.; Chen, J.; Huang, L.; Ye, R.; Xu, J.; Han, Y.-F. "Covalently Grafting Cobalt Porphyrin onto Carbon Nanotubes for Efficient CO_2 Electroreduction," *Angewandte Chemie International Edition* **2019**, *58*, 6595-6599. http://dx.doi.org/https://doi.org/10.1002/anie.201900499
(48) Torbensen, K.; Han, C.; Boudy, B.; von Wolff, N.; Bertail, C.; Braun, W.; Robert, M. "Iron Porphyrin Allows Fast and Selective Electrocatalytic Conversion of CO_2 to CO in a Flow Cell," *Chemistry – A European Journal* **2020**, *26*, 3034-3038. http://dx.doi.org/https://doi.org/10.1002/chem.202000160
(49) Zhang, X.; Wang, Y.; Gu, M.; Wang, M.; Zhang, Z.; Pan, W.; Jiang, Z.; Zheng, H.; Lucero, M.; Wang, H.; Sterbinsky, G. E.; Ma, Q.; Wang, Y.-G.; Feng, Z.; Li, J.; Dai, H.; Liang, Y. "Molecular engineering of dispersed nickel phthalocyanines on carbon nanotubes for selective CO2 reduction," *Nature Energy* **2020**, *5*, 684-692. http://dx.doi.org/10.1038/s41560-020-0667-9
(50) Milosevic, M.; Berets, S. L. "A REVIEW OF FT-IR DIFFUSE REFLECTION SAMPLING CONSIDERATIONS," *Applied Spectroscopy Reviews* **2002**, *37*, 347-364. http://dx.doi.org/10.1081/ASR-120016081
(51) Péré, E.; Cardy, H.; Cairon, O.; Simon, M.; Lacombe, S. "Quantitative assessment of organic compounds adsorbed on silica gel by FTIR and UV–VIS spectroscopies: the contribution of diffuse reflectance spectroscopy," *Vibrational Spectroscopy* **2001**, *25*, 163-175. http://dx.doi.org/https://doi.org/10.1016/S0924-2031(00)00113-2
(52) Liaudet, E.; Battaglini, F.; Calvo, E. J. "Electrochemical study of sulphonated ferrocenes as redox mediators in enzyme electrodes," *J. Electroanal. Chem.* **1990**, *293*, 55-68. http://dx.doi.org/10.1016/0022-0728(90)80052-8
(53) Fukuda, T.; Kobayashi, N. "UV-Visible Absorption Spectroscopic Properties of Phthalocyanines and Related Macrocycles," In *Handbook of Porphyrin Science*; World Scientific Publishing Company: 2010; Vol. Volume 9, p 1-644.
(54) Bayda, M.; Dumoulin, F.; Hug, G. L.; Koput, J.; Gorniak, R.; Wojcik, A. "Fluorescent H-aggregates of an asymmetrically substituted mono-amino Zn(ii) phthalocyanine," *Dalton Transactions* **2017**, *46*, 1914-1926. http://dx.doi.org/10.1039/C6DT02651F

(55) Botnar, A.; Tikhomirova, T.; Kazaryan, K.; Bychkova, A.; Maizlish, V.; Abramov, I.; Vashurin, A. "Synthesis and properties of tetrasubstituted phthalocyanines containing cyclohexylphenoxy-groups on the periphery," *Journal of Molecular Structure* **2021**, *1238*, 130438. http://dx.doi.org/https://doi.org/10.1016/j.molstruc.2021.130438
(56) Dilber, G.; Durmuş, M.; Kantekin, H. "Non-aggregated zwitterionic Zinc(II) phthalocyanine complexes in water with high singlet oxygen quantum yield," *Dyes and Pigments* **2019**, *160*, 267-284. http://dx.doi.org/https://doi.org/10.1016/j.dyepig.2018.08.019
(57) Gouloumis, A.; González-Rodríguez, D.; Vázquez, P.; Torres, T.; Liu, S.; Echegoyen, L.; Ramey, J.; Hug, G. L.; Guldi, D. M. "Control Over Charge Separation in Phthalocyanine−Anthraquinone Conjugates as a Function of the Aggregation Status," *Journal of the American Chemical Society* **2006**, *128*, 12674-12684. http://dx.doi.org/10.1021/ja055344+
(58) Kameyama, K.; Morisue, M.; Satake, A.; Kobuke, Y. "Highly Fluorescent Self-Coordinated Phthalocyanine Dimers," *Angewandte Chemie International Edition* **2005**, *44*, 4763-4766. http://dx.doi.org/https://doi.org/10.1002/anie.200501199
(59) Ziminov, A. V.; Sidunets, Y. A.; Fundamensky, V. S.; Gurzhiy, V. V.; Ramsh, S. M. "Synthesis, characterization, and investigation of photochemical properties of tetra-substituted zinc phthalocyanines bearing 4-(3,5-dimethyl-1H-pyrazol-1-yl)phenyl moiety with different linker heteroatoms," *Inorganica Chimica Acta* **2020**, *501*, 119306.
http://dx.doi.org/https://doi.org/10.1016/j.ica.2019.119306
(60) Martin, P. C.; Gouterman, M.; Pepich, B. V.; Renzoni, G. E.; Schindele, D. C. "Effects of ligands, solvent, and variable sulfonation on dimer formation of aluminum and zinc phthalocyaninesulfonates," *Inorganic Chemistry* **1991**, *30*, 3305-3309.
http://dx.doi.org/10.1021/ic00017a016
(61) Palewska, K.; Sworakowski, J.; Lipiński, J. "Molecular aggregation in soluble phthalocyanines – Chemical interactions vs. π-stacking," *Optical Materials* **2012**, *34*, 1717-1724. http://dx.doi.org/https://doi.org/10.1016/j.optmat.2012.02.009

3. Evaluating Poly(4-Vinylpyridine) Layer Protonation Using Infrared Spectroscopy

3.0. Preface

This chapter discusses the effects of bulk pH and electrolyte concentration on the activity, selectivity, and mechanism of the CO_2 reduction reaction and hydrogen evolution reaction with CoPc-P4VP layers. Specifically, it details my contributions to the project from IR spectroscopy. Sections of this chapter (3.2-3.4) are heavily modified from a manuscript in preparation for submission. In Section 3.5 I draw brief conclusions from the manuscript, then provide an outline of how the spectroscopic studies from the manuscript can be greatly expanded to provide a detailed *in situ* understanding of the nature of the CoPc-P4VP composite layer during electrolysis.

I conceived of the idea to use IR spectroscopy to determine fractional protonation of the polymer, performed sample preparation and IR spectroscopy, and contributed to the interpretation and framing of the results. Taylor L. Soucy was the primary author on the manuscript and was responsible for all electrochemical studies, sample preparation, ICP-MS analysis of the samples, as well as data organization, manuscript writing, figure creation, and preparation of the manuscript. Jonah B. Eisenberg collected some of the electrochemical experiments for one figure and assisted in sample preparation as well as some data organization and interpretation. Dr. Charles C. L. McCrory provided direction for the project and useful insight and expertise for electroanalytical techniques and experimental interpretation.

3.1. Abstract

Composite layers of cobalt phthalocyanine (CoPc) encapsulated in poly(4-vinylpyridine) (P4VP) are a useful model system for understanding the influence of catalytic microenvironment on the activity, selectivity, and mechanism of the CO_2 reduction reaction (CO_2RR) in heterogenized molecular systems. In this work, we explore the effects of bulk electrolyte composition on the fractional protonation of the P4VP layer, and thus on the electrocatalytic behavior of reduction reactions in the composite layer. We demonstrate that activity and selectivity for the CO_2RR improves as the bulk solution pH increases, while total activity—including competitive HER—reaches a peak at intermediate pH. We correlate this behavior with decreasing fractional protonation of the layer at high pH, as observed with infrared spectroscopy. We further determine that the concentration of the electrolyte significantly impacts catalysis, as the activity for the HER scales with bulk phosphate concentration. IR spectroscopy of the corresponding layers reveals that high electrolyte concentrations in the buffer solution drive protonation of the layer. We conclude that both the pH and the electrolyte concentration of the buffer solution are critical factors in determining the protonation state of the CoPc-P4VP layer, and thus the microenvironment of reductive catalysis. We provide significant future directions for this work, including *in situ* spectroelectrochemical measurements to better understand how the protonation of the layer influences the electrochemical behavior.

3.2: Introduction

The electrocatalytic CO_2 reduction reaction (CO_2RR) could convert CO_2 from industrial waste streams into value-added products as a strategy for harnessing intermittent renewable energy sources.[1-11] However, in aqueous electrolytes, the CO_2RR competes with the hydrogen evolution reaction (HER) which reduces protons to molecular hydrogen at a similar overpotential.[12] Both solid-state and molecular catalysts have been tested, each of which poses challenges for activity and selectivity for the CO_2RR over HER. Cobalt phthalocyanine is a modestly active catalyst for the CO_2RR when deposited onto a carbon substrate. The presumed mechanism of the CO_2RR and competing HER on CoPc is shown in Figure 3.1.[13]

Previous work[13-18] has demonstrated that encapsulating CoPc in a poly(4-vinylpyridine) polymer layer enhances both activity and selectivity through various effects, including an outer sphere proton relay providing transport of protons to the catalytic sites.[13] This proton relay is illustrated in Figure 3.2. The kinetic isotope effect of CO_2 reduction on CoPc provided evidence of the proton relay. CoPc alone has a KIE of ~1, indicating that a proton transfer step is not rate-determining, while CoPc with an axial pyridine (CoPc(py)) has a KIE of ~3, indicating that the rate-determining step does involve a proton transfer. CoPc encapsulated in P4VP (CoPc-P4VP) has an intermediate KIE, and further proton inventory studies using fractionally deuterated solutions provided evidence of an aggregate inverse KIE due to rate-influencing proton transfer events in the relay. The proton inventory technique has been used extensively in understanding biological catalytic mechanisms,[19-22] and provided strong evidence that protons are transported to the CoPc active sites through a relay rather than through diffusion.

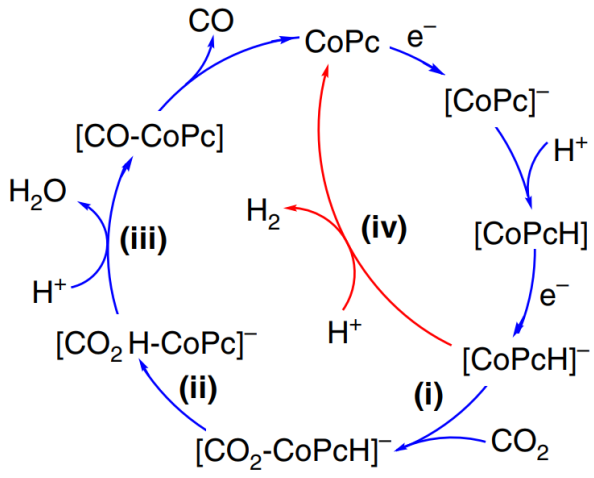

Figure 3.1 An illustration of the competing mechanisms of the CO_2RR and HER on CoPc. Reproduced with permission from Ref. 13. Copyright 2019 Liu, Y. and McCrory, C.C.L. Published by Springer Nature under a Creative Commons CC BY 4.0 license http://creativecommons.org/licenses/by/4.0.

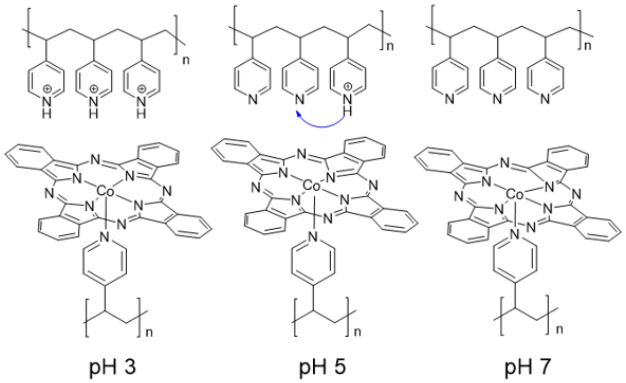

Figure 3.2 Proposed mechanism of proton relay in CoPc-P4VP layer as a function of bulk pH. We expect that as the proton concentration in the bulk solution increases, the polymer changes from fully deprotonated to fully protonated, with an intermediate partially-protonated region dictated by the polymer pKa and the availability of electrolyte anions.

In previous studies of the CoPc-P4VP system, we used a single electrolyte condition, chosen to achieve partial protonation of the layer based on the presumed pyridyl pKa: 0.1 M phosphate buffer titrated to pH 5, then bubbled with CO_2. The effectiveness of P4VP for modulating proton transport was attributed to a combination of the general hydrophobicity of the layer—which we expected to hinder the intercalation of water through the layer and thus deprecate diffusion as a major source of proton transport—and the proton flow channels provided by the regularly-spaced, protonatable pyridyl moieties. However, we expected that the effectiveness of both factors would be altered by the composition of the bulk electrolyte solution outside the layer. A change in the solution should change the extent of intercalation of water, protons, and electrolyte ions, and thus the effectiveness of the proton relay mechanism for promoting CO_2RR activity and selectivity. In light of this finding we undertook a comprehensive, systematic study of how the electrolyte composition affects the catalytic outcomes of the encapsulated CoPc-P4VP model system.

Previous studies have discussed how the selectivity of CO_2 electroreduction of copper and gold can cause changes in product distribution and activity.[23,24] Numerous studies have discussed that pH is important in practical applications for the reduction of CO_2 in an electrochemical fuel cell system, especially when considering the impact of electrolyte identity and concentration and how these experimental parameters can impact the local pH.[25-27] As membrane-coated electrocatalysts have become ubiquitous throughout the literature, the role of counterions and the electrolyte composition has been an outstanding question with regards to the intercalation of ions within the polymer membrane. This is particularly difficult to study within a polymer where the moieties have a relevant pKa (about 3.5 as determined by potentiometric titration) and therefore an artificial buffering system. Similar work by Koper and coworkers showed the importance of

performing systematic studies to determine the interconnected role of cation concentration and pH by performing alkaline HER on a gold electrode, and showed that activity increased with increasing alkali metal concentration, but at higher concentration, the dependence on metal cations diminished and activity decreased.[28] In this study, we altered three factors in the buffer solution: 1) the pH of the solution, 2) the concentration of phosphate, and 3) the addition of perchlorate. Changes in the activity, selectivity, and mechanism of the CO_2RR in the resultant systems were evaluated electrochemically. Experiments were also conducted without CO_2 (i.e., with HER as the only catalytic process) to isolate the influence of proton transfer kinetics without the complication of reaction selectivity. These results were then correlated to IR spectroscopic observation of the partial protonation of P4VP layers, which provided crucial information about relative protonation between different conditions. We believe that insights from this study will prove useful for the community as polymer-catalyst composite systems are implemented into industrially relevant technologies.

We first analyzed the influence of bulk solution pH. We found that selectivity for the CO_2RR drops off as the pH of the bulk solution decreases, as the higher proton concentration in the bulk solution increases the fractional protonation of the polymer, making more protons available relative to CO_2 and thus driving up the HER rate. Experiments without CO_2 confirmed that HER activity decreased with increasing pH. However, total reductive activity (including both HER and CO_2RR) peaks at around pH 5. We also determined that the kinetic isotope effect (KIE) of the catalytic system decreases at higher pH, suggesting an alteration in mechanism whereby a catalytic proton-transfer event is no longer rate-determining. These observations were supplemented by comparisons of electrolyte concentration. We found that the catalytic activity, as evaluated with HER alone, increased with increasing electrolyte concentration. This suggested that

the partial protonation of the P4VP layer was enhanced by the higher concentration of electrolyte, and this hypothesis was confirmed with spectroscopic characterization. We observed that this increase in the layer protonation was driven not only by phosphate, but also by additional sodium perchlorate. We therefore determined that as the ionic concentration of the bulk solution increased, the partitioning of anions into the P4VP layer also increased, and thus increased the ability of the pyridyl moieties to hold protons due to greater capacity for charge balancing. Finally, we determined that the KIE of the catalytic system increased with increasing electrolyte concentration. Together, the KIE results from this study and our previous work suggest that the catalytic proton transfer event is rate-limiting only when the partial protonation of the P4VP layer is sufficient to enable rapid transport of protons to the catalytic site.

3.2. Methods

Materials

All purchased chemicals were used as received, unless otherwise specified. All water used in this study was ultrapure water (18.2 MΩ cm resistivity), prepared via purification by a Thermo Scientific GenPure UV-TOC/UF x CAD-plus water purification system. Carbon dioxide (CO_2, 99.8%) was purchased from Cryogenic Gases and was used as received, and nitrogen (N_2) was boil-off gas from a liquid nitrogen source and was used without further purification. The following chemicals were purchased from Sigma Aldrich and used as received: graphite powder (GP, synthetic < 20 μm), cobalt phthalocyanine (CoPc, 97%), poly-4-vinylpyridine (P4VP, average Mw ~ 160,000), N, N-dimethylformamide (DMF, ACS grade), sodium phosphate monobasic (BioXtra, >99.0%), Nafion-117 cation exchange membrane (Nafion), ferrocene carboxylic acid (97%), and sodium hydroxide (NaOH, TraceMetal grade). Sodium perchlorate anhydrous was purchased from

Oakwood Chemical. Sodium perchlorate monohydrate ($NaClO_4$, 97%) was obtained from Alfa Aesar. Nitric acid (TraceMetal grade, 67-70%) was purchased from Fisher Scientific. Cobalt ICP standard (1000 ppm in 3% HNO_3) was purchased from Ricca Chemical Company. Glassy carbon disk electrodes (GCEs, 4 mm thick, 5 mm in diameter, effective electrode area 0.196 cm^2) were purchased from HTW Hochtemperatur-Werkstoff GmbH. Edge-plane graphite electrodes (EPGs, total area of 5 mm with 3.8 mm EPG disk encapsulated in epoxy, effective electrode area 0.114 cm^2) were purchased from Pine Research Instrumentation.

Electrolyte Solution Preparation and pH Measurements

Unless otherwise stated, all experiments were performed in phosphate/perchlorate electrolyte solutions with concentrations explicitly stated in the main text. Experiments performed to determine the pH dependence of the electrochemical system were performed in electrolyte solutions of 0.4 M NaH_2PO_4 added to 0.5 M $NaClO_4$ in order to minimize any ionic strength differences across a variety of pH levels. Experiments used to study the activity dependence of buffer concentration were performed in varying concentrations of phosphate/perchlorate buffer systems as specified in the main text. Importantly, all electrochemical glassware were vigorously washed, and prior to their use, the cells and Nafion membrane separators to be used in the electrochemical studies were soaked in water for at least 12 hours prior to the experiments to ensure that all salt was removed from the cell.

Prior to each experiment, the working chamber was sparged with the appropriate gas by using a section of Tygon tubing for at least 30 minutes. The pH after sparging varied from between 4.1 to 4.5 and was adjusted to the desired pH level for the experiment by titrating 1 M NaOH or 10% H_3PO_4 into the electrolyte while it was blanketed by CO_2 or N_2 and sealed under 1 atm of the appropriate gas. All pH measurements were conducted with a Fisher Scientific Accumet AB200

pH meter with an Atlas Scientific pH probe calibrated at three points with pH = 4.01, 7.00, and 10.01 calibration standards (Fisher Scientific).

Preparation of Catalyst

CoPc-polymer/GP deposition inks were prepared as previously described.[30] The preparation conditions and resultant loadings of catalyst, polymer, and graphite powder can be found in Table B.1.

CoPc-P4VP deposition inks (no graphite powder)

A solution of 0.05 mM CoPc in DMF was prepared by the addition of 0.0029 g of CoPc to 100 mL of DMF in a duct tape-jacketed 100 mL glass media jar (Fisher Scientific ®). The mixture was sonicated for 1 hour and then vortexed for 1 minute at 3000 rpm. Following the preparation of the 0.05 mM CoPc/DMF solution, 0.015 g P4VP was added to 5 mL of the CoPc/DMF mixture in a duct tape-jacketed 20 mL scintillation vial to create a 0.05 mM CoPc – 0.3% w/v P4VP in DMF. The P4VP was allowed to disperse by sonication for 30 minutes.

CoPc-polymer deposition inks with graphite powder

A solution of 0.05 mM CoPc in DMF was prepared by the addition of 0.0029 g of CoPc to 100 mL of DMF in a duct tape-jacketed 100 mL glass jar (Fisher Scientific ®). The mixture was sonicated for 1 hour and then vortexed for 1 minute at 3000 rpm. Following the preparation of the 0.05 mM CoPc/DMF solution, 0.03 g polymer was added to 1 mL of the CoPc/DMF mixture in a 20 mL duct tape-jacketed scintillation vial to create a 0.05 mM CoPc – 3% w/v polymer in DMF. The P4VP was allowed to disperse by sonication for 30 minutes. A mass of 0.01 g of graphite powder was then added to the CoPc-polymer mixture to create a 0.05 mM CoPc – 3% P4VP – 1% w/v GP preparation suspension. The suspension was allowed to disperse via sonication for 30 minutes. A Teflon stir bar was then added to the scintillation vial and the CoPc-polymer/GP

mixture was magnetically stirred by stir plate at 500 rpm for 12 h. After stirring, the preparation suspension was centrifuged in a 2 mL centrifuge tube (Fisherbrand™ Premium Microcentrifuge tube) at 14,000 rpm for 30 minutes at -4 ºC in an Eppendorf 5430R refrigerated centrifuge. The supernatant was decanted, and 1 mL of fresh DMF was added. The suspension was then vortexed for 30 sec at 3000 rpm, and sonicated for 30 sec.

Preparation of Modified Electrodes

Prior to modification, glassy carbon electrodes (GCEs) were polished on a Struers Labo Pol-5 polishing instrument with a LaboForce-1 specimen mover. The GCE disks were loaded into a custom-made brass electrode holder held by the specimen mover with polishing side on a MDFloc (Struers) synthetic nap polishing pad and were sequentially polished with diamond abrasive slurries (DiaDuo-2, Struers) in an order of 9 µm, 6 µm, 3 µm, and 1 µm diameter particle slurries for 1 minute. The speed of the was held at 200 rpm and, in the opposite rotation direction from the platen, the specimen mover was held at a speed of 8 rpm. Between each polish of the sequential diamond size, the electrodes were rinsed with water. After the final polishing step, the GCE disks were sonicated in isopropyl alcohol for 3 minutes, followed by water for 3 minutes, and in 1 M HNO_3 for 30 minutes. The electrodes were then rinsed with water and dried under an N_2 stream. In order to decrease any likelihood of water being present and skewing results due to the use of deuterated electrolyte, all electrodes were dried in an oven at 60ºC for 10 minutes prior to the drop casting of deposition ink. The electrodes were coated by drop casting 5 µL of the CoPc-P4VP/GP deposition ink, allowing the surface to dry in an oven at 60ºC for 10 minutes, and then was followed by a second coating of 5 µL of the deposition ink and drying at the same temperature.

Edge-plane graphite electrodes (EPGs) were polished by manually hand-polishing on a 600-git silicon carbide polishing paper (Buehler, CarbiMet) with water for 10 seconds. The electrodes

were rinsed with water then sonicated in isopropyl alcohol for 1 minute, rinsed with water, sonicated in water for 1 minute, and then dried under an N_2 stream. Prior to drop casting, the electrodes were allowed to dry in an oven for 10 minutes at 60ºC. A volume of 5 µL of the CoPc-P4VP deposition ink was drop cast onto the polished EPG and was allowed to dry in an oven for 10 minutes at 60 ºC.

Cobalt Loading Determination

Catalyst loading was determined as previously described.[16] After centrifugation, the graphitic pellet was digested by the addition of 15 mL TraceMetal Grade 1 M HNO_3. The solution was stirred overnight, and then was filtered using a cellulose syringe (Pore Size 0.45 µm, Titan 3 regenerated cellulose, Fisher Scientific) to remove the polymer and graphite powder. The metal content was then measured using inductively coupled plasma-mass spectrometry (ICP-MS, PerkinElmer Nexion2000). The ICP-MS was calibrated using internal standards at 10, 50, 100, and 500 ppb and standard nitric acid blank at 0 ppb. The conversion from ppb to molar CoPc loading in the deposition ink is shown **Error! Reference source not found.**- **Error! Reference source not found.**.

$$X \text{ ppb} \times \frac{\frac{1\ \mu g}{\text{L}}}{1 \text{ ppb}} \times 0.015 \text{ L} = \text{mass Co in } \mu\text{g} \tag{1}$$

$$\text{mass in } \mu\text{g x } \frac{1 \text{ mol Co}}{58.93 \text{ g Co}} \times \frac{10^{-6} \text{ g}}{1\ \mu\text{g}} = \text{ mol CoPc} \tag{2}$$

$$\frac{\text{mol CoPc}}{0.0010 \text{ L initial deposition ink}} = M \text{ CoPc in deposition ink} \tag{3}$$

Electrochemical Measurements

Electrochemical measurements were conducted using a Bio-Logic SP200 potentiostat/galvanostat, and data were recorded using the Bio-Logic EC-Lab software package. Reference electrodes were commercial saturated calomel electrode (SCE), externally referenced to ferrocenecarboxylic acid in pH 7, 0.2 M phosphate buffer (0.284 V vs. SCE), and auxiliary electrodes were carbon rods (99.999%, Strem Chemicals Inc.). Working electrodes were the modified GCEs or EPGs described in the previous section. In all cases, the working electrode was separated from the auxiliary electrode by a Nafion membrane. Unless otherwise noted, all electrochemical measurements were conducted at least three times with independently prepared electrodes, all values reported are the average of these repetitions, and all reported errors are standard deviations. The errors of interpretations that required mathematical operators were the standard errors of two standard deviations (for example, kinetic isotope measurements that required division of two average measurements).

For rotating disk electrode (RDE) chronoamperometric (CA) step measurements, the modified GCE working compartment was assembled using a Pine Research Instrumentation E6-series change disk RDE assembly attached to an MSR rotator. CA measurements were conducted at 1600 rotations per minute (rpm) with a single 6-minute potential step held at -0.647 V vs. RHE (V vs. SCE varied depending on the electrolyte pH), to ensure equivalent thermodynamic potential against the concentration of protons. The 1600 rpm rotation rate was used to ensure steady-state CO_2 and/or proton delivery to the electrode surface in a way that is not present in a longer controlled potential electrolysis (CPE) experiment where substrate delivery is dependent on diffusion or convection by magnetic stirring.

RDE-CA measurements were conducted in a custom two-compartment glass cell. In the first compartment, the working electrode with GCE assembly was suspended in 30 mL buffer solution with 3 gas inlets and one inlet for the reference electrode. The second compartment contained ~15 mL solution with the auxiliary electrode. The compartments were separated by a Nafion membrane. Both compartments were sparged with the gas (CO_2 or N_2) for ~30 minutes prior to each set of measurements, and the headspace was blanketed with the corresponding gas during the measurements. The gas used for all electrochemical experiments was first saturated with electrolyte solvent by bubbling the gas through a gas washing bottle filled with the same electrolyte solvent (water or deuterium oxide) used in the cell to minimize electrolyte evaporation in the cell during the course of the measurements. Solution resistance of the cell was measured prior to the experiment and was compensated via software at a rate of 85% via a positive feedback loop software correction. Solution resistance varied across electrolyte concentrations but were generally between 50 and 300 Ω.

CPE experiments were conducted at room temperature in custom, gas-tight, two-chamber U-cells. The modified working electrode was held in a RDE internal hardware kit (Pine Research Instrumentation) and mounted into a custom PEEK sleeve. For the electrolysis measurements, the main chamber held the working electrode and an SCE reference electrode in ~ 25 mL electrolyte, and the headspace was measured after each experiment by measuring the amount of water needed to refill the main chamber. The auxiliary chamber held the auxiliary carbon rod electrode in 15 mL electrolyte. The two chambers were separated by Nafion cation exchange membrane. Prior to each experiment, both chambers were sparged with CO_2 for ~20 min, the pH was adjusted, the cell was sparged with CO_2 for ~20 min, and then the main chamber was sealed under CO_2 atmosphere. The pH of the electrolyte was measured immediately prior to the sealing of the cell after CO_2 purge.

The resistance of the cell was measured with a single-point high-frequency impedance measurement but was not compensated over the course of the experiment. In general, our electrochemical cell for CPE had Ru ~ 150 Ω in all pH solutions.

Product Detection and Quantification

After CPE, gaseous and liquid samples were collected and analyzed using gas chromatography (GC) and high-performance liquid chromatography (HPLC), respectively. For gaseous samples, analysis was conducted using a Thermo Scientific Trace 1310 GC system with two separate analyzer channels for the detection of H_2 and C1-C2 products. A Pressure-Lok gas-tight syringe (10 mL, Valco VICI Precision Sampling, Inc.) was used to collect 5 mL aliquots from the main chamber headspace of the cell, and each aliquot was injected directly into the 3 mL sample loop. Using a custom valve system, column configuration, and method provided by Thermo Scientific, gases were separated such that H_2 was detected on the first channel using an Ar carrier gas and thermal conductivity detector (TCD) and all other gases were detected on the second channel using a He carrier gas and a TCD. The GC system was calibrated using calibration gas mixtures (SCOTTY Specialty Gas) at H_2 = 0.02, 0.05, 0.5, and 1% v/v and CO = 0.02, 0.05, 0.5, 1, and 7% v/v. Chromatographs were analyzed by using the Chromeleon Console. Faradaic efficiencies of gaseous products were calculated via Equation 4:

$$\mathrm{FE} = \frac{\frac{V_{HS}}{V_g} \times G \times n \times F}{Q} \tag{4}$$

where V_{HS} is the headspace volume in mL of the working chamber, V_g is the molar volume of gas at 25ºC and 1.0 atm (24500 mL/mol), G is the volume percent of gaseous product determined by GC (%), n is the number of electrons required for each product (n = 2 for H_2 and CO), F is the Faraday constant (C/mol) and Q is the charge passed in Coulombs.

Ex Situ Infrared Spectroscopy

To spectroscopically evaluate protonation of P4VP layers by different buffer solutions, *ex situ* transmission infrared experiments were performed using a Nicolet iS50 FTIR with an MCT detector. Each P4VP layer was prepared by drop casting 38.1 µL of a 1% P4VP/DMF solution onto a clean 0.5" diameter uncoated CaF_2 window (Thorlabs) and dried in an oven at 60°C overnight to drive off all DMF. Buffer solutions were prepared and brought to the desired pH as described above. Onto each P4VP-coated window, a 150 µL buffer droplet was deposited and allowed to soak for 45 minutes. The buffer droplet was then removed via pipette, and remaining buffer was wicked away using a Kimwipe. The window was dried in an oven at 60°C for 1 hour. To collect spectra (before and after buffer exposure), the windows were mounted inside the FTIR transmission chamber, and backgrounded against a clean CaF_2 window with a dry N_2 purge. Each spectrum was collected with 128 scans at 2 cm^{-1} resolution (data spacing of 0.241 cm^{-1}).

3.4. Results and Discussion

The primary techniques we used to evaluate the influence of bulk solution on the P4VP layer were electrochemical—rotating disk voltammetry to gauge total activity and controlled potential electrolysis to extract the underlying product distributions. These techniques were crucial for understanding the net effect of the solution on the catalytic outcomes but did not provide direct insight into protonation state of the layer. We turned to infrared spectroscopy as a straightforward method of evaluating relative layer protonation between pH values. P4VP has a rich infrared spectrum, but we focused on a set of characteristic ring-stretching bands in the 1400-1650 cm^{-1} region. These bands are closely analogous to those observed in pyridine, and previous studies have made band assignments for pyridine,[31] pyridinium,[32,33] and P4VP.[34,35] Moreover, a body of

research has explored the IR spectra of protonated P4VP specifically,[36-40] using major peak shifts between the protonated and unprotonated states to evaluate proton transfer between species in blends of P4VP and acidic polymers. The pyridinyl ring vibrational modes are susceptible to a change in the quaternization of the N atom, including through protonation. The 8a ring stretching mode appearing at 1596 cm^{-1} in neutral P4VP shifts to 1637 cm^{-1} when P4VP is protonated. [32,36-38] This band does not overlap significantly with other bands in the region, making its relative intensity between spectra a convenient indicator of the layer's protonation state.

We used an *ex situ* method to evaluate the relative protonation of P4VP layers exposed to different buffers. Water has a significant absorbance band between 1500 cm^{-1} and 1700 cm^{-1} which greatly complicates both *in situ* measurements and wet *ex situ* measurements of the ring-stretching region. Because of this, we had to evaluate dry P4VP layers. Our method involved exposing the layer to a droplet of buffer for 45 minutes, giving sufficient time for partitioning of buffer species into the layer. All excess buffer was then removed, leaving only that which had soaked into the layer. The layer was then dried, removing the remaining intercalated water but leaving behind the intercalated ions. While we do not expect that the resulting protonation of these model dried layers is exactly the same as for the corresponding layers in solution, we use protonation trends to draw insight about how the buffer composition influences protonation in the electrochemical system.

pH Effects

In previous studies the electrolyte used for all electrochemical studies of CoPc-P4VP was 0.1 M sodium phosphate titrated to pH 5 and saturated with CO_2. This pH was chosen based on the pKa of the pyridyl moieties. We note that the pKa of protonated pyridyl residues of a P4VP polymer is measured to be approximately 3.5 by potentiometric titration, considerably lower than the pKa of the monomeric analogue, presumably due to the hydrophobic backbone of the polymer.

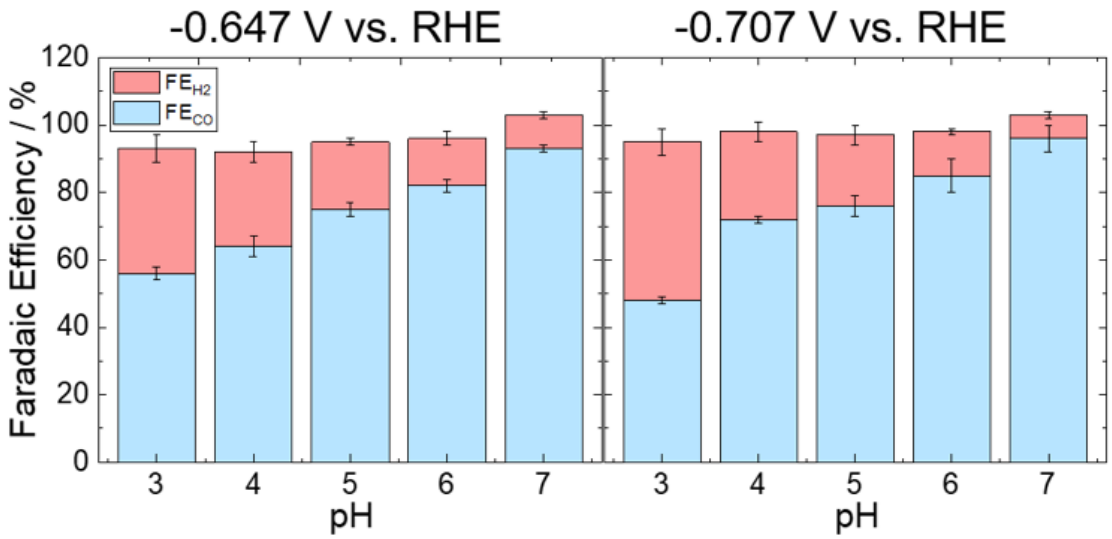

Figure 3.3 Reaction selectivity as a function of pH, measured by faradaic efficiency of the CO_2RR product, CO, and the HER product, H_2. As the pH increases, the reaction selectivity for CO_2RR also increases. This trend holds at -0.647 V vs. RHE (where a majority of experiments in this paper were studied) and a more negative potential of -0.707 V vs RHE, with a considerably higher H_2 production at pH 3. Controlled potential electrolysis experiments were performed in a sealed H-cell in 0.4 M phosphate/0.5 M perchlorate electrolyte as described in the Experimental Section. Faradaic efficiency values can be found in Table B.2and Table B.3.

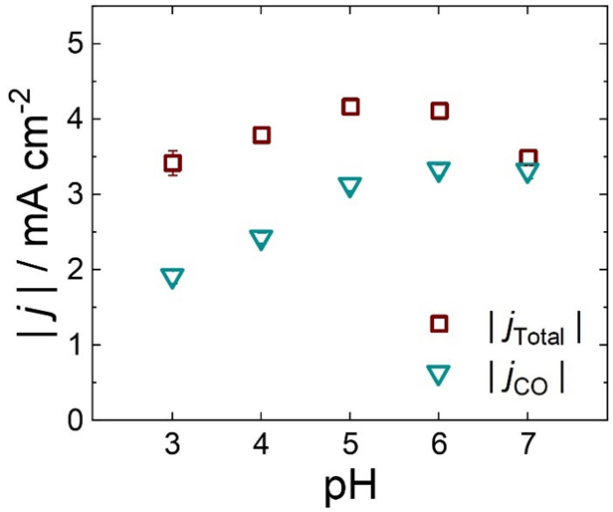

Figure 3.4 Total activity of CoPc-P4VP/GP/GCE (j_{Total} , red square) and activity corrected for CO production (j_{CO}, blue triangle) showing a peak in total activity near pH 5 and a plateau in activity for CO production that begins near pH 5. Activity measurements were taken under rotation at 1600 rpm via a 6-min CA step at -0.647 V vs. RHE in 0.4 M phosphate 0.5 M perchlorate electrolyte. Activity values can be found in Table B.4.

We proposed that fractional protonation of pyridyl moieties in the P4VP layer could be modeled as a function of the solution pH and the pyridyl pKa. As the solution becomes more acidic, we expect the fractional protonation of the layer to increase, reaching about 50% protonation when the solution pH is equal to the polymer pKa.

We postulated that an increase in pH of the electrolyte would result in a corresponding increase in reaction selectivity for the CO_2RR over the competing HER. At low pH the availability of protons within the polymer as seen by fractional protonation would increase the likelihood that CoPc-catalyzed HER would proceed, while higher pH and lower fractional protonation would provide the dual result of an increase of hydrophobicity of the polymer layer (increasing the CO_2 concentration within the polymer film) and a decrease in available protons, which decreases the likelihood of HER. As seen in Figure 3.3, we did observe an increase in Faradaic efficiency for the CO_2RR as the pH increased, as measured by product analysis of controlled potential electrolysis (CPE) experiments. Furthermore, measurements of total activity were performed via rotating disk voltammetry and corrected for CO production using the CPE data. The activity results are presented in Figure 3.4, where we observe that while total activity peaks at around pH 5, the activity of the CO_2RR is highest in the pH 6-7 range.

We used *ex situ* IR spectroscopy at different pH values as described above to gauge the relative protonation. As seen in Figure 3.5, the intensity of the 1637 cm^{-1} band increases as the pH of the buffer solution decreases, indicating a greater layer protonation as expected. This trend held across all buffer concentrations tested, as shown in Figure B.1. Together with the electrochemical results, this confirmed that the solution pH is a crucial factor in determining the extent of protonation in the P4VP layer.

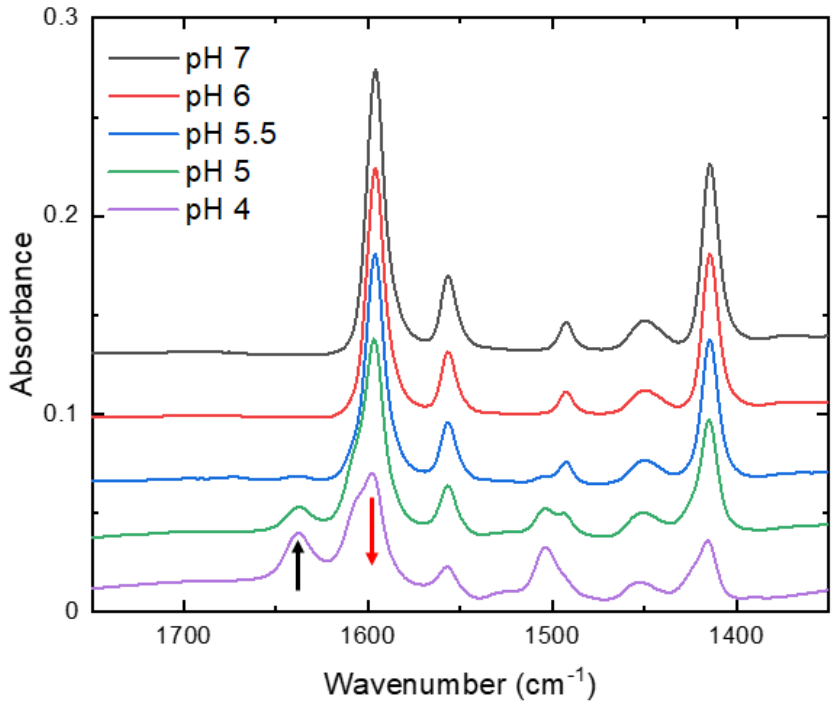

Figure 3.5 Representative transmission infrared spectra of P4VP layers exposed to 0.2 M sodium phosphate buffer at a range of pH values. The spectra are presented at an offset but without further backgrounding or normalization. The black arrow marks the 1637 cm^{-1} band that rises with decreasing buffer pH, while the red arrow marks the 1596 cm^{-1} peak which shrinks with decreasing buffer pH.

Electrolyte Effects

In order for the pyridyl moieties of the P4VP to become protonated, it is necessary for a counterion to be present. In previous studies we have not explicitly accounted for this fact, but it became relevant in order to understand the relationship between the solution pH and the fractional protonation of the P4VP layer. Reaching a higher partial protonation of the P4VP layer would necessitate a higher concentration of anions in the layer to counterbalance the additional charge. From a practical perspective, it was necessary to increase the phosphate concentration from the previously-used 0.1 M to 0.4 M in order to reach a bulk solution pH of 7 with CO_2 bubbling. We also added 0.5 M sodium perchlorate to maintain a relatively consistent ionic strength across the pH ranges. We expected that the electrolyte concentration would not directly determine the protonation of the layer, and instead anticipated that the bulk pH would be the crucial factor—sufficient anions would diffuse into the layer to reach an equilibrium protonation fraction determined by the relationship between bulk pH and pyridyl pKa.

However, we found that increasing the electrolyte concentration dramatically influenced the activity and selectivity of the CoPc-P4VP system. The reaction selectivity of the CO_2RR over the HER decreased slightly at pH 5 compared to a solution of 0.1 M phosphate. In general, we saw that increasing electrolyte concentration at a common pH resulted in a mild decrease in selectivity for the CO_2RR over the HER (see Table B.5 for a comparison of the CoPc-P4VP/GP/GCE system under different levels of electrolyte concentration). As seen in other studies, persistent alkalinity is maintained close to the electrode surface when an electrode is performing CO_2RR, as the consumption of protons drives up the local pH.[41] A higher concentration of buffer prevents the buffer breakdown and maintains the low pH close to the electrode surface, which results in a lower pH and therefore more HER over the CO_2RR.

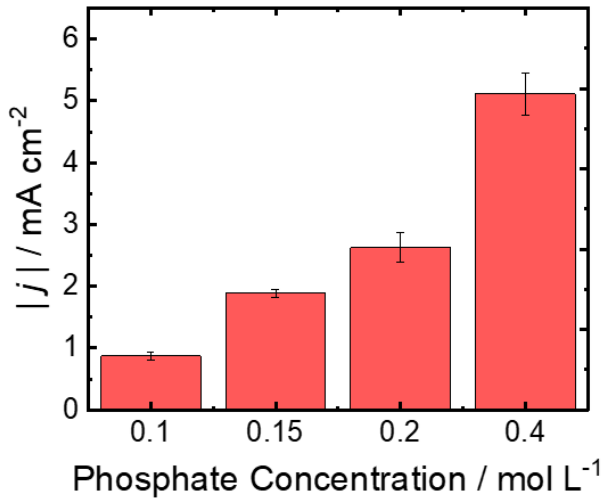

Figure 3.6 Electrolyte-dependent activity of CoPc-P4VP/GP/GCE in 0.4 M phosphate 0.5 M perchlorate electrolyte at pH 5 for the production of H_2 (HER) under an N_2 atmosphere. The system shows an increase in activity as the concentration of phosphate increases. Activity measurements were taken under rotation at 1600 rpm via a 6-min CA step at -0.647 V vs. RHE. Activity values can be found in Table B.6.

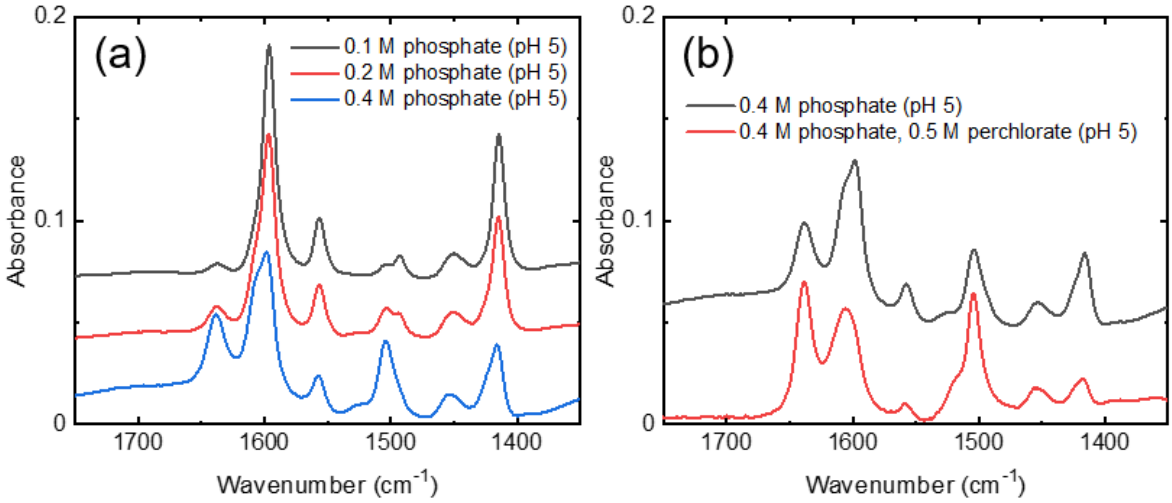

Figure 3.7 Representative transmission infrared spectra of P4VP layers exposed to pH 5 buffers at a range of electrolyte concentrations. The spectra are presented at an offset but without further backgrounding or normalization. a) Comparison of spectra with 0.1, 0.2 and 0.4 M sodium phosphate buffers without perchlorate. b) Comparison of 0.4 M sodium phosphate buffers with and without 0.5 M sodium perchlorate.

Comparisons of reductive activity between different phosphate concentrations without perchlorate were also done under N_2 atmosphere (allowing only HER) to eliminate any confounding effects from reaction selectivity. The results are presented in Figure 3.6, where HER activity is evaluated at increasing bulk phosphate concentrations. We find that activity for the HER rises roughly proportionally to phosphate concentration. IR spectroscopy confirmed that increasing phosphate concentrations drove a higher level of protonation in the polymer. As seen in Figure 3.7a, the intensity of the 1637 cm^{-1} band at a representative pH of 5 increases substantially with increasing phosphate concentration. However, the comparison between a 0.4 M phosphate solution and a 0.4 M phosphate, 0.5 M perchlorate solution reveals that the increase in protonation is not limited to the phosphate in the solution. As seen in Figure 3.7b, the perchlorate also appears to contribute to increasing the fractional protonation of the layer. We also performed a study evaluating the time dependence of the layer protonation. We found that the resulting spectra (Figure B.2) were largely unaffected by the buffer soak time, indicating that partitioning of protons and electrolyte into the layer from the buffer occurs rapidly, reaching an equilibrium within a few minutes. Contrary to our initial expectation that P4VP fractional protonation would be independent of bulk electrolyte concentration, we found that fractional protonation scales with increasing buffer concentration. We attribute this simply to a higher equilibrium partitioning of the electrolyte into the layer, which raises the anion concentration and thus the maximum protonation that can be achieved at a specific solution pH.

3.5. Conclusions

This study serves as a comprehensive introduction to the effects of bulk pH and electrolyte concentration on the activity, selectivity, and mechanism of electrochemical reduction of CO_2 and

protons using a CoPc-P4VP polymer composite layer. Through a combination of electrochemical experiments and *ex situ* spectroscopic characterization, we determined that the bulk pH and the electrolyte concentration both play a role in determining the fractional protonation of the pyridyl residues in the layer. Total reductive activity peaks at about pH 5 and has a decreasing Faradaic efficiency for the CO_2RR over the HER as pH decreases. Additionally, activity for the HER increases with increasing electrolyte concentration in the buffer. Infrared spectra of P4VP layers exposed to these buffers reveal that fractional protonation of the layer trends upward both as pH decreases and as electrolyte concentration increases. This study provides unequivocal evidence that carefully controlling both parameters is crucial for tuning the fractional protonation—and by extension, the activity and selectivity of the CO_2RR—of the composite layer.

3.6. Future Directions

Ex Situ Measurements

The *ex situ* evaluation of P4VP layer protonation is imperfect and could be expanded in a number of ways. While we can be confident that the general trends in protonation hold between the dried layers and the actual electrocatalyst material, there may be a significant difference in the actual fractional protonation values. For this reason, in this study we solely compared trends between the electrochemical and spectroscopic data and did not use the spectra to predict a precise value of fractional protonation at each condition. Further measurements could also be made to evaluate how changing the size of the anion alters the equilibrium partitioning into the layer. Additionally, results included in the full version of this manuscript but not included here demonstrate that the catalytic response of the CoPc-P4VP layer changes dramatically under some conditions as a result of switching from H_2O to D_2O solutions, as evidenced by changes in the

kinetic isotope effect (KIE) of HER when pH and electrolyte concentration are changed. We expect that this is unlikely to manifest in the dried *ex situ* measurements where the partitioning of species between the P4VP layer and electrolyte is allowed to reach equilibrium, and thus is not influenced by electrolysis-related kinetic effects, but it may be valuable to confirm that the H_2O and D_2O solutions yield similar results.

Quantifying the precise fractional protonation could also be valuable. There are two plausible methods for determining a fractional protonation value from the intensity of the 1637 cm^{-1} band. The first would be to compare its intensity with that of the 1596 cm^{-1} band, which is identified as being the same vibrational mode in the unprotonated pyridyl moiety.[32,34,36-38] A simple proportion should suffice to extract a relative protonation. However, this approach is complicated by the appearance of an overlapping 1607 cm^{-1} band in the protonated species, itself a shift of the 1555 cm^{-1} band from the unprotonated species. Careful backgrounding and peak deconvolution would be needed to ensure an accurate and dependable value for the 1596 cm^{-1} intensity, especially at very high protonations where it is reduced to a shoulder on the larger 1607 cm^{-1} band. The other method would involve a comparison of the 1637 cm^{-1} ring stretching band with the CH_2 bending mode that appears around 1450 cm^{-1},[34,37] which arises from the polymer backbone and is unaffected by the protonation state of the pyridyl. This peak would first be used to normalize the 1637 cm^{-1} mode intensity between spectra, allowing them to be compared regardless of any variations in the quantity of polymer in the beam path arising from inconsistencies in optical positioning, layer thickness, or P4VP density. However, to extract an absolute fractional protonation from this method, one would need to prepare a P4VP layer with 100% protonation with which to compare the normalized peak intensities. This is probably feasible and would

involve depositing the P4VP layer from an acidified alcohol solution instead of DMF.[37] Ideally, both methods would be employed and used to crosscheck.

In Situ Measurements

The ultimate goal of this project is to make *in situ* measurements of pyridyl protonation in the P4VP layer to more directly probe how factors such as anion identity, solution pH, electrolyte concentration, and modifications to the layer structure influence the electrochemical behavior. There are some key advantages to performing an *in situ* spectroelectrochemical measurement instead of an ex situ measurement with a dried P4VP layer. For one, the presence of water in the layer may have a significant effect on the protonation state that is not accounted for in the dried layer, due to hydrogen bonding networks, polymer swelling, etc. More importantly, a spectroelectrochemical measurement allows the protonation state of the polymer to be measured under catalytic potential. A steady state fractional protonation can be determined at different applied voltages using simple step voltammetry, and innumerable variations in condition can be used to probe various effects. Depending on the sensitivity of the spectroscopic technique, it may also be possible to probe different layer depths to observe a gradient in protonation between the electrode surface and the solution interface. Some anions may also have IR signatures which allow their presence in the layer to be verified independently of layer protonation, providing additional information about ion intercalation.

The key challenge for this system is the IR absorbance of water, which necessitates using deuterated solutions. D_2O also has a peak overlapping the ring-stretching region, but it has a much smaller intensity and can likely be accounted for through backgrounding. As an example, a preliminary experiment was performed in which a droplet of D_2O was placed on a dried P4VP layer (as described in the Methods section), then tightly sandwiched with an additional CaF_2

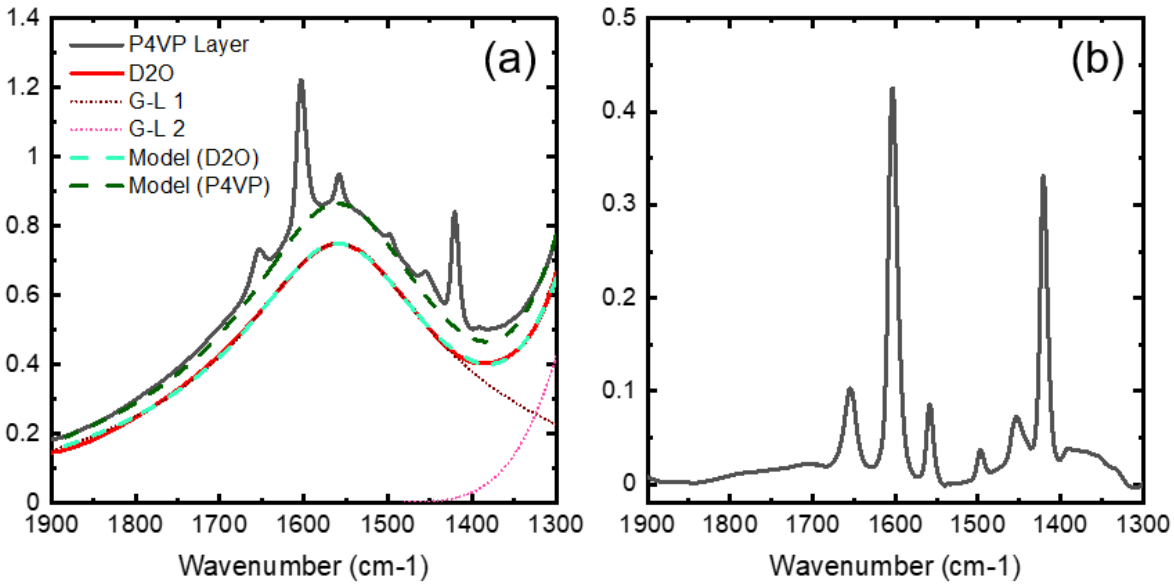

Figure 3.8 Demonstration of a simple subtraction of the overlapping D_2O band from the P4VP ring-stretching region. a) Two Gaussian-Lorentzian curves are used to fit a spectrum with D_2O alone. The intensities of these curves are then increased to make a model background fit to the spectrum with a D_2O-soaked P4VP layer. b) The resulting spectrum with the D_2O peak subtracted out.

window, creating a D_2O-hydrated P4VP layer. As seen in Figure 3.8a, the overlapping peak from this thin D_2O layer is small enough to be subtracted out using a model spectrum from D_2O alone, leaving only the P4VP peaks (Figure 3.8b). An in situ spectroelectrochemical apparatus for these measurements would ideally use an internal reflection technique such as SEIRAS[42] which probes only the P4VP layer itself and does not penetrate into the bulk solution.

However, using this spectroelectrochemical system does come with additional challenges. Deuterated buffer solution may be needed in large quantities and must be stored and handled carefully to minimize hydrogen exchange. The intense D_2O band centered around 2500 cm^{-1} will likely drown out any features of interest above ~2000 cm^{-1}, though this problem also exists with H_2O solutions at a slightly different wavenumber range. Crucially, care must be taken to not overinterpret the applicability of D_2O results to H_2O systems. As mentioned above, measurements not included here demonstrate that the catalytic response of the CoPc-P4VP layer changes between H_2O to D_2O solutions, as evidenced by changes in the KIE of HER. This could substantially affect the results from spectroelectrochemical experiments and make them difficult to compare directly to other systems. Finally, other variations in the layer composition between a spectroelectrochemical system and a practical electrocatalytic system (such as the presence or absence of carbon additives that may obfuscate the IR signal) mean that these measurements will probably remain in the territory of "model" system.

With these challenges in mind, the use of a commercial spectroelectrochemical cell such as the Jackfish cell from Pike Technologies seems prudent. This cell is designed for SEIRAS experiments and can use microgrooved Si ATR wafers as the substrate/window instead of a large face-angled Si crystal. I envision two likely systems which could be investigated with the Jackfish apparatus that would give useful information about the behavior of the P4VP layers, as illustrated

in Figure 3.9. The first (Figure 3.9a) would involve sputtering a thin layer of Pt onto the Si window, then drop casting a P4VP layer. This system could be used to evaluate how different modifications to the conditions influence layer protonation during catalytic turnover for HER on the Pt surface. In this system, catalysis should only be occurring at the Pt surface, allowing the transport of protons and another species through the entire P4VP layer to be evaluated. Different loadings of P4VP could be used to see how layer thickness influences transport. The other systems would use a layer of C deposited on the Si, possibly using pyrolyzed photoresist,[43] onto which a CoPc-P4VP layer is drop cast. This system could then be used to evaluate spectroelectrochemical behavior for both the HER (Figure 3.9b) and the CO_2RR (Figure 3.9c). With a profusion of adjustable conditions for all elements of this system, this investigation should provide an opportunity to probe many aspects of the CoPc-P4VP composite layers. While it will likely remain a "model" system, the results will be broadly useful to the electrocatalysis community, where issues of catalyst layer hydration, pH, and substrate transport are critical to the creation of efficient and long-lasting electrolyzers.

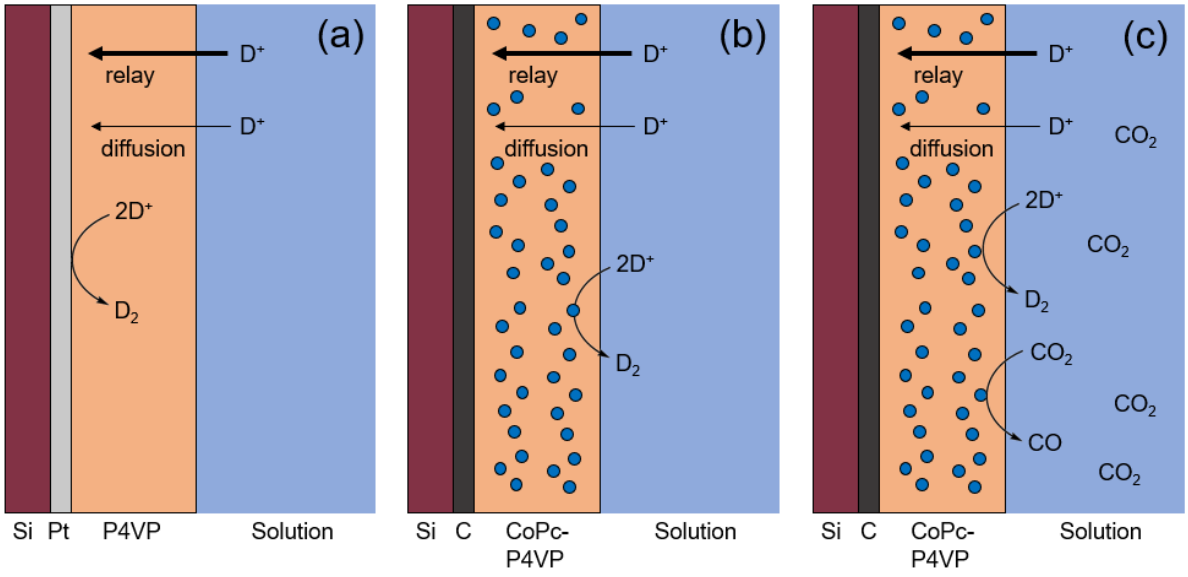

Figure 3.9 Three systems for in situ *spectroelectrochemical analysis of reductive catalysis in CoPc-P4VP composite layers. a) P4VP on Pt surface for evaluation of HER. b) CoPc-P4VP on carbon surface for evaluation of HER. c) CoPc-P4VP on carbon surface for evaluation of CO_2RR.*

3.7. References

(1) Roy, S. C.; Varghese, O. K.; Paulose, M.; Grimes, C. A. "Toward Solar Fuels: Photocatalytic Conversion of Carbon Dioxide to Hydrocarbons," *ACS Nano* **2010**, *4*, 1259-1278. http://dx.doi.org/10.1021/nn9015423

(2) Verma, S.; Kim, B.; Jhong, H.-R. M.; Ma, S.; Kenis, P. J. A. "A Gross-Margin Model for Defining Technoeconomic Benchmarks in the Electroreduction of CO2," *ChemSusChem* **2016**, *9*, 1972-1979. http://dx.doi.org/https://doi.org/10.1002/cssc.201600394

(3) Nocera, D. G. "Solar Fuels and Solar Chemicals Industry," *Accounts of Chemical Research* **2017**, *50*, 616-619. http://dx.doi.org/10.1021/acs.accounts.6b00615

(4) Spurgeon, J. M.; Kumar, B. "A comparative technoeconomic analysis of pathways for commercial electrochemical CO2 reduction to liquid products," *Energy & Environmental Science* **2018**, *11*, 1536-1551. http://dx.doi.org/10.1039/C8EE00097B

(5) Luna, P. D.; Hahn, C.; Higgins, D.; Jaffer, S. A.; Jaramillo, T. F.; Sargent, E. H. "What would it take for renewably powered electrosynthesis to displace petrochemical processes?," *Science* **2019**, *364*, eaav3506. http://dx.doi.org/doi:10.1126/science.aav3506

(6) Crabtree, R. H. "Alternate Strategies for Solar Fuels from Carbon Dioxide," *ACS Energy Letters* **2020**, *5*, 2505-2507. http://dx.doi.org/10.1021/acsenergylett.0c01359

(7) Mustafa, A.; Lougou, B. G.; Shuai, Y.; Wang, Z.; Tan, H. "Current technology development for CO2 utilization into solar fuels and chemicals: A review," *Journal of Energy Chemistry* **2020**, *49*, 96-123. http://dx.doi.org/https://doi.org/10.1016/j.jechem.2020.01.023

(8) Jin, S.; Hao, Z.; Zhang, K.; Yan, Z.; Chen, J. "Advances and Challenges for the Electrochemical Reduction of CO2 to CO: From Fundamentals to Industrialization," *Angewandte Chemie International Edition* **2021**, *60*, 20627-20648. http://dx.doi.org/https://doi.org/10.1002/anie.202101818

(9) Park, S.; Wijaya, D. T.; Na, J.; Lee, C. W. "Towards the Large-Scale Electrochemical Reduction of Carbon Dioxide," *Catalysts* **2021**, *11*, 253.

(10) Senftle, T. P.; Carter, E. A. "The Holy Grail: Chemistry Enabling an Economically Viable CO2 Capture, Utilization, and Storage Strategy," *Accounts of Chemical Research* **2017**, *50*, 472-475. http://dx.doi.org/10.1021/acs.accounts.6b00479

(11) Abe, T.; Imaya, H.; Yoshida, T.; Tokita, S.; Schlettwein, D.; Wöhrle, D.; Kaneko, M. "Electrochemical CO 2 reduction catalysed by cobalt octacyanophthalocyanine and its mechanism," *Journal of Porphyrins and Phthalocyanines* **1997**, *1*, 315-321.

(12) Kuhl, K. P.; Cave, E. R.; Abram, D. N.; Jaramillo, T. F. "New insights into the electrochemical reduction of carbon dioxide on metallic copper surfaces," *Energy & Environmental Science* **2012**, *5*, 7050-7059. http://dx.doi.org/10.1039/C2EE21234J

(13) Liu, Y.; McCrory, C. C. L. "Modulating the mechanism of electrocatalytic CO_2 reduction by cobalt phthalocyanine through polymer coordination and encapsulation," *Nature Communications* **2019**, *10*, 1683. http://dx.doi.org/10.1038/s41467-019-09626-8

(14) Kramer, W. W.; McCrory, C. C. L. "Polymer coordination promotes selective CO_2 reduction by cobalt phthalocyanine," *Chemical Science* **2016**, *7*, 2506-2515. http://dx.doi.org/10.1039/C5SC04015A

(15) Rivera Cruz, K. E.; Liu, Y.; Soucy, T. L.; Zimmerman, P. M.; McCrory, C. C. L. "Increasing the CO2 Reduction Activity of Cobalt Phthalocyanine by Modulating the σ-Donor Strength of Axially Coordinating Ligands," *ACS Catalysis* **2021**, *11*, 13203-13216. http://dx.doi.org/10.1021/acscatal.1c02379

(16) Soucy, T. L.; Liu, Y.; Eisenberg, J. B.; McCrory, C. C. L. "Enhancing Electrochemical Carbon Dioxide Reduction by Polymer-Encapsulated Cobalt Phthalocyanine through Incorporation of Graphite Powder.," *ChemRxiv* **2021**. http://dx.doi.org/10.33774/chemrxiv-2021-bz00c
(17) Abe, T.; Yoshida, T.; Tokita, S.; Taguchi, F.; Imaya, H.; Kaneko, M. "Factors affecting selective electrocatalytic CO_2 reduction with cobalt phthalocyanine incorporated in a polyvinylpyridine membrane coated on a graphite electrode," *Journal of Electroanalytical Chemistry* **1996**, *412*, 125-132. http://dx.doi.org/10.1016/0022-0728(96)04631-1
(18) Yoshida, T.; Kamato, K.; Tsukamoto, M.; Iida, T.; Schlettwein, D.; Wöhrle, D.; Kaneko, M. "Selective electroacatalysis for CO_2 reduction in the aqueous phase using cobalt phthalocyanine/poly-4-vinylpyridine modified electrodes," *Journal of Electroanalytical Chemistry* **1995**, *385*, 209-225. http://dx.doi.org/10.1016/0022-0728(94)03762-R
(19) Schowen, K. B.; Schowen, R. L. "[29] Solvent isotope effects on enzyme systems," In *Methods in Enzymology*; Academic Press: 1982; Vol. 87, p 551-606.
(20) Schowen, R. L. "The use of solvent isotope effects in the pursuit of enzyme mechanisms," *J. Labelled Compd. Radiopharm.* **2007**, *50*, 1052-1062. http://dx.doi.org/10.1002/jlcr.1436
(21) Efimov, I.; Badyal, S. K.; Metcalfe, C. L.; Macdonald, I.; Gumiero, A.; Raven, E. L.; Moody, P. C. E. "Proton Delivery to Ferryl Heme in a Heme Peroxidase: Enzymatic Use of the Grotthuss Mechanism," *Journal of the American Chemical Society* **2011**, *133*, 15376-15383. http://dx.doi.org/10.1021/ja2007017
(22) Pankhurst, K. L.; Mowat, C. G.; Rothery, E. L.; Hudson, J. M.; Jones, A. K.; Miles, C. S.; Walkinshaw, M. D.; Armstrong, F. A.; Reid, G. A.; Chapman, S. K. "A Proton Delivery Pathway in the Soluble Fumarate Reductase from Shewanella frigidimarina," *Journal of Biological Chemistry* **2006**, *281*, 20589-20597.
(23) Varela, A. S.; Kroschel, M.; Reier, T.; Strasser, P. "Controlling the selectivity of CO2 electroreduction on copper: The effect of the electrolyte concentration and the importance of the local pH," *Catalysis Today* **2016**, *260*, 8-13. http://dx.doi.org/https://doi.org/10.1016/j.cattod.2015.06.009
(24) Jiang, X.; Li, H.; Yang, Y.; Gao, D. "pH dependence of CO2 electroreduction selectivity over size-selected Au nanoparticles," *Journal of Materials Science* **2020**, *55*, 13916-13926. http://dx.doi.org/10.1007/s10853-020-04983-y
(25) Zhang, Z.; Melo, L.; Jansonius, R. P.; Habibzadeh, F.; Grant, E. R.; Berlinguette, C. P. "pH Matters When Reducing CO2 in an Electrochemical Flow Cell," *ACS Energy Letters* **2020**, *5*, 3101-3107. http://dx.doi.org/10.1021/acsenergylett.0c01606
(26) Henckel, D. A.; Counihan, M. J.; Holmes, H. E.; Chen, X.; Nwabara, U. O.; Verma, S.; Rodríguez-López, J.; Kenis, P. J. A.; Gewirth, A. A. "Potential Dependence of the Local pH in a CO2 Reduction Electrolyzer," *ACS Catalysis* **2020**, *11*, 255-263. http://dx.doi.org/10.1021/acscatal.0c04297
(27) Lu, X.; Zhu, C.; Wu, Z.; Xuan, J.; Francisco, J. S.; Wang, H. "In Situ Observation of the pH Gradient near the Gas Diffusion Electrode of CO2 Reduction in Alkaline Electrolyte," *Journal of the American Chemical Society* **2020**, *142*, 15438-15444. http://dx.doi.org/10.1021/jacs.0c06779
(28) Goyal, A.; Koper, M. T. M. "The Interrelated Effect of Cations and Electrolyte pH on the Hydrogen Evolution Reaction on Gold Electrodes in Alkaline Media," *Angewandte Chemie International Edition* **2021**, *60*, 13452-13462. http://dx.doi.org/https://doi.org/10.1002/anie.202102803

(29) Fife, T. H.; Bruice, T. C. "THE TEMPERATURE DEPENDENCE OF THE ΔpD CORRECTION FOR THE USE OF THE GLASS ELECTRODE IN D2O," *The Journal of Physical Chemistry* **1961**, *65*, 1079-1080. http://dx.doi.org/10.1021/j100824a525
(30) Soucy, T. L.; Liu, Y.; Eisenberg, J. B.; McCrory, C. C. L. "Enhancing the Electrochemical CO2 Reduction Activity of Polymer-Encapsulated Cobalt Phthalocyanine Films by Modulating the Loading of Catalysts, Polymers, and Carbon Supports," *ACS Applied Energy Materials* **2021**. http://dx.doi.org/10.1021/acsaem.1c02689
(31) Wong, K. N.; Colson, S. D. "The FT-IR spectra of pyridine and pyridine-d5," *Journal of Molecular Spectroscopy* **1984**, *104*, 129-151. http://dx.doi.org/https://doi.org/10.1016/0022-2852(84)90250-9
(32) Cook, D. "VIBRATIONAL SPECTRA OF PYRIDINIUM SALTS," *Canadian Journal of Chemistry* **1961**, *39*, 2009-2024. http://dx.doi.org/10.1139/v61-271
(33) Barrow, G. M. "The nature of hydrogen bonded ion-pairs: the reaction of pyridine and carboxylic acids in chloroform," *Journal of the American Chemical Society* **1956**, *78*, 5802-5806.
(34) Atvars, T. D. Z.; Dibbern, D. N.; Sabadini, E. "Infrared Spectroscope And Conformational Analysis Of Poly(4-Vinyl Pyridine) and Its Model Compounds," *Spectroscopy Letters* **1987**, *20*, 1-15. http://dx.doi.org/10.1080/00387018708082271
(35) Kurimura, Y.; Tsuchida, E.; Kaneko, M. "Preparation and properties of some water-soluble cobalt (III)–poly-4-vinylpyridine complexes," *Journal of Polymer Science Part A-1: Polymer Chemistry* **1971**, *9*, 3511-3519.
(36) Smith, P.; Eisenberg, A. "Infrared spectroscopic study of blends of poly(styrene-co-styrenesulfonic acid) with poly(styrene-co-(4-vinylpyridine))," *Macromolecules* **1994**, *27*, 545-552. http://dx.doi.org/10.1021/ma00080a032
(37) Panov, V. P.; Vorontsov, E. D.; Evdakov, V. P. "Spectroscopic determination of the extent of protonation and alkylation of poly-4-vinylpyridine derivatives," *Journal of Applied Spectroscopy* **1975**, *23*, 958-962. http://dx.doi.org/10.1007/BF00608822
(38) Chen, W.; Sauer, J. A.; Hara, M. "The effect of ionic cross-links on the deformation behavior of homoblends made of poly(styrene-co-styrenesulfonic acid) and poly(styrene-co-4-vinylpyridine)," *Polymer* **2003**, *44*, 7729-7738. http://dx.doi.org/https://doi.org/10.1016/j.polymer.2003.09.053
(39) Qin, S.; Qin, D.; Ford, W. T.; Herrera, J. E.; Resasco, D. E. "Grafting of Poly(4-vinylpyridine) to Single-Walled Carbon Nanotubes and Assembly of Multilayer Films," *Macromolecules* **2004**, *37*, 9963-9967. http://dx.doi.org/10.1021/ma048692p
(40) Sakurai, K.; Douglas, E. P.; MacKnight, W. J. "Spectroscopic study of an ionic blend made from the acid form of sulfonated polystyrene and poly [ethyl acrylate-co-(4-vinylpyridine)]," *Macromolecules* **1992**, *25*, 4506-4510.
(41) Yang, K.; Kas, R.; Smith, W. A. "In Situ Infrared Spectroscopy Reveals Persistent Alkalinity near Electrode Surfaces during CO2 Electroreduction," *Journal of the American Chemical Society* **2019**, *141*, 15891-15900. http://dx.doi.org/10.1021/jacs.9b07000
(42) Osawa, M. "In-situ Surface-Enhanced Infrared Spectroscopy of the Electrode/Solution Interface," In *Advances in Electrochemical Science and Engineering* 2006, p 269-314.
(43) Devadoss, A.; Chidsey, C. E. "Azide-modified graphitic surfaces for covalent attachment of alkyne-terminated molecules by “click” chemistry," *Journal of the American Chemical Society* **2007**, *129*, 5370-5371.

4. Polarization Modulation Infrared Reflection-Absorption Spectroscopy for Characterizing Electrocatalytic Surfaces

4.1. Abstract

Reflective IR spectroscopy is a crucial technology for probing the structure and reactivity of electrode surfaces *ex situ* and *in situ*. In a two-stage process, we developed a table optical module and spectroelectrochemical flow cell for performing polarization-modulation IR reflection-absorption spectroscopy (PM-IRRAS) analyses of electrochemical systems. In the first stage, a dry ex situ PM-IRRAS arrangement was used to evaluate the packing density, azide mole fraction, and "click" completion of mixed monolayers of methyl- and azide-terminated alkanethiols on gold surfaces. In the second stage, we designed, constructed, and tested a flow cell for *in situ* detection of electrochemical species adsorbed on metal electrode surfaces. Technical problems stymied the use of this apparatus for *in situ* electrochemical applications, but insights gained from the process will be essential for further development of spectroelectrochemical capabilities in the McCrory group.

4.2: Introduction

While conventional transmission IR measurements can be helpful for probing certain systems, most electrocatalyst characterization would greatly benefit from IR spectroscopy with

enhanced surface selectivity. While the details vary between techniques, this is most commonly achieved through some type of reflectance spectroscopy, in which the IR beam is reflected off the surface which it is probing rather than transmitted through. Many techniques are available for this purpose,[1] including sum frequency generation (SFG),[2, 3] subtractively normalized interfacial Fourier transform IR spectroscopy (SNIFTIRS),[4, 5] surface enhanced Raman spectroscopy (SERS),[6-8] and surface enhanced IR reflection-absorption spectroscopy (SEIRAS).[9] Any surface IR technique will have certain advantages and disadvantages, as well as restrictions on the type of sample for which it is appropriate.

Of critical importance for the characterization of electrocatalytic materials is the difference between internal reflectance and external reflectance, as illustrated in Figure 4.1. In an internal reflectance technique such as SEIRAS, the sample is deposited as a thin layer atop the IR window, and the IR beam is reflected off the back of the sample, extending an evanescent wave into the sample itself, causing absorbance. This causes in inherent limitation, in that the sample of interest must be able to be deposited onto the window in a thin layer. This precludes the easy study of single-crystal metal electrodes or other macroscale surfaces but does have the benefit that attenuation of the beam by the electrolyte solution is not a problem. In contrast, external reflective techniques direct the beam through the electrolyte itself to reflect off the top of the electrocatalytic surface. This allows reflective materials of any morphology to be studied but introduces complications from beam passage through the electrolyte.

Polarization-Modulation Infrared Reflection-Absorption Spectroscopy

We were interested in developing the capability to perform spectroscopic experiments on a variety of electrocatalytic surfaces *in situ*, including with single-crystal metals. As such, we turned to the external technique infrared reflection-absorption spectroscopy (IRRAS, IRAS, or

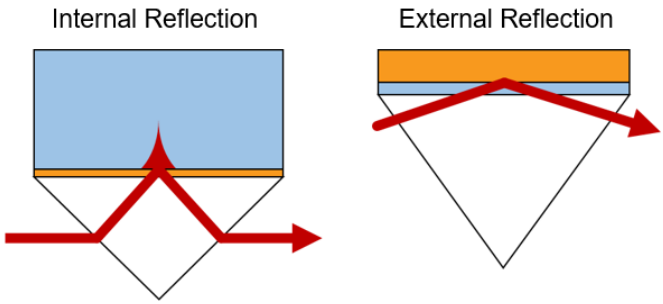

Figure 4.1 Diagram comparing the beam paths of internal and external reflection in situ infrared absorption techniques.

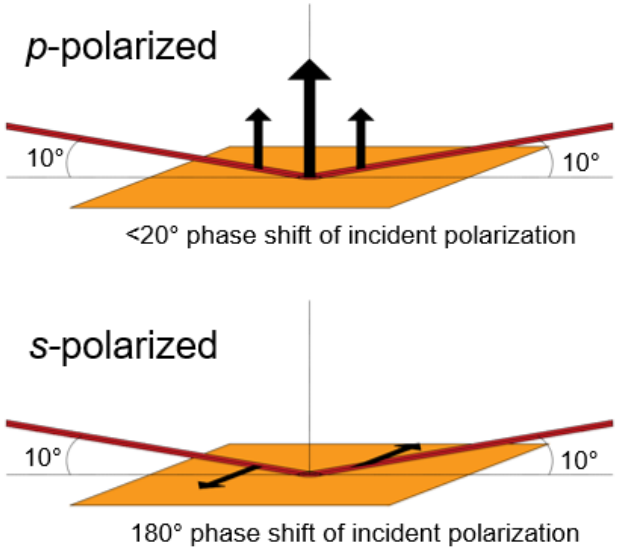

Figure 4.2 Diagram of the reflection-induced phase shifts of p- and s-polarized light incident at a grazing angle on a reflective surface. For the p-polarized case, the two beam vectors combine constructively at the surface to produce enhanced absorbance, while in the s-polarized case they combine destructively to attenuate surface absorbance.

RAIRS),[1, 10-14] and more specifically polarization-modulation IRRAS (PM-IRRAS). The PM-IRRAS technique has been reviewed extensively elsewhere,[5, 15, 16] but a short explanation of its salient features is given here. An infrared beam incident on a surface at a grazing angle can be broken into two polarization components: a *p*-polarized which is roughly perpendicular to the surface, and an *s*-polarized component that is roughly parallel, as seen in Figure 4.2. At the grazing angle, the *s*-polarized component of the reflected light undergoes a 180-degree phase shift. Near the sample surface, the incoming and outgoing beams will experience destructive interference in the *s*-polarized component, attenuating absorbance of this component by vibrational modes near the surface. In contrast, the *s*-polarized component undergoes minimal phase shift upon reflection,[5] and the incoming and outgoing beams therefore experience constructive interference in the *p*-polarized component, causing an enhancement in absorbance. The difference in absorbances between these two components is the key to IRRAS—because the absorbances are equivalent between the two components everywhere other than the surface (e.g., in the surrounding atmosphere or solution), the difference between these two components gives surface-specific vibrational information. In a basic IRRAS measurement, two spectra are collected sequentially: one using light that has been *s*-polarized relative to the surface, and another that has been *p*-polarized, simply by adjusting the position of a polarizer placed in the beam path. By subtracting the *s*-polarized spectrum from the *p*-polarized spectrum, a surface spectrum can be derived.

PM-IRRAS builds upon this technique by the addition of a polarization modulation step, which allows simultaneous collection of the *s*- and *p*-polarized spectra, eliminating potential spectral artifacts due to background drift.[17] To accomplish this, a photoelastic modulator (PEM) is placed in the beam path after the polarizer. The PEM contains a piezoelectric component to which an alternating voltage is applied. The voltage frequency is tuned to produce a half-wave retardation

in the polarized beam, rapidly modulating it between *s*- and *p*-polarizations. After the beam reaches the detector, a synchronous sampling demodulator (SSD) outputs two demodulated signals: a difference signal (p-s) and a sum signal (p+s). PM-IRRAS spectra are generally presented in terms of (p-s)/(p+s), or $\Delta R/R$.[15]

PM-IRRAS does have a number of restrictions on the types of samples it is appropriate for. The sample surface must be inherently IR reflective, which generally restricts its use to metals or thin layers atop metal surfaces. The surface selectivity is also not absolute—the difference signal will still detect species with (with declining sensitivity) out to a distance of about half the wavelength of light. In the IR range, this translates to between 1 and 10 microns. While this is not a critical limitation for ex situ measurements performed in air—especially if the chamber can be purged to remove water vapor and CO_2—it is a major restriction for in situ PM-IRRAS through liquid layers.[5] Since conventional PM-IRRAS uses a glow bar source rather than a laser, it has overall low sensitivity. The target molecule must be relatively abundant on the sample surface to be detectable. Moreover, PM-IRRAS will only detect molecules that have a vibrational component perpendicular to the sample surface. IRRAS, with or without polarization modulation, has most commonly been used to characterize polymerized surfaces,[18] alkanethiol self-assembled monolayers,[19-23] and sub-monolayer quantities of adsorbed small molecules on metal surfaces,[24-28] including *in situ* electrochemical systems.

In situ PM-IRRAS in an electrochemical cell presents a further set of challenges.[5, 29, 30] The beam must pass through at least four different phase interfaces as it passes from the air to the window, the window to the liquid electrolyte, and back out again (see Figure 4.3). Each interface will result in some amount of beam loss due to reflection. Additionally, the beam must pass through an IR-absorbing electrolyte layer, causing further attenuation in the wavenumber regions where

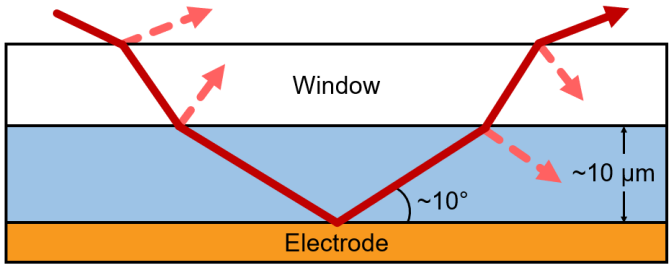

Figure 4.3 Diagram demonstrating the potential beam attenuation due to reflection for an IR beam passing through four phase boundaries in an external reflection in situ spectroelectrochemical cell.

the electrolyte absorbs.[5] Calculations done by Zamlynny also reveal that there is a PM-IRRAS "hot spot" with enhanced absorbance about ~10 microns past the electrolyte surface.[31] To avoid both this hot spot and overall beam attenuation, the spectroelectrochemical cell must be constructed with an extraordinarily thin electrolyte layer. The optimal layer thickness depends on a number of factors that have been reviewed in detail by Zamlynny and coworkers.[5, 32] The thin electrolyte layer provides additional challenges for the electrochemical experiment, especially the rapid depletion of the electrochemical active species within the thin layer. Due to the long collection times required by PM-IRRAS experiments, a flow cell must be employed to force the constant replenishment of electrolyte.

With these experimental parameters in mind, we envisioned two different phases for deployment of the PM-IRRAS technique in the lab. First would be an *ex situ* phase, in which the basic PM-IRRAS components were acquired and built into a functional apparatus. In this phase, PM-IRRAS could be used to characterize alkanethiol self-assembled monolayers on gold surfaces, in support of a project spearheaded by Robert Bonsall. In the second phase, we constructed a PM-IRRAS spectroelectrochemical flow cell (SEC-FC) for *in situ* detection of electrochemical intermediates on metal electrode surfaces. The results of these two phases are detailed in sections 4.2, 4.3, and 4.4.

Theory of PM-IRRAS Characterization of Alkanethiol Self-Assembled Monolayers

PM-IRRAS and related grazing-angle IR techniques have frequently been applied to the study of self-assembled monolayers (SAMs) on metal surfaces, particularly the well-studied system of alkanethiol monolayers on gold.[33-39] Alkanethiol SAMs tend to be highly ordered,[35] making interpretation of their spectra relatively straightforward, and information can be gleaned

from the spectra about SAM packing density and orientation. Alkanethiol SAMs have significant industrial relevance in nanotechnology and biosensing, making their study otherwise useful.[40]

Alkanethiol SAMs have also been proposed as a system for tethering molecular catalysts to electrode surfaces to form heterogenized systems.[33, 34] The main goal of such a system would be to ease spectroelectrochemical monitoring of the catalytic process, since a tethered molecular system with rapid catalytic turnover, combined with surface-selective spectroscopy, could be used to effectively "concentrate" the intermediate species and make it more available to be studied. Using an azide-capped SAM, the CuACC "click" reaction can be used to covalently tether an ethynyl-terminated catalyst molecule to the metal surface.[33] However, alkanethiol SAMs do not have good reductive stability past about -1 V vs Ag/AgCl, limiting their utility for this application. We have been interested in probing this reductive desorption process, especially with mixed monolayers in which azide-capped tethering chains are mixed with space-filling uncapped alkanethiol chains.[34] This system is illustrated in Figure 4.4, and provides two crucial handles for infrared spectroscopy: 1) the C-H stretching region around 2900 cm^{-1}, where the position and intensity of peaks can give information about the monolayer packing, and 2) the azide stretch region around 2100 cm^{-1}, which can give a quantitative measurement assessment of the amount of azide groups on the surface.

The C-H region peaks are well-understood and were described by Chidsey and coworkers in 1987.[35] For a basic alkanethiol SAM, five peaks appear: a CH_3 asymmetric mode around 2938 cm^{-1}, a CH_2 asymmetric mode around 2920 cm^{-1}, a CH_2 symmetric mode around 2851 cm^{-1}, and two Fermi resonance CH_3 symmetric modes around 2878 and 2938 cm^{-1} (see Figure 4.5). The intensities of the CH_3 peaks should be unaffected by the chain length, while the CH_2 peaks should scale with the number of methylene groups in the chain. Meanwhile, the large CH_2 asymmetric

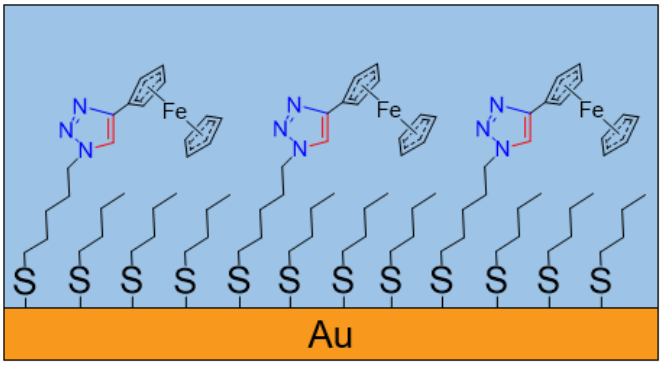

Figure 4.4 Diagram of an example mixed azide-terminated and methyl-terminated monolayer in which ethynyl ferrocene has been clicked to the azide groups. For visual simplicity the alkyl chains have fewer methylene groups than in studied systems.

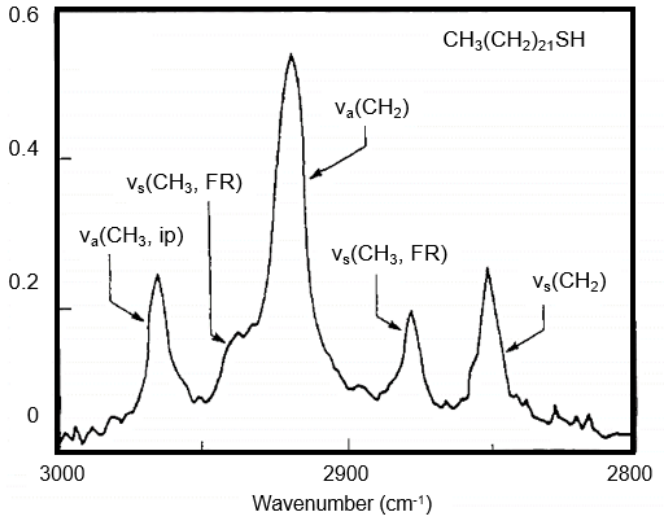

Figure 4.5 Peak assignments in the CH stretching spectral region of an alkanethiol self-assembled monolater. Adapted with permission from Ref. 35. Copyright 1987 American Chemical Society.

mode is highly sensitive to the packing density of the layer, and by extension its level of order. As packing density increases the peak will blueshift from around 2924 cm^{-1} (a "liquid-like" disordered arrangement) to as low as 2918 cm^{-1} (approaching a more crystalline structure).[35, 36] The strong azide peak is also helpful in characterizing mixed systems. Intensity of the azide stretch scales with its prevalence on the surface, allowing it to both serve as a monitor of azide mole fraction in the mixed layer, and an indication of the extent of click completion, since the click reaction breaks the azide structure.

Application of PM-IRRAS to Probing Heterogenous Electrocatalysis of Nitrate and other Small Molecules

The ultimate goal of PM-IRRAS development in the McCrory group is the *in situ* observation of electrochemical processes on electrode surfaces. In particular, we aimed to use PM-IRRAS to detect adsorbed reaction intermediates of NO^{3-}, NO^{2-}, and NO reduction on well-defined heterogeneous metallic electrode surfaces, providing mechanistic insights for these key nitrogen cycle reactions and informing rational development of selective electrocatalysts. PM-IRRAS is ideal for this application—being an external reflectance technique it can be applied to study macroscale single-crystal metal electrodes, and as discussed previously, the real-time backgrounding provided by polarization modulation makes it insensitive to the significant background shifting expected for a complex electrochemical flow cell apparatus. Electrochemical reduction of nitrate and associated intermediate species to dinitrogen is a promising method for remediation of nitrogen compounds in drinking water[41] and liquid radioactive waste.[42]

Nitrate reduction can proceed via multiple pathways, and product selectivity varies considerably between materials. While the ideal product for wastewater remediation is N_2, nitrate

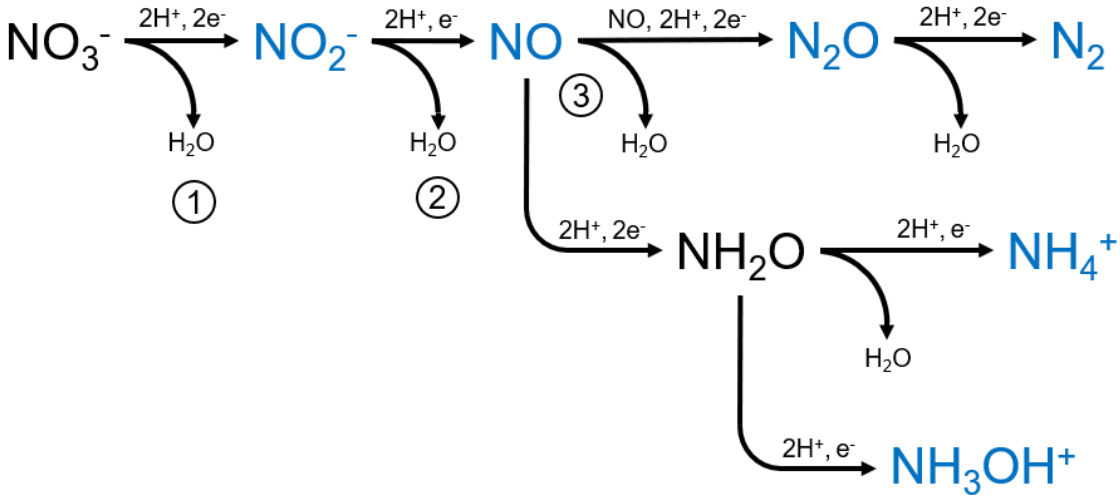

Figure 4.6 Schematic of electrochemical nitrate reduction pathways, highlighting 1) the rate-determining step of nitrate reduction to nitrite, 2) the fast step of nitrite reduction to nitrous oxide, and 3) the selectivity-determining step of nitrous oxide reduction.

reduction can also produce N_2O, NH_3OH^+, or NH_4^+ as major byproducts (Figure 4.6).[43] The primary challenge is that the *rate-determining* step in the NO_3^- reduction process is the initial 2 e^- reduction to NO_2^-, while the major *selectivity-determining* step is the reduction of NO.[43] Research into new electrocatalytic materials for nitrate reduction focuses on combining two or more metals in an attempt to successfully pair a rate-enhancing metal (catalyzing the $NO_3^- \rightarrow NO_2^-$ transformation) with a selectivity-enhancing metal to drive subsequent N_2 formation.[44-47] In order to rationally design such catalysts, it is essential to have a fundamental understanding of how the identity of the metal affects product selectivity due to formation potentials and binding character of reductive intermediates. *In situ* spectroelectrochemistry would permit observation of how the formation potentials, binding energies, and binding modes of long-lived intermediates on the surface vary as a function of electrode identity and applied potential, and how these factors influence product selectivity.

4.3: Construction of PM-IRRAS Table Optical Module and *Ex Situ* Characterization of Alkanethiol Self-Assembled Monolayers on Gold Surfaces

Table Optical Module Arrangement and Data Treatment

In the first phase of developing a PM-IRRAS system for characterization of electrocatalyst samples, we designed and built an apparatus for the *ex situ* PM-IRRAS evaluation of dry samples in air. This phase permitted us to troubleshoot and optimize the PM-IRRAS optical arrangement before using it for the more complex *in situ* spectroelectrochemical cell. The apparatus consisted of a Nicolet iS50 FTIR spectrometer purchased from Thermo Fisher Scientific, and a custom-built external table optical module (TOM). The optical arrangement of the TOM is diagrammed in Figure 4.7, and photographs of the TOM in operation are provided in Figure C.1. Briefly, the

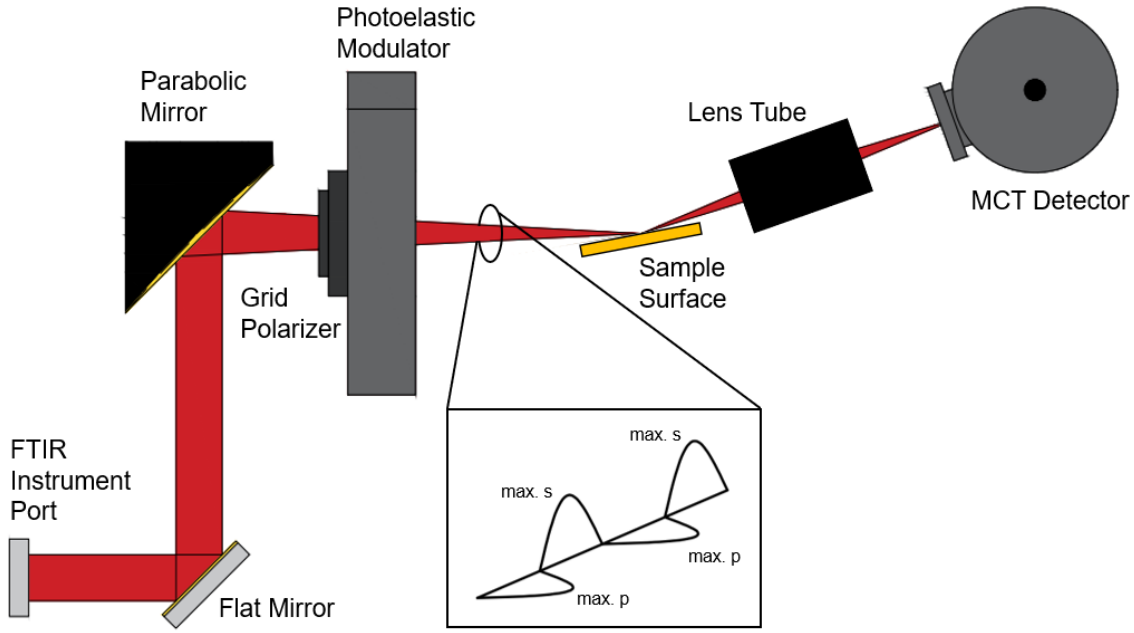

Figure 4.7 Diagram of the PM-IRRAS TOM optical arrangement. The IR beam path is represented in red.

collimated FTIR beam from the spectrometer is directed through an external port, then converged using a parabolic mirror with a 9-inch focal distance. The converging beam passes through a vertically-mounted grid polarizer, then through the PEM mounted at 45°. A driving voltage alternating at 50.08 kHz is applied to the PEM, which modulates the IR beam between maximum *p*-polarization and maximum *s*-polarization. The sample is arranged at the focal point of the converging beam using a rotating mount and positioned so that the central axis of the beam is at about 80-82° from the surface normal (8-10° grazing angle). The beam reflected off the sample surface—now diverging—passes through a lens tube containing two biconvex CaF_2 lenses that first collimate and then reconverge the beam, whereupon it reaches the MCT detector. The MCT detector passes the modulated signal through the synchronous sampling demodulator (SSD), which demodulates the signal into two components: the sum (p+s) signal and the difference (p-s) signal. Finally, the OMNIC software provides the PM-IRRAS spectrum $\Delta R/R$, as well as the sum signal (effectively a background spectrum).

The PEM oscillation must be optimized for a specific wavelength at which it produces perfect half-wave retardation. As the wavelength moves further from the point of optimization, the half-wave retardation becomes offset. This phenomenon produces a background curve described by a Bessel function, taking the form of one or more arches (See Figure 4.8). The PM-IRRAS spectrum sits atop this curve, and its intensity is distorted along the spectrum in proportion to the height of the Bessel curve (i.e., peaks at the apex of the Bessel curve will be proportionally enlarged relative to peaks near the base of the Bessel curve). Because the Bessel curve is imperfect, modeling it directly by use of a true Bessel function is impractical. Instead, a polynomial curve is generally used to fit the curve within a selected portion of the spectrum. Our method for performing this correction is illustrated in Figure 4.9. Briefly, a portion of the spectrum is selected that contains

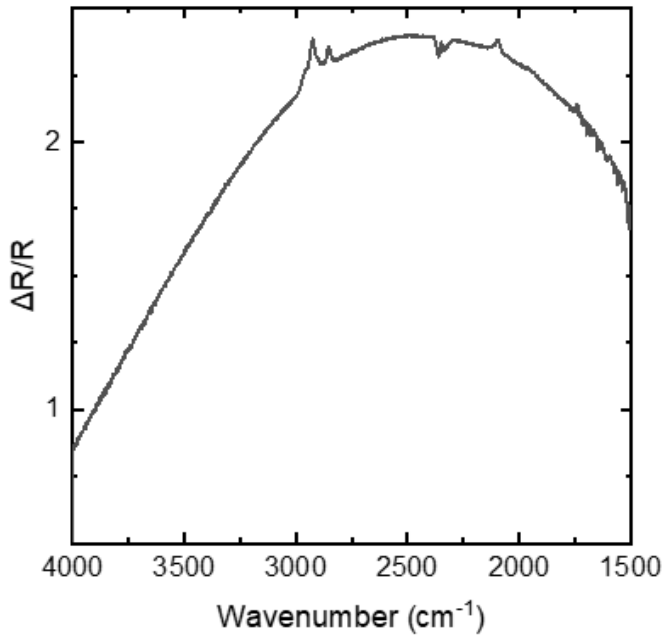

Figure 4.8 Example PM-IRRAS spectrum demonstrating the Bessel curve. The PEM has been optimized at 2900 cm-1, and the sample is an alkanethiol SAM on gold.

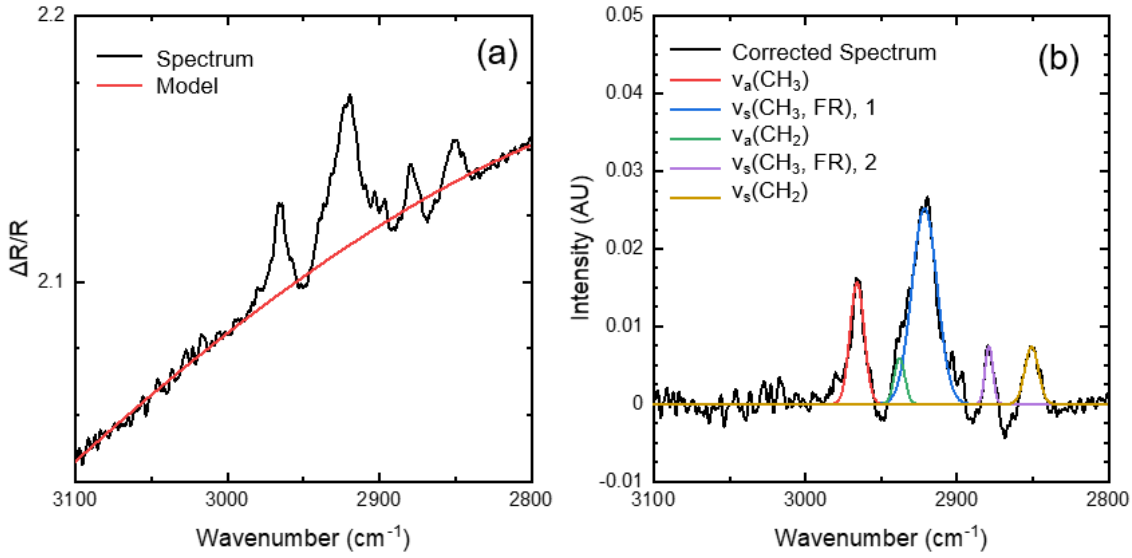

Figure 4.9 Demonstration of data treatment for a decanethiol SAM on a gold surface. a) removal of the Bessel background using an inverse exponential curve, and b) fitting of the backgrounded spectrum using Gaussian curves.

the peak(s) of interest and some adjacent sections of the Bessel curve without distinct peaks. An inverse exponential or polynomial function is used to produce a model curve closely matching the path of the underlying Bessel curve (Figure 4.9a). A generalized reduced gradient (GRG) nonlinear method is then used to systematically vary the model curve parameters in the regions beyond the peaks of interest, producing an optimized fit. The spectrum is then divided by the model curve, resulting in a backgrounded PM-IRRAS spectrum in arbitrary intensity units vs. a flat baseline (Figure 4.9b). Due to noise in the background, the PM-IRRAS spectra typically need a further peak fitting applied before precise information about peak position and intensity can be extracted. For alkanethiol spectra, the peak fitting in the C-H region is predicated on the peak assignments discussed in Section 4.1. A model with up to five Gaussian peaks in the region is appropriate depending on the exact SAM structure: a SAM with 100% azide-capped SAMs should have no CH_3 peaks, though the perpetual presence of adventitious carbon means this is truer in theory than in practice. An example of a Gaussian peak-fitting is presented in (Figure 4.9b). Briefly, a set of Gaussians are constructed in the spectral region of interest and the parameters adjusted to create a rough approximation of the measured spectrum. Care must be taken to ensure that the modeled peaks have some basis in expected physical reality. It may be prudent to "pin" certain parameters, such as peak positions that are not known to substantially vary. The sum of the peaks produces a model spectrum, and this model can then be optimized using the GRG nonlinear method, applied within the peak region.

Care must be taken not to overinterpret the PM-IRRAS results, as several factors complicate the data. The PM-IRRAS signal is overall weak and susceptible to noise that has proven difficult to eliminate. Significant background oscillations occur and become more noticeable at higher resolutions as seen in Figure C.2. We have typically performed measurements at 2 cm^{-1}

resolution as a compromise between data collection time, ease of fitting, and accuracy of peak shape. While the spectra at 8 cm^{-1} resolution look "cleaner," this is an artifact of the increased data spacing, and peak positions derived from spectra at lower resolutions must be treated with appropriate skepticism. Details of the optical arrangement may also produce data inconsistencies. In Figure C.3, different spectra are presented using the same sample with variations in beam aperture setting (Figure C.3a) and grazing angle (Figure C.3b). Because the spectra vary so wildly with these minor variations—including both the apparent peak intensities and positions—it is essential to use internal standards in experimental designs and to avoid making direct comparisons between different data sets that may have been collected with variations in the optical positions. As such, we have primarily used PM-IRRAS to evaluate trends within a set of data collected at a single set of conditions and a fixed set of optical positions. Finally, adventitious carbon is a potential obfuscating factor when evaluating carbonaceous samples such as alkanethiol SAMs. In our open-air TOM, adventitious carbon is effectively impossible to eliminate. Adventitious carbon causes peaks to appear in the CH region even for ostensibly clean surfaces and provides a possible source of error when evaluating these samples.

Experimental Results

Further evaluation of PM-IRRAS results for alkanethiol mixed SAMs are expected to be included in forthcoming publications, and key results are highlighted here mainly to serve as an example of the types of data which can be feasibly collected with the PM-IRRAS TOM. As an initial proof of concept, we collected spectra for a series of methyl-terminated alkanethiols of varying chain lengths: 1-dodecanethiol, 1-decanethiol, 1-octanethiol, and 1-hexanethiol. The alkanethiol SAMs were deposited from ethanol onto Si wafer surfaces with a sputtered Au layer.

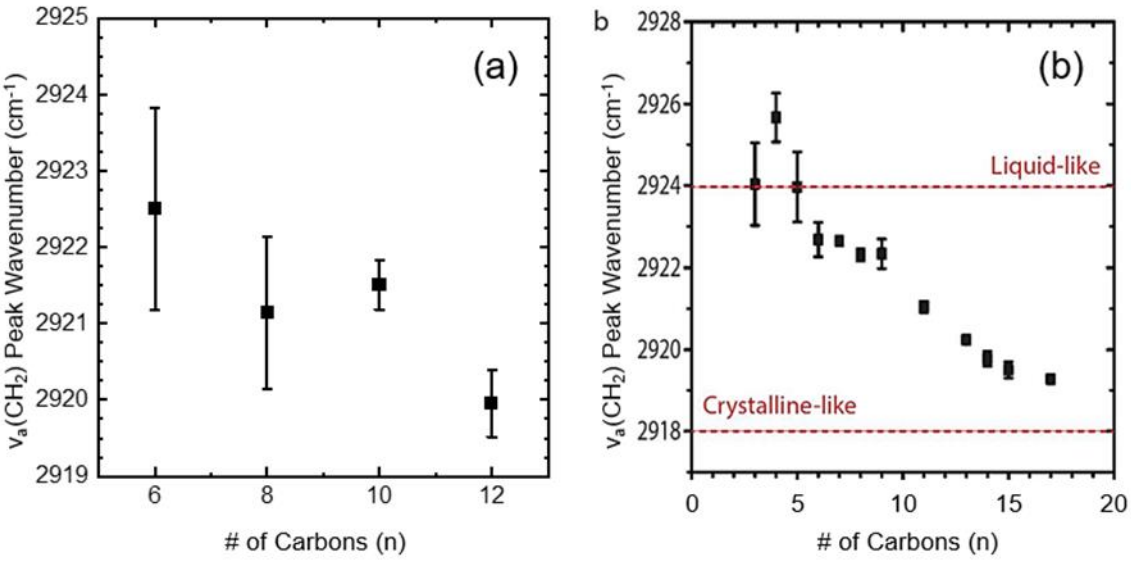

Figure 4.10 Variation in the methylene asymmetric mode ($\nu_a(CH_2)$) position as a function of methyl-terminated alkanethiol chain length. Data collected by our group is presented in (a), and a literature example for comparison (b) has been adapted with permission from Ref. 36. Copyright 2017 American Chemical Society.

After being rinsed with EtOH and dried in a stream of nitrogen, spectra were collected for three SAM surfaces of each alkanethiol chain length. The PEM optimization was set to 2900 cm^{-1}. 1024 scans were collected for each sample, with a 2 cm^{-1} resolution, 30% aperture, and ~8° grazing angle. After removing the Bessel background and performing Gaussian peak fitting, the positions of the CH_2 asymmetric stretches for each chain length were averaged. These data are presented in Figure 4.10. The results roughly matched what is reported in the literature,[35, 36] with the peak wavenumber redshifting as the SAM chain length increased, consistent with a transition from a more liquid-like state to a more crystalline state. The results indicated both that the PM-IRRAS TOM was functioning as expected, and that the process used for SAM surface synthesis was sufficient for creating well-packed layer.

We then evaluated the packing and azide coverage of mixed monolayers, which were also prepared on Au-sputtered Si surfaces via deposition from ethanol. Comparison of the azide mole fraction on the surface was performed by integration of the 2100 cm^{-1} azide stretching mode. Corrected PM-IRRAS spectra for a range of azide mole fractions (ratio of azido-undecanethiol to decanethiol in the deposition solution) are presented in Figure 4.11a. The PEM optimization was set to 2100 cm^{-1}. 1024 scans were collected for each sample, with a 2 cm^{-1} resolution, 30% aperture, and ~8° grazing angle. In Figure 4.11b, integrations for each mole fraction are presented using two different integration methods: 1) direct integration of the normalized spectrum between 2050 cm^{-1} and 2150 cm^{-1}, and 2) integration of a Gaussian peak fitted to the normalized spectrum as described in the previous section. In both cases, the integration scaled approximately linearly with the azide mole fraction, suggesting that the azide mole fraction of the deposited layer corresponded closely to the mole fraction in solution. These data support a similar conclusion made by Chidsey and coworkers.[34] In a separate set of measurements, the azide stretching mode

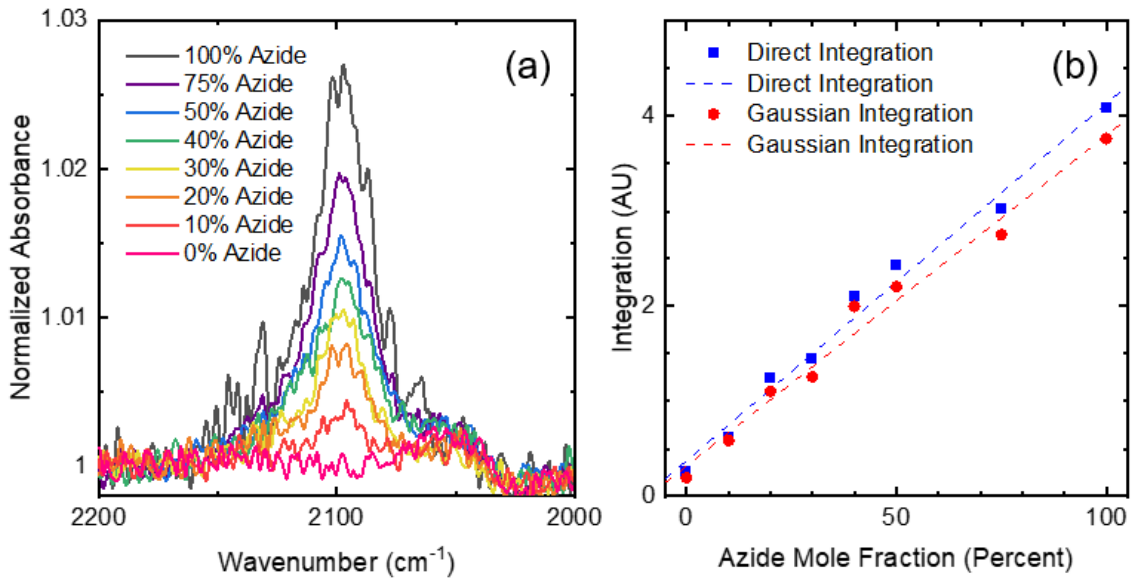

Figure 4.11 PM-IRRAS evaluation of azide coverage as a function of azido-undecanethiol mole fraction in the deposition solution. a) Example spectra collected at 2100 cm^{-1} PEM optimization for samples at a range of deposition mole fractions. b) Direct and Gaussian integrations of the azide stretching modes, demonstrating linear relationship between azide mole fraction in solution and in the resulting SAM

.

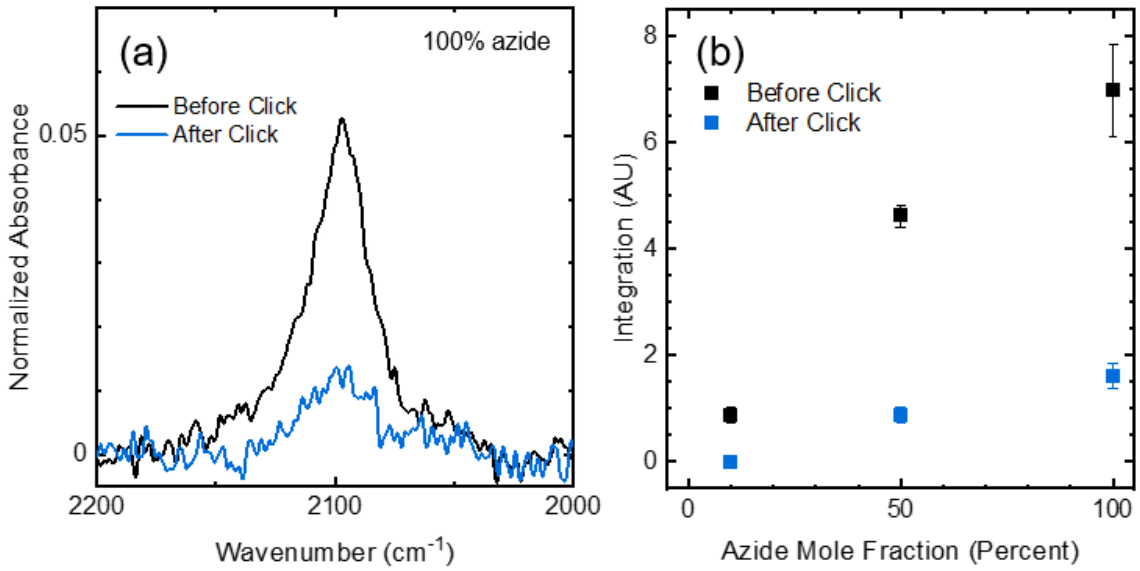

Figure 4.12 PM-IRRAS detection of azide loss on mixed monolayer surfaces due to click reaction. a) Example spectra collected at 2100 cm^{-1} PEM optimization on a 100% azido-undecanethiol SAM before and after the click reaction. b) Comparison of azide loss from click for 100%, 50%, and 10% azido-undecanethiol SAMs. Each data point is the average of three measurements, and error bars are the first standard deviation.

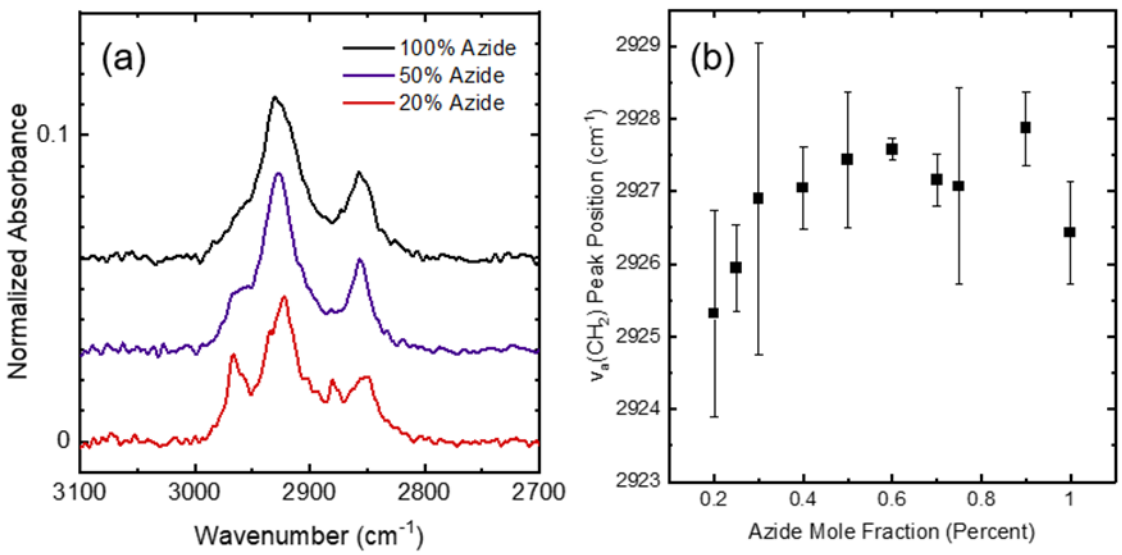

Figure 4.13 PM-IRRAS evaluation of the C-H stretching modes for mixed monolayers. a) Representative spectra at 100%, 50%, and 20% mole fraction of azido-undecanethiol, showing appearance of CH_3 modes as the fraction of decanethiol increases (0%, 50%, and 80% respectively). b) Variation in the methylene asymmetric mode ($\nu_a(CH_2)$) position as a function of azido-undecanethiol mole fraction. Each data point is the average of three measurements, and error bars are the first standard deviation.

was evaluated for surfaces with 100%, 50%, and 10% azide mole fraction before and after a CuACC click reaction to add ferrocene groups to the azide-terminated chains. As shown in Figure 4.12, the azide peak intensity fell substantially after the click reaction. For higher azide coverages, some azide remained unclicked, likely due to steric hindrance.

Spectra were also collected for mixed monolayers of azido-undecanethiol and decanethiol in the C-H stretching region. Various data sets were collected with varying conditions, all of which demonstrated that the mixed monolayers had relatively poor packing density. Example spectra at 100%, 50%, and 20% mole fraction are presented in Figure 4.13a, along with a full set of data demonstrating variation in the asymmetric CH_2 stretching mode as a function of azide mole fraction in Figure 13b. The data appear to indicate a small redshift in the peak position as the fraction of azido-undecanethiol decreases, but the large errors make it difficult to say with certainty. Regardless, all spectra have an asymmetric CH_2 mode position well above 2924 cm^{-1}, indicating a liquid-like level of crystallinity.

4.4: Design and Construction of a PM-IRRAS Spectroelectrochemical Flow Cell

Overview of Design Principles

To aid our investigations of electrochemical surfaces, we designed and constructed a PM-IRRAS spectroelectrochemical flow cell (SEC-FC). A few different example cells from the literature were used as reference during the design,[48-53] especially that of Zamlynny and Lipkowski.[5] The finalized design of the SEC-FC is presented in Figure 4.14, with additional angles in Figure C.4 and an exploded view in Figure C.5. The design went through several iterative stages before the finalized design was settled on, and the part number designations are artifacts of this

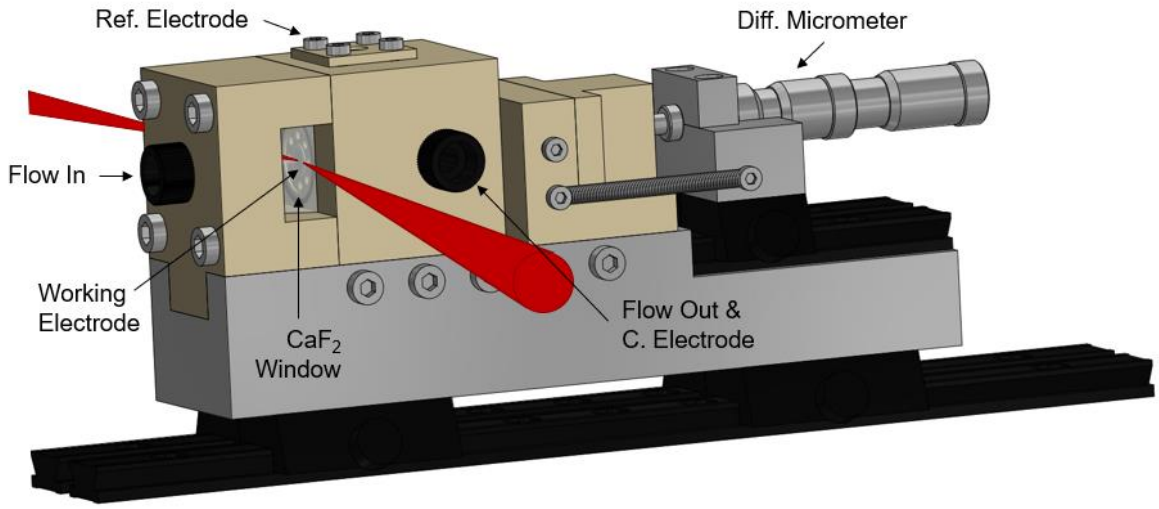

Figure 4.14 Design illustration of the PM-IRRAS SEC-FC. The reference electrode, counter electrode, external tubing, pump, and positioning components are not included. The IR beam passing through the cell is represented in red.

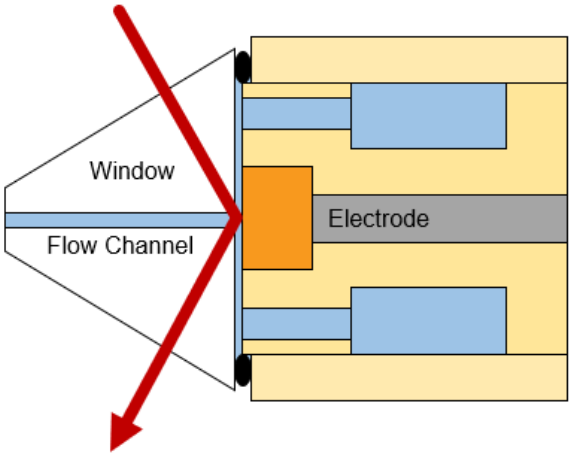

Figure 4.15 The path of the beam through the well is schematically represented with a top view. The components are not shown to scale. Blue regions represent the electrolyte present in the flow channel, thin layer, and solution reservoir.

process (e.g., Part 3 was eliminated partway through the design, and the finalized design therefore does not have a Part 3).

Based on the restrictions of PM-IRRAS and the types of samples we were interested in characterizing, we had several different parameters in mind when designing our own SEC-FC. In PM-IRRAS, analyte species at a reflective surface are probed using an IR beam incident on the surface at a grazing angle (~80° from the surface normal). PM-IRRAS can be used to investigate solid-liquid interfaces, though the thickness of the liquid layer must be minimized. As such, the SEC-FC was designed around control of the gap between the optical window and the working electrode, which could be adjusted by increments of 0.1 microns using a differential micrometer. Cell rigidity and extremely precise machining were needed to ensure that the position of the electrode shaft exactly was perpendicular to the IR window.

In order to maximize the IR beam throughput, we used a CaF_2 crystal beveled at 60° as the optical window. The angle requirements of PM-IRRAS make it impractical to use a flat window for measurements, as the throughput of the IR beam will be significantly reduced due to reflection at the air/window interface. By using a modified triangular prism for the window, we caused the beam to strike the window at an angle favorable for high transmission. The use of a 60° bevel was intended to balance the need for an inclined surface for the incoming beam with commercial availability of the appropriate optics. A diagram of the CaF_2 window and beam is presented in Figure 4.15.

The need for a thin layer for the optical portion of the experiment was in conflict with the demands of the electrochemical experiment. Over the timespan of data collection for a single PM-IRRAS experiment, the amount of analyte in a stagnant 10-micron electrolyte layer would be completely consumed, making the spectroscopic data useless. In order to work around this

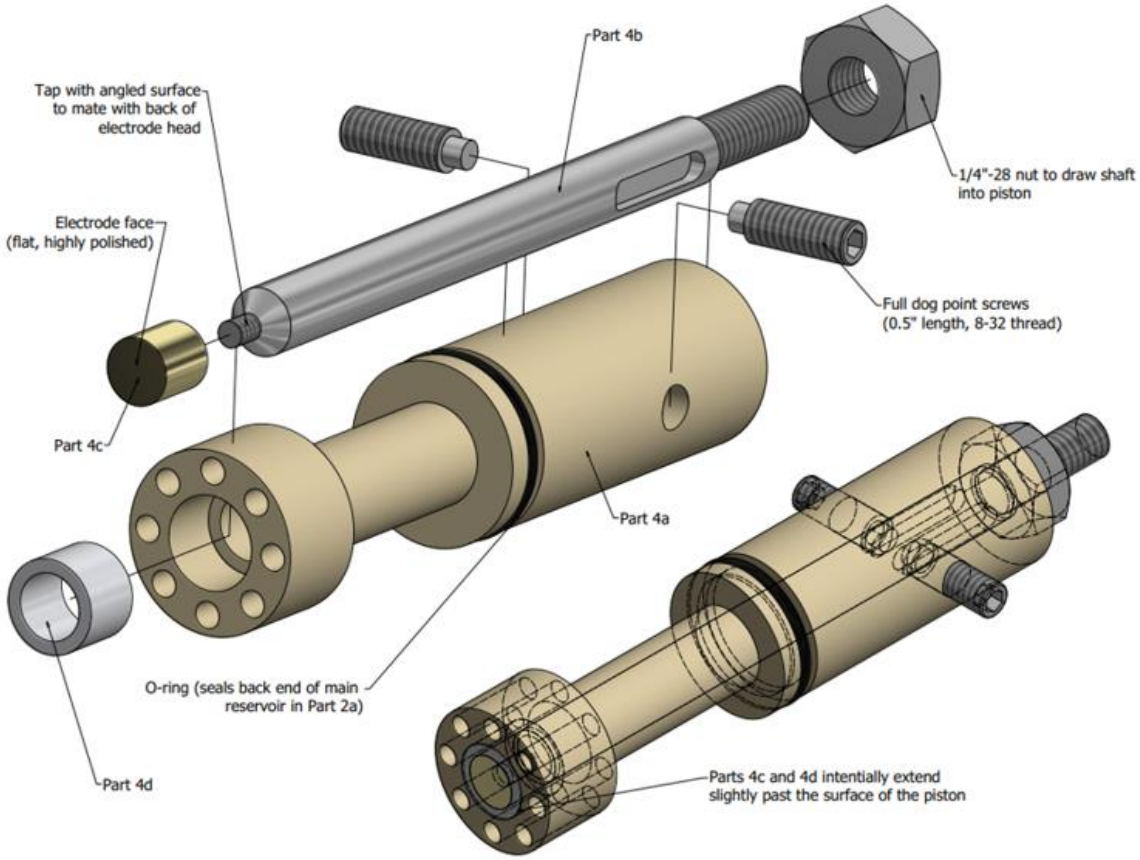

Figure 4.16 A schematic representation of the working electrode assembly of the PM-IRRAS SEC-FC. The identity and function of the individual components is detailed in the next section.

limitation, we designed the SEC-FC as a flow cell, with the electrolyte being continuously drawn though a flow channel in the center of the window by a syringe pump during the experiment. The flow within the thin electrolyte layer constantly replenished the supply of analyte, allowing consistent spectroscopic measurements to be done over the long timescales required for PM-IRRAS.

The SEC-FC was designed with maximum modularity in mind. The cell was constructed with many different parts to simplify assembly, disassembly, and cleaning. Modularity of the working electrode was a significant design concern. In particular, we wanted a working electrode assembly that could accommodate a variety of single-crystal metal electrodes, and an attachment method that allowed it to be mounted in the call without contacting the working surface, avoiding damage to any delicate surface structures or layers. Furthermore, it was necessary for the working electrode to be securely encased in a Teflon sheath that prevented solution contact with any electrical components other than the WE surface itself. The resulting structure can be seen in Figure 4.16, incorporating a threaded rod onto which a tapped electrode head is attached. The rod-electrode assembly can then be drawn back into the sheath and piston without contacting the front surface.

The choice of materials for the cell was critical to ensure both the rigidity of the structure and to prevent organic or metallic contamination of the electrolyte solution, even with moderately corrosive solutions. The polymer polyphenylene sulfide (PPS) was selected for most cell components (Parts 1a, 2a, 4a, 5a, and 5b) due to a combination of exceptional chemical resistance and minimal malleability. Components not in contact with the solution were primarily made from either aluminum (for the base [Part 2b], the micrometer clamp [Parts 6a and 6b], and the Thorlabs-

supplied optical rails and carriers) or stainless steel (the WE rod [Part 4b]). The contact surface for the micrometer head (Part 5c) was made from Vespel polymer.

Design Details and Assembly of the PM-IRRAS SEC-FC

The SEC-FC is divided into a series of parts whose numbers roughly corresponding to stages in its assembly. However, since significant iteration occurred during the design process, the numbers as presented in the finalized design are not a perfect indicator of assembly order. As such, the design is presented here in a non-numeric order. The design schematics for each part, including solid model views, can be found in Appendix C, Figure C.8 through Figure C.16.

The structural core of the SEC-FC comprises Parts 2a and 2b, which we refer to as the cell body and the base respectively. The base is constructed from aluminum and has attachments on the bottom for a set of optical rails to enable precise lateral positioning. The top has additional rail attachments for positioning of Part 6. The remainder of the top consists of a precisely machined rectangular groove into which the remainder of the cell components are fitted. The cell body fits snugly into the groove and is pinned in place with a set of three 1/4" shoulder screws. The body itself has a complex set of features positioned around a central bore that serves as the outer wall of the electrolyte reservoir. In the front, the cell body has a large O-ring glad which forms a seal with the optical window. On the left and right sides are taps for 1/2-20 PEEK pipe fitting, leading into short shafts that direct electrolyte flow in and out of the reservoir. On top is another shaft to accommodate the reference electrode, held in place through O-ring compression via a clamp.

Part 1b is a 60°-beveled CaF_2 prism that serves as the optical window, provided as a custom order by Crystran Ltd. A 1 mm bore drilled through the window serves as a flow channel. Part 1a, the cell front, fits into the groove of the base. It contains a cutout that holds the CaF_2 window, and

a tapped flow channel with an O-ring gland on the front that mates with the flow channel cutting through the window. On the central vertical axis of the cell body are two 1/4" slip fit holes that mate with set pins on Part 1a, and at each corner is another hole to admit a 1/4” shoulder screw. Together, these hold the cell front and body together as a rigid assembly that compression-seals the optical window.

Part 4 contains the working electrode, and Part 5 holds Part 4 in place. Part 4 consists of a piston (4a), electrode shaft (4b), and electrode sheath (4d). The piston has a complex structure as it serves a number of roles in the cell. First, the thin middle section forms the inner wall of the electrolyte reservoir. An O-ring behind this section seals the reservoir from the back. A series of 8 bores on the front connect the electrolyte reservoir with the thin electrolyte layer between the working electrode and window. The piston also holds the working electrode shaft in position. The shaft fits tightly into the bore running through the central axis of the piston. The threaded knob and angled surface on the front of the shaft mate with the electrode head (Part 4c). In the back, two slots on either side of the electrode shaft accommodate perpendicular dog point screws.

Part 5a holds the piston assembly in place. The bottom section fits into the groove of the cell base and can be temporarily pinned in place with a shoulder screw to aid assembly. The key feature of Part 5a is the central bore, which accommodates the piston and matches up to the corresponding bore in Part 2a. On either side of Part 5a are tapped holes for the full dog point screws. During assembly, the Teflon electrode sheath is first fitted into the front of the piston. Then the electrode head is fitted onto the shaft, which is then inserted into the piston from the front, passing through the sheath. The piston is pinned in place by the dog point screws. These pass through the threaded portion into the unthreaded holes on the sides of the piston, and then fit loosely into the slots on the shaft. Next, a nut is screwed onto the threaded portion of the shaft. As

it pushes against the back of Part 5a, the shaft is drawn backwards due to the dog point screws, which prevent the shaft from rotating along with the nut. The electrode head can therefore be drawn back until its surface is flush with the Teflon sheath. This entire process avoids ever touching the front surface of the electrode head. Finally, the dog point screws are brough firmly into contact with the shaft slots, pinning the shaft in place and providing an electrical contact to the electrode. Part 5b is then fitted over the back of the electrode shaft and screwed in place. Part 5b primarily exists to hold Part 5c, which is a rigid Vespel disk that provides a hard, non-conductive contact surface for the micrometer. The entire structure consisting of all subparts of Parts 4 and 5 is hereafter referred to as the working electrode assembly (WEA).

The differential micrometer (Newport DM-13L) held in place by Parts 6a and 6b serves to precisely position the WEA within the cell. Part 6a attaches to optical rails atop the cell base. The micrometer is placed with its attachment surface in the semicircular groove, and then Part 6b is fitted on top and screwed in place to hold the micrometer. With the WEA pinned in place, the micrometer assembly (MA) is fitted onto the rails and the pushing surface of the micrometer brought into contact with Part 5c. The rail carriers are pinned in place. Small, tapped holes on Parts 5a and 6a are then used to attach steel springs on either side. These provide tension that holds the WEA and the MA together as the micrometer is extended and retracted. Finally, the pin holding the WEA to the base is removed, allowing the micrometer to position the WEA as desired to form a thin electrolyte layer between the working electrode and window.

4.5: Testing PM-IRRAS Electrochemical Flow Cell

We had three primary goals for the initial testing and data collection with the SEC-FC: 1) demonstrate surface selectivity in the in situ PM-IRRAS, 2) correlate a change in spectra with a

change in electrochemical behavior, and 3) validate the flow dynamics. To accomplish these goals, we planned to carry out the following validation cycle using the adsorption and desorption of a spectroelectrochemical probe molecule as a model system. We settled on trying reversible cyanate ($^{-}$OCN) or thiocyanate ($^{-}$SCN) adsorption on a polycrystalline copper surface based on previous reports successfully using these as probe systems.[17, 54, 55] We planned to use the following experimental cycle to verify cell functionality:

1. Fill cell with a blank electrolyte solution and hold the electrode at a negative potential,
2. Flow a potassium [thio]cyanate solution into the cell,
3. Apply a positive potential to the electrode, causing formation of a [thio]cyanate monolayer through oxidative oxidation,
4. Flow a blank electrolyte solution into the cell,
5. Apply a negative potential to the electrode, causing reductive desorption of the monolayer.

PM-IRRAS spectra would be collected at each step in this process. For cyanate on the copper electrode we anticipated observing a solution-phase band around 2168 cm^{-1}, and at positive potentials the appearance of a surface-bound cyanate species at 2275 cm^{-1}.[54, 55] For thiocyanate, the corresponding surface mode was expected at either 2070 cm^{-1} for an S-bound species or 2140 cm^{-1} for an N-bound species.[17, 55]

Initial testing of the cell was made difficult by an array of factors. In general it was difficult to get any sort of reliable probe peak, even from the electrolyte layer. On any given attempt, this could have been due to low probe concentration, poorly aligned optics, air bubbles, surface degradation, or other unrealized issues. We therefore adopted a somewhat scattershot approach to

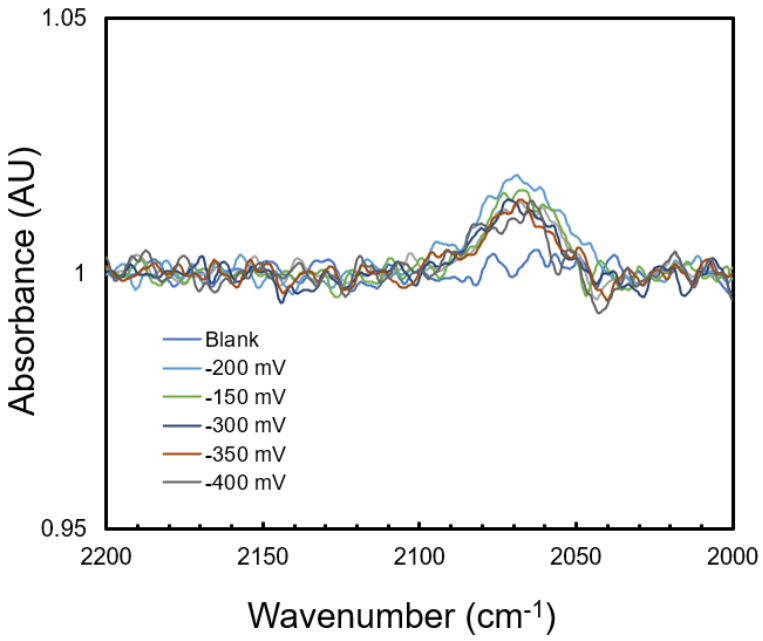

Figure 4.17 In situ PM-IRRAS spectra collected in an Ar-sparged 0.1 M KOH solution (blank) and 0.1 M KOH with 25 mM potassium thiocyanate with a polycrystalline Cu electrode. Electrode potential was adjusted above and below the thiocyanate adsorption potential of about -250 mV vs SCE. A 15 mL/h flow was used while thiocyanate solution was present.

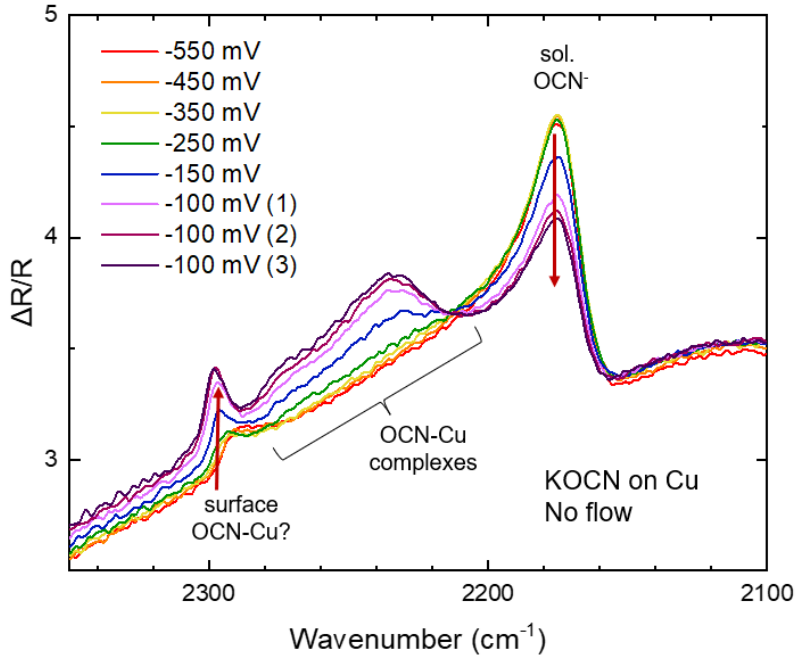

Figure 4.18 In situ PM-IRRAS spectra collected in an Ar-sparged 100 mM potassium cyanate solution using a polycrystalline Cu electrode without flow. The working electrode voltage was ramped from -550 mV to -100 mV vs. SCE, then held at -100 mV for three scans. Arrows indicate peaks of interest as described in the text.

cell testing wherein many parameters were being changed at once to try and find a set of conditions that worked sufficiently well to collect data and make further refinements. From the beginning, we also experienced problems with determining and reliably reproducing window-electrode distances. Attempting to gauge the gap thickness based on the cell resistance using measurement of the IR drop encountered problems with hysteresis (Figure C.6), which suggested that the window position had some flex, and pushing the piston up against it caused movement. Despite early setbacks, we were eventually able to observe the appearance of a thiocyanate peak at 2070 cm^{-1} in a 25 mM solution, which was assigned to the solution species (Figure 4.17). Changes in the voltage applied to the copper electrode appeared to make no change to the thiocyanate peak under 15 mL/h flow, nor did they induce the growth of additional peaks.

The poor results from early tests caused us to rethink our approach and try using KOCN at a higher concentration (100 mM) without flow or further electrolyte, relying on depletion of the cyanate content in the thin layer and steady growth of the surface peaks to allow identification. The resulting spectra are presented in Figure 4.18. Tentative peak identifications were made based primarily on a report from Brandt and coworkers.[54] The electrode was initially held at -550 mV, well below the potential of oxidative adsorption, and then stepped positive. Below -150 mV a large partially bipolar band was seen in the region between 2150 and 2200 cm^{-1}, which was assigned to the unbound solution-phase cyanate anion. A small band was also observed around 2290 cm^{-1}. Once the solution was stepped to -150 mV, a decrease was seen in the solution-phase band, as would be expected from depletion of the thin layer. The small band at 2290 cm^{-1} also rose sharply, suggesting it could be the surface-bound species. However, a broad band or set of bands also appeared in the intermediate region between 2280 and 2200 cm^{-1}. Along with the 2290 cm^{-1} band, these rose as the potential was stepped to -100 mV, where it was held for three sets of scans. The

2290 cm^{-1} appeared to reach a maximum, as might be expected if the cyanate had reach complete coverage on the surface, but the middle bands continued to rise with successive scans. Based on this behavior, these bands appeared to derive from one or more complexed Cu-OCN species in solution, suggesting the cyanate not only adsorbed, but actually dissolved the Cu surface.

This finding was supported by further testing using electrolyte flow. A blank solution of 200 mM sodium perchlorate was flowed into the cell, then 200 mM sodium perchlorate with 200 mM sodium cyanate. Under flow, the adsorbed cyanate peak was observed at OCV. As seen in Figure 4.19a, the electrode voltage was then toggled positive and negative of OCV, causing the peak to disappear positive of OCV and reappear negative of OCV. The exact position of OCV varied with electrode position due to the voltage differences induced by the cell resistance. No peaks were observed between the free solution-phase $^{-}$OCN and the assigned surface-bound species, indicating that the complexed Cu-OCN species were being removed rapidly from the thin layer as they formed, and supporting the assignment of the band at 2290 cm^{-1} to the adsorbed OCN. However, further experiments attempting to confirm this assignment by maintaining the surface-bound species once the perchlorate blank was flowed through the thin layer were unsuccessful (Figure 4.19b). When the electrode was held at about -300 mV vs SCE to match the OCV, the surface cyanate band disappeared along with the solution-phase band.

Altogether, these results provided tantalizing evidence that the SEC-FC could function as intended: we had likely detected a surface species, demonstrated a spectroelectrochemical response, and validated the flow dynamics of the cell. However, we also determined that the Cu/cyanate probe system suffered from significant degradation of the Cu surface during experiments. In addition to the electrochemical evidence for Cu dissolution, we also observed visible macroscale degradation and oxidation of the electrode. We determined that transitioning to

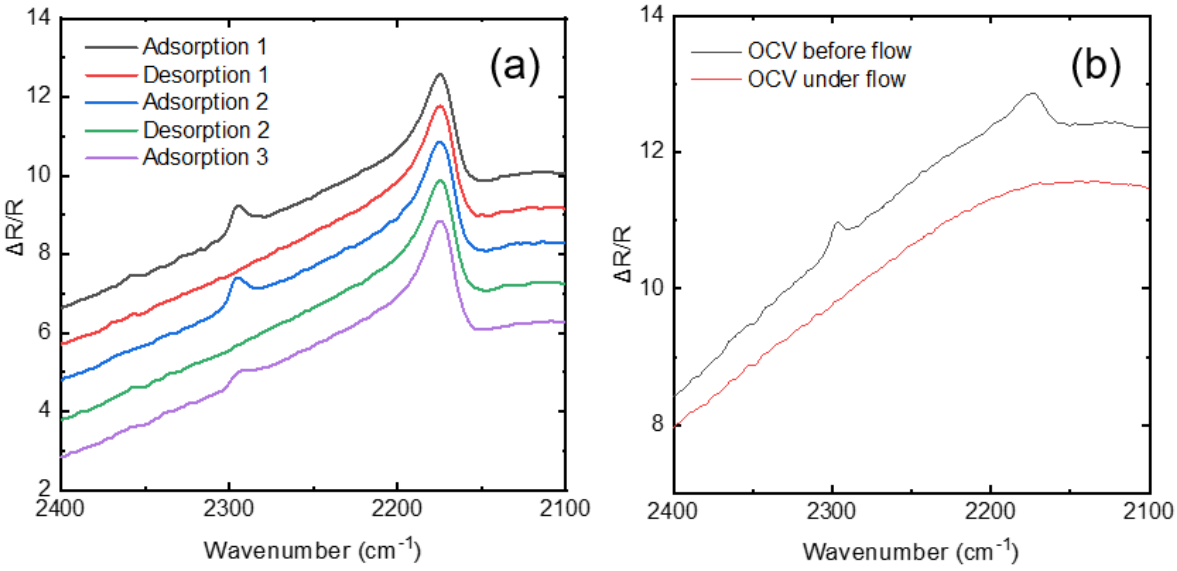

Figure 4.19 In situ PM-IRRAS spectra collected in Ar-sparged 0.2 M sodium perchlorate solution (blank) and 0.2 M sodium perchlorate with 100 mM sodium cyanate with a polycrystalline electrode. All spectra are under 10 mL/h flow. a) The working electrode potential is toggled positive and negative of the open circuit voltage (about -300 mV), which reflects the adsorption potential of the cyanate. Spectra are presented offset for clarity, with two adsorption/desorption cycles followed by a final adsorption. b) The working electrode is held at the OCV potential (OCV not permitted to float) as a blank solution is flowed into the cell. The peaks assigned to both the surface and solution cyanate species disappear as blank solution is flowed in.

an Au surface could provide a more stable platform for cyanate adsorption relative to Cu. Reports from various groups had gotten a good spectroelectrochemical response from Au-OCN surface species.[55-57] We expected the adsorption band for cyanate on gold to appear between 2190 and 2220 cm^{-1}, alongside the 2168 cm^{-1} solvated cyanate.

Due to the intrinsic difficulties in acquiring a precisely machined and tapped electrode of pure gold, we decided to prepare machined Ti electrodes which would then be electropolished and sputtered with Au to form a polycrystalline Au surface. The electropolish procedure was based on a report from Kim and coworkers,[58] and involved a rough polish of the electrode surface with 600-grit sandpaper followed by immersion in a 1 M NaCl solution in 20% ethanol and 80% ethylene glycol and application of a +20 V voltage against a stainless steel counter electrode. Many combinations of voltage and polishing time were attempted, none of which produced a surface that was both flat and macroscopically smooth—the procedure generally caused surface pitting, rounding of the surface edges, or both. Some examples of electropolished surfaces with different polishing times are provided in Figure C.7. The electropolish was abandoned in favor of a sequential diamond polish to 0.1 microns followed by Au sputtering.

Adsorbed cyanate was not observed when this system was tested, as seen in Figure 4.20. There are several possible reasons for this. A poorly defined surface could be causing problems with the optical requirements of the experiment or causing a low coverage of the end-on cyanate adsorption orientation needed for PM-IRRAS detection. Adventitious carbon on the Au surface could be preventing coordination of cyanate species, which would necessitate rigorous cleaning procedures and the impractical sequestration of the gold surface from ambient air during the cell assembly and filling process. Moreover, there is expected to be a large potential gradient across the electrode surface due to voltage dynamics. This would mean that the voltage applied by the

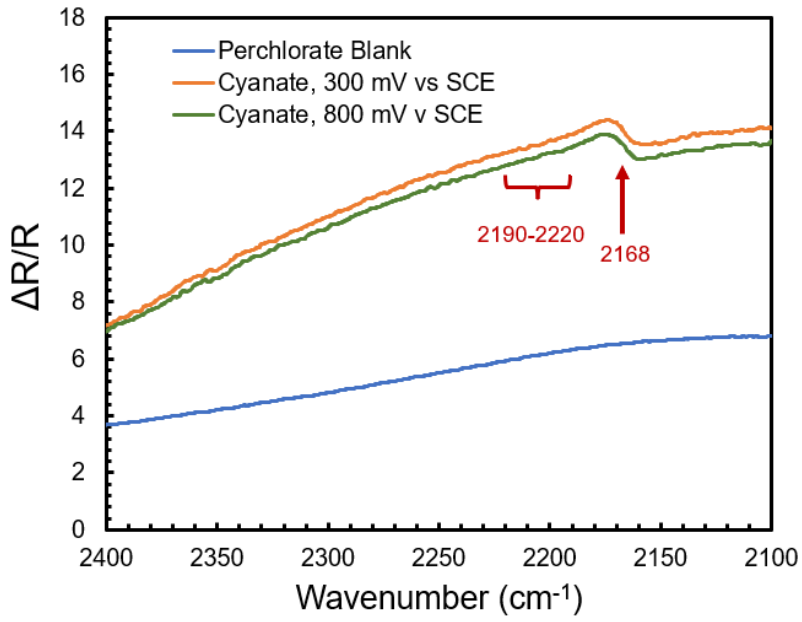

Figure 4.20 In situ PM-IRRAS spectra collected in an Ar-sparged 0.2 M sodium perchlorate solution (blank) and 0.2 M sodium perchlorate with 100 mM sodium cyanate with an Au-coated Ti electrode. The working electrode voltage was stepped positive and negative of the expected adsorption potential of around 350 mV vs SCE.

potentiostat does not necessarily match up to the true potential difference between the working and counter electrodes on the portion of the electrode surface being sampled. Thiourea and deposited azido-alkanethiols were also tried as probe systems and also did not show surface peaks in the PM-IRRAS spectra. The PM-IRRAS SEC-FC was then set aside in favor of other projects after we determined it was unlikely to produce useful experimental data within a workable timeframe.

Challenges of the PM-IRRAS SEC-FC Design

Our testing of the PM-IRRAS SEC-FC highlighted five major flaws in the design and implementation of the SEC-FC apparatus that prevented it from being used effectively to produce reliable data. As seen with the Cu-cyanate data, the apparatus could theoretically produce detectable spectroelectrochemical responses, but a number of practical issues were at play.

First, we had no reliable method for focusing the IR beam onto the surface. The IR beam is quite weak after passing through the polarizer and PEM, and so normal methods of determining IR laser position were not helpful. The visible-range guiding laser produced by the FT-IR to demonstrate beam position is no longer accurate once passed through the external PM-IRRAS optics, though it can be used for a first approximation of the beam position and focal point. However, once the beam passes into the cell, even that guide is no longer available. In general the positioning was done using total beam intensity at the detector as a guide. However we also found that the PPS surfaces of the cell can reflect the IR beam, making this positioning method untenable.

Second, we had no reliable method for determining the distance between the electrode and the window, and thus the thickness of the electrolyte layer. As seen in Figure C.6, trying to gauge the size of the electrode-window gap using resistance monitoring mainly served to demonstrate that hysteresis occurs, indicating some flex in the system. This meant that the position of the

micrometer was not necessarily an accurate indicator of the position of the electrode relative to the window. Eventually, we settled for a scheme by which the electrode was pushed all the way against the window, then retracted a set distance until solution flow was able to happen by hand operation the inlet syringe. This approach has myriad issues, including possible damage to the electrode, damage to the CaF_2 crystal window, and no absolute measurement of the gap size.

Third, the apparatus lacked the infrastructure to permit reproducible positioning. The external optics are all moved separately. This problem is a purely mechanical one which could be solved by building a rotating stage with adjustable, locking x, y, z, and rotational axes. However, such a setup was unavailable to us at the time when the apparatus was being built, and so we relied on hand positioning each optical component. This was incredibly time consuming and had very minimal reproducibility.

Fourth, air bubbles near the electrode surface could never be completely removed. While the general flow structure worked well, edges of electrode-window gap tended to form air bubbles during filling which were difficult to fully remove. The bubbles could be causing beam attenuation by providing a complex refractive environment and producing scattering. They could also be introducing dissolved oxygen into the otherwise N_2-sparged solution.

Lastly, while the electrode design had been intended to aid modularity, it actually vastly limited the available electrode materials and caused significant problems with electrode preparation. The intent had been to allow single-crystal electrodes to be attached to the apparatus and drawn backwards into the electrode sheath without either contacting the front surface or breaking a soldered bond. Moreover, it would allow different electrodes to be swapped in and out easily. However, our problems with the Ti-based electrodes served as a early indication of some the problems: imprecision and markings from the machining, difficulties in achieving surface

smoothness, and complications from deposition of materials that aren't suitable for machining, such as gold.

4.6: Conclusions

PM-IRRAS is an attractive technique for analysis of electrocatalytic surfaces, though its advantages are tempered with some major restrictions and technical complications. We designed and constructed *ex situ* and *in situ* apparatuses for conducting PM-IRRAS experiments. We were successful in collecting useful data with the *ex situ* tabletop module, which will see continuing use for the characterization of alkanethiol self-assembled monolayers and related systems where good sample reflectance is ensured and where important features are present under ambient conditions. The design of the SEC-FC addressed the needs of ambitious experimental goals. Its key innovation from previously published designs was the use of a novel working electrode assembly that permitted electrode modularity and prevented surface contact during use. While the PM-IRRAS SEC-FC accomplished many of its design goals and functioned perfectly from a mechanical perspective, this iteration of the design was found to be unfeasible for use as a robust spectroelectrochemical apparatus. Although some spectroelectrochemical data were collected, measurements were hampered by an array of fundamental problems which caused the project to be shelved. Thoughts on future directions for building a usable spectroelectrochemical cell are found in the following section.

4.7. Future Directions

Ex Situ Measurements

Despite the challenges encountered with the *in situ* PM-IRRAS SEC-FC, the ex situ PM-IRRAS TOM functions well and is expected to be quite useful into the near future as alkanethiol SAMs on gold and other metal surfaces continue to be an area of research in the group. PM-IRRAS is extraordinarily well-suited to this application, as attested by its presence in other literature reports. A few mechanical modifications to the TOM could improve ease of usability. The first would be the replacement of the dual lens tube with a small parabolic mirror to focus the beam into the detector. This is a standard feature of commercial optical layouts, and it is unclear in retrospect why we used lenses. In the absence the flow cell, the lenses are the only CaF_2 optics in the beam path and are therefore preventing detection of any bands below about 1200 cm^{-1}. Future operators of the TOM should also consider a large rotational stage can be acquired for the sample holder, focusing optics (lens tube or parabolic mirror), and detector. Again, this is a standard feature of commercial optical layouts which we forewent in favor of a more flexible (but finicky) set of optomechanics. While the TOM functions without it, such a stage would greatly simplify sample repositioning and make the TOM more broadly usable.

Future users could also design a simple electrochemical compression cell, accommodating an Au-sputtered Si wafer and using a spacer to control the gap size, to enable rudimentary *in situ* PM-IRRAS analysis of SAM electrochemical behavior without the substantial electrode positioning and flow infrastructure of the SEC-FC. A 60° beveled CaF_2 prism is probably still the best optical window for such a cell, and the set acquired for the SEC-FC could be repurposed.

In Situ Measurements

Future work on an *in situ* IR reflective spectroelectrochemical apparatus should carefully consider the minimum experimental goals and what technique is best equipped to meet those goals. PM-IRRAS was originally chosen with specific experiments in mind and is likely not the most appropriate choice for the majority of experiments with electrocatalytic systems. The need for a thin electrolyte layer on the scale of tens of microns is a major design and usage constraint, introducing problems with both the optical conditions and the electrochemical conditions of the experiment. In any case where an internal reflectance technique can be used, it would be the better choice—in general, unless it is necessary to use a single-crystal metal electrode (or one that is a macroscale chunk of metal for some essential reason) for the experiment, an internal reflectance technique should be preferred. As mentioned in Section 3.6, SEIRAS could be an excellent technique for *in situ* investigations of spectroelectrochemical responses in polymer layers.

While a full systematic redesign of the PM-IRRAS SEC-FC is beyond the scope of this dissertation, I will lay out some basic imperatives for any new design in the event that it becomes necessary. First, as mentioned above, the essential design constraints must be determined, and all other considerations should be secondary to achieving those design constraints. The SEC design presented here had several design constraints that may have been less crucial than anticipated, including encasement of the working electrode in a highly protective PPS and Teflon structure, which led to many problems in the end. Other designs have generally settled for a more minimal encasement of the non-working surfaces, such as with epoxy. Next, some reliable method is needed for achieving a consistent window-electrode gap distance. Our design avoided spacers in favor of something more adjustable, but incorporation of a ~10 micron spacer would vastly simplify electrode positioning. Finally, additional resources must be invested into external positioning

infrastructure for the cell, including at a minimum a 3-axis stage to hold the cell, and a rotational stage to allow the angle to be readily changed without needing to entirely reposition the external optics.

4.8. References

(1) Zaera, F. "New advances in the use of infrared absorption spectroscopy for the characterization of heterogeneous catalytic reactions," *Chemical Society Reviews* **2014**, *43*, 7624-7663. http://dx.doi.org/10.1039/C3CS60374A

(2) Bain, C. D. "Sum-frequency vibrational spectroscopy of the solid/liquid interface," *Journal of the Chemical Society, Faraday Transactions* **1995**, *91*, 1281-1296. http://dx.doi.org/10.1039/FT9959101281

(3) Tadjeddine, A.; Peremans, A. "Vibrational spectroscopy of the electrochemical interface by visible infrared sum-frequency generation," *Surface Science* **1996**, *368*, 377-383. http://dx.doi.org/https://doi.org/10.1016/S0039-6028(96)01079-5

(4) Pons, S.; Foley, J. K.; Russell, J.; Seversen, M. "Interfacial Infrared Vibrational Spectroscopy," In *Modern Aspects of Electrochemistry: Volume 17*; Bockris, J. O. M., Conway, B. E., White, R. E., Eds.; Springer US: Boston, MA, 1986, p 223-302.

(5) Zamlynny, V.; Lipkowski, J. "Quantitative SNIFTIRS and PM IRRAS of Organic Molecules at Electrode Surfaces," In *Advances in Electrochemical Science and Engineering* 2006, p 315-376.

(6) Pemberton, J. E.; Guy, A. L.; Sobocinski, R. L.; Tuschel, D. D.; Cross, N. A. "Surface enhanced Raman scattering in electrochemical systems: The complex roles of surface roughness," *Applied Surface Science* **1988**, *32*, 33-56. http://dx.doi.org/https://doi.org/10.1016/0169-4332(88)90072-4

(7) Tian, Z. Q. "Surface-enhanced Raman spectroscopy: advancements and applications," *Journal of Raman Spectroscopy* **2005**, *36*, 466-470. http://dx.doi.org/https://doi.org/10.1002/jrs.1378

(8) Wu, D.-Y.; Li, J.-F.; Ren, B.; Tian, Z.-Q. "Electrochemical surface-enhanced Raman spectroscopy of nanostructures," *Chemical Society Reviews* **2008**, *37*, 1025-1041. http://dx.doi.org/10.1039/B707872M

(9) Osawa, M. "In-situ Surface-Enhanced Infrared Spectroscopy of the Electrode/Solution Interface," In *Advances in Electrochemical Science and Engineering* 2006, p 269-314.

(10) Raval, R. "Probing the nature of molecular chemisorption using RAIRS," *Surface Science* **1995**, *331-333*, 1-10. http://dx.doi.org/https://doi.org/10.1016/0039-6028(95)00126-3

(11) Zaera, F.; Janssens, T. V. W.; Öfner, H. "Reflection absorption infrared spectroscopy and kinetic studies of the reactivity of ethylene on Pt(111) surfaces," *Surface Science* **1996**, *368*, 371-376. http://dx.doi.org/https://doi.org/10.1016/S0039-6028(96)01078-3

(12) Rodriguez, J. A.; Hanson, J. C.; Chupas, P. J.; Rodriguez, J. a.; Rodriguez, J. a.; Hanson, J. C.; Chupas, P. J. *In-Situ Characterization of Heterogeneous Catalysts*; John Wiley & Sons, Incorporated: Oxford, UNITED STATES, 2013.

(13) Wieckowski, A.; Korzeniewski, C.; Braunschweig, B.; Braunschweig, B. *Vibrational Spectroscopy at Electrified Interfaces*; John Wiley & Sons, Incorporated: Somerset, UNITED STATES, 2013.

(14) Brand, I. "Application of Polarization Modulation Infrared Reflection Absorption Spectrosocpy Under Electrochemical Control for Structural Studies of Biomimetic Assemblies," *Zeitschrift für Physikalische Chemie* **2016**, *230*, 133-183. http://dx.doi.org/doi:10.1515/zpch-2014-0657

(15) Buffeteau, T.; Desbat, B.; Turlet, J. M. "Polarization Modulation FT-IR Spectroscopy of Surfaces and Ultra-thin Films: Experimental Procedure and Quantitative Analysis," *Appl. Spectrosc.* **1991**, *45*, 380-389.

(16) Frey, B. L.; Corn, R. M.; Weibel, S. C. "Polarization-Modulation Approaches to Reflection–Absorption Spectroscopy," In *Handbook of Vibrational Spectroscopy* 2001.
(17) Richmond, W. N.; Faguy, P. W.; Jackson, R. S.; Weibel, S. C. "Comparison between Real-Time Polarization Modulation and Static Linear Polarization for in Situ Infrared Spectroscopy at Electrode Surfaces," *Analytical Chemistry* **1996**, *68*, 621-628. http://dx.doi.org/10.1021/ac950918m
(18) Tagliazucchi, M.; De Leo, L. P. M.; Cadranel, A.; Baraldo, L. M.; Völker, E.; Bonazzola, C.; Calvo, E. J.; Zamlynny, V. "PM IRRAS spectroelectrochemistry of layer-by-layer self-assembled polyelectrolyte multilayers," *Journal of Electroanalytical Chemistry* **2010**, *649*, 110-118. http://dx.doi.org/https://doi.org/10.1016/j.jelechem.2010.02.013
(19) Elzein, T.; Fahs, A.; Brogly, M.; Elhiri, A.; Lepoittevin, B.; Roger, P.; Planchot, V. "Adsorption of Alkanethiols on Gold Surfaces: PM-IRRAS Study of the Influence of Terminal Functionality on Alkyl Chain Orientation," *The Journal of Adhesion* **2013**, *89*, 416-432. http://dx.doi.org/10.1080/00218464.2013.757521
(20) Elzein, T.; Brogly, M.; Schultz, J. "Quantitative calculation of the orientation angles of adsorbed polyamides nanofilms," *Polymer* **2003**, *44*, 3649-3660. http://dx.doi.org/https://doi.org/10.1016/S0032-3861(03)00293-3
(21) Zamlynny, V.; Zawisza, I.; Lipkowski, J. "PM FTIRRAS Studies of Potential-Controlled Transformations of a Monolayer and a Bilayer of 4-Pentadecylpyridine, a Model Surfactant, Adsorbed on a Au(111) Electrode Surface," *Langmuir* **2003**, *19*, 132-145. http://dx.doi.org/10.1021/la026488u
(22) Pensa, E.; Vericat, C.; Grumelli, D.; Salvarezza, R. C.; Park, S. H.; Longo, G. S.; Szleifer, I.; Méndez De Leo, L. P. "New insight into the electrochemical desorption of alkanethiol SAMs on gold," *Phys Chem Chem Phys* **2012**, *14*, 12355-12367. http://dx.doi.org/10.1039/c2cp41291h
(23) Sang, L.; Mudalige, A.; Sigdel, A. K.; Giordano, A. J.; Marder, S. R.; Berry, J. J.; Pemberton, J. E. "PM-IRRAS Determination of Molecular Orientation of Phosphonic Acid Self-Assembled Monolayers on Indium Zinc Oxide," *Langmuir* **2015**, *31*, 5603-5613. http://dx.doi.org/10.1021/acs.langmuir.5b00129
(24) Álvarez, B.; Rodes, A.; Pérez, J. M.; Feliu, J. M.; Rodríguez, J. L.; Pastor, E. "Spectroscopic Study of the Nitric Oxide Adlayers Formed from Nitrous Acid Solutions on Palladium-Covered Platinum Single-Crystal Electrodes," *Langmuir* **2000**, *16*, 4695-4705. http://dx.doi.org/10.1021/la991473q
(25) Bae, I. T.; Barbour, R. L.; Scherson, D. A. "In Situ Fourier Transform Infrared Spectroscopic Studies of Nitrite Reduction on Platinum Electrodes in Perchloric Acid," *Analytical Chemistry* **1997**, *69*, 249-252. http://dx.doi.org/10.1021/ac960769n
(26) Roedel, E.; Urakawa, A.; Kureti, S.; Baiker, A. "On the local sensitivity of different IR techniques: Ba species relevant in NOx storage-reduction," *Physical Chemistry Chemical Physics* **2008**, *10*, 6190-6198. http://dx.doi.org/10.1039/B808529C
(27) Flaherty, D. W.; Berglund, S. P.; Mullins, C. B. "Selective decomposition of formic acid on molybdenum carbide: A new reaction pathway," *Journal of Catalysis* **2010**, *269*, 33-43. http://dx.doi.org/https://doi.org/10.1016/j.jcat.2009.10.012
(28) Dupont, C.; Loffreda, D.; Delbecq, F.; Santos Aires, F. J. C.; Ehret, E.; Jugnet, Y. "A High Pressure PM-IRRAS Study of CO and O2 Coadsorption and Reactivity on PtSn Alloy Surfaces," *The Journal of Physical Chemistry C* **2008**, *112*, 10862-10867. http://dx.doi.org/10.1021/jp802416f

(29) Faguy, P. W.; Fawcett, W. R. "Infrared Reflection-Absorption Spectroscopy of the Electrode/Electrolyte Solution Interface: Optical Considerations," *Appl. Spectrosc.* **1990**, *44*, 1309-1316.
(30) Iwasita, T.; Nart, F. C. "In situ infrared spectroscopy at electrochemical interfaces," *Progress in Surface Science* **1997**, *55*, 271-340. http://dx.doi.org/https://doi.org/10.1016/S0079-6816(97)00032-4
(31) Zamlynny, V. "The effect of a metal surface proximity on the Reflection Absorption Spectroscopy (RAS) signal," *Journal of Electroanalytical Chemistry* **2017**, *785*, 80-89. http://dx.doi.org/https://doi.org/10.1016/j.jelechem.2016.12.012
(32) Blatt, S.; Roscoe, S. G.; Zamlynny, V. "Effect of electrode position on features of electrochemical Polarization Modulation Infrared Reflection Absorption Spectroscopy (PM IRRAS)," *Journal of Electroanalytical Chemistry* **2010**, *649*, 102-109. http://dx.doi.org/https://doi.org/10.1016/j.jelechem.2010.02.012
(33) Collman, J. P.; Devaraj, N. K.; Chidsey, C. E. D. "'Clicking" Functionality onto Electrode Surfaces," *Langmuir* **2004**, *20*, 1051-1053. http://dx.doi.org/10.1021/la0362977
(34) Collman, J. P.; Devaraj, N. K.; Eberspacher, T. P. A.; Chidsey, C. E. D. "Mixed Azide-Terminated Monolayers: A Platform for Modifying Electrode Surfaces," *Langmuir* **2006**, *22*, 2457-2464. http://dx.doi.org/10.1021/la052947q
(35) Porter, M. D.; Bright, T. B.; Allara, D. L.; Chidsey, C. E. D. "Spontaneously organized molecular assemblies. 4. Structural characterization of n-alkyl thiol monolayers on gold by optical ellipsometry, infrared spectroscopy, and electrochemistry," *Journal of the American Chemical Society* **1987**, *109*, 3559-3568. http://dx.doi.org/10.1021/ja00246a011
(36) Yeon, H.; Wang, C.; Van Lehn, R. C.; Abbott, N. L. "Influence of Order within Nonpolar Monolayers on Hydrophobic Interactions," *Langmuir* **2017**, *33*, 4628-4637. http://dx.doi.org/10.1021/acs.langmuir.7b00226
(37) Fies, W. A.; Dugger, J. W.; Dick, J. E.; Wilder, L. M.; Browning, K. L.; Doucet, M.; Browning, J. F.; Webb, L. J. "Direct Measurement of Water Permeation in Submerged Alkyl Thiol Self-Assembled Monolayers on Gold Surfaces Revealed by Neutron Reflectometry," *Langmuir* **2019**, *35*, 5647-5662. http://dx.doi.org/10.1021/acs.langmuir.9b00541
(38) Vericat, C.; Vela, M. E.; Benitez, G.; Carro, P.; Salvarezza, R. C. "Self-assembled monolayers of thiols and dithiols on gold: new challenges for a well-known system," *Chemical Society Reviews* **2010**, *39*, 1805-1834. http://dx.doi.org/10.1039/B907301A
(39) Rajalingam, K.; Hallmann, L.; Strunskus, T.; Bashir, A.; Wöll, C.; Tuczek, F. "Self-assembled monolayers of benzylmercaptan and para-cyanobenzylmercaptan on gold: surface infrared spectroscopic characterization," *Physical Chemistry Chemical Physics* **2010**, *12*, 4390-4399. http://dx.doi.org/10.1039/B923628G
(40) Vericat, C.; Vela, M. E.; Benitez, G. A.; Gago, J. A. M.; Torrelles, X.; Salvarezza, R. C. "Surface characterization of sulfur and alkanethiol self-assembled monolayers on Au(111)," *Journal of Physics: Condensed Matter* **2006**, *18*, R867-R900. http://dx.doi.org/10.1088/0953-8984/18/48/r01
(41) Martínez, J.; Ortiz, A.; Ortiz, I. "State-of-the-art and perspectives of the catalytic and electrocatalytic reduction of aqueous nitrates," *Applied Catalysis B: Environmental* **2017**, *207*, 42-59. http://dx.doi.org/https://doi.org/10.1016/j.apcatb.2017.02.016
(42) Rahman, R. O. A.; Ibrahium, H. A.; Hung, Y.-T. "Liquid Radioactive Wastes Treatment: A Review," *Water* **2011**, *3*. http://dx.doi.org/10.3390/w3020551

(43) Duca, M.; Koper, M. T. M. "Powering denitrification: the perspectives of electrocatalytic nitrate reduction," *Energy & Environmental Science* **2012**, *5*, 9726-9742. http://dx.doi.org/10.1039/C2EE23062C
(44) de Vooys, A. C. A.; van Santen, R. A.; van Veen, J. A. R. "Electrocatalytic reduction of NO3− on palladium/copper electrodes," *Journal of Molecular Catalysis A: Chemical* **2000**, *154*, 203-215. http://dx.doi.org/https://doi.org/10.1016/S1381-1169(99)00375-1
(45) da Cunha, M. C. P. M.; Nart, F. C. "Reduction of Nitrite Ions on a Pt90Rh10 Electrode," *physica status solidi (a)* **2001**, *187*, 25-32. http://dx.doi.org/https://doi.org/10.1002/1521-396X(200109)187:1<25::AID-PSSA25>3.0.CO;2-#
(46) Duca, M.; Kightley, J.; Garbarino, S.; Guay, D. "The Art of Decoration: Rhodium-Modified Platinum Films with Preferential (100) Orientation as Electrocatalysts for Nitrate Reduction and Dimethyl Ether Oxidation," *The Journal of Physical Chemistry C* **2017**, *121*, 15233-15247. http://dx.doi.org/10.1021/acs.jpcc.7b04332
(47) Duca, M.; Sacré, N.; Wang, A.; Garbarino, S.; Guay, D. "Enhanced electrocatalytic nitrate reduction by preferentially-oriented (100) PtRh and PtIr alloys: the hidden treasures of the 'miscibility gap'," *Applied Catalysis B: Environmental* **2018**, *221*, 86-96. http://dx.doi.org/https://doi.org/10.1016/j.apcatb.2017.08.081
(48) Bockris, J. O. M.; Yang, B. "A thin-layer flow cell for in-situ infrared reflection—absorption spectroscopic measurements of the electrode/electrolyte interphase," *Journal of Electroanalytical Chemistry and Interfacial Electrochemistry* **1988**, *252*, 209-214. http://dx.doi.org/https://doi.org/10.1016/0022-0728(88)85083-6
(49) Meier, D. M.; Urakawa, A.; Mäder, R.; Baiker, A. "Design and performance of a flow-through polarization-modulation infrared reflection-absorption spectroscopy cell for time-resolved simultaneous surface and liquid phase detection under concentration and temperature perturbations," *Review of Scientific Instruments* **2009**, *80*, 094101. http://dx.doi.org/10.1063/1.3213605
(50) Nichols, R. J.; Bewick, A. "SNIFTIRS with a flow cell: the identification of the reaction intermediates in methanol oxidation at Pt anodes," *Electrochimica Acta* **1988**, *33*, 1691-1694. http://dx.doi.org/https://doi.org/10.1016/0013-4686(88)80244-5
(51) Roth, J. D.; Weaver, M. J. "The electrooxidation of carbon monoxide on platinum as examined by surface infrared spectroscopy under forced hydrodynamic conditions," *Journal of Electroanalytical Chemistry and Interfacial Electrochemistry* **1991**, *307*, 119-137. http://dx.doi.org/https://doi.org/10.1016/0022-0728(91)85543-X
(52) Tadayyoni, M. A.; Weaver, M. J. "Adsorption and electrooxidation of carbon monoxide at the gold-aqueous interface studied by surface-enhanced Raman spectroscopy," *Langmuir* **1986**, *2*, 179-183. http://dx.doi.org/10.1021/la00068a012
(53) Nakamura, M.; Shibutani, K.; Hoshi, N. "In-situ Flow-Cell IRAS Observation of Intermediates during Methanol Oxidation on Low-Index Platinum Surfaces," *ChemPhysChem* **2007**, *8*, 1846-1849. http://dx.doi.org/https://doi.org/10.1002/cphc.200700244
(54) Brandt, K.; Vogler, E.; Parthenopoulos, M.; Wandelt, K. "In situ and ex situ FTIR characterization of a cyanate adlayer on Cu (1 1 1)," *Journal of Electroanalytical Chemistry* **2004**, *570*, 47-53.
(55) Bron, M.; Holze, R. "Cyanate and thiocyanate adsorption at copper and gold electrodes as probed by in situ infrared and surface-enhanced Raman spectroscopy," *Journal of Electroanalytical Chemistry* **1995**, *385*, 105-113.

(56) Cheuquepán, W.; Rodes, A.; Orts, J. M.; Feliu, J. M. "Spectroelectrochemical detection of specifically adsorbed cyanurate anions at gold electrodes with (111) orientation in contact with cyanate and cyanuric acid neutral solutions," *Journal of Electroanalytical Chemistry* **2017**, *800*, 167-175.
(57) Corrigan, D. S.; Weaver, M. J. "Adsorption and oxidation of benzoic acid, benzoate, and cyanate at gold and platinum electrodes as probed by potential-difference infrared spectroscopy," *Langmuir* **1988**, *4*, 599-606.
(58) Kim, D.; Son, K.; Sung, D.; Kim, Y.; Chung, W. "Effect of added ethanol in ethylene glycol–NaCl electrolyte on titanium electropolishing," *Corrosion science* **2015**, *98*, 494-499.

5. Conclusions and Recommendations for Future Study

5.1. Conclusions

The work presented in this dissertation aimed to advance our understanding of electrocatalytic materials through fundamental spectroscopic and microscopic analysis of model systems from which we can draw insight about how to rationally design more complex catalytic systems. Our primary focus was the electrochemical reduction of CO_2 to fuels and other value-added products, which could prove to be a breakthrough technology for decarbonization of the energy economy in the coming decades. In Chapter 1 we explored the state of the field for the CO_2RR, including challenges associated with gas-fed CO_2 electrolyzers needed for industrial scaling, finding that there is much room for improvement in understanding and controlling the microenvironment of CO_2 catalysis. We proposed that further exploration of heterogenized molecular catalyst systems—including polymer-catalyst composites such as CoPc-P4VP—could yield breakthroughs in producing electrolyzers that combine high catalytic throughput, a strong selectivity for desirable carbon products, and sufficient stability for long-term use. We then highlighted previous work by our group on the CoPc-P4VP system and noted areas in which characterization of the polymer-catalyst composite layer structure was needed, specifically CoPc aggregation and the fractional protonation of the P4VP in buffered electrolyte solutions.

In Chapter 2 we investigated how P4VP, as a polymer capable of coordinating axially to CoPc, can serve to disaggregate the catalyst in the deposition solution and in the deposited layer.

We found that P4VP is well-suited to creating a disaggregated solid solution of CoPc. Based on our findings, we describe this effect in two phases: 1) P4VP axially coordinates to CoPc in the deposition solution, improving overall solvation of the initially aggregated CoPc; and 2) P4VP holds the monomeric CoPc apart during layer deposition through a combination of axial coordination and π-stacking interactions, preventing reaggregation. We also found that Nafion, a ubiquitous catalyst binding polymer in the heterogenous electrochemical literature, had little or no efficacy for disaggregating CoPc. Our primary tool in this investigation was UV-Vis spectroscopy, which we used to evaluate the relative monomerization of CoPc in both the deposition solution and the deposited layer. Scanning electron microscopy was used to directly image CoPc aggregates in support of the UV-Vis results. Finally, electrocatalytic results confirmed that CoPc-P4VP layers were more active and selective for the CO_2RR than CoPc-Nafion layers, which we partially attribute to the variation in disaggregation. This work is of critical importance for the design of CO_2 electrolyzers using CoPc and similar molecular catalysts, as it demonstrates that the choice of polymer greatly impacts the dispersion of the catalyst, and thus the maximum achievable turnover frequency of the catalyst.

In Chapter 3 we returned to the CoPc-P4VP system to understand how the electrolyte buffer solution interacts with the polymer. In particular, we explored how variations in the composition of the bulk solution are reflected in the fractional protonation of the polymer's pyridyl moieties. The fractional protonation serves as an indicator of layer hydration, but also impacts the functionality of the proton relay delivering protons to the catalytic sites. The electrocatalytic response to changing pH and buffer concentration was correlated with a direct observation of protonation in the P4VP layers using *ex situ* infrared spectroscopy. As anticipated, we found that decreasing the pH of the bulk solution increased the protonation of the P4VP layer, which

correlated with an increasing activity for hydrogen reduction, and thus a decreased selectivity for the CO_2RR. Less expected was the observation that increasing the buffer electrolyte concentration caused a proportional increase in the protonation of the layer, and likewise a higher activity for the HER. We understand this as the effect of greater equilibrium partitioning of the electrolyte ions into the polymer layer, which in turn increases ability of the layer to be protonated because of the higher availability of anions for charge balancing. We also expect that higher protonation correlates with a higher level of layer hydration. These results may be especially impactful for the design of gas-fed electrolyzers, where maintenance of the essential triple phase junction requires careful control of hydration and a rapid but controlled delivery of protons.

In Chapter 4 we explored the application of the surface-selective PM-IRRAS technique to electrocatalytic systems. In a two-phase process, we designed and built both a tabletop optical module for *ex situ* PM-IRRAS analysis of surface structures and a spectroelectrochemical flow cell for *in situ* detection of electrocatalytic species. The TOM was used to investigate the packing quality of alkanethiol self-assembled monolayers. A number of functional goals and technical restrictions informed our design of the PM-IRRAS SEC-FC. The finalized design was constructed and tested but suffered from a number of flaws that greatly hindered its practical usability. However, the design process and failure modes were informative and may serve as a guide to future work in this area within our research group.

5.2. Recommendations for Future Study

Recommendations of continuing work in various projects have been outlined in previous sections of this dissertation, so this section will propose some more speculative work. To date, researchers have only scratched the surface of work to implement polymer-catalyst composite

materials in gas-fed CO_2 electrolyzers. The design space is wide open, with an incredible array of tunable features that could be used to carefully control layer hydration, substrate and product transport, conductivity, catalyst electronic structure, and more. Work by Sargent, Sinton, and coworkers mentioned in Chapter 1.2 is a window into what the future could hold for polymer-catalyst architectures.[1] Strategies to introduce multiple functional domains into the polymer seem particularly promising, and polymer chemistry is certainly up to the challenge of building intricate block copolymers for this purpose.[2-4] P4VP and derivatives have a role to play in this vision, as work in our group has demonstrated its efficacy for improving multiple aspects of catalysis. Copolymerization of P4VP with a CO_2 transport polymer[5-8] would be one obvious route for investigation. Copolymerization or blend deposition with a more conductive polymer could also be fruitful, as P4VP is currently limited as a catalyst composite material by its dependence on codeposited carbon black or nanotubes.[9]

However, more complex catalyst materials bring their own challenges, and must continue to be guided by fundamental studies that probe the underlying reasons why particular systems are or are not effective. *Ex situ* and *in situ* spectroscopic studies continue to play a major role, both to characterize structural features and to correlate mechanistic features to electrochemical results.[10,11] My investigations in Chapters 2 and 3 demonstrate the types of fundamental spectroscopic studies of model systems where the results can directly inform understanding of the more complex systems that are difficult to probe directly. For GDE systems it is especially important to understand the extent of hydration and ion transport in the layer, as these determine whether the triple phase boundary is correctly situated in the catalyst layer. Direct detection of anion bands in the layer would provide a spectroscopic handle for hydration through the proxy of simultaneous ion intercalation. In situ X-ray absorbance spectroscopy (XAS) studies would also be valuable to probe

how different conditions and catalyst layer compositions influence the electronic structure of the molecular catalyst metal centers. XAS could also provide information about the dispersion of CoPc or other molecular catalysts in the composite layer.[12]

Eventually, *in situ* infrared techniques could also be useful for detecting and characterizing reaction intermediates such as CO_2 or CO adducts on metal centers within the polymer composite layer. This would provide information both about the mechanism (the detection of an adduct could indicate a long residence time on the metal site and thus confirm electrochemical identification of a rate-determining step) and about transport (variations in the intensity of adduct peaks could provide information about how different conditions alter the diffusion distance of CO_2 into the layer).

Overall, there is still a tremendous amount of room to achieve critical breakthroughs in CO_2 electrolyzer technologies, and more resources should be supplied to both fundamental and applied research in this field. Decarbonization of the energy system must be achieved in the next few decades, and CO_2 reduction has the potential to serve as a key method for turning sequestered carbon emissions into something of value. Much more work is needed to reach that goal in practical and economical systems, but the results of this dissertation contribute some of the groundwork for the future of carbon recycling.

5.3. References

(1) Arquer, F. P. G. d.; Dinh, C.-T.; Ozden, A.; Wicks, J.; McCallum, C.; Kirmani, A. R.; Nam, D.-H.; Gabardo, C.; Seifitokaldani, A.; Wang, X.; Li, Y. C.; Li, F.; Edwards, J.; Richter, L. J.; Thorpe, S. J.; Sinton, D.; Sargent, E. H. "CO2 electrolysis to multicarbon products at activities greater than 1 A cm," *Science* **2020**, *367*, 661-666. http://dx.doi.org/doi:10.1126/science.aay4217

(2) Polymeropoulos, G.; Zapsas, G.; Ntetsikas, K.; Bilalis, P.; Gnanou, Y.; Hadjichristidis, N. "50th Anniversary perspective: polymers with complex architectures," *Macromolecules* **2017**, *50*, 1253-1290.

(3) Lutz, J. P.; Hannigan, M. D.; McNeil, A. J. "Polymers synthesized via catalyst-transfer polymerization and their applications," *Coordination Chemistry Reviews* **2018**, *376*, 225-247.

(4) Moon, J. D.; Freeman, B. D.; Hawker, C. J.; Segalman, R. A.; ACS Publications: 2020; Vol. 53, p 5649-5654.

(5) Bazargani, Z.; Sabzi, F. "Chapter 25 - Gas Transport Through Interpenetrating Polymer Networks," In *Transport Properties of Polymeric Membranes*; Thomas, S., Wilson, R., S, A. K., George, S. C., Eds.; Elsevier: 2018, p 533-546.

(6) Wang, S.; Li, X.; Wu, H.; Tian, Z.; Xin, Q.; He, G.; Peng, D.; Chen, S.; Yin, Y.; Jiang, Z. "Advances in high permeability polymer-based membrane materials for CO 2 separations," *Energy & Environmental Science* **2016**, *9*, 1863-1890.

(7) Deng, L.; Kim, T.-J.; Hägg, M.-B. "Facilitated transport of CO2 in novel PVAm/PVA blend membrane," *Journal of Membrane Science* **2009**, *340*, 154-163.

(8) Matsuyama, H.; Terada, A.; Nakagawara, T.; Kitamura, Y.; Teramoto, M. "Facilitated transport of CO2 through polyethylenimine/poly (vinyl alcohol) blend membrane," *Journal of Membrane Science* **1999**, *163*, 221-227.

(9) Soucy, T. L.; Liu, Y.; Eisenberg, J. B.; McCrory, C. C. L. "Enhancing the Electrochemical CO2 Reduction Activity of Polymer-Encapsulated Cobalt Phthalocyanine Films by Modulating the Loading of Catalysts, Polymers, and Carbon Supports. ," *ACS Applied Energy Materials* **2021**, *ASAP*. http://dx.doi.org/10.1021/acsaem.1c02689

(10) Zaera, F. "New advances in the use of infrared absorption spectroscopy for the characterization of heterogeneous catalytic reactions," *Chemical Society Reviews* **2014**, *43*, 7624-7663. http://dx.doi.org/10.1039/C3CS60374A

(11) Hunger, M.; Weitkamp, J. "In situ IR, NMR, EPR, and UV/Vis spectroscopy: Tools for new insight into the mechanisms of heterogeneous catalysis," *Angewandte Chemie International Edition* **2001**, *40*, 2954-2971.

(12) Corbin, N.; Zeng, J.; Williams, K.; Manthiram, K. "Heterogeneous molecular catalysts for electrocatalytic CO2 reduction," *Nano Research* **2019**, *12*, 2093-2125. http://dx.doi.org/10.1007/s12274-019-2403-y

Appendix A. Supplementary Information for Chapter 2

Supplementary Tables for Chapter 2

Sample	CoPc / M	Peak Monomer Abs.
CoPc/DMF	2×10^{-5}	0.43 ± 0.05
	1×10^{-5}	0.37 ± 0.04
	5×10^{-6}	0.33 ± 0.04
	2×10^{-6}	0.15 ± 0.02
	1×10^{-6}	$0.07_5 \pm 0.01_3$
	5×10^{-7}	0.036 ± 0.005
	0	0.002 ± 0.001
CoPc/DMF with 1% w/v of P4VP	2×10^{-5}	0.96 ± 0.09
	1×10^{-5}	0.61 ± 0.05
	5×10^{-6}	0.34 ± 0.03
	2×10^{-6}	0.13 ± 0.01
	1×10^{-6}	0.07 ± 0.01
	5×10^{-7}	0.034 ± 0.004
	0	0.002 ± 0.000
CoPc/DMF with 1% w/v of P4CS	2×10^{-5}	0.6 ± 0.1
	1×10^{-5}	0.48 ± 0.06
	5×10^{-6}	0.29 ± 0.06
	2×10^{-6}	0.11 ± 0.01
	1×10^{-6}	0.06 ± 0.01
	5×10^{-7}	0.022 ± 0.005
	0	0.003 ± 0.001

Table A.1. Mean peak absorbances measured for CoPc and CoPc-polymer deposition solutions in DMF. Columns 1-2 designate the type of sample and the analytical concentration of CoPc in units of M. Column 3 details the baseline-corrected CoPc monomer Q-band peak absorbance as an average across seven independently prepared samples. Errors the are first standard deviation of the measured peak absorbances.

Sample	CoPc / M	Peak Monomer Abs.
CoPc/py/DMF	2×10^{-5}	1.46 ± 0.02
	1×10^{-5}	0.90 ± 0.02
	5×10^{-6}	0.456 ± 0.004
	2×10^{-6}	0.187 ± 0.009
	1×10^{-6}	0.094 ± 0.004
	5×10^{-7}	0.048 ± 0.003
	0	0.001 ± 0.000
CoPc/py/DMF with 1% w/v of P4VP	2×10^{-5}	1.42 ± 0.04
	1×10^{-5}	0.09 ± 0.05
	5×10^{-6}	0.45 ± 0.02
	2×10^{-6}	0.19 ± 0.01
	1×10^{-6}	0.094 ± 0.004
	5×10^{-7}	0.047 ± 0.003
	0	0.002 ± 0.001
CoPc/py/DMF with 1% w/v of P4CS	2×10^{-5}	1.42 ± 0.03
	1×10^{-5}	0.83 ± 0.05
	5×10^{-6}	0.40 ± 0.03
	2×10^{-6}	0.17 ± 0.01
	1×10^{-6}	0.084 ± 0.006
	5×10^{-7}	0.044 ± 0.003
	0	0.005 ± 0.002

Table A.2 Mean peak absorbances measured for CoPc and CoPc-polymer deposition solutions in 95% DMF, 5% pyridine. Columns 1-2 designate the type of sample and the analytical concentration of CoPc in units of M. Column 3 details the baseline-corrected CoPc monomer Q-band peak absorbance as an average across three independently prepared samples. Errors the are first standard deviation of the measured peak absorbances.

Sample	CoPc / M	Peak Monomer Abs.
CoPc/mixed	2×10^{-5}	0.24 ± 0.01
	1×10^{-5}	0.19 ± 0.02
	5×10^{-6}	0.16 ± 0.02
	2×10^{-6}	0.09_5 ± 0.02
	1×10^{-6}	0.055 ± 0.009
	5×10^{-7}	0.030 ± 0.004
	0	0.000 ± 0.000
CoPc/mixed with 1% w/v of P4VP	2×10^{-5}	0.43 ± 0.04
	1×10^{-5}	0.32 ± 0.03
	5×10^{-6}	0.203 ± 0.007
	2×10^{-6}	0.11 ± 0.01
	1×10^{-6}	0.06 ± 0.01
	5×10^{-7}	0.034 ± 0.006
	0	0.001 ± 0.000
CoPc/mixed with 1% w/v of Nafion	2×10^{-5}	0.28 ± 0.02
	1×10^{-5}	0.25 ± 0.02
	5×10^{-6}	0.23_5 ± 0.05
	2×10^{-6}	0.13 ± 0.01_5
	1×10^{-6}	0.07 ± 0.02
	5×10^{-7}	0.034 ± 0.007
	0	0.005 ± 0.001

Table A.3 Mean peak absorbances measured for CoPc and CoPc-polymer deposition solutions in mixed solvent. For CoPc and CoPc-P4VP, the mixed solvent had a total composition of 80% DMF, 15.6% 2-propanol, 4% water, and 0.4% methanol. For CoPc-Nafion, the mixed solvent had a total composition of 80% DMF and 20% Nafion solvent as supplied by Sigma Aldrich. Columns 1-2 designate the type of sample and the analytical concentration of CoPc in units of M. Column 3 details the baseline-corrected CoPc monomer Q-band peak absorbance as an average across five independently prepared samples. Errors the are first standard deviation of the measured peak absorbances.

Sample	CoPc / M	Peak Monomer Abs.
CoPc/py/mixed	2×10^{-5}	1.53 ± 0.08
	1×10^{-5}	1.0 ± 0.1
	5×10^{-6}	0.51 ± 0.06
	2×10^{-6}	0.21 ± 0.03
	1×10^{-6}	$0.11 \pm 0.01_5$
	5×10^{-7}	0.054 ± 0.008
	0	0.001 ± 0.000
CoPc/py/mixed with 1% w/v of P4VP	2×10^{-5}	1.51 ± 0.09
	1×10^{-5}	1.0 ± 0.1
	5×10^{-6}	$0.51 \pm 0.06_5$
	2×10^{-6}	0.21 ± 0.03
	1×10^{-6}	$0.10_5 \pm 0.02$
	5×10^{-7}	0.054 ± 0.008
	0	0.001 ± 0.000
CoPc/py/mixed with 1% w/v of Nafion	2×10^{-5}	$1.52_5 \pm 0.09$
	1×10^{-5}	$1.1 \pm 0.1_5$
	5×10^{-6}	0.61 ± 0.08
	2×10^{-6}	0.25 ± 0.03
	1×10^{-6}	0.13 ± 0.02
	5×10^{-7}	0.065 ± 0.008
	0	0.000 ± 0.000

Table A.4 Mean peak absorbances measured for CoPc and CoPc-polymer deposition solutions in mixed solvent with pyridine. For CoPc and CoPc-P4VP, the mixed solvent had a total composition of 75% DMF, 5% pyridine, 15.6% 2-propanol, 4% water, and 0.4% methanol. For CoPc-Nafion, the mixed solvent had a total composition of 75% DMF, 5% pyridine, and 20% Nafion solvent as supplied by Sigma Aldrich. Columns 1-2 designate the type of sample and the analytical concentration of CoPc in units of M. Column 3 details the baseline-corrected CoPc monomer Q-band peak absorbance as an average across three independently prepared samples. Errors the are first standard deviation of the measured peak absorbances.

Deposition Solution CoPc Concentration / M	CoPc Loading in Deposited Layer / mol/cm^2
2×10^{-5}	6.2×10^{-11}
1×10^{-5}	3.1×10^{-11}
5×10^{-6}	1.6×10^{-11}
2×10^{-6}	6.2×10^{-12}

Table A.5 CoPc loadings for the diffuse reflectance samples are presented in terms of moles of CoPc per cm^2 of sample surface. Because each sample slide was of equal area (1 inch × 1 inch) and had an equal aliquot of solution drop cast onto it (200 µL), the loading for each sample is directly proportional to the deposition solution concentration. The latter quantity has been used to identify the CoPc loading in the main text to ease comparison between the solution-phase transmission UV-Vis results and the solid-phase diffuse reflectance results, and this table has been included for clarity.

		Peak Monomer Absorbance / F(R)				
Sample	Dep. Soln. CoPc Conc. / M	Mean	1st Qu.	Median	2nd Qu.	IQR
CoPc	2×10^{-5} M	3.6×10^{-4}	9.0×10^{-5}	1.4×10^{-4}	3.1×10^{-4}	2.2×10^{-4}
	1×10^{-5} M	8.3×10^{-5}	5.9×10^{-5}	7.6×10^{-5}	9.3×10^{-5}	3.3×10^{-5}
	5×10^{-6} M	5.4×10^{-5}	2.6×10^{-5}	4.1×10^{-5}	7.0×10^{-5}	4.4×10^{-5}
	2×10^{-6} M	5.1×10^{-5}	3.6×10^{-5}	4.3×10^{-5}	5.2×10^{-5}	1.7×10^{-5}
	0	1.4×10^{-5}	4.0×10^{-6}	8.2×10^{-6}	2.4×10^{-5}	2.0×10^{-5}
CoPc-P4VP	2×10^{-5} M	0.019	0.0055	0.012	0.035	0.029
	1×10^{-5} M	0.0056	0.0019	0.0041	0.0070	0.0051
	5×10^{-6} M	0.0021	9.8×10^{-4}	0.0018	0.0026	0.0016
	2×10^{-6} M	4.7×10^{-4}	2.1×10^{-4}	3.5×10^{-4}	6.3×10^{-4}	4.2×10^{-4}
	0	2.5×10^{-5}	2.0×10^{-5}	2.7×10^{-5}	2.9×10^{-5}	8.9×10^{-6}
CoPc-P4CS	2×10^{-5} M	0.0036	0.0014	0.0022	0.0050	0.0036
	1×10^{-5} M	6.3×10^{-4}	2.5×10^{-4}	5.1×10^{-4}	9.0×10^{-4}	6.5×10^{-4}
	5×10^{-6} M	3.8×10^{-4}	8.6×10^{-5}	1.6×10^{-4}	4.1×10^{-4}	3.3×10^{-4}
	2×10^{-6} M	9.4×10^{-5}	4.1×10^{-5}	9.5×10^{-5}	1.2×10^{-4}	7.5×10^{-5}
	0	2.3×10^{-5}	1.0×10^{-5}	1.7×10^{-5}	3.6×10^{-5}	2.6×10^{-5}
CoPc-Nafion	2×10^{-5} M	4.5×10^{-4}	7.5×10^{-5}	2.1×10^{-4}	5.7×10^{-4}	4.9×10^{-4}
	1×10^{-5} M	5.4×10^{-5}	2.3×10^{-5}	4.1×10^{-5}	7.6×10^{-5}	5.3×10^{-5}
	5×10^{-6} M	6.2×10^{-5}	2.3×10^{-5}	4.5×10^{-5}	9.1×10^{-5}	6.8×10^{-5}
	2×10^{-6} M	4.2×10^{-5}	2.4×10^{-5}	3.5×10^{-5}	5.5×10^{-5}	3.1×10^{-5}
	0	2.0×10^{-5}	1.2×10^{-5}	1.6×10^{-5}	2.6×10^{-5}	1.4×10^{-5}

Table A.6 Statistical data are presented for diffuse reflectance UV-Vis measurements of deposited layers. The values correspond to the box-and-whiskers plots presented in Figure 2.6a and Figure A.6. Quartile and median values were determined using OriginLab.

		Peak Monomer Absorbance / F(R)				
Sample	Dep. Soln. CoPc Conc. / M	Mean	1st Qu.	Median	2nd Qu.	IQR
CoPc(py)	2×10^{-5} M	2.4×10^{-4}	7.8×10^{-5}	1.0×10^{-4}	3.0×10^{-4}	2.2×10^{-4}
	1×10^{-5} M	1.6×10^{-4}	1.0×10^{-4}	1.3×10^{-4}	2.0×10^{-4}	1.0×10^{-4}
	5×10^{-6} M	9.1×10^{-5}	2.7×10^{-5}	3.6×10^{-5}	1.1×10^{-4}	7.9×10^{-5}
	2×10^{-6} M	3.7×10^{-5}	1.0×10^{-5}	1.6×10^{-5}	3.2×10^{-5}	2.1×10^{-5}
	0*	1.4×10^{-5}	4.0×10^{-6}	8.2×10^{-6}	2.4×10^{-5}	2.0×10^{-5}
CoPc(py)-P4VP	2×10^{-5} M	0.026	0.0045	0.012	0.045	0.040
	1×10^{-5} M	0.013	0.0036	0.0069	0.018	0.014
	5×10^{-6} M	0.0021	5.8×10^{-4}	0.0015	0.0023	0.0017
	2×10^{-6} M	6.6×10^{-4}	7.7×10^{-5}	2.0×10^{-4}	7.1×10^{-4}	6.3×10^{-4}
	0*	2.5×10^{-5}	2.0×10^{-5}	2.7×10^{-5}	2.9×10^{-5}	8.9×10^{-6}
CoPc(py)-P4CS	2×10^{-5} M	0.016	0.0043	0.0093	0.020	0.016
	1×10^{-5} M	0.0052	0.0012	0.0045	0.0071	0.0049
	5×10^{-6} M	7.6×10^{-4}	1.8×10^{-4}	4.5×10^{-4}	0.0010	8.2×10^{-4}
	2×10^{-6} M	1.4×10^{-4}	3.7×10^{-5}	7.5×10^{-5}	1.6×10^{-4}	1.3×10^{-4}
	0*	2.3×10^{-5}	1.0×10^{-5}	1.7×10^{-5}	3.6×10^{-5}	2.6×10^{-5}
CoPc(py)-Nafion	2×10^{-5} M	5.7×10^{-4}	1.4×10^{-4}	4.0×10^{-4}	7.0×10^{-4}	5.5×10^{-4}
	1×10^{-5} M	1.1×10^{-4}	4.8×10^{-5}	6.3×10^{-5}	1.2×10^{-4}	7.3×10^{-5}
	5×10^{-6} M	3.8×10^{-5}	2.8×10^{-5}	3.6×10^{-5}	4.1×10^{-5}	1.3×10^{-5}
	2×10^{-6} M	3.8×10^{-5}	2.6×10^{-5}	3.7×10^{-5}	4.9×10^{-5}	2.3×10^{-5}
	0*	2.0×10^{-5}	1.2×10^{-5}	1.6×10^{-5}	2.6×10^{-5}	1.4×10^{-5}

Table A.7 Statistical data are presented for diffuse reflectance UV-Vis measurements of deposited layers. The values correspond to the box-and-whiskers plots presented in Figure 2.6b and Figure A.7. Quartile and median values were determined using OriginLab.

	CoPc	CoPc(py)	CoPc-P4VP	CoPc(py)-P4VP	CoPc-P4CS	CoPc(py)-P4CS	CoPc-Nafion	CoPc(py)-Nafion
A	23	0	10	0	9	0	68	6
B	12	0	6	0	14	0	45	32
C	13	5	6	0	7	2	50	1
Avg	**16.00**	**1.67**	**7.33**	**0.00**	**10.00**	**0.67**	**54.33**	**13.00**

Table A.8 CoPc aggregate particle counts are presented for each of three independently prepared samples for each deposition condition, along the average count. All samples had an area of 1 cm × 1 cm onto which was drop cast 20.0 µL of a 2 x 10^{-5} M CoPc or CoPc(py) solution, resulting in a constant CoPc loading of 4 × 10^{-10} mol/cm^2.

	$\| j \|$ / mA cm^{-2}	$\pm \| j \|$ / mA cm^{-2}
CoPc-Nafion	0.56	0.08
CoPc-P4VP	1.56	0.12
CoPc(py)-Nafion	0.81	0.02
CoPc(py)-P4VP	1.65	0.37

Table A.9 Electrochemical activity values for conditions shown in Figure 2.9 are presented in terms of absolute current per unit area. Experiments were performed as described in the Rotating Disk Electrode Chronoamperometry portion of the Methods section.

	Q / C	± Q / C	FE_{CO} / %	± FE_{CO} / %	FE_{H2} / %	± FE_{H2} / %
CoPc-Nafion	0.21	0.04	67.7	11.8	25.1	1.4
CoPc-P4VP	0.92	0.09	89.6	1.1	4.0	0.7
CoPc(py)-Nafion	0.39	0.18	52.1	1.4	41.6	4.8
CoPc(py)-P4VP	1.07	0.28	86.8	1.5	5.3	1.6

Table A.10 Controlled potential electrolysis values for conditions shown in Figure 2.9 are presented in terms of charge passed (Q) and Faradaic efficiency for CO and H_2. Experiments were performed as described in the Controlled Potential Electrolysis portion of the Methods section.

Supplementary Figures for Chapter 2

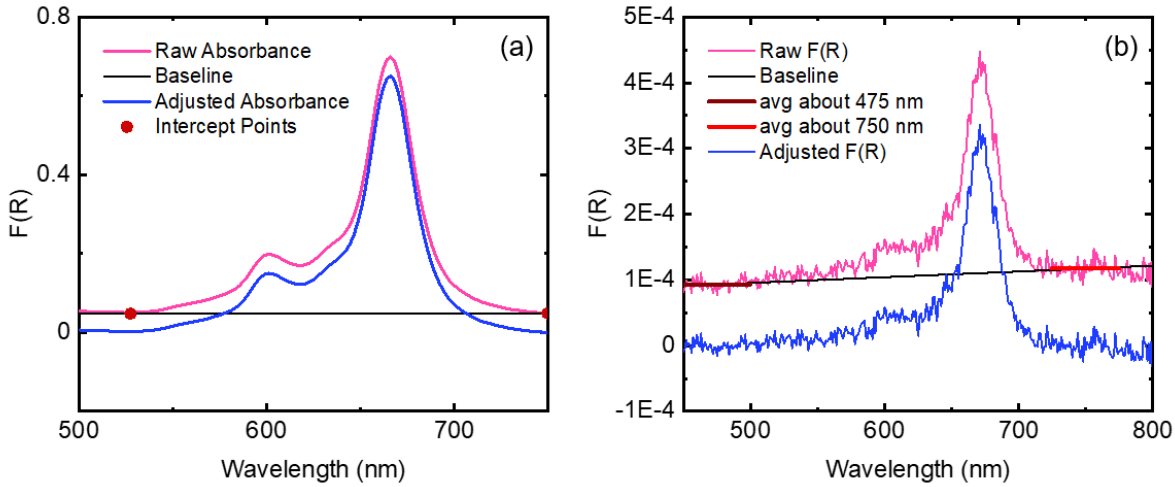

Figure A.1 a) Example of a linear background subtraction for transmission data. Using Microsoft Excel, a line was drawn that intersected the UV-Vis spectrum at 750 nm on one end, and at the local minimum between 450 and 550 nm at the other end. The area under this line was subtracted from the area under the spectrum, and the maximum absorbance of the monomer peak was determined. b) Example of a linear background subtraction for diffuse reflectance data. Using Microsoft Excel, a line was drawn that intersected the average F(R) about 475 nm on one end, and the average F(R) about 750 nm at the other end. The area under this line was subtracted from the area under the spectrum, and the maximum absorbance of the monomer peak was determined.

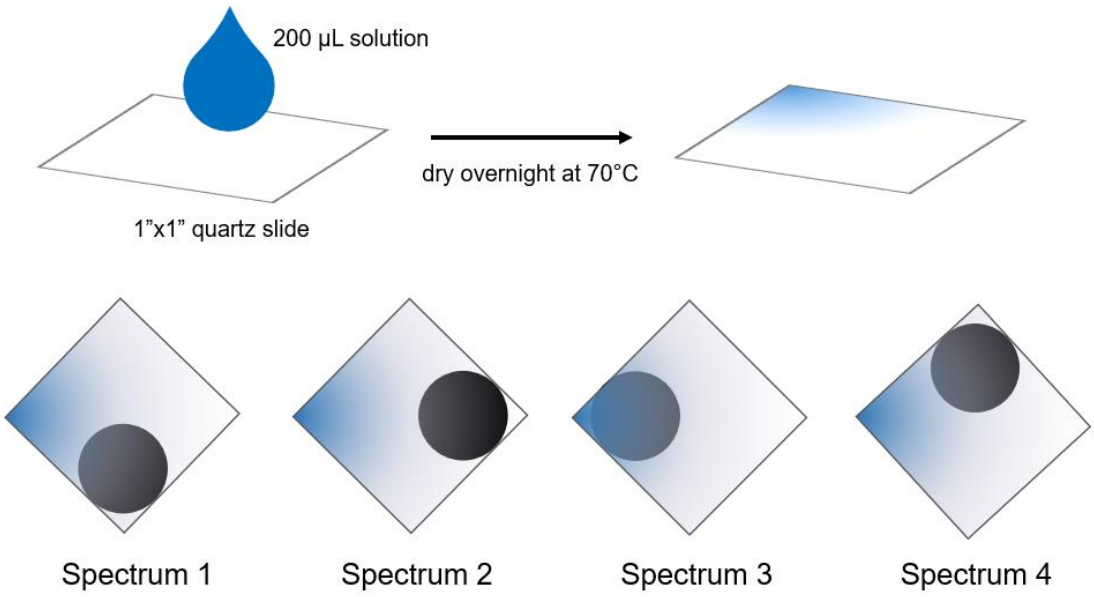

Figure A.2 Diagram of the experimental method for depositing CoPc and CoPc-polymer layers and collecting diffuse reflectance UV-Vis data. Drop casting of the solutions resulted in non-uniform layers, typically with a higher concentration of CoPc in one corner of the slide. To account for this variation, four spectra were collected for each slide, one with each corner of the slide positioned over the beam aperture (represented by a black circle).

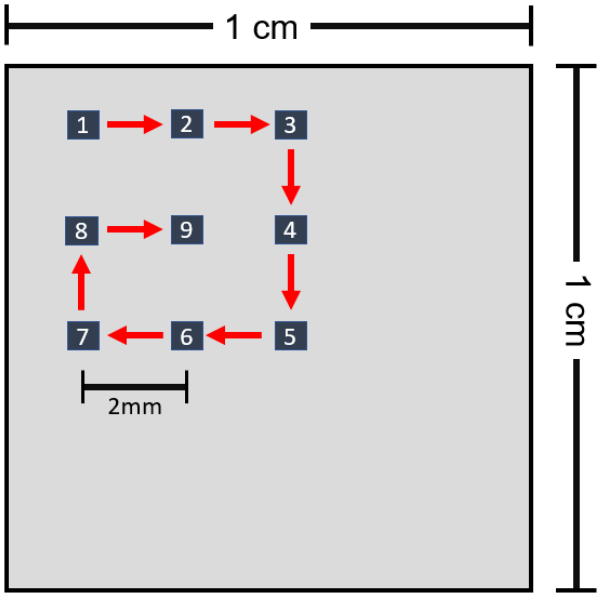

Figure A.3 Diagram of the experimental method for collecting SEM particle counting data. A CoPc or CoPc/polymer layer was deposited onto a 1 cm × 1 cm silicon wafer, which was attached to an aluminum SEM stub using double-sided conductive tape. Inside the SEM chamber, samples were positioned such that their sides were roughly parallel with the instrument's internal X and Y axes. A semi-random spot towards the -X, +Y corner of the sample was selected, then the sampling spot was moved in 2.0 mm increments in the pattern shown above. At each location, an SEM image was collected at x250 magnification, 5.0 keV beam energy, 0.40 nA beam current.

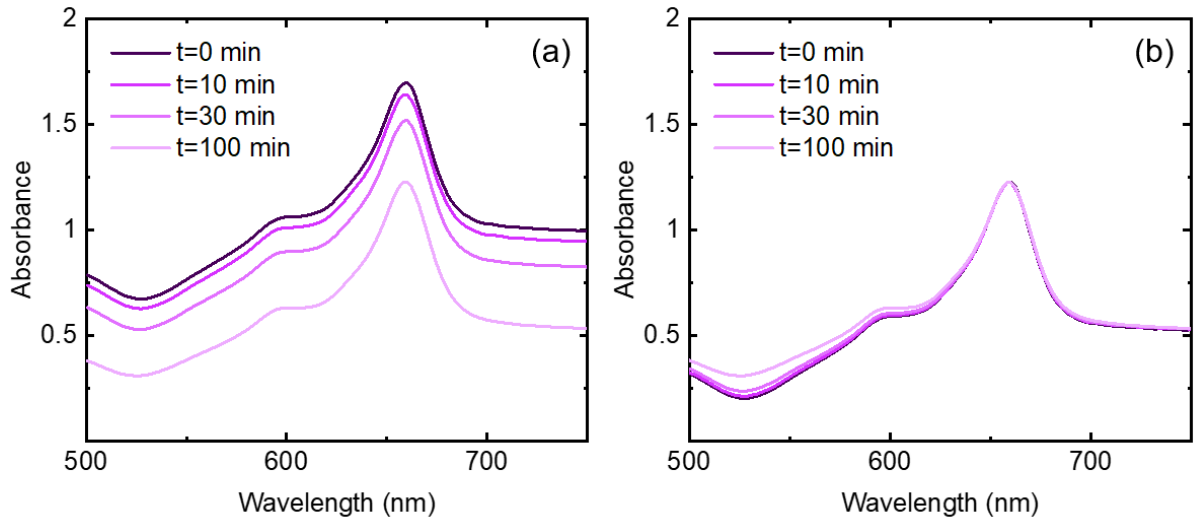

Figure A.4 To demonstrate the large quantity of undissolved CoPc particles causing scattering at high concentrations, a 5×10^{-4} M solution of CoPc in DMF was prepared and vortexed thoroughly to temporarily suspend undissolved particles. 2 mL of the solution was placed in a quartz cuvette, then allowed to settle without further mixing while UV-Vis spectra (a) were collected at various time points. In (b), these spectra have been normalized to the height of the t=100 spectrum by simple background subtraction. These data demonstrate that the suspended particles do not contribute to the Q-band peaks—which remain of a constant height and shape—but rather create a background of scattering across all visible wavelengths.

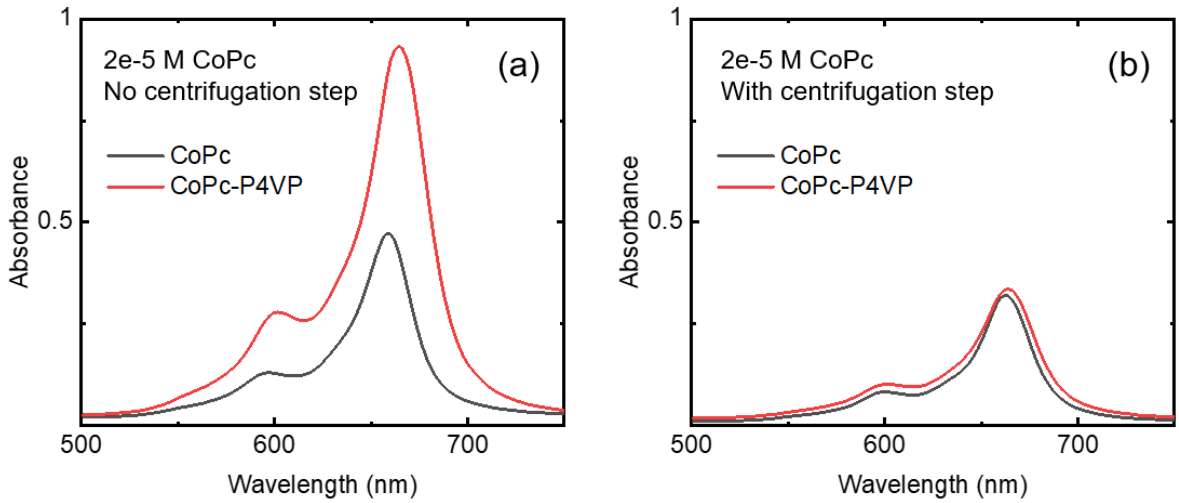

Figure A.5 UV-Vis spectra of CoPc and CoPc-P4VP ink samples (a) with and (b) without a centrifugation step. To prepare the samples in (b), the $2x10^{-5}$ M CoPc stock solution was centrifuged for 10 min at 6000 RPM after sonication, before preparation of the final deposition inks. When a centrifugation step was added to remove undissolved suspended CoPc particles, the subsequent addition of P4VP did not enhance CoPc monomer Q-band absorbance, indicating that the solvation of aggregate particles—rather than an intrinsic change in molar attenuation coefficient due to axial coordination—is responsible for the absorbance difference seen between the CoPc and CoPc-P4VP cases.

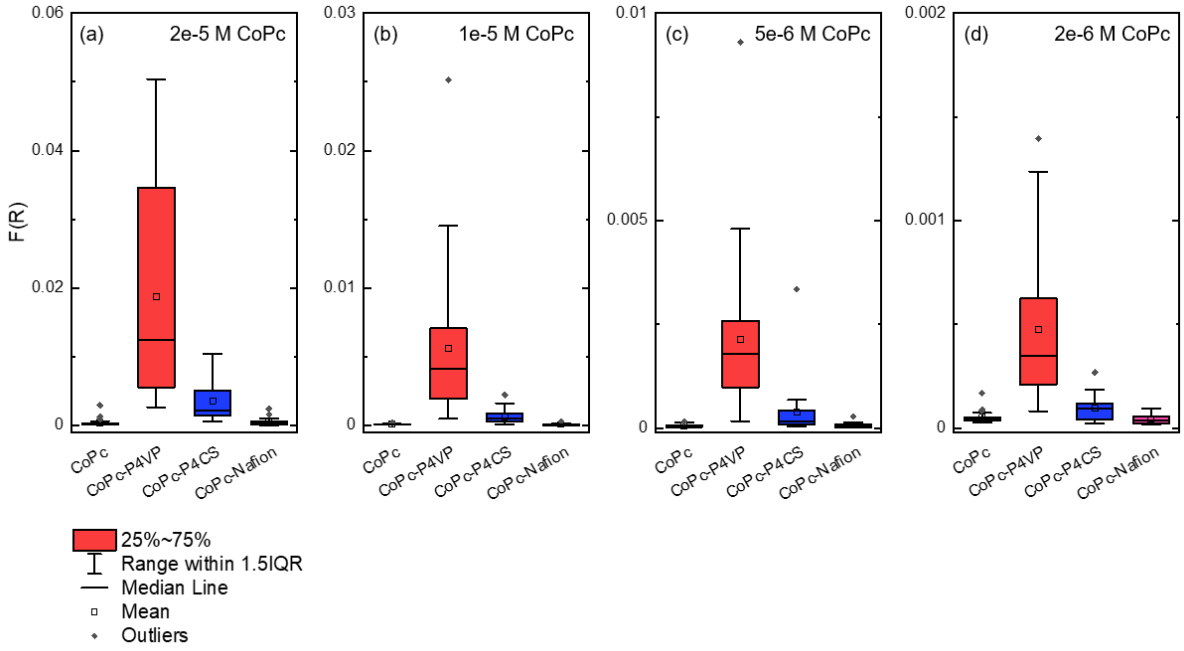

Figure A.6 Box-and-whiskers plots demonstrating the data spread for diffuse reflectance F(R) values for all CoPc samples at concentrations: a) 2×10^{-5} M, b) 1×10^{-5} M, c) 5×10^{-6} M, d) 2×10^{-6} M. F(R) values are analogous to absorbance.

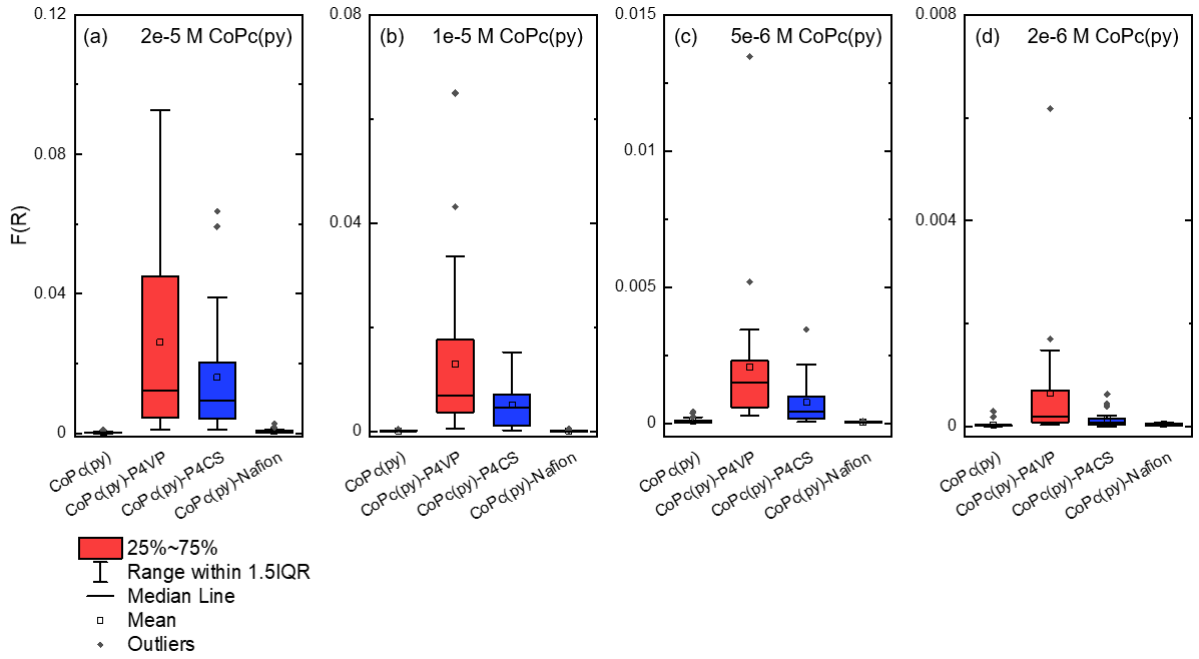

Figure A.7 Box-and-whiskers plots demonstrating the data spread for diffuse reflectance F(R) values for all CoPc(py) samples at concentrations: a) 2×10^{-5} M, b) 1×10^{-5} M, c) 5×10^{-6} M, d) 2×10^{-6} M. F(R) values are analogous to absorbance.

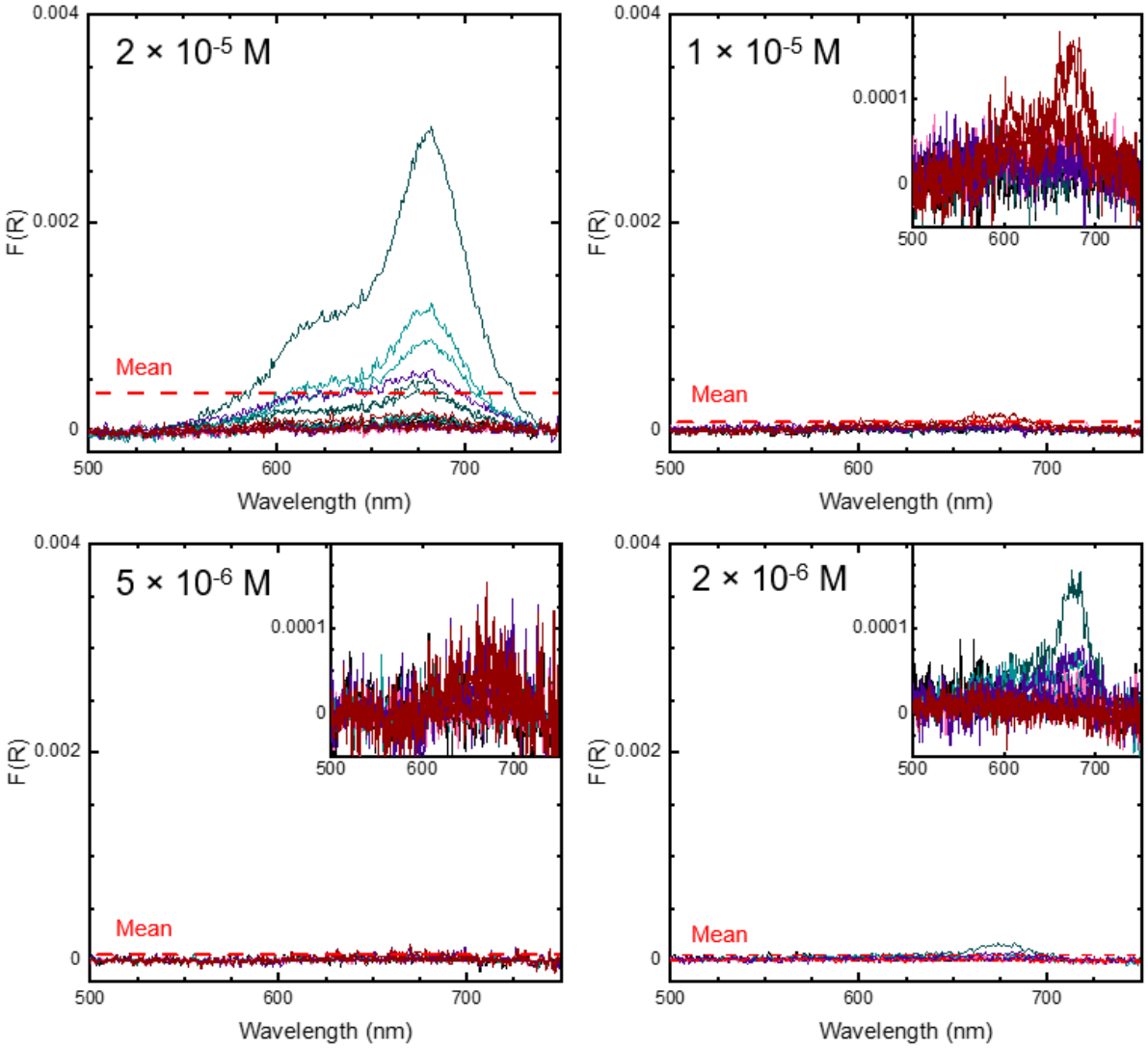

Figure A.8 Plots of all diffuse reflectance spectra for CoPc samples without polymer, labelled by concentration of CoPc in the deposition solution. To demonstrate that the primary contribution to variance is inhomogeneity of the sample layer, each color represents a specific sample from which four separate spectra were taken. Primary figures are kept at the same scale to demonstrate how overall Q-band absorbance changes with loading, while inset figures are scaled to demonstrate variance within each loading. A dashed line denotes the mean peak absorbance for each loading. Spectra have been baseline corrected as described in the Methods section, but not otherwise normalized.

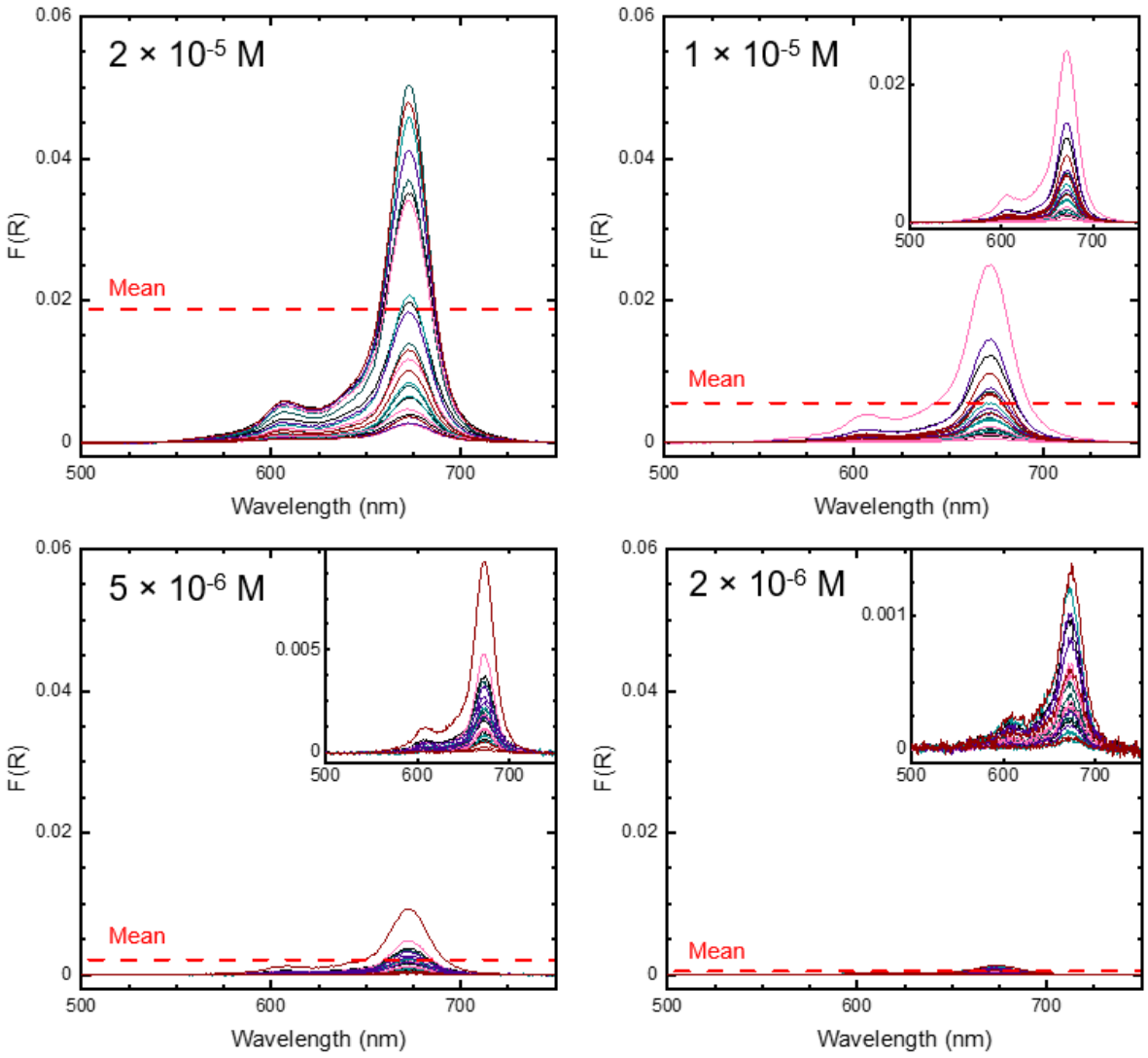

Figure A.9 Plots of all diffuse reflectance spectra for CoPc-P4VP samples, labelled by concentration of CoPc in the deposition solution. To demonstrate that the primary contribution to variance is inhomogeneity of the sample layer, each color represents a specific sample from which four separate spectra were taken. Primary figures are kept at the same scale to demonstrate how overall Q-band absorbance changes with loading, while inset figures are scaled to demonstrate variance within each loading. A dashed line denotes the mean peak absorbance for each loading. Spectra have been baseline corrected as described in the Methods section, but not otherwise normalized.

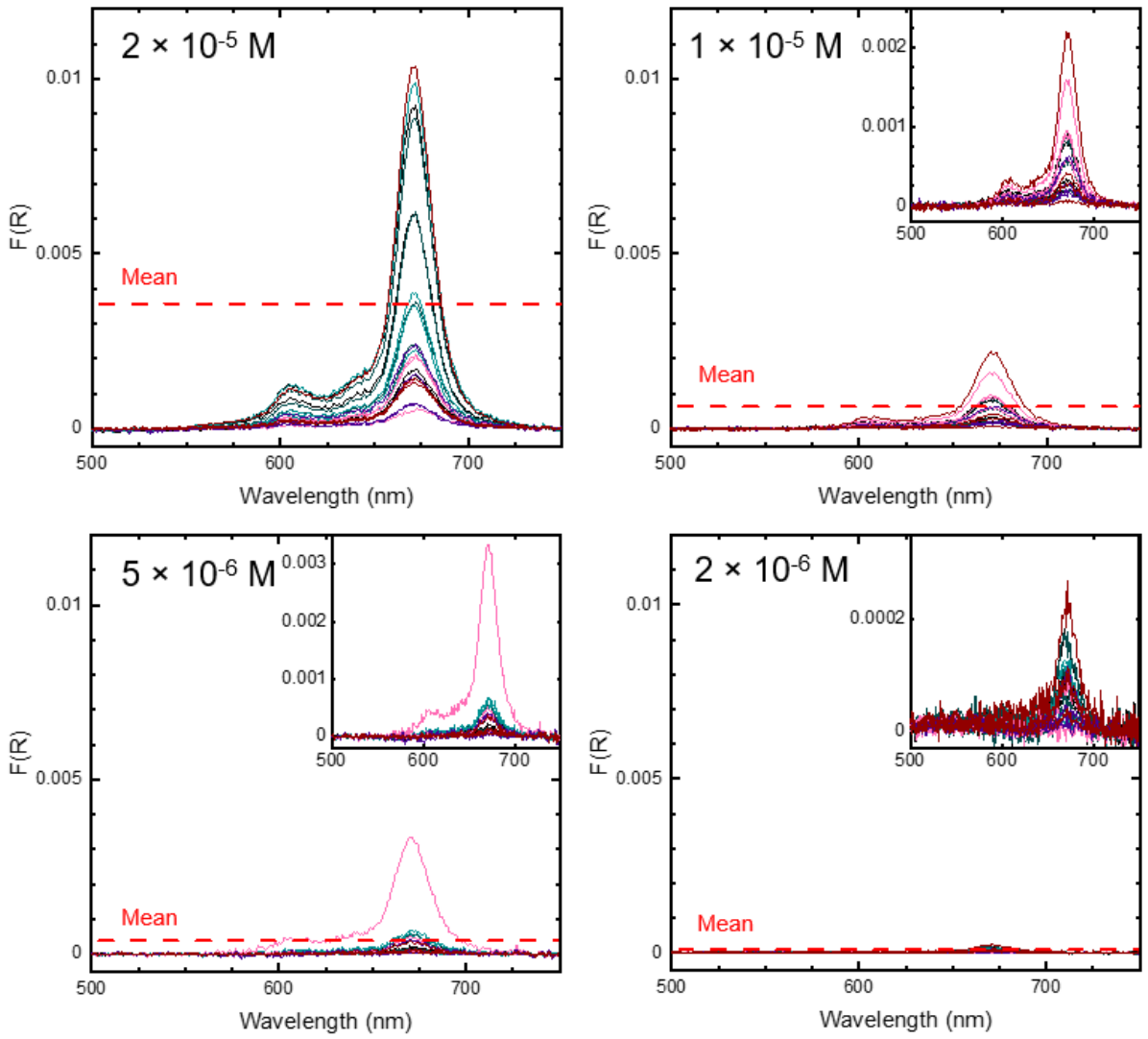

Figure A.10 Plots of all diffuse reflectance spectra for CoPc-P4CS samples, labelled by concentration of CoPc in the deposition solution. To demonstrate that the primary contribution to variance is inhomogeneity of the sample layer, each color represents a specific sample from which four separate spectra were taken. Primary figures are kept at the same scale to demonstrate how overall Q-band absorbance changes with loading, while inset figures are scaled to demonstrate variance within each loading. A dashed line denotes the mean peak absorbance for each loading. Spectra have been baseline corrected as described in the Methods section, but not otherwise normalized.

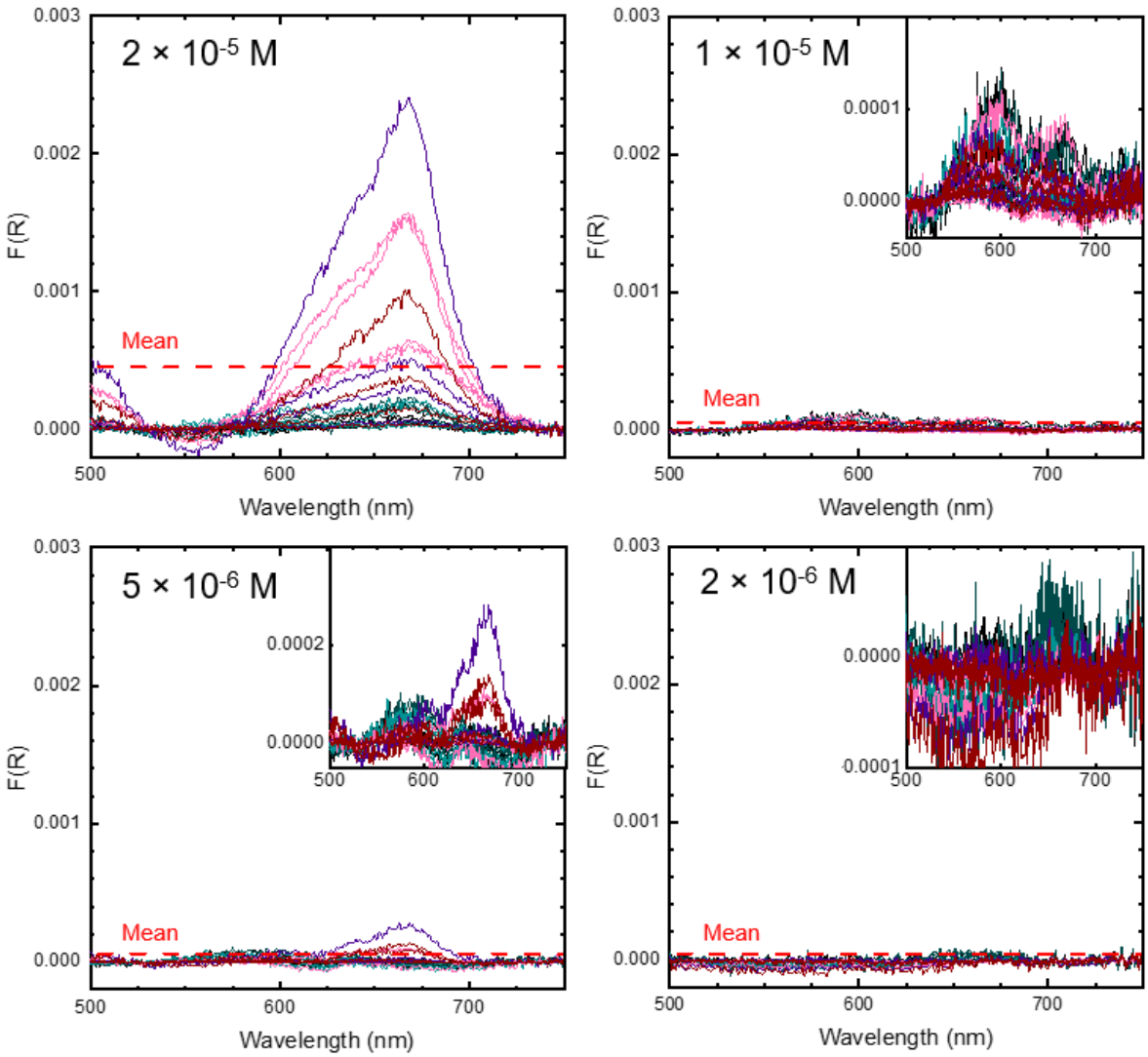

Figure A.11 Plots of all diffuse reflectance spectra for CoPc-Nafion samples, labelled by concentration of CoPc in the deposition solution. To demonstrate that the primary contribution to variance is inhomogeneity of the sample layer, each color represents a specific sample from which four separate spectra were taken. Primary figures are kept at the same scale to demonstrate how overall Q-band absorbance changes with loading, while inset figures are scaled to demonstrate variance within each loading. A dashed line denotes the mean peak absorbance for each loading. Spectra have been baseline corrected as described in the Methods section, but not otherwise normalized.

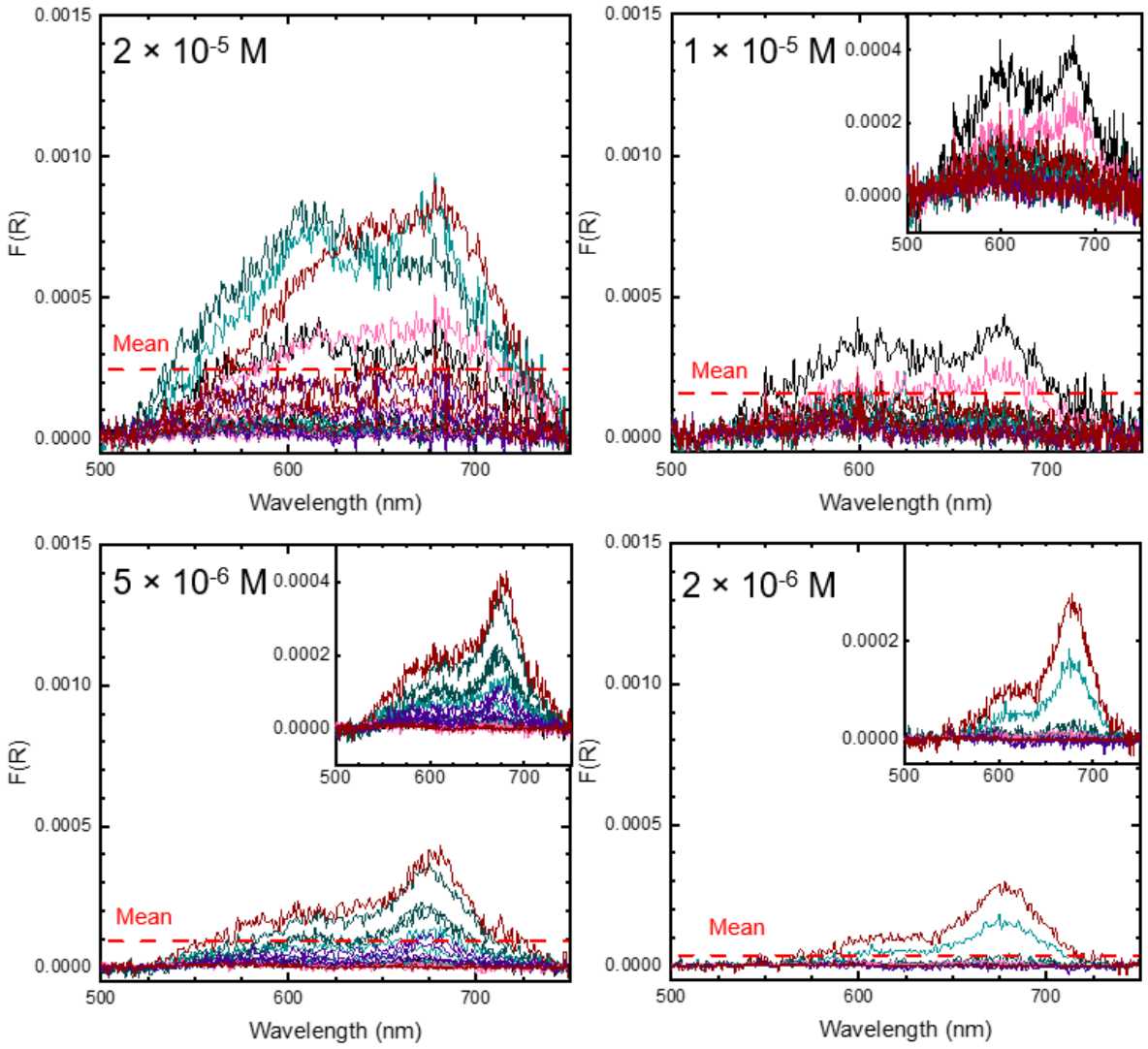

Figure A.12 Plots of all diffuse reflectance spectra for CoPc(py) samples without polymer, labelled by concentration of CoPc in the deposition solution. To demonstrate that the primary contribution to variance is inhomogeneity of the sample layer, each color represents a specific sample from which four separate spectra were taken. Primary figures are kept at the same scale to demonstrate how overall Q-band absorbance changes with loading, while inset figures are scaled to demonstrate variance within each loading. A dashed line denotes the mean peak absorbance for each loading. Spectra have been baseline corrected as described in the Methods section, but not otherwise normalized.

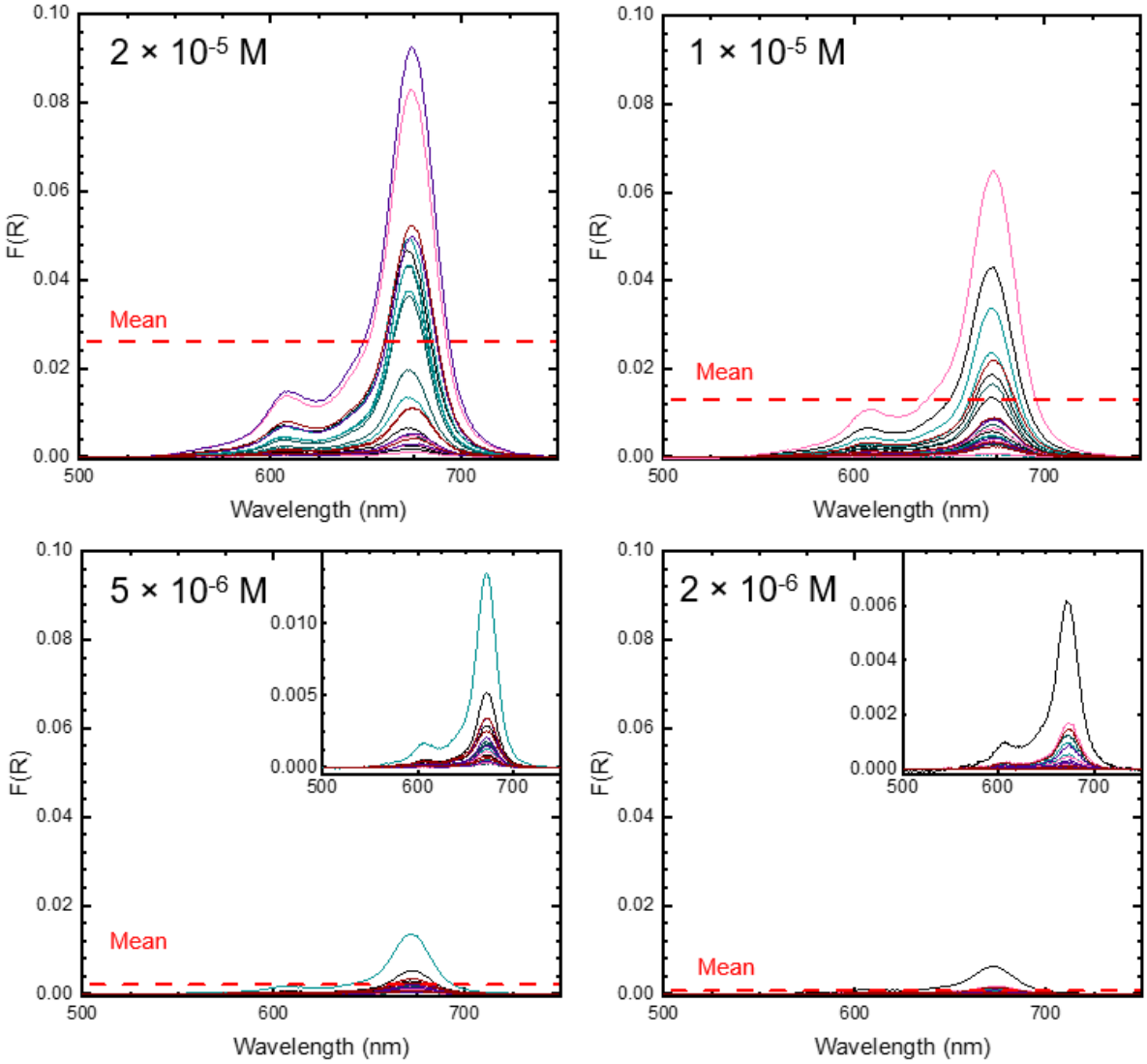

Figure A.13 Plots of all diffuse reflectance spectra for CoPc(py)-P4VP samples, labelled by concentration of CoPc in the deposition solution. To demonstrate that the primary contribution to variance is inhomogeneity of the sample layer, each color represents a specific sample from which four separate spectra were taken. Primary figures are kept at the same scale to demonstrate how overall Q-band absorbance changes with loading, while inset figures are scaled to demonstrate variance within each loading. A dashed line denotes the mean peak absorbance for each loading. Spectra have been baseline corrected as described in the Methods section, but not otherwise normalized.

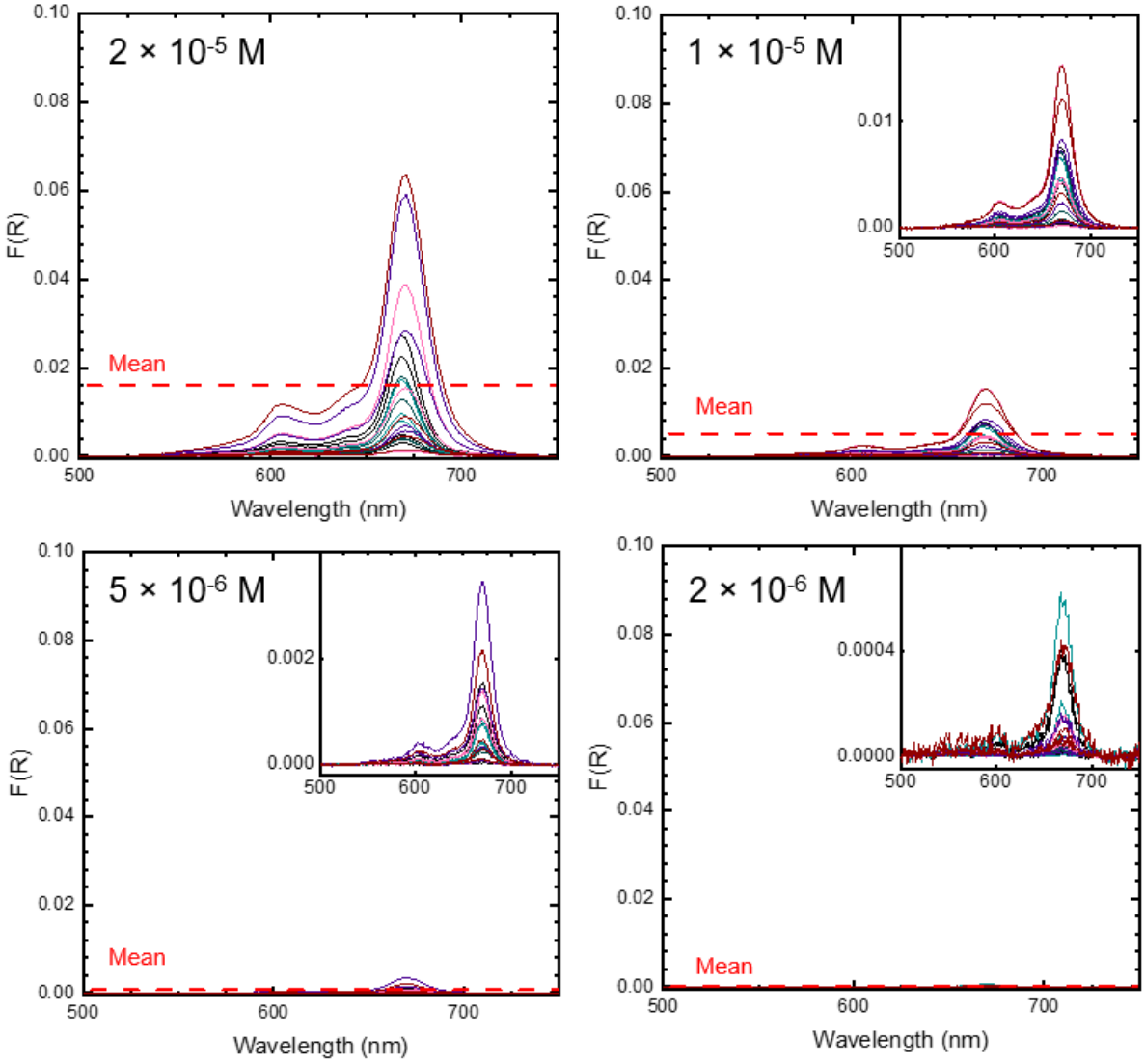

Figure A.14 Plots of all diffuse reflectance spectra for CoPc(py)-P4CS samples, labelled by concentration of CoPc in the deposition solution. To demonstrate that the primary contribution to variance is inhomogeneity of the sample layer, each color represents a specific sample from which four separate spectra were taken. Primary figures are kept at the same scale to demonstrate how overall Q-band absorbance changes with loading, while inset figures are scaled to demonstrate variance within each loading. A dashed line denotes the mean peak absorbance for each loading. Spectra have been baseline corrected as described in the Methods section, but not otherwise normalized.

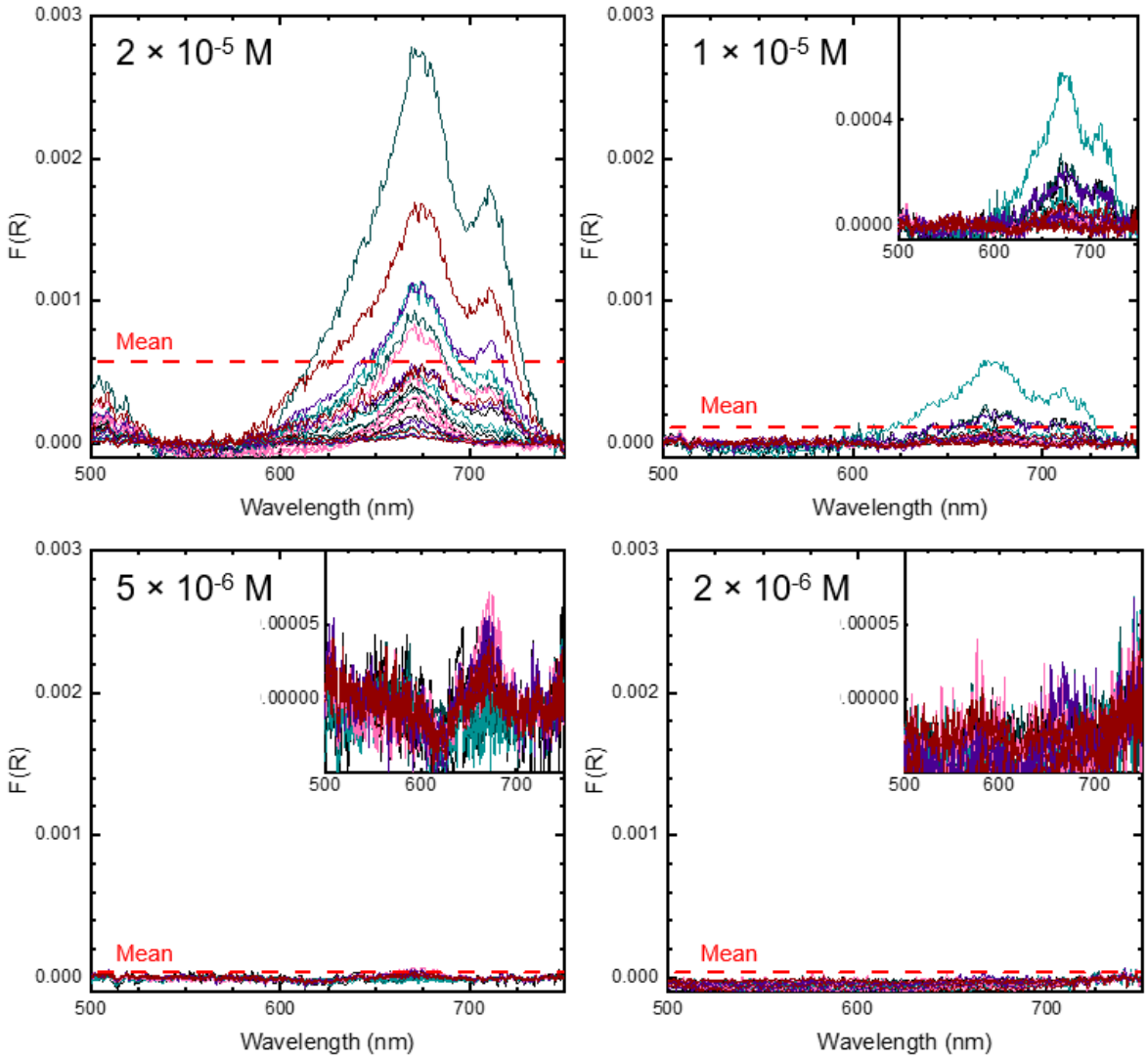

Figure A.15 Plots of all diffuse reflectance spectra for CoPc(py)-Nafion samples, labelled by concentration of CoPc in the deposition solution. To demonstrate that the primary contribution to variance is inhomogeneity of the sample layer, each color represents a specific sample from which four separate spectra were taken. Primary figures are kept at the same scale to demonstrate how overall Q-band absorbance changes with loading, while inset figures are scaled to demonstrate variance within each loading. A dashed line denotes the mean peak absorbance for each loading. Spectra have been baseline corrected as described in the Methods section, but not otherwise normalized.

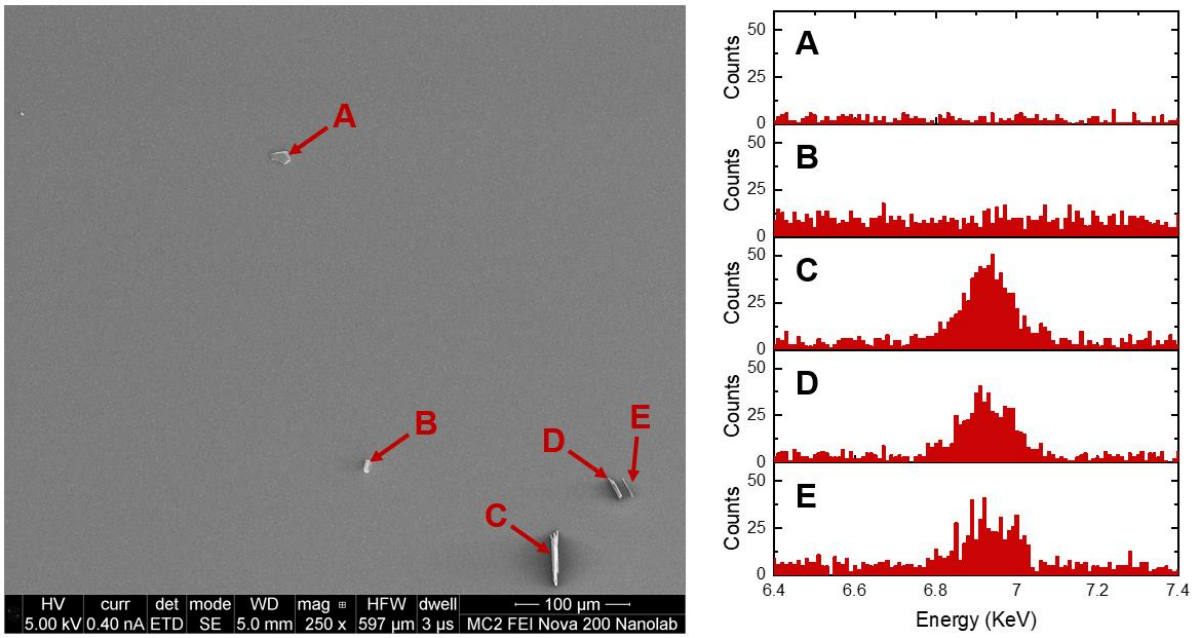

Figure A.16 The procedure for CoPc particle counting is demonstrated. Within the x250 magnification image, five particles (A, B, C, D, and E) were identified on the Si surface. Based on the morphology C, D, and E appear to be CoPc particles. This identification was confirmed by EDX point spectra at each particle location (presented on the right), where particles C, D, and E display Co K-edge peaks at about 6.9 keV.

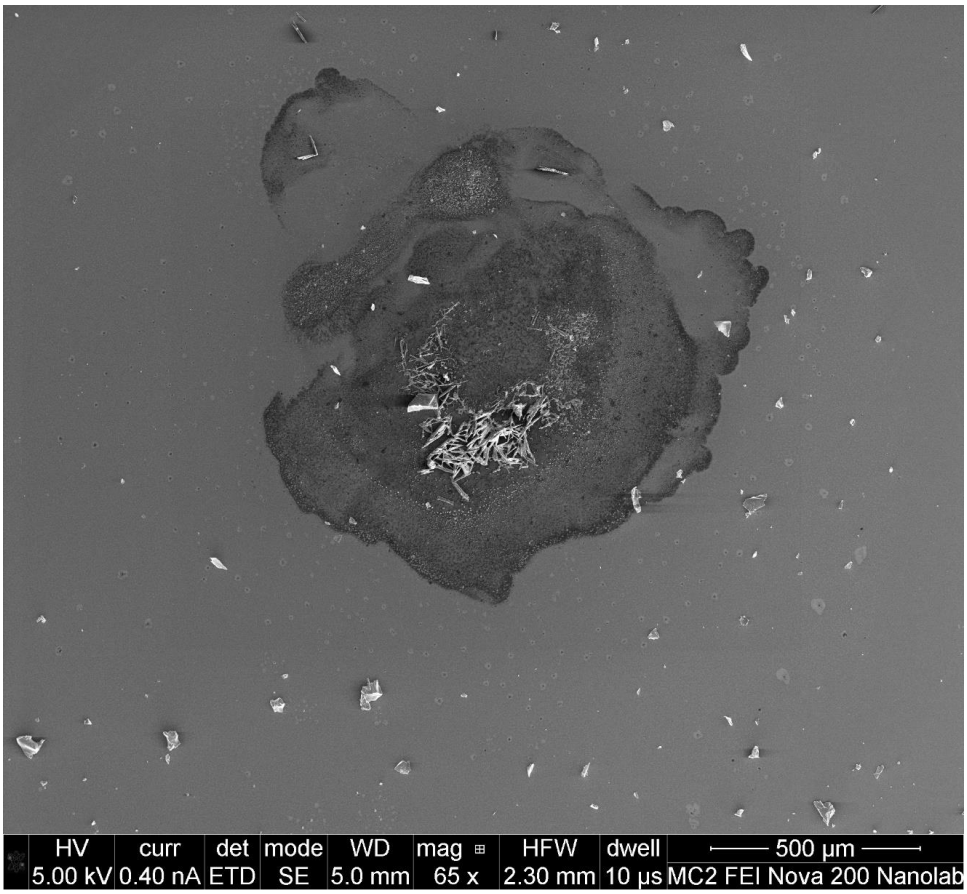

Figure A.17 Representative CoPc-NP nucleation spot at x65 magnification

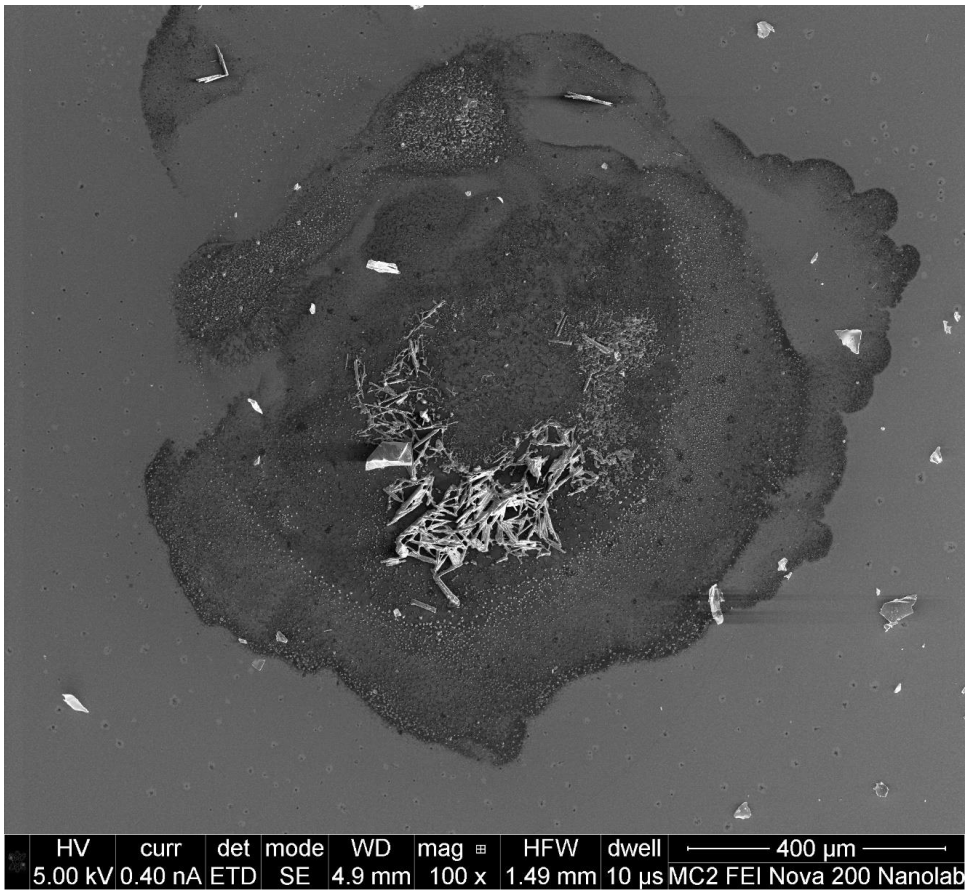

Figure A.18 Representative CoPc-NP nucleation spot at x100 magnification.

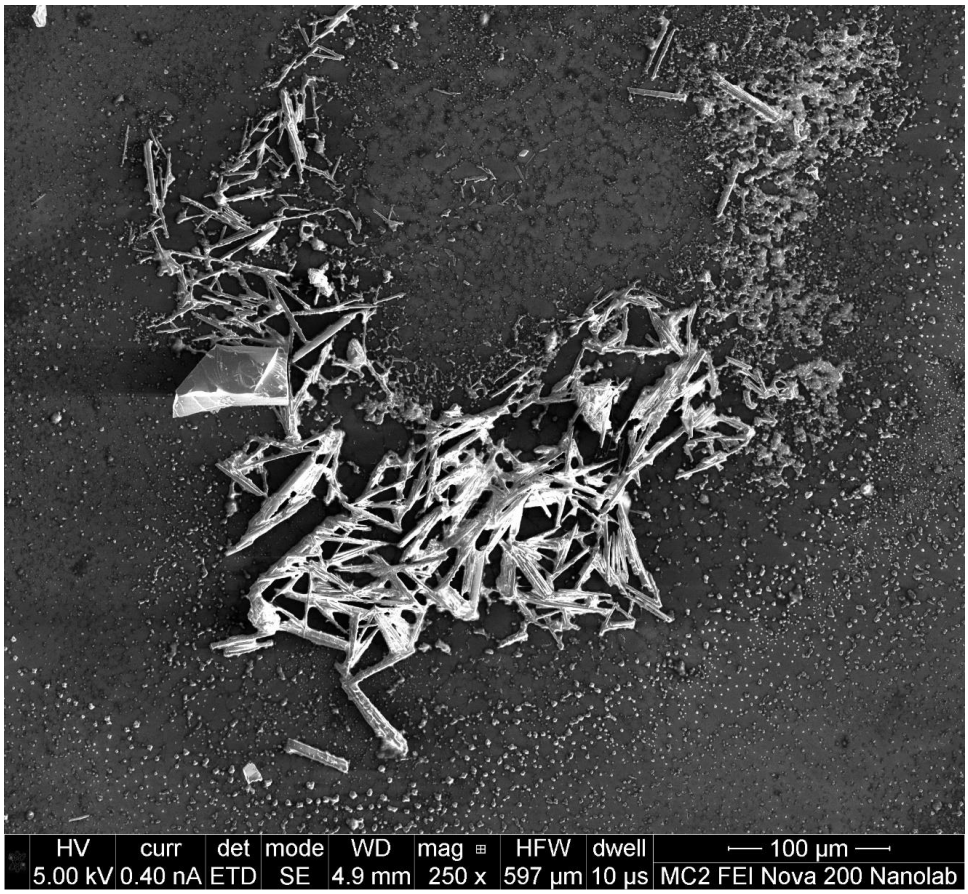

Figure A.19 Representative CoPc-NP nucleation spot at x100 magnification.

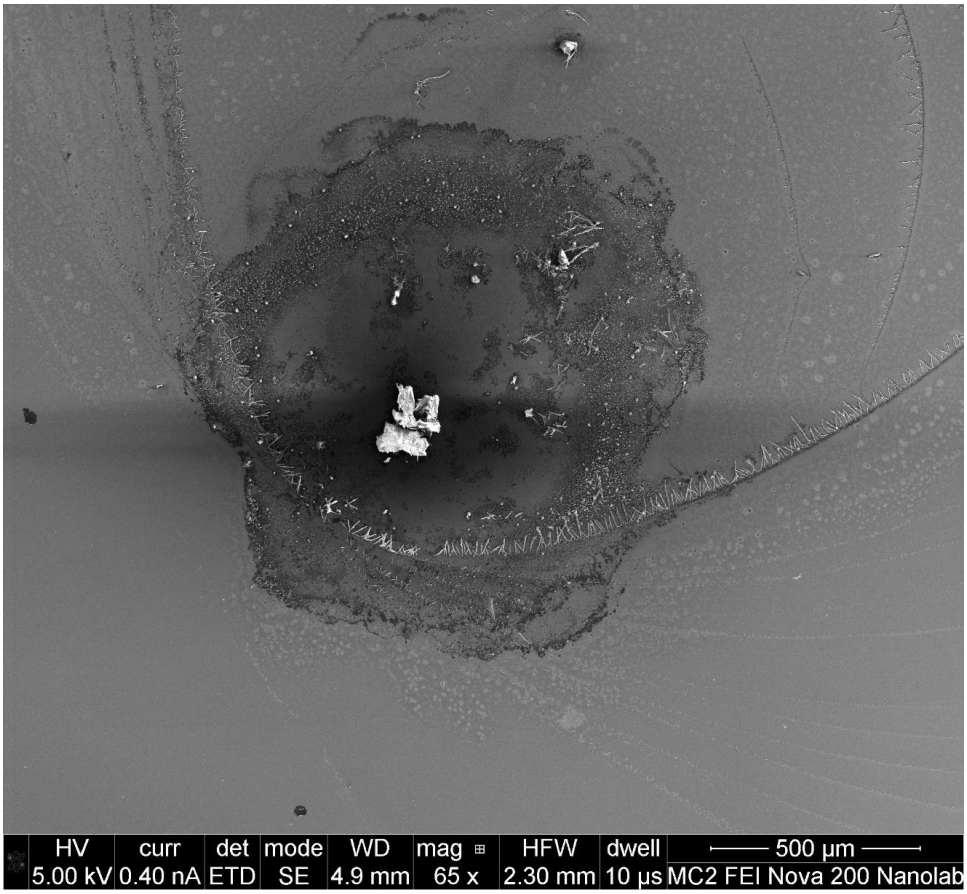

Figure A.20 Representative CoPc(py)-NP nucleation spot at x65 magnification.

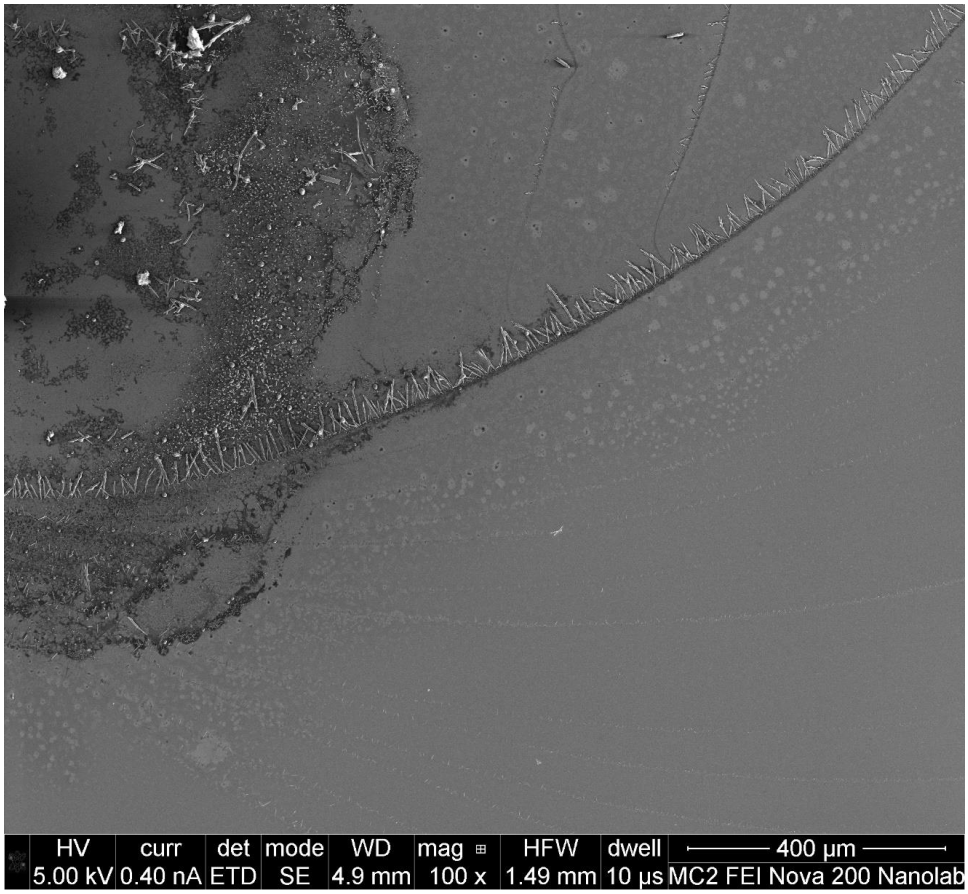

Figure A.21 Representative CoPc(py)-NP nucleation spot at x100 magnification

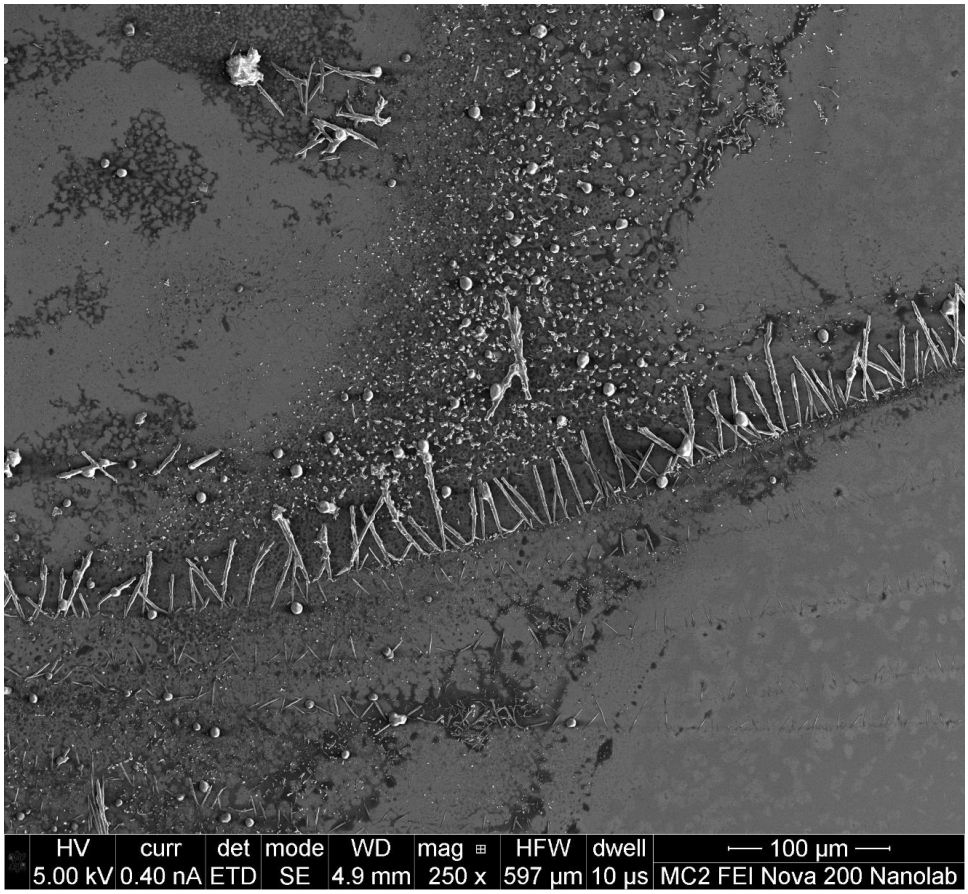

Figure A.22 Representative CoPc(py)-NP nucleation spot at x250 magnification

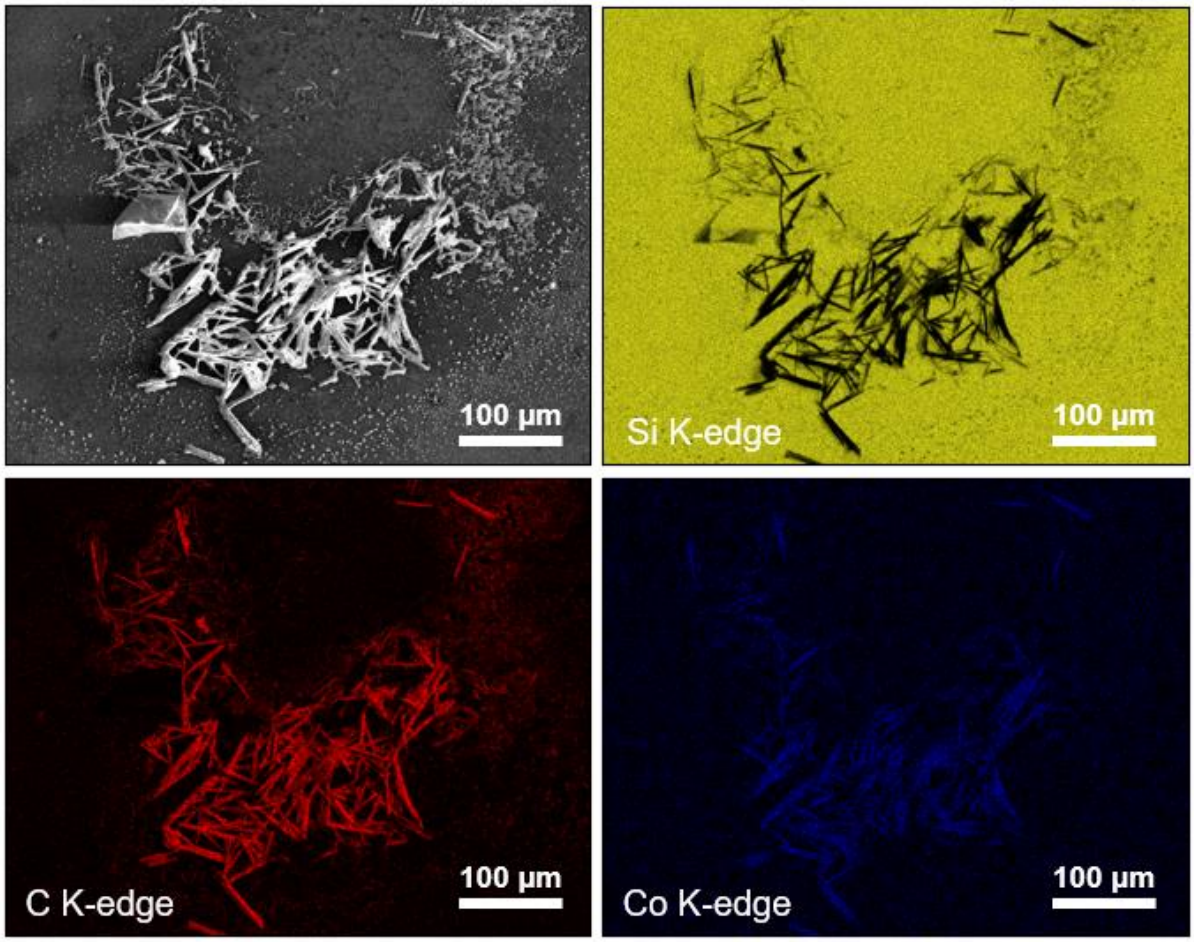

Figure A.23 EDX maps of C, Si, and Co for representative CoPc-NP nucleation spot presented in Figure 2.8.

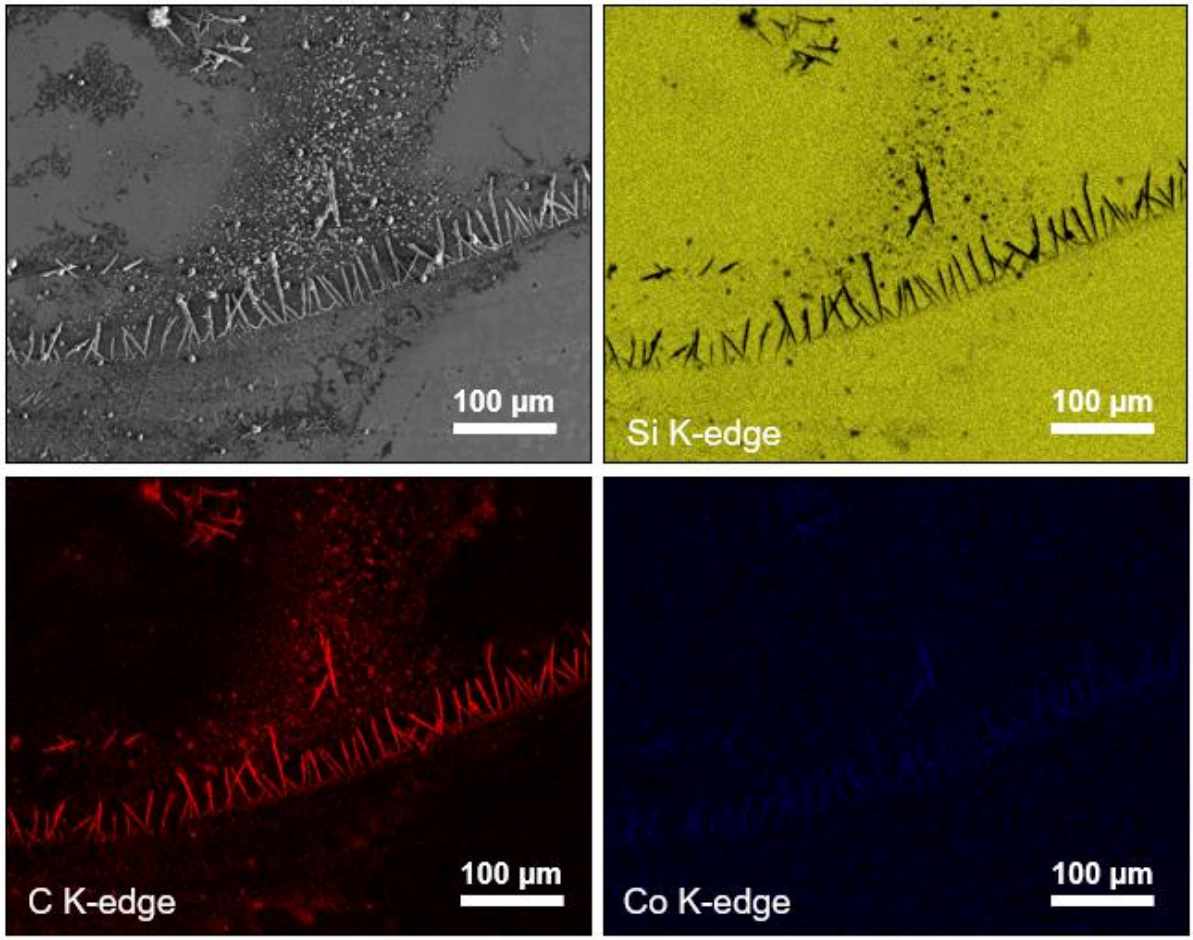

Figure A.24 EDX maps of C, Si, and Co for representative CoPc(py)-NP nucleation spot presented in Figure 2.8.

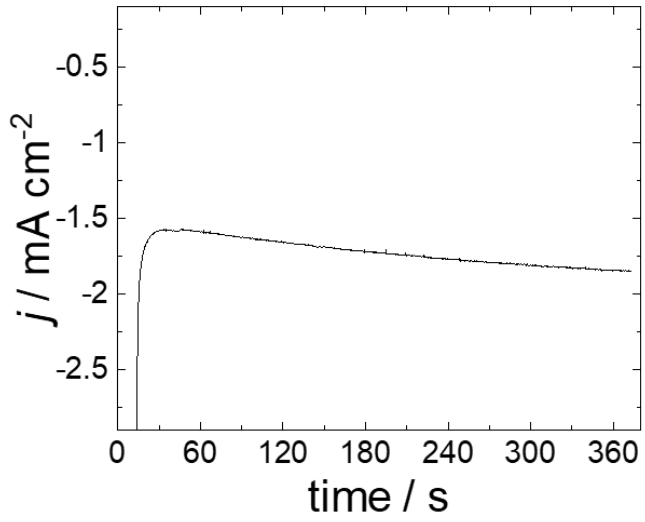

Figure A.25 CoPc(py)-P4VP/EPG representative rotating disk electrode chronoamperometric (RDE-CA) current density trace performed under rotation at 1600 rpm for 6 min in pH 4.7 0.1 M NaH_2PO_4 under CO_2 atmosphere, prepared according to the Methods section.

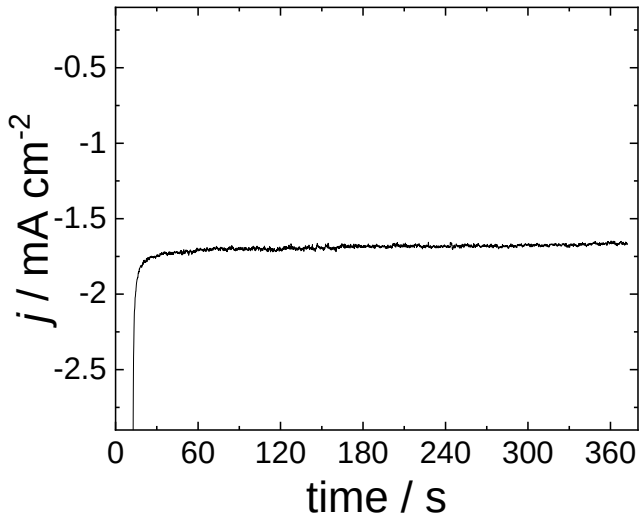

Figure A.26 CoPc-P4VP/EPG representative rotating disk electrode chronoamperometric (RDE-CA) current density trace performed under rotation at 1600 rpm for 6 min in pH 4.7 0.1 M NaH_2PO_4 under CO_2 atmosphere, prepared according to the Methods section.

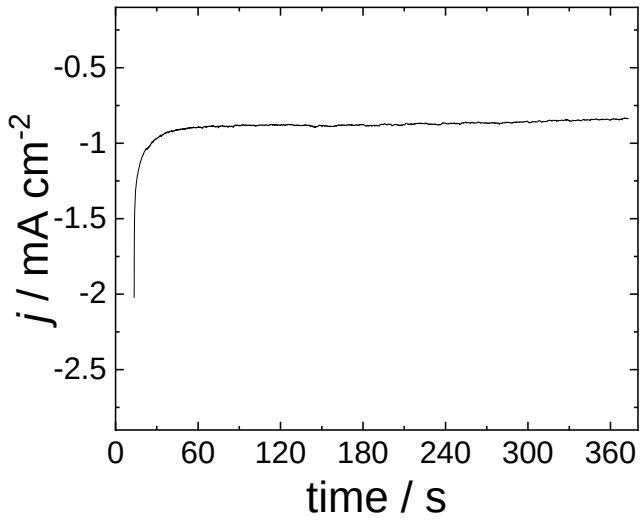

Figure A.27 CoPc(py)-Nafion/EPG representative rotating disk electrode chronoamperometric (RDE-CA) current density trace performed under rotation at 1600 rpm for 6 min in pH 4.7 0.1 M NaH_2PO_4 under CO_2 atmosphere, prepared according to the Methods section.

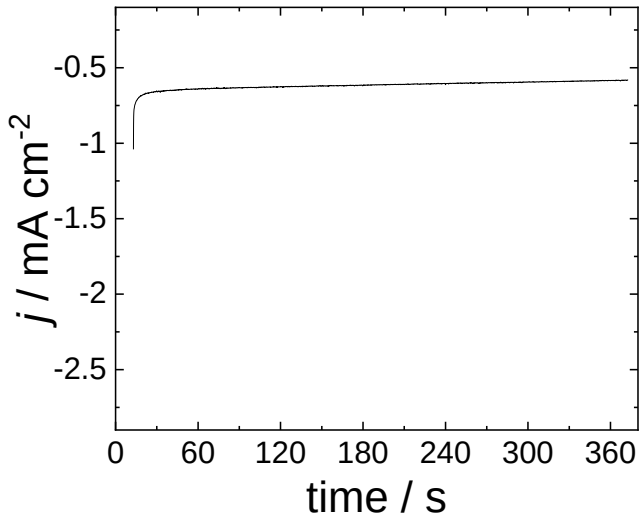

Figure A.28 CoPc(py)-Nafion/EPG representative rotating disk electrode chronoamperometric (RDE-CA) current density trace performed under rotation at 1600 rpm for 6 min in pH 4.7 0.1 M NaH_2PO_4 under CO_2 atmosphere, prepared according to the Methods section.

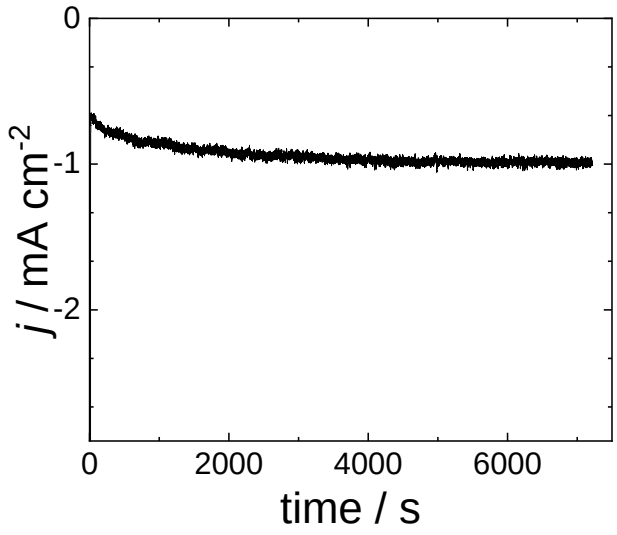

Figure A.29 CoPc(py)-P4VP/EPG representative controlled potential electrolysis current density trace performed for 2 hours in pH 4.7 0.1 M NaH_2PO_4 under CO_2 atmosphere, prepared according to the Methods section.

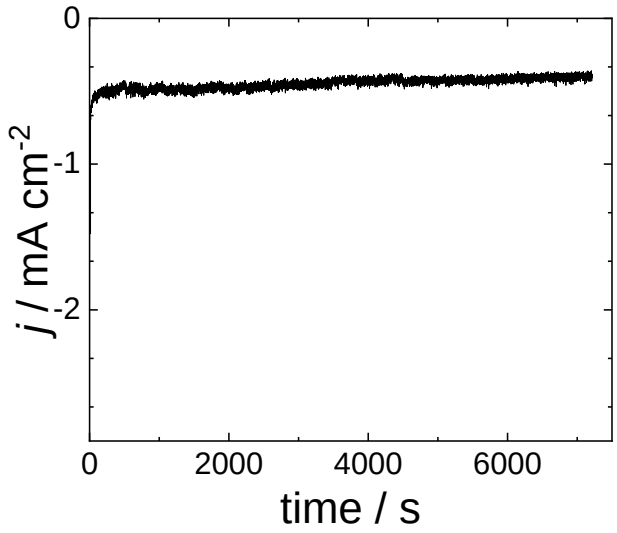

Figure A.30 CoPc(py)-Nafion/EPG representative controlled potential electrolysis current density trace performed for 2 hours in pH 4.7 0.1 M NaH_2PO_4 under CO_2 atmosphere, prepared according to the Methods section.

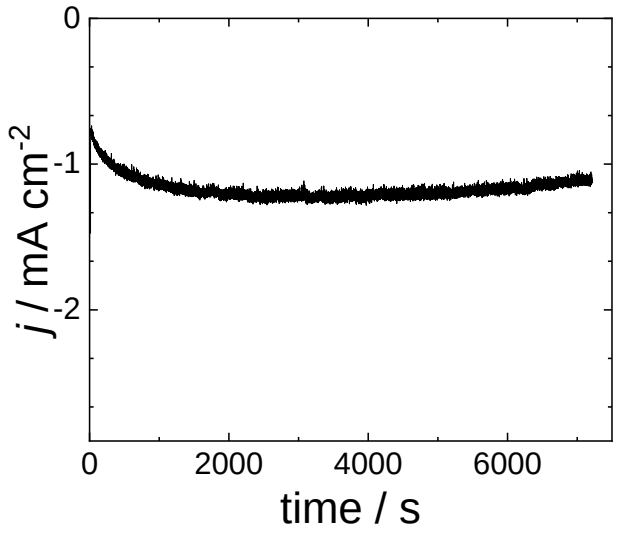

Figure A.31 CoPc-P4VP/EPG representative controlled potential electrolysis current density trace performed for 2 hours in pH 4.7 0.1 M NaH_2PO_4 under CO_2 atmosphere, prepared according to the Methods section.

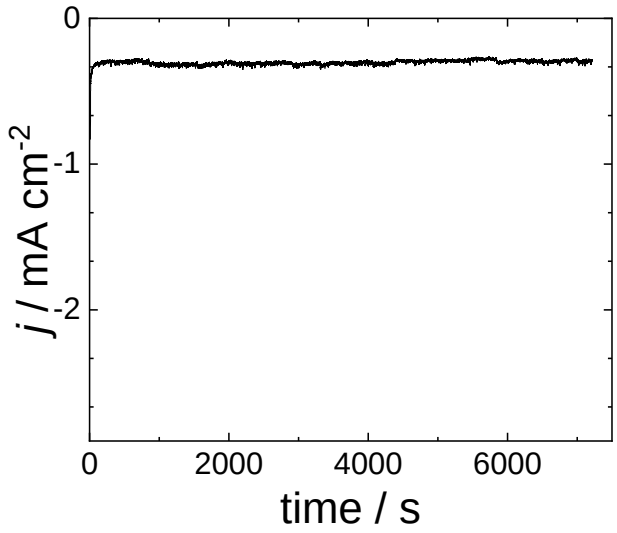

Figure A.32 CoPc-Nafion/EPG representative controlled potential electrolysis current density trace performed for 2 hours in pH 4.7 0.1 M NaH_2PO_4 under CO_2 atmosphere, prepared according to the Methods section.

Appendix B. Supplementary Information for Chapter 3

Supplementary Tables for Chapter

	Before Centrifugation			After Centrifugation			Electrode Loading		
	Preparation Suspension Loading			Deposition Ink Loading			Deposition Ink Drop Cast		
	CoPc / mM	Polymer / mg mL^{-1}	GP / mg mL^{-1}	CoPc / mM	Polymer / mg mL^{-1}	GP / mg mL^{-1}	CoPc / 10^{-9} mol cm^{-2}	Polymer / mg cm^{-2}	GP / mg cm^{-2}
CoPc-P4VP/ GP/GCE	0.05	30	10	0.026 ± 0.003	3.01 ± 0.97	10	1.30 ± 0.16	0.117 ± 0.049	0.513
CoPc-P2VP/ GP/GCE	0.05	30	10	0.035 ± 0.003	9.03 ± 2.54	10	1.79 ± 0.17	0.463 ± 0.1306	0.513
CoPc-P4VP/EPG	No centrifugation			0.05	3.0	0	1.27	0.076	0

Table B.1 CoPc preparation methods and loadings for deposition ink used for the all graphite powder systems (CoPc-P4VP/GP and CoPc-P2VP/GP), where columns 1-3 detail the concentrations of cobalt phthalocyanine (CoPc), poly-(4-vinylpyridine) (P4VP), and graphite powder (GP) in the preparation suspension 4-6 detail the measured conditions of the preparation conditions of the CoPc loading, P4VP loading, and GP loading, with errors being the standard deviation of at least 3 individually prepared measurements. Columns 7-9 detail the catalyst, polymer, and GP loading on the 0.196 cm^2 glassy carbon electrodes (GCEs). Additionally, this includes the data for CoPc-P4VP/EPG that was used as a control. There was no centrifugation in this system, so columns 4-6 detail the measured conditions of the preparation conditions of the CoPc loading and P4VP loading as directly prepared for the deposition ink. Columns 7-9 detail the CoPc, polymer, and GP loading on the total surface area of the electrode surface, 0.196 cm^2 (conductive surface area: 0.114 cm^2 due to encapsulating non-conductive polymer epoxy).

	Charge / C	FE_{CO} / %	FE_{H2} / %	FE_{Total} / %
pH 3	2.8 ± 0.6	55 ± 2	37 ± 4	93 ± 3
pH 4	2.8 ± 0.5	64 ± 3	28 ± 3	93 ± 3
pH 5	3.9 ± 0.5	75 ± 2	20 ± 1	96 ± 2
pH 6	3.2 ± 0.2	81 ± 2	14 ± 3	96 ± 2
pH 7	3.2 ± 0.6	93 ± 1	11 ± 2	101 ± 5

Table B.2 CPE Results for data presented in Figure 3.3a of CoPc-P4VP/GP/GCE electrocatalyzed 2 hour experiments run under CO_2 atmosphere at a potential of -0.646 V vs RHE. The experiments were run at the specified pH after the addition of CO_2 and the reported errors are standard deviations of at least 3 measurements.

	Charge / C	FE_{CO} / %	FE_{H2} / %	FE_{Total} / %
pH 3	1.9 ± 0.3	48 ± 1	47 ± 4	92 ± 5
pH 4	3.6 ± 1.1	72 ± 1	26 ± 4	98 ± 2
pH 5	2.6 ± 0.3	76 ± 3	20 ± 3	97 ± 1
pH 6	2.9 ± 0.5	85 ± 5	13 ± 1	98 ± 4
pH 7	3.0 ± 0.1	95 ± 4	7 ± 1	103 ± 6

Table B.3 CPE Results for data presented in Figure 3.3b of CoPc-P4VP/GP/GCE electrocatalyzed 2 hour experiments run under CO_2 atmosphere at a potential of -0.706 V vs RHE. The experiments were run at the specified pH after the addition of CO_2 and the reported errors are standard deviations of at least 3 measurements.

pH	$\lvert j \rvert$ @ -0.647 V vs RHE / mA cm^{-2}	Standard Deviation $\pm \lvert j \rvert$ @ -0.647 V vs RHE / mA cm^{-2}	$\lvert j_{CO} \rvert$ @ -0.647 V vs RHE / mA cm^{-2}	Standard Error $\pm \lvert j_{CO} \rvert$ @ -0.647 V vs RHE / mA cm^{-2}
3	3.4	0.1	1.9	0.1
4	3.8	0.1	2.4	0.1
5	4.1	0.1	3.1	0.1
6	4.1	0.1	3.3	0.1
7	3.5	0.1	3.3	0.1

Table B.4 Activity results as seen in Figure 3.4 of rotating disk chronoamperometry (RDE-CA) step experiment at -0.647 V vs RHE, conducted under 1 atm CO_2 in 0.4 M NaH_2PO_4 and 0.5 M $NaClO_4$ at the specified pH under 1600 rpm rotation rate for CoPc-P4VP/GP/GCE with 10 mg/mL graphite powder in the catalyst ink solution, corresponding to a loading of 0.51 mg cm^{-2}. The $\lvert j_{CO} \rvert$ value is the activity multiplied by the product distribution as measured by controlled potential electrolysis (see Table B.2) and the standard error is the combination of the standard deviations of the two measurements.

System	[NaH_2PO_4] / M	[$NaClO_4$] / M	Charge / C	FE_{CO} / %	FE_{H2} / %	FE_{Total} / %
CoPc-P4VP/GP/GCE pH 4.7	0.1	0.5	4.0 ± 0.5	81 ± 3	16 ± 2	98 ± 1
CoPc-P4VP/GP/GCE pH 5	0.4	0.5	3.9 ± 0.5	75 ± 2	20 ± 1	96 ± 2
CoPc-P4VP/GP/GCE pH 4.7	0.1	0	2.8 ± 0.8	83 ± 1	14 ± 4	97 ± 3

Table B.5 Controlled potential electrolysis results collected at -0.647 V vs RHE. electrocatalyzed by CoPc-P4VP/GP/GCE at varying buffer composition. The standard deviations are also presented (the average of at least 3 measurements). Electrolyte concentration is specified within the table and was run under CO_2 atmosphere.

[Phosphate] / M	[Perchlorate] / M	$\|j\|$ @ -0.647 V vs RHE / mA cm^{-2}	Standard Deviation $\pm \|j\|$ @ -0.647 V vs RHE / mA cm^{-2}
0.1	0	0.87	0.06
0.15	0	1.88	0.07
0.2	0	2.63	0.24
0.4	0	5.11	0.33

Table B.6 Activity data for the RDE-CAs measurements as shown in in Figure 3.6. These studies show the HER activity as electrocatalyzed by CoPc-P4VP/GP/GCE and measured as a function of electrolyte concentration. All experiments run at pH 5 with specified electrolyte concentration under N_2 atmosphere.

Supplementary Figures for Chapter 3

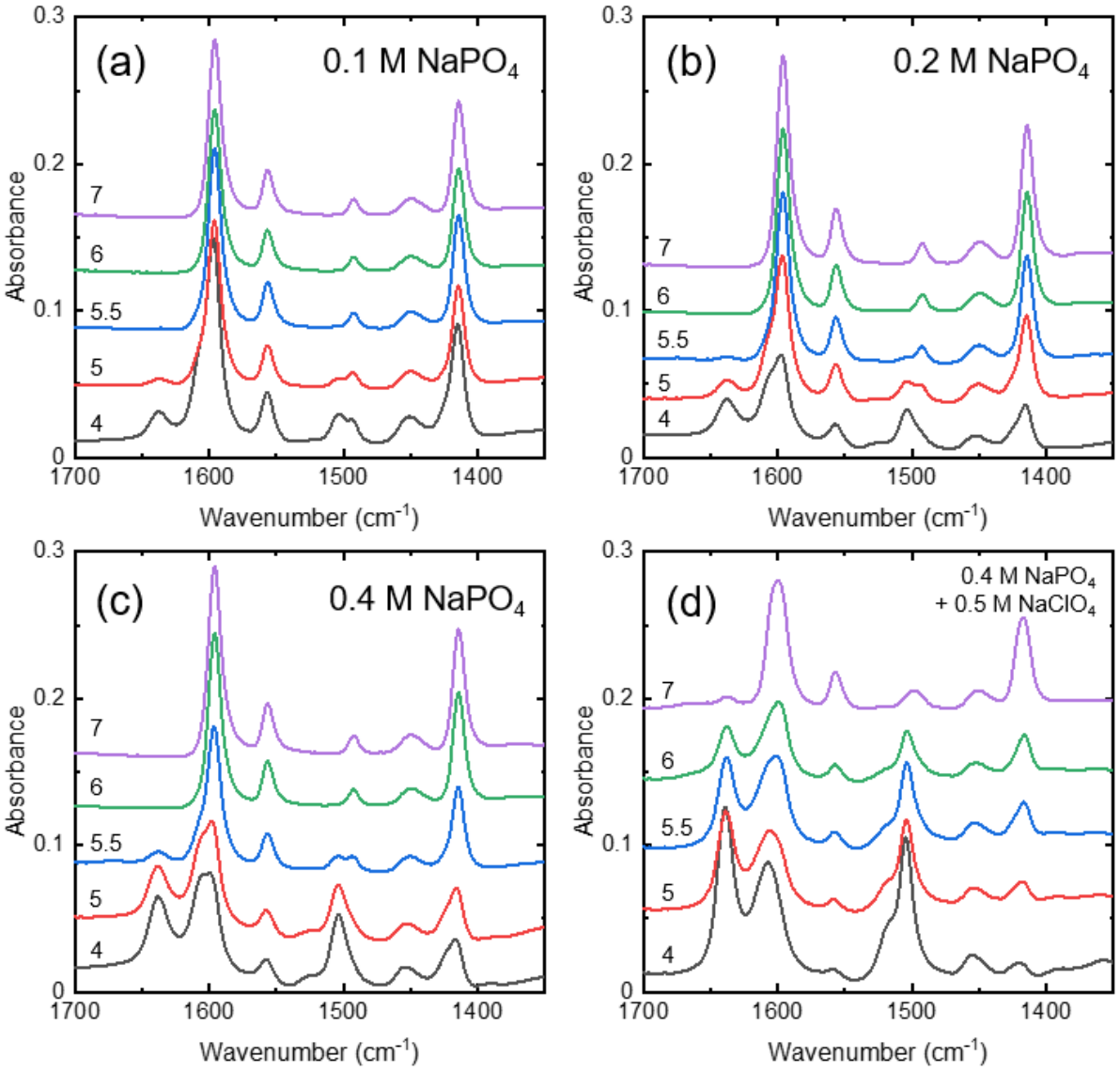

Figure B.1 Comparison of representative transmission infrared spectra of P4VP layers exposed to buffer solutions with pH values listed to the left and above each spectrum. The spectra are presented at an offset but without further backgrounding or normalization. a) Layers exposed to 0.1 M sodium phosphate. b) Layers exposed to 0.2 M sodium phosphate. c) Layers exposed to 0.4 M sodium phosphate. d) Layers exposed to 0.4 M phosphate with 0.5 M sodium perchlorate.

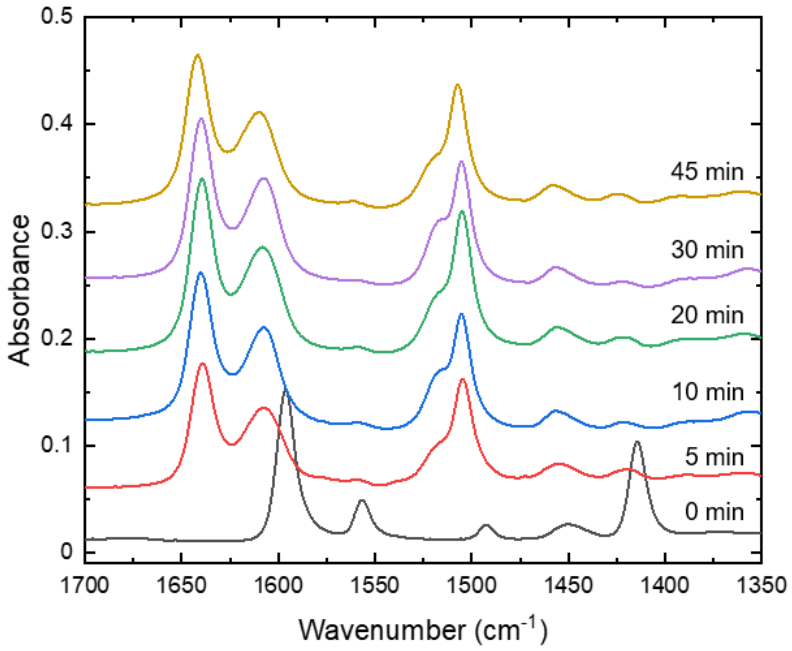

Figure B.2 Representative transmission infrared spectra of P4VP layers exposed to 0.4 M sodium phosphate buffer for varying times as listed. The spectra are presented at an offset but without further backgrounding or normalization. There is no noticeable dependence on soak time past 5 minutes.

Appendix C. Supplementary Information for Chapter 4

Supplementary Figures for Chapter 4

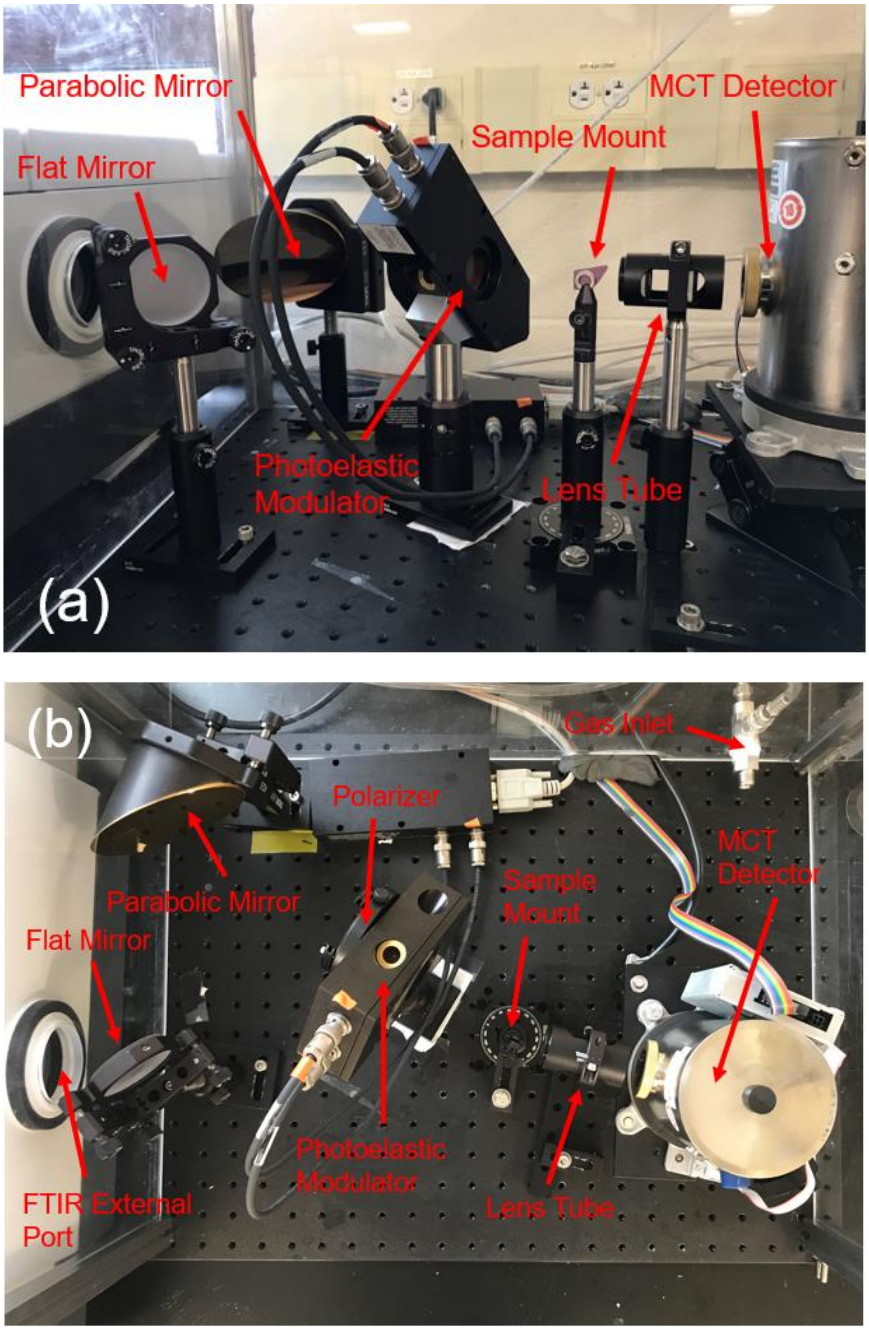

Figure C.1 Labelled photographs of the TOM components. a) side view. b) top view

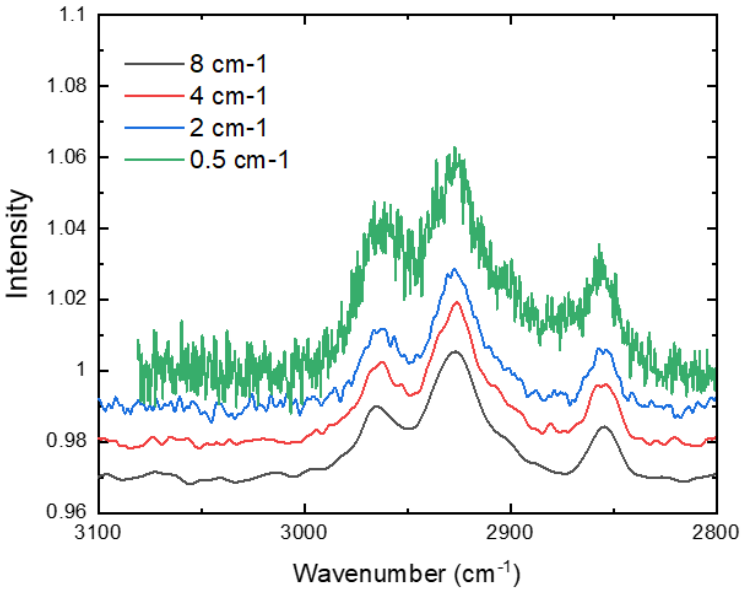

Figure C.2 Comparison of CH stretching region for the same alkanethiol SAM on gold at 4 different resolution settings in OMNIC software. All other settings are the same. The resolution is different from—but scales with—the data spacing. At 0.5 cm $^{-1}$ resolution, significant background oscillation becomes apparent.

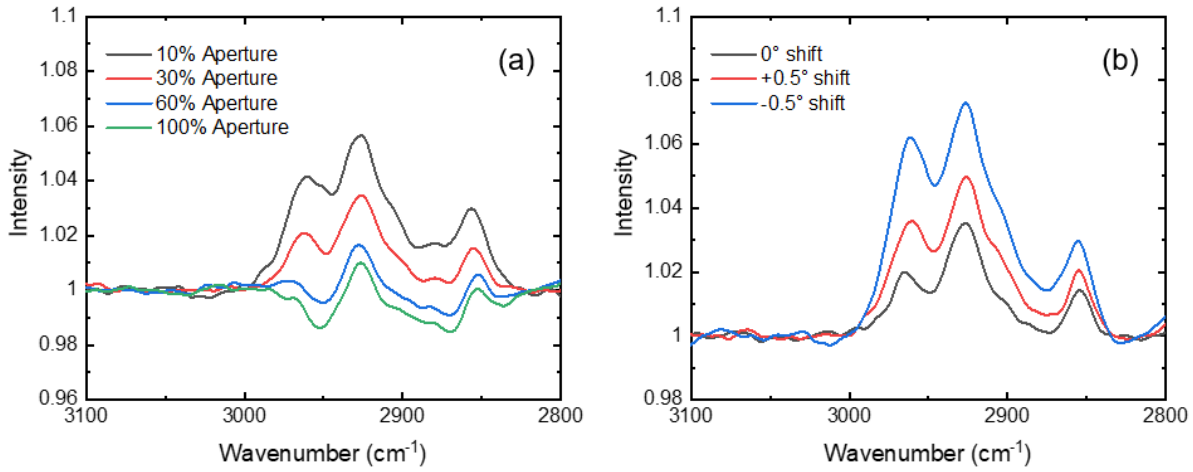

Figure C.3 Comparisons of CH stretching region for the same alkanethiol SAM on gold. a) Size of beam aperture was changed between 100% open and 10% open. All other settings held constant. b) Optics shifted to +0.5° and -0.5° grazing angle. No changes were made to the software settings.

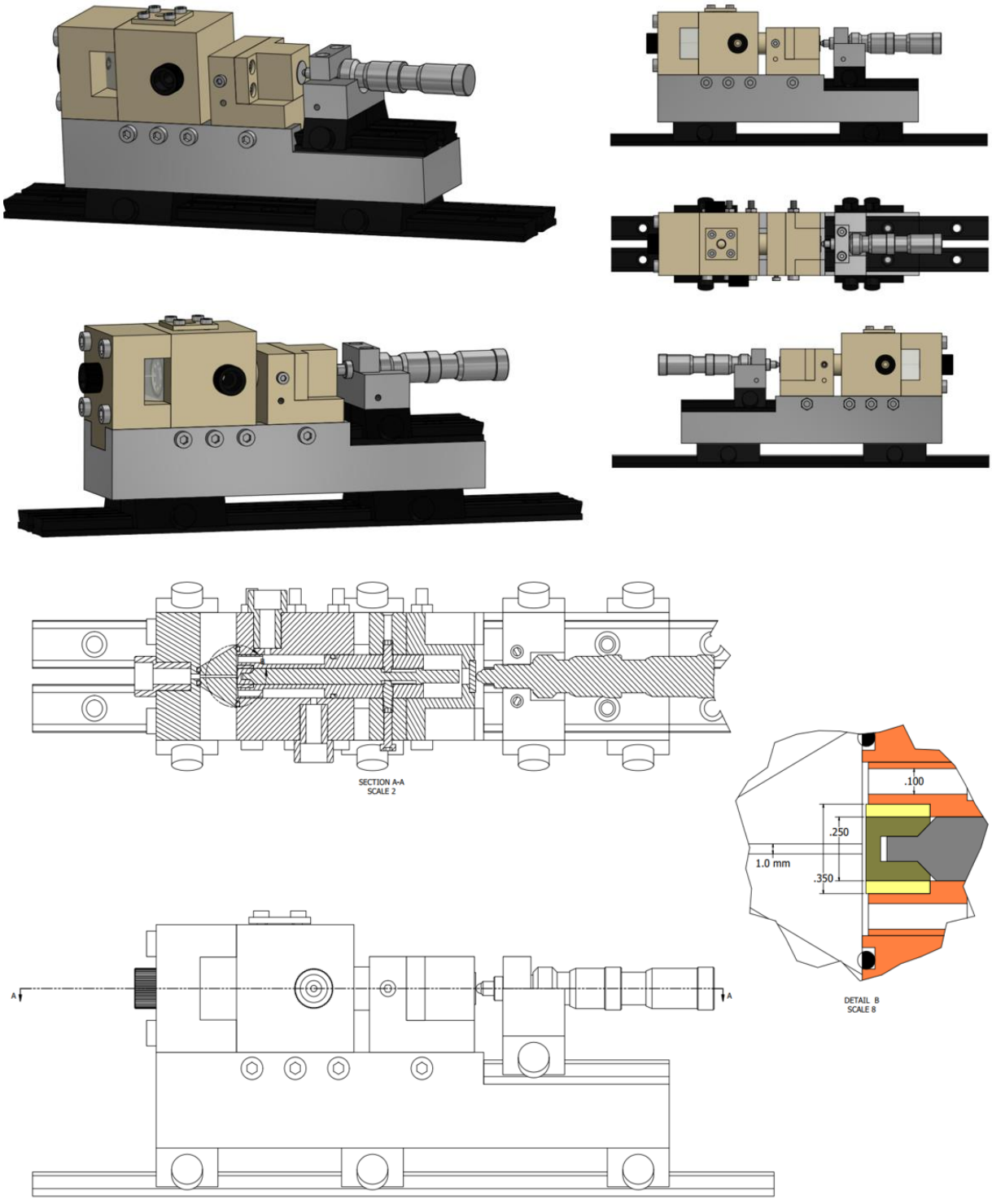

Figure C.4 Additional views of the PM-IRRAS SEC-FC

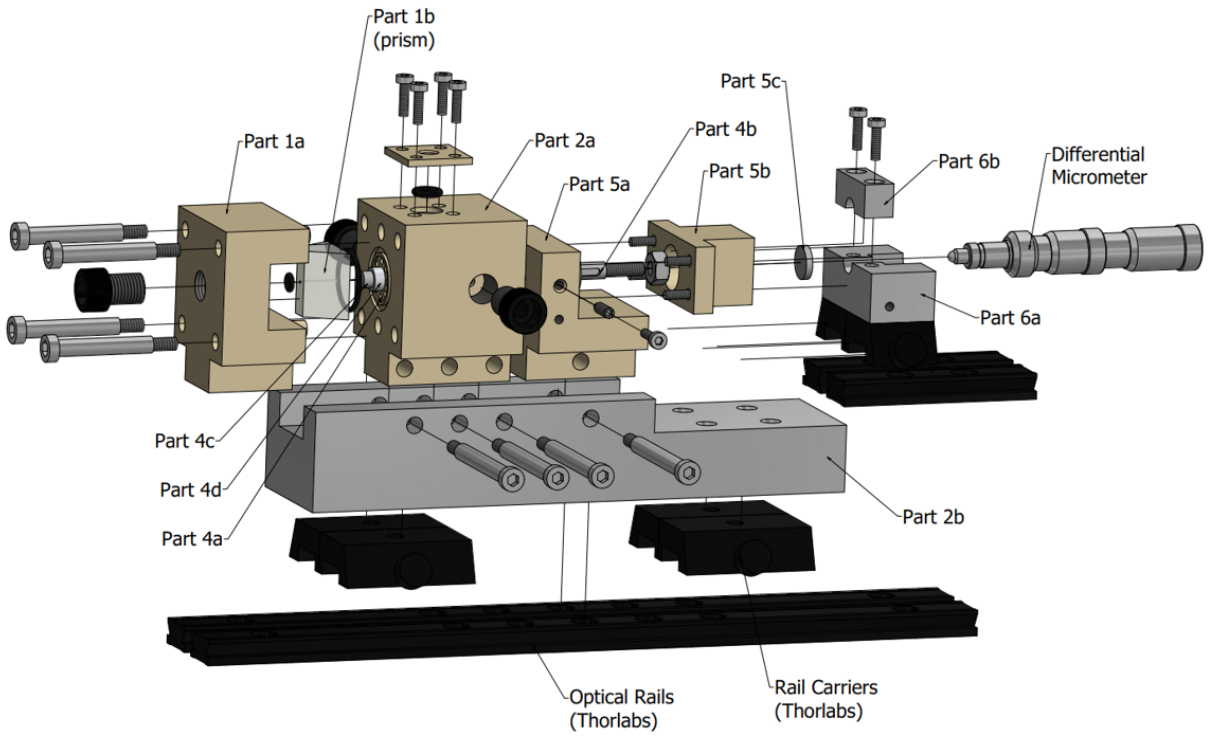

Figure C.5 Exploded view of the PM-IRRAS SEC-FC demonstrating the relative positioning of components

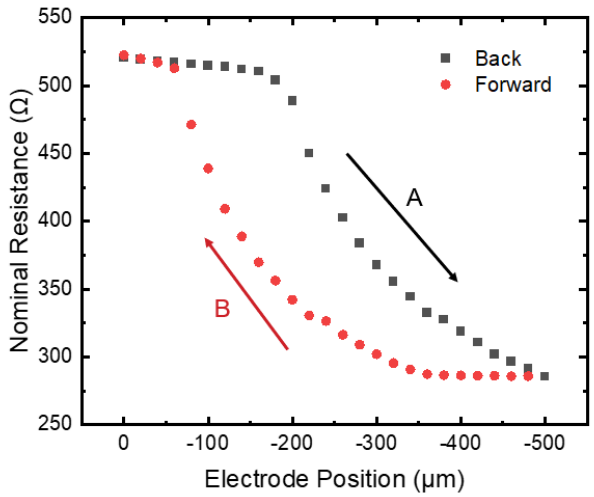

Figure C.6 Plot of micrometer setting vs. nominal resistance of the PM-IRRAS SEC-FC as measured by ZIR drop. Solution was 0.1 M KOH. First the micrometer was positioned with the electrode pressed against the window, then incrementally retracted (A). Upon reaching -500 microns, from electrode-window contact, incrementally moved forward again (B), demonstrating hysteresis that indicates flex in the positioning system.

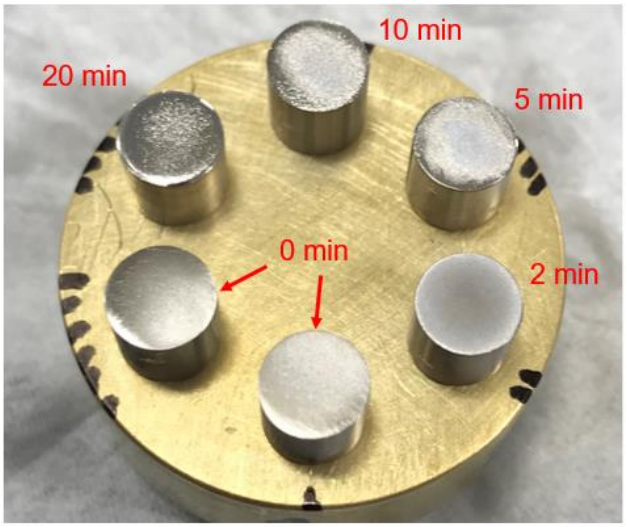

Figure C.7 Photograph of Ti electrodes with (2-20 min) and without (0 min) an electropolishing step after sequential diamond polish. Depending on the polishing time, effects range from oxidative filming to extreme pitting and edge rounding.

Schematic Figures of PM-IRRAS SEC-FC Parts

The following schematics were originally prepared using AutoDesk Inventor as a guide for machining the SEC-FC parts. They are included here as a useful visual aid to understanding the structure and function of the cell.

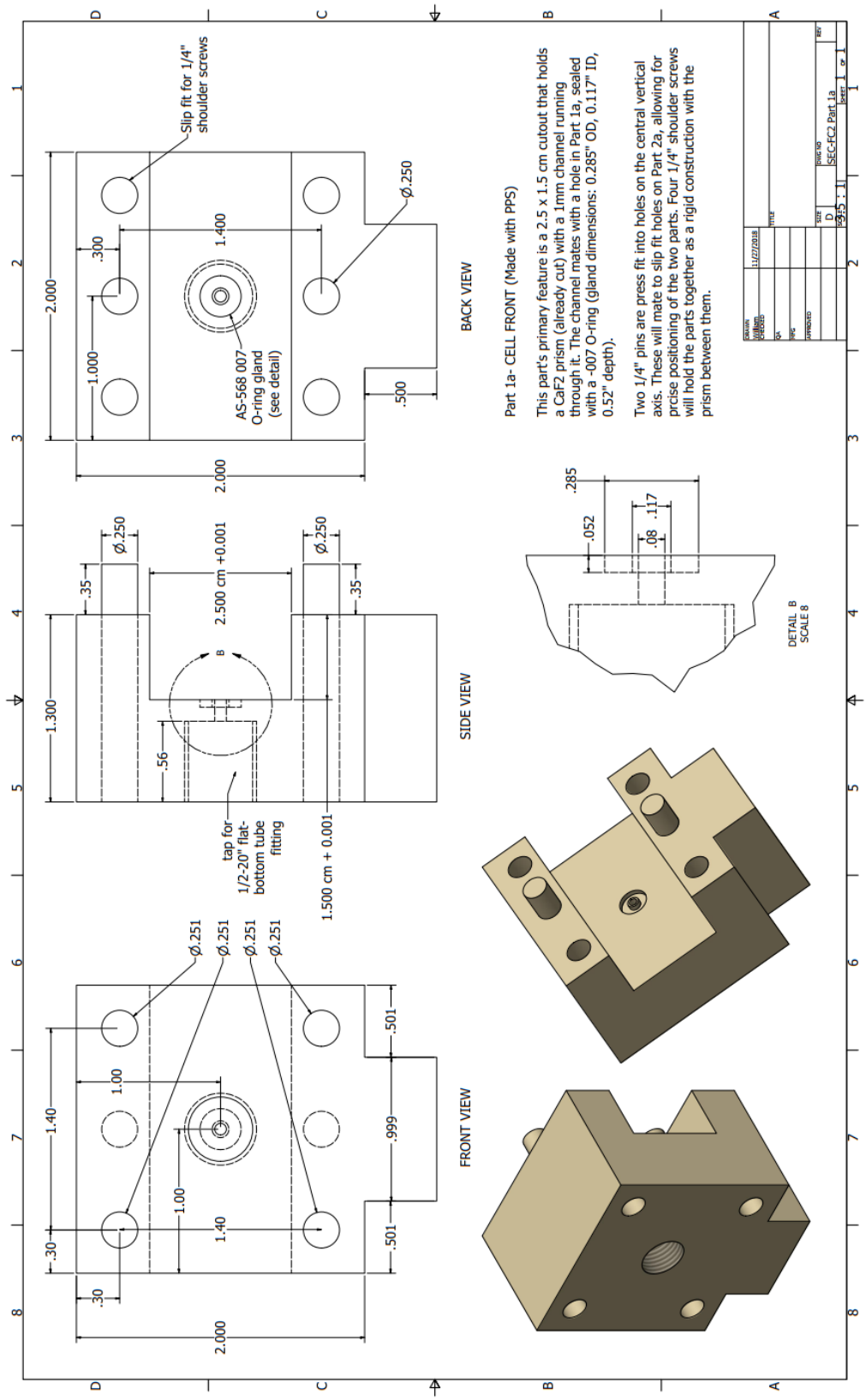

Figure C.8 Part 1a schematic

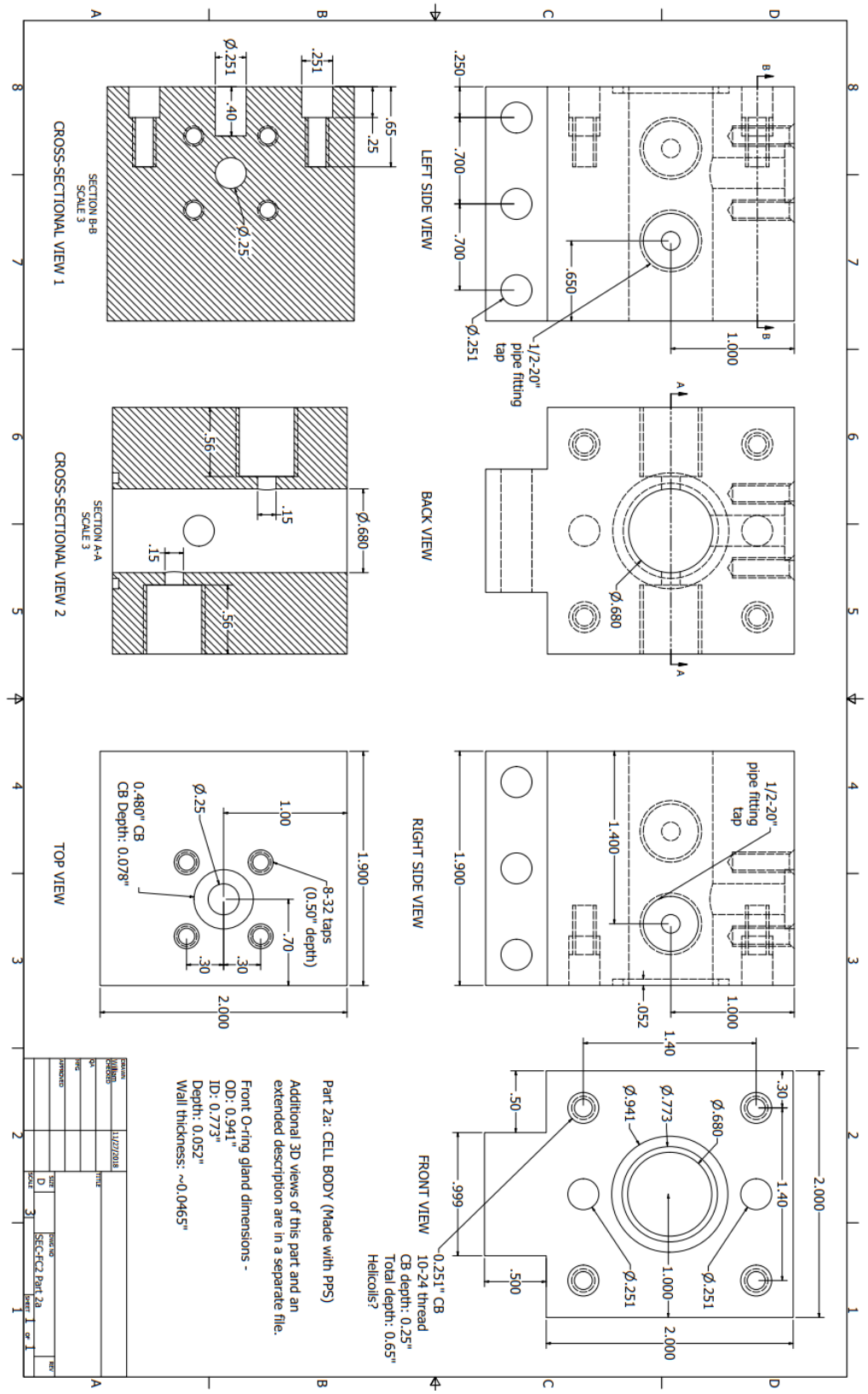

Figure C.9 Part 2a schematic 1

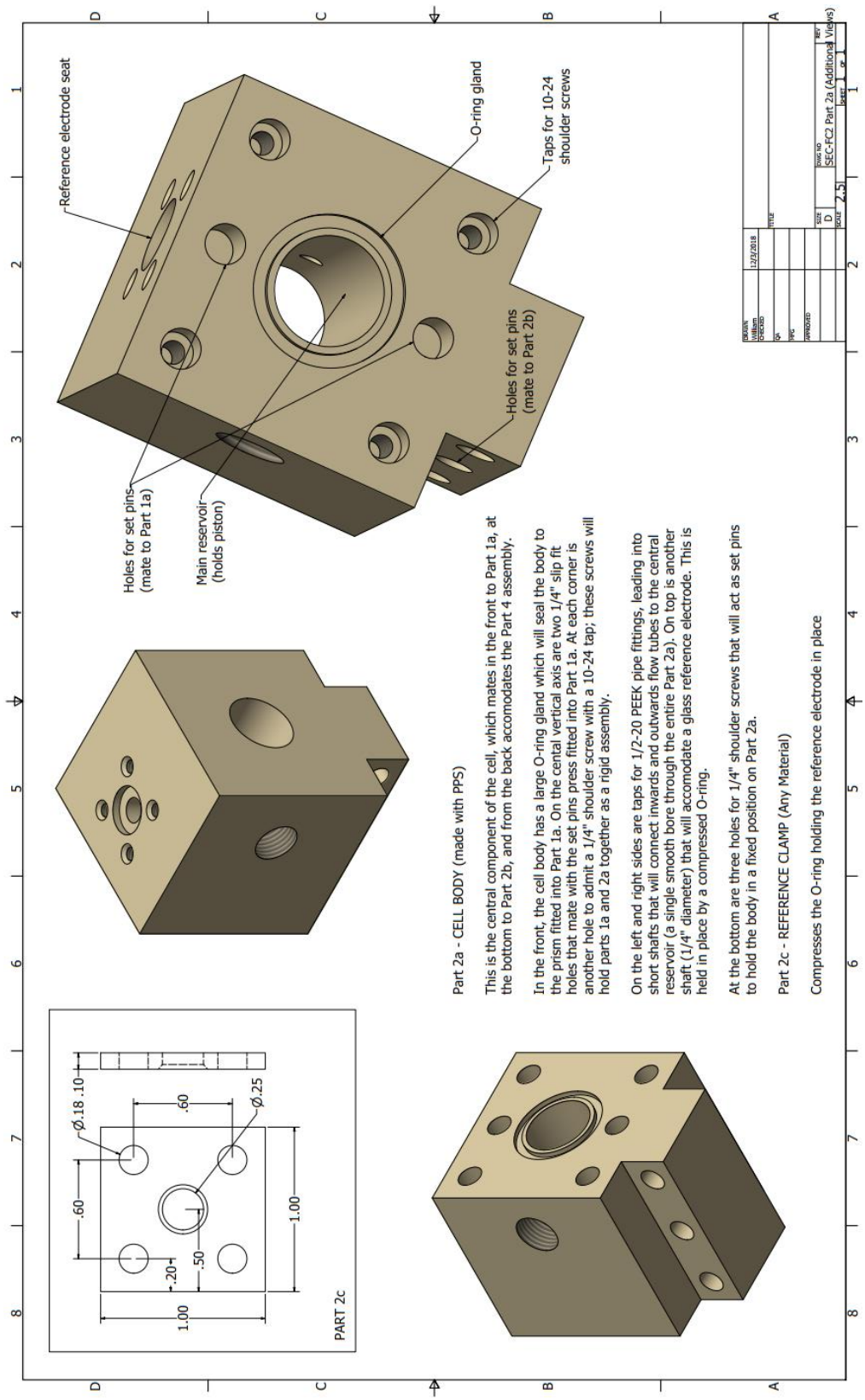

Figure C.10 Part 2a schematic 2

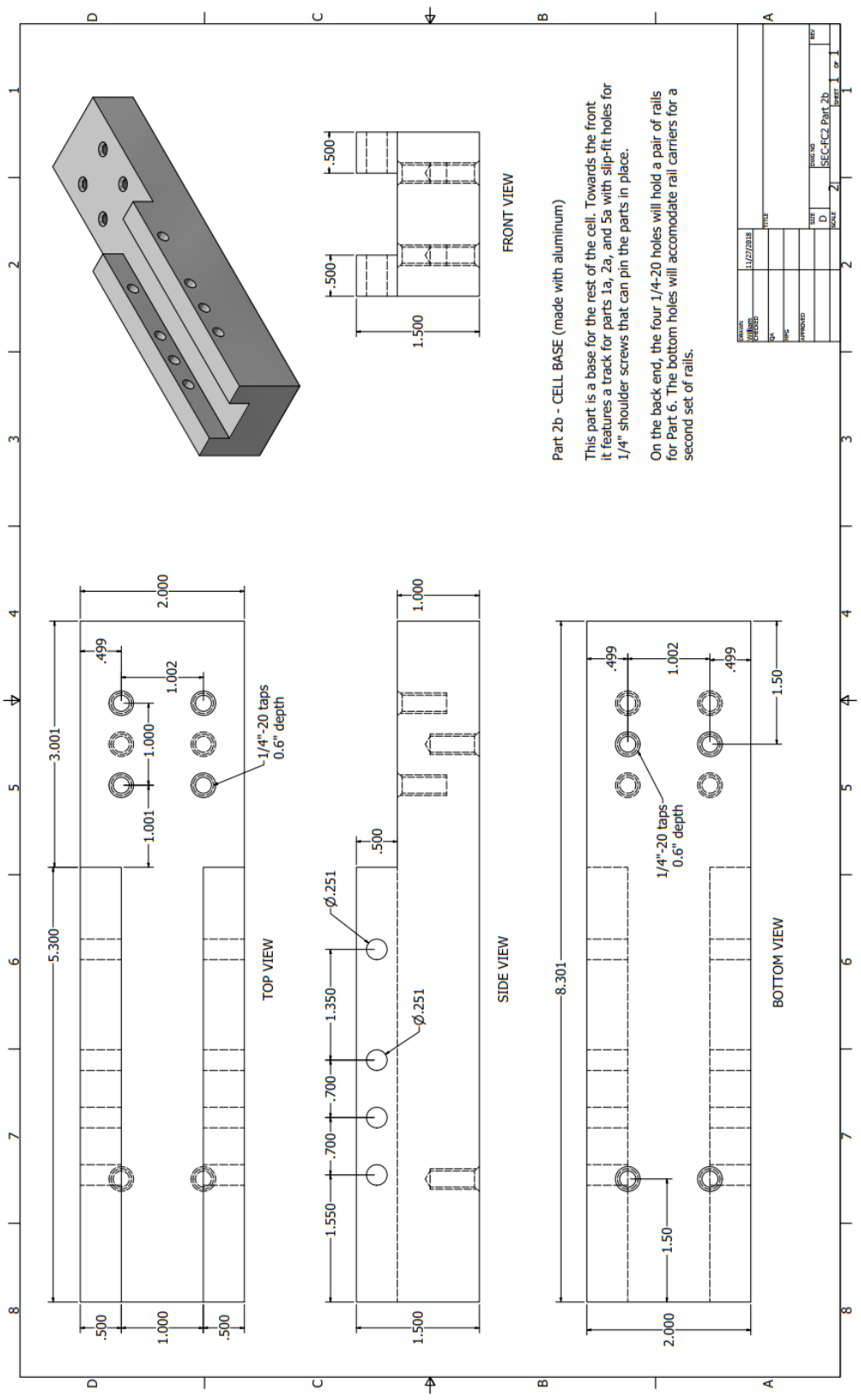

Figure C.11 Part 2b schematic

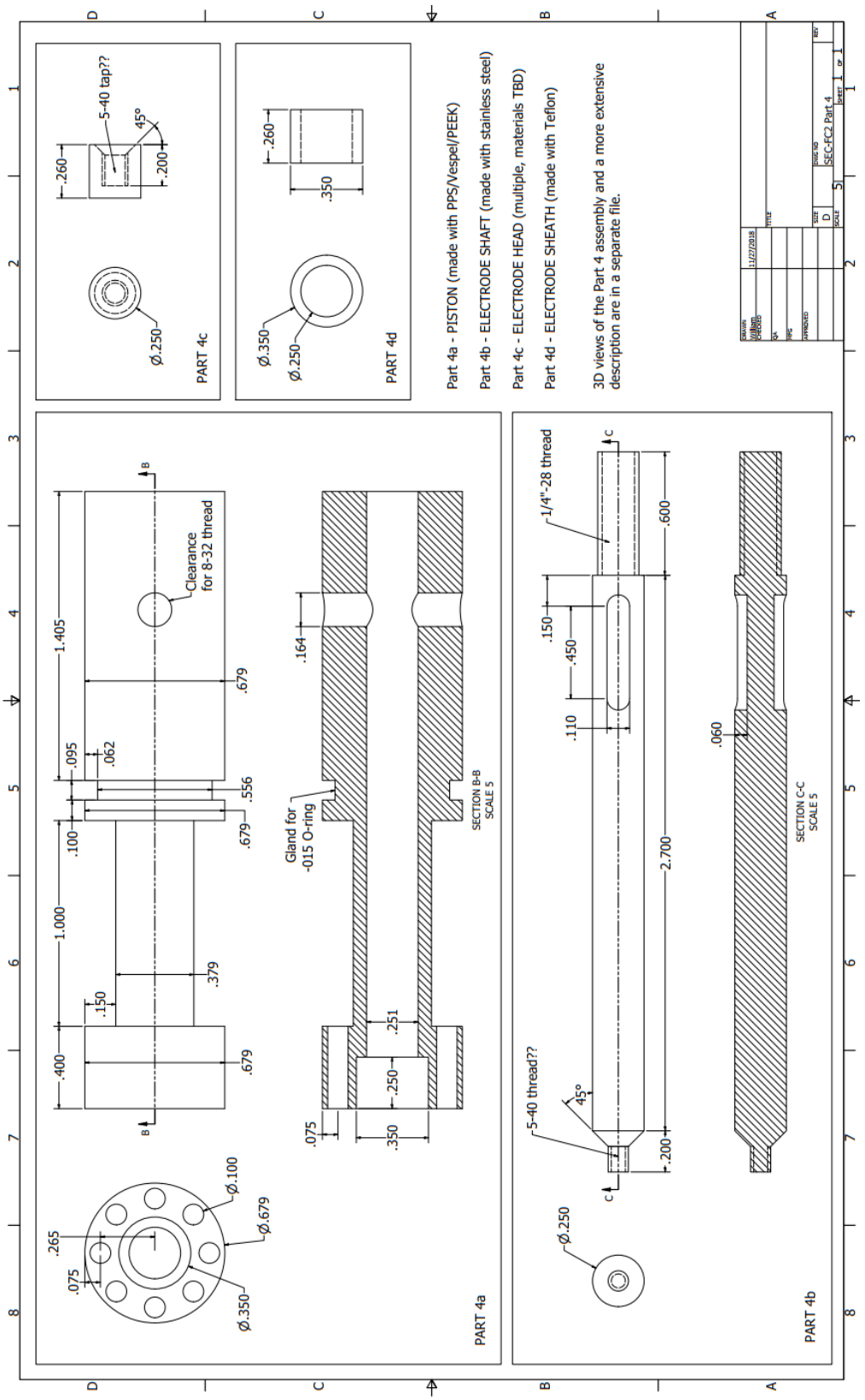

Figure C.12 Parts 4a-d schematic 1

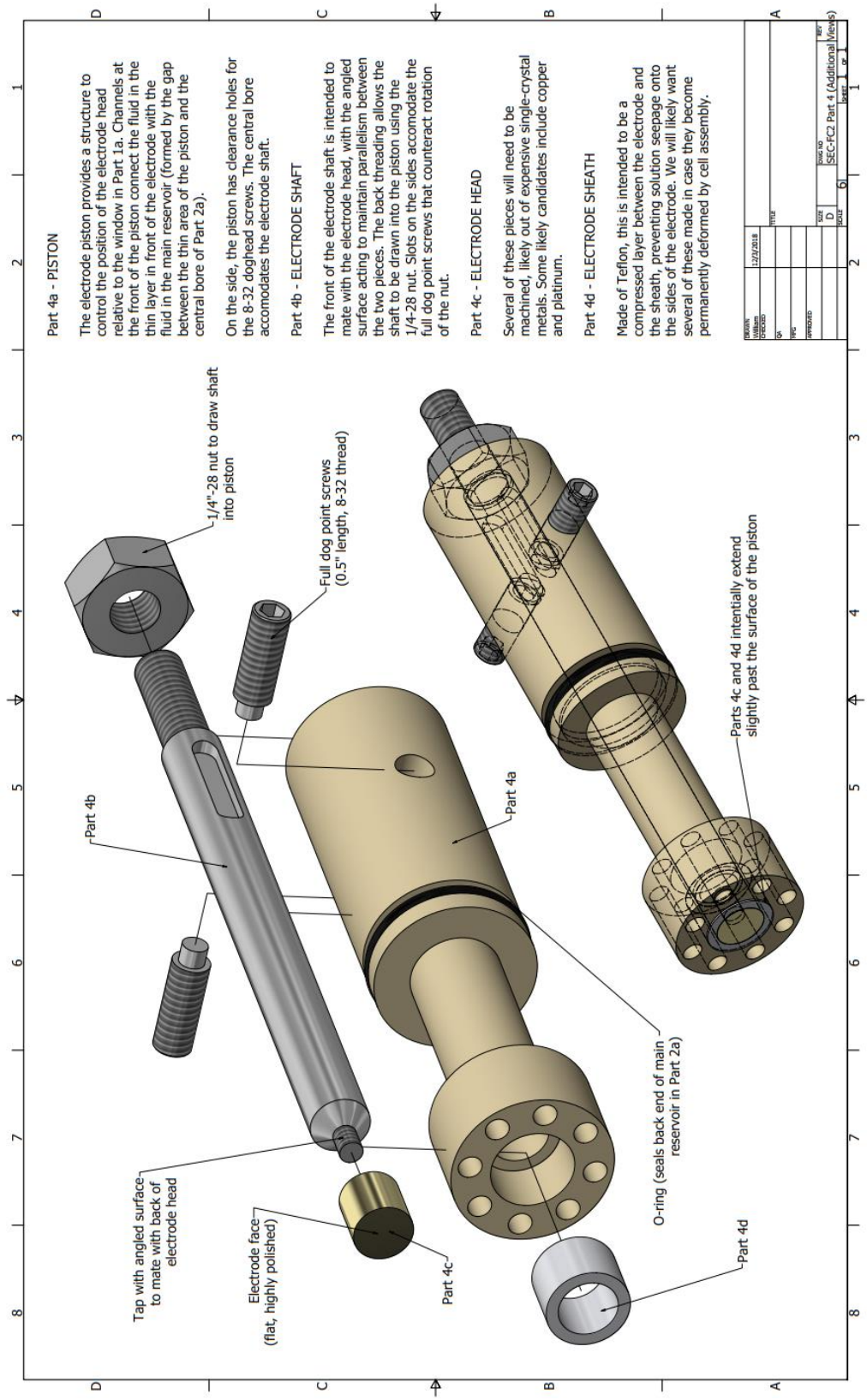

Figure C.13 Parts 4a-d schematic 2

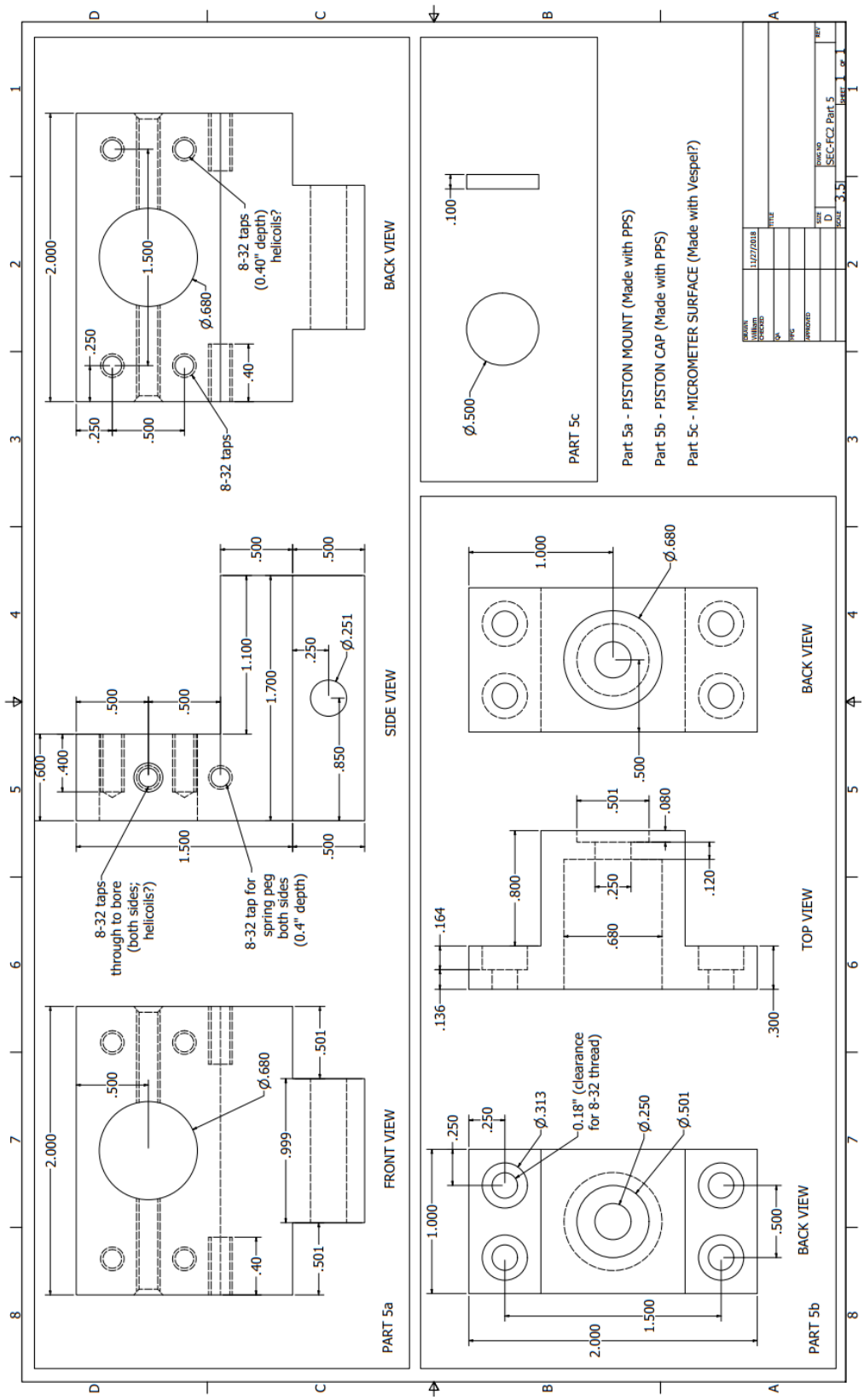

Figure C.14 Parts 5a-c schematic 1

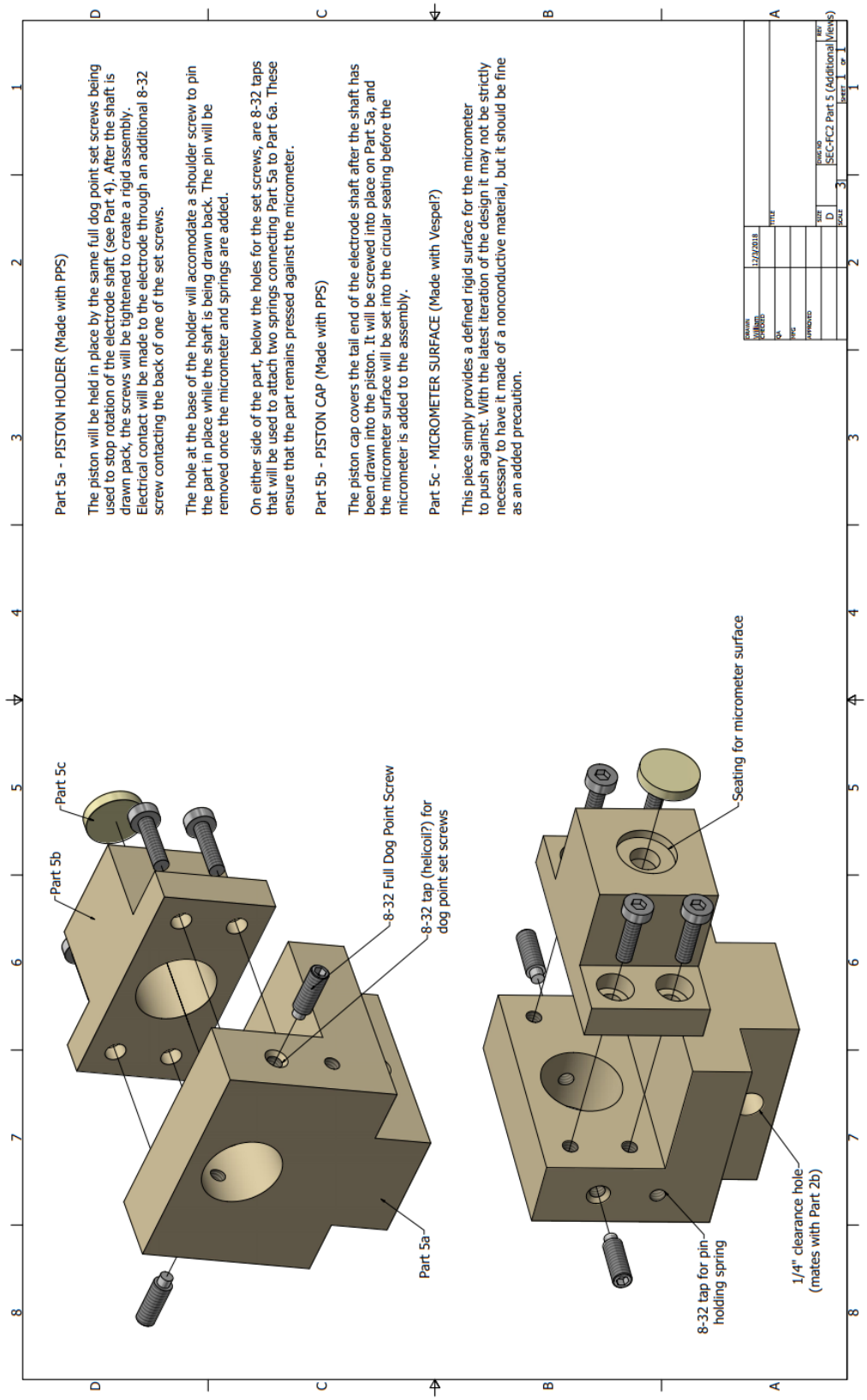

Figure C.15 Parts 5a-c schematic 2

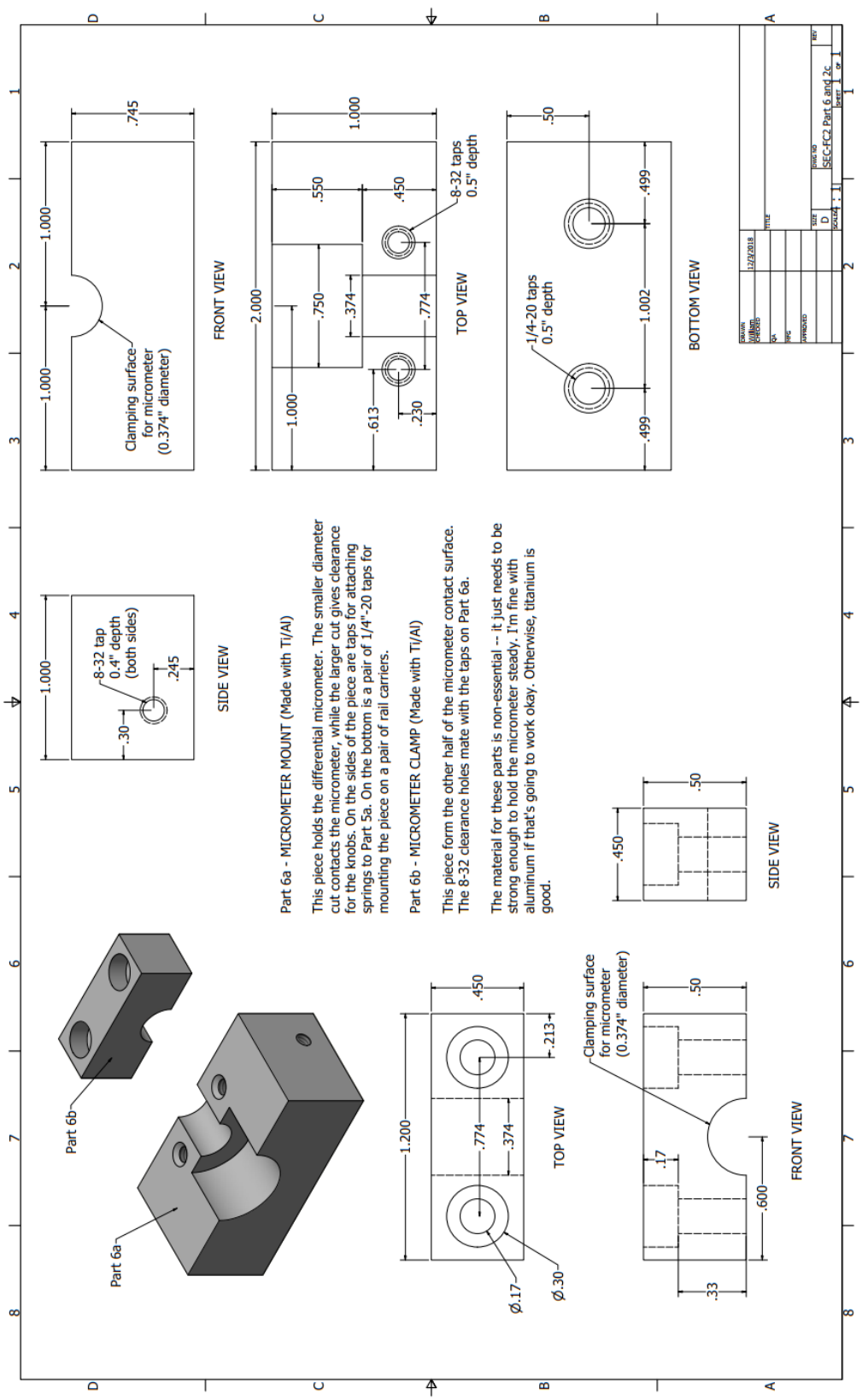

Figure C.16 Parts 6a-b schematic